STUDY AND DEVELOPMENT OF LAYERED LI-NI-MN-CO OXIDE POSITIVE ELECTRODE MATERIALS FOR LITHIUM ION BATTERIES

by

Jing Li

Submitted in partial fulfilment of the requirements

for the degree of Doctor of Philosophy

at

Dalhousie University

Halifax, Nova Scotia

August 2016

To those who taught me

To those who will teach me

TABLE OF CONTENTS

LIST OF TABLES

LIST OF FIGURES

ABSTRACT

Layered Li-Ni-Mn-Co oxides (NMC) with low cobalt content are promising positive electrode materials for Li-ion batteries. However, the detailed structural properties of these materials are still debated. This thesis work, in part, focused on a systematic study of layered NMC samples to understand the dependence of electrochemical properties on structure and transition metal composition, as well as the structural evolution of layered NMC materials during lithium intercalation.

The calendar and cycle lifetimes of lithium-ion cells are affected by the structural stability of active electrode materials as well as parasitic reactions between the charged electrode materials and electrolyte that occur in lithium-ion batteries. It is necessary to explore the failure mechanisms of layered NMC/graphite cells to guide future improvements. This thesis work, in part, thoroughly studied the failure mechanisms of $LiNi_{0.8}Mn_{0.1}Co_{0.1}O_2$/graphite cells from the perspectives of the bulk structural stability, surface structure reconstruction and electrolyte oxidation.

Core-shell (CS) structured positive electrode materials based on layered NMC could be the next generation of positive electrode materials for high energy density lithium-ion batteries. This is because a high energy core material (Ni-rich NMC), with poor stability against the electrolyte, can be protected by a thin layer of a stable and active shell material with lower Ni and higher Mn content. A large part of this thesis focused on the development of CS materials using Li-rich and Mn-rich materials as the protecting shell for voltages above 4.5 V, and on an understanding of inter-diffusion phenomena observed during the synthesis of core-shell materials.

LIST OF ABBREVIATIONS USED

a, b, c	Unit cell lengths
BSE	Backscattered electron
BMF	Blown microfibre separator
C	C as in C-rate
C	Concentration of an element
CE	Coulombic efficiency
CS	Core-shell
CSTR	Continuously stirred tank reactor
d	Atomic plane spacing
$\widetilde{D}$	Interdiffusion coefficient
$\widetilde{D}_{ij}^{n}$	Ternary interdiffusion coefficient
$\widetilde{D}_{i,\Delta c}^{eff}$	Effective diffusion coefficient
DEC	Diethyl carbonate
DMC	Dimethyl carbonate
EA	Elemental analysis
EC	Ethylene carbonate
EMC	Ethyl methyl carbonate
EDS	Energy dispersive spectroscopy
EELS	Energy loss spectroscopy
EIS	Electrochemical impedance spectroscopy
EV	Electric vehicle
f	Atomic scattering factor
F	Geometrical structure factor
FIB	Focused ion beam
FWHM	Full width at half maximum
GC-MS	Gas chromatography coupled with mass spectrometry
H_k	Full width at half maximum of the k^{th} reflection
h	Hours

HAADF	High angle annular dark field
(*h k l*)	Miller indices
HPC	High precision charger
I	Current, intensity of x-rays
I_k	Intensity from the k^{th} Bragg reflection
ICP-OES	Inductively coupled plasma optical emission spectroscopy
IRC	Irreversible capacity
K	Constant from Thompson equation (3.2)
LCO	Lithium cobalt oxide
LiBOB	$LiB(C_2O_4)_2$
L_k	Lorentz-Polarization factor
Li-rich NMC	Layered $Li_{1+x}M_{1-x}O_2$ (M = Ni, Mn and Co, x > 0)
M	Molarity (mol/l)
M_k	Multiplicity of the k^{th} reflection
MMDS	Methylene methanedisulfonate
MSO4	A mixed metal sulfate solution
n_j	Site occupancy factor of atom j
NMC	Li-Ni-Mn-Co Oxides
NMC111	$LiNi_{0.33}Mn_{0.33}Co_{0.33}O_2$
NMC442	$LiNi_{0.42}Mn_{0.42}Co_{0.16}O_2$
NMC532	$LiNi_{0.5}Mn_{0.3}Co_{0.2}O_2$
NMC622	$LiNi_{0.6}Mn_{0.2}Co_{0.2}O_2$
NMC811	$LiNi_{0.8}Mn_{0.1}Co_{0.1}O_2$
NMP	1-methyl-2-pyrrolidone
P_k	Possible modification of intensity due to preferred orientation
ppm	Parts per million
PVDF	Polyvinylidene fluoride
Q	Capacity
R	Goodness of fit factor of Rietveld refinement
R	Radius
Regular NMC	Layered $LiNi_xMn_yCo_zO_2$ (x+y+z = 1)

RPM	Rotations per minute
S	Scale factor
SE	Secondary electrons
SEI	Solid electrolyte interphase
SEM	Scanning electron microscopy
STEM	Scanning transmission electron microscopy
T	Temperature
TTSPi	Tris(trimethylsilyl)phosphite
u,v,w	Fractional atomic coordinates
U,V,W	Refinable parameters for the peak width
V	Voltage, volume
$\bar{V}$	Average voltage
UHPC	Ultra high precision charger
CAD	Canadian dollars
wt%	Weight percent
x	Position
XANES	X-ray absorption near edge spectroscopy
XRD	X-ray diffraction
VC	Vinylene carbonate
θ	Scattering angle in XRD
Δt	Time step
Δx	Spatial step
Δv	Cell volume
ΔV	Difference between the average charge and discharge voltage

ACKNOWLEDGEMENTS

I would like to thank my supervisor, Dr. Jeff Dahn, for his support, encouragement and guidance. Discussion with him was always inspiring. I was excited to work in this lab, and am still excited to work here. It is the place where I gained the most of experiences, and had the most fun of my life.

I would also like to thank the 'Dahn lab' members who taught me, argued with me, helped me and laughed with me. My gratitude goes to Eric McCalla, John Camardese, Ramesh Shunmugasundaram, Jian Xia, Stephen Glazier, Kathlyne Nelson, Remi Petibon, Laura Downie, Lin Ma, Robbie Sanderson, David Stevens and many others. I would also like to thank my summer student Renny Doig who directly contributed to this work.

I am always thankful to my family and friends who have supported me throughout. I am very grateful as always to my guru who taught me to be humble.

Halifax, May, 2016

Jing Li

CHAPTER 1. INTRODUCTION

In the face of imminent climate change caused by the combustion of fossil fuels, new, sustainable, environmentally-friendly energy production and storage technologies must be developed.[1] Lithium-ion battery powered electric cars are strong candidates for the replacement of gasoline-powered cars. Lithium-ion batteries have the advantages of high energy density, rapid charge/discharge capability, high coulombic and energy efficiency and relatively long life time, compared to the other types of batteries such as lead acid and nickel metal hydride batteries, which render it the best candidate for powering electric vehicles.[2,3] In 2014, Tesla Motors announced the Tesla Giga-factory, which is expected to reduce the production cost of lithium-ion batteries used in Tesla products by 30%. The projected capacity of the Giga-factory is 50 GWh/year in 2020 (source from https://en.wikipedia.org/wiki/Gigafactory_1, last checked on Aug. 19, 2016). The recently released Tesla Model 3 is anticipated to have a base price of $35,000 and boast a range of 215 miles between charges. Nevertheless, a significant improvement in the energy density and lifetime of lithium-ion batteries, as well as significant cost reduction, is required for more market penetration of electric vehicles.

Layered lithium cobalt oxide (LCO) is the most common positive electrode material used in portable electronic devices. Cobalt is expensive ($23/ kg on April. 20, 2016)[4], and cobalt-free, or low cobalt alternatives, are required for price reduction. As a result, layered Li-Ni-Mn-Co oxide (NMC) systems with low cobalt content have been extensively studied.[5–10] NMC positive electrode materials for Li-ion batteries are now used at a level

of 35,000 metric tons per year at 2014.[11] However, the detailed structural properties of these materials are still debated. This thesis work, in part, focuses on a systematic study of the phase diagram of layered NMC to understand the dependence of electrochemical properties on structure and transition metal composition.

The calendar and cycle lifetimes of lithium-ion cells are affected by the structural stability of active electrode materials as well as parasitic reactions between the charged electrode materials and electrolyte that occur in lithium-ion batteries.[12–14] The degree of lithium utilization in $LiCoO_2$ is limited to ~75% in order avoid the O3 – H1-3 – O1 phase transformation when $LiCoO_2$ charged above 4.55 V.[15] Additionally, parasitic reactions, such as electrolyte oxidation at the positive electrode/electrolyte interface, can ultimately cause cell failure.[16–19] The rate of the parasitic reactions is related to both the catalytic role of the positive electrode material surface, which depends on its composition and surface area[17,20], as well as on the stability of the electrolyte[16–19]. Electrolyte additives[21–25] and core-shell positive electrode materials[26–28] have been used to reduce the rate and extent of parasitic reactions, and as a result, increase capacity retention and lifetime of high-voltage Li-ion cells. Another major part of this thesis is therefore aimed at studying the failure mechanism of NMC as a function of the potential range chosen for cycle testing, the results of which will aid in further developments.

Layered Li-Ni-Mn-Co oxide materials are excellent positive electrodes candidates for cost effective LIBs.[29,30] A large operating voltage window (upper cut-off voltage higher than 4.5 V in full cells) is needed to further increase the energy density, and minimal electrolyte oxidation is required so the life-time of the cells will not be sacrificed.[31] Besides the

development of novel electrolyte systems using additives or new solvents[21,31–38], coatings on the positive electrode material can minimize electrolyte oxidation in high voltage cells.[39–43]

Core-shell (CS) structured positive electrode materials based on NMC could be the next generation of positive electrode materials for high energy density lithium-ion batteries. This is because a high energy core material, with poor stability against the electrolyte, can be protected by a thin layer of a stable and active shell material with lower Ni and higher Mn content.[26] Core-shell or gradient $LiNi_xMn_yCo_zO_2$ ($x + y + z = 1$) materials for voltages lower than 4.4 V were first developed by Y. K. Sun's group[27,44,45]. These have a high Ni content in the core and increasing Mn content from the core to the surface, with a maximum Mn content on the surface of ~50%. A large part of this thesis will be focused on the development of CS materials using Li-rich and Mn-rich materials [29,46] as the protecting shell for voltages above 4.5 V, and on an understanding of inter-diffusion phenomena observed during the synthesis of core-shell materials.

As an outline of the thesis, Chapter 1 will give a brief introduction to lithium ion batteries, which will focus heavily on the positive electrode materials. Chapter 2 will give a further review of layered Li-Ni-Mn-Co oxide (NMC) as a positive electrode material. The structural and electrochemical properties, failure mechanisms and methods for extending the lifetime of NMC based cells such as coatings and core-shell structures will be described. Chapter 3 describes the experimental tools and theory used throughout this work. Chapter 4 describes a structural and electrochemical study of the Li–Mn–Ni Oxide system within the layered single phase region. Chapter 5 presents an *in-situ* x-ray

diffraction study of layered Li–Ni–Mn–Co oxides and discusses the effect of particle size (secondary) on lithium-rich NMC materials during the first two cycles. Chapter 6 presents a study of the failure mechanisms of cells based on $LiNi_{0.8}Mn_{0.1}Co_{0.1}O_2$ (NMC811) positive electrode material. Chapter 7 further explores the possible failure mechanism of the NMC811 cells by using transmission electron microscopy to study the surface structure reconstruction. Chapter 8 describes the synthesis and characterization of lithium-rich core-shell positive electrode materials with low irreversible capacity and mitigated voltage fade. Chapter 9 discusses the interdiffusion of transition metals in layered NMC materials during sintering of a binary system, which was found during synthesis of core-shell materials. Chapter 10considers the effect of interdiffusion in a ternary system. The effects of the initial shell thickness, sintering temperature and interdiffusion during sintering on the electrochemical performance of core-shell positive electrode materials will be shown. Chapter 11 summarizes this thesis and makes suggestions for future work.

1.1 Lithium-Ion Batteries

Lithium ion batteries typically consist of a positive electrode, a negative electrode, a separator and electrolyte. The electrochemically active materials for the positive electrode are typically a lithium metal oxide ($LiMO_2$) or a lithium metal phosphate, which have either a layered or tunnel structure. The negative electrode material is typically graphitic carbon, which has a layered structure. The active materials are mixed with a binder, typically polyvinylidene fluoride (PVDF) or carboxymethylcellulose and a conductive additive, typically carbon black or graphite. The mixture adheres to a metal foil current collector (Al foil for the positive side and Cu foil for the negative side). The positive and negative

electrodes are electrically isolated by a microporous polyethylene or polypropylene separator film.[2]

Both the positive and negative electrode materials can act as hosts to reversibly incorporate lithium in their structures during electrochemical intercalation processes. Lithium is removed or inserted into the host while the host structure is not significantly disrupted. Figure 1.1 shows the schematic of the electrochemical process in a Li-ion cell. During the charge, while an external current is applied, lithium ions are removed from the positive material, $LiMO_2$, (de-intercalation) and inserted into the negative material, graphitic carbon (Li_xC), (intercalation), while electrons are removed from the transition metal 3d band and added to the carbon 2p band in the negative side.[47] This process is reversed during discharge.[2,48–50]

The two half reactions can be represented by the following equations[2]:

$$\mathrm{LiMO_2} \underset{D}{\overset{C}{\rightleftharpoons}} x\mathrm{Li^+} + x\mathrm{e^-} + \mathrm{Li_{1-x}MO_2} \tag{1}$$

$$\mathrm{yC} + x\mathrm{Li^+} + x\mathrm{e^-} \underset{D}{\overset{C}{\rightleftharpoons}} \mathrm{yLi}\underset{\overline{y}}{x}\mathrm{C} \tag{2}$$

The total reaction can be represented by:

$$\mathrm{LiMO_2} + y\mathrm{C} \underset{D}{\overset{C}{\rightleftharpoons}} \mathrm{Li_{1-x}MO_2} + \mathrm{yLi}\underset{\mathrm{y}}{\mathrm{x}}\mathrm{C} \tag{3}.$$

In these equations, $LiMO_2$ represents the lithium metal oxide, such as $LiCoO_2$ (LCO), as the positive electrode material, and C represents graphitic carbon as the negative electrode material.

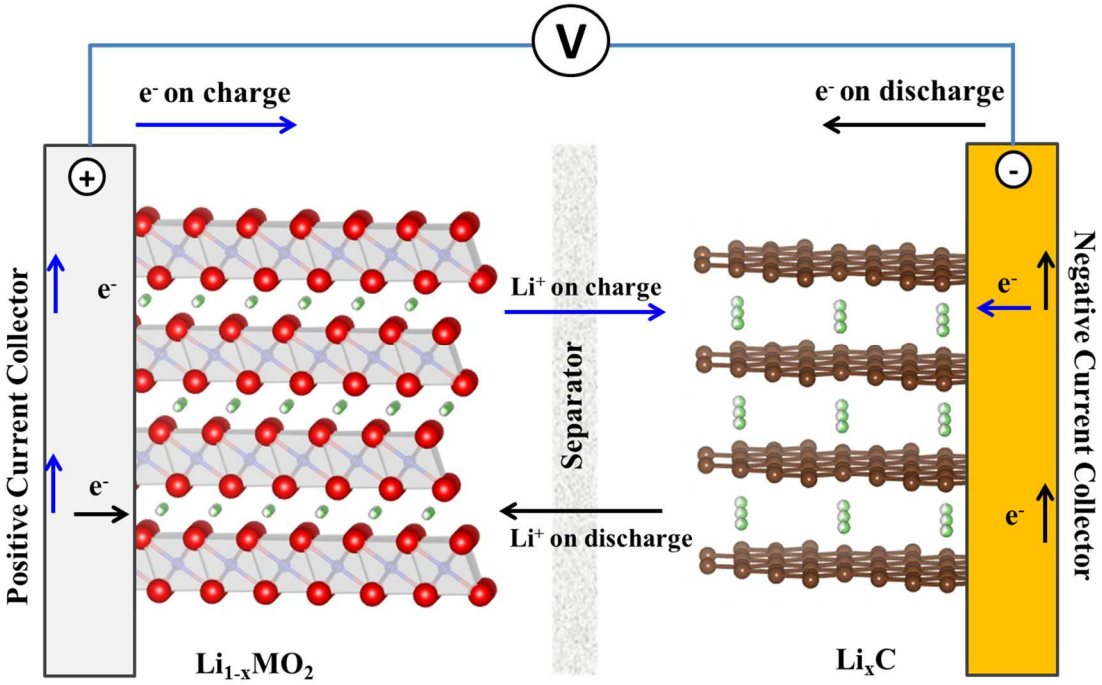

Figure 1.1 Schematic of electrochemical process in a Li-ion cell.

The *C* above the left arrow indicates the charge process while the *D* below the right arrow indicates the discharge process. *x* and *y* are selected based on the molar capacity of each electrode material. Normally, x is ~0.5 for LCO and y is ~0.16 for LiC_6[51,52]. The upper limit of *x* can affect the structural stability of the positive material and its reactivity with the electrolyte[12]. The open-circuit voltage of a cell is defined by the difference of the chemical potentials of the positive and negative electrode, $V_{OC} = (\mu_n - \mu_p)/e$ and e is the magnitude of the electric charge.[50]

Cells using graphitic carbon, or other negative electrode materials other than metallic lithium, are referred to as "full cells". Cells using metallic lithium as the counter electrode material are refed to as "half cells" (also referred to as a lithium battery).[2] Both full cells and half cells will be discussed in this thesis. Full cells are chemically less reactive, safer, and offer longer cycle life than rechargeable lithium batteries.[2] Safety issues with lithium metal are attributed to the changing of morphology of lithium as a cell is cycled which increases its surface area without limit.[2] Additionally, using metallic lithium as the negative electrode would significantly decrease the volumetric energy density of the cell due to the poor cycling efficiency of lithium metal, which requires excess lithium to achieve reasonable lifetime.[53] However, half cells are very useful for preliminary studies of the electrochemical properties of new positive electrode materials such as measuring the voltage - composition curve, determining specific capacity, measuring differential capacity and estimating charge-discharge cycle-life.[2]

1.2 Positive Electrode Materials

The most commonly used positive electrode materials in commercial cells are lithiated metal oxides, such as layered $LiCoO_2$, $LiNi_xMn_yCo_zO_2$, $LiNi_{0.8}Co_{0.15}Al_{0.05}O_2$ (NCA) and $LiMn_2O_4$ (spinel) or lithiated metal phosphates such as $LiFePO_4$.[2,13,14,48–50] The most common commercialized types of NMC materials are $LiNi_{1/3}Mn_{1/3}Co_{1/3}O_2$ (NMC111), $LiNi_{0.42}Mn_{0.42}Co_{0.16}O_2$ (NMC442), $LiNi_{0.5}Mn_{0.3}Co_{0.2}O_2$ (NMC532), and $LiNi_{0.6}Mn_{0.2}Co_{0.2}O_2$ (NMC622). Recently, Ni-rich NMC materials (with more than 60% Ni among the transition metals)[54–64], such as $LiNi_{0.8}Mn_{0.1}Co_{0.1}O_2$ (NMC811), have drawn industrial attention due to their high specific capacity. Li-rich and Mn-rich NMC

materials[46,65–76] , such as $Li[Li_{1/3-2x/3}Ni_xMn_{2/3-x/3}]O_2$ $(0 \leq x \leq 0.5)$[77–79] , have been intensely studied as well. Desirable properties of a positive electrode material include the ability to incorporate a large amount of lithium (high capacity), a stable structure while lithium is reversibly de-intercalated during charge and discharge, and compatibility with other components in the cell. High electronic conductivity and lithium ion mobility are also required for fast charge and discharge. Additionally, the positive electrode materials must be prepared from inexpensive materials with a low cost synthesis process. These are the requirements that must be satisfied for the selection and development of positive electrode materials[2,13,48–50]

The positive electrode materials mentioned above have one of three structure types: a layered structure or ordered rock-salt, a $MgAl_2O_4$-like spinel-type structure, or a $(Mg,Fe)_2SiO_4$ like olivine-type structure.[2,13,48–50] Materials with the layered structure will be the focus of this thesis.

Figure 1.2 shows the O3-type layered structure for LCO, NCA and NMC, which can be described in the $R\bar{3}m$ space group. Lithium is on the 3a sites (lithium layer), transition metals are on the 3b sites (transition metal layer) and oxygen is on the 6c sites.[6] The reason it is called the O3 structure is that the unit cell contains **three** MO_2 slabs and that the transition metal and lithium atoms only occupy the **octahedral** sites.[13] The stacking sequence, using the notation for the stacking of hexagonal close packed planes, is shown in Figure 1.2 as well. The Greek letter indicates the Li position, the small letter indicates the transition metal position and the capital letter indicates the oxygen position.

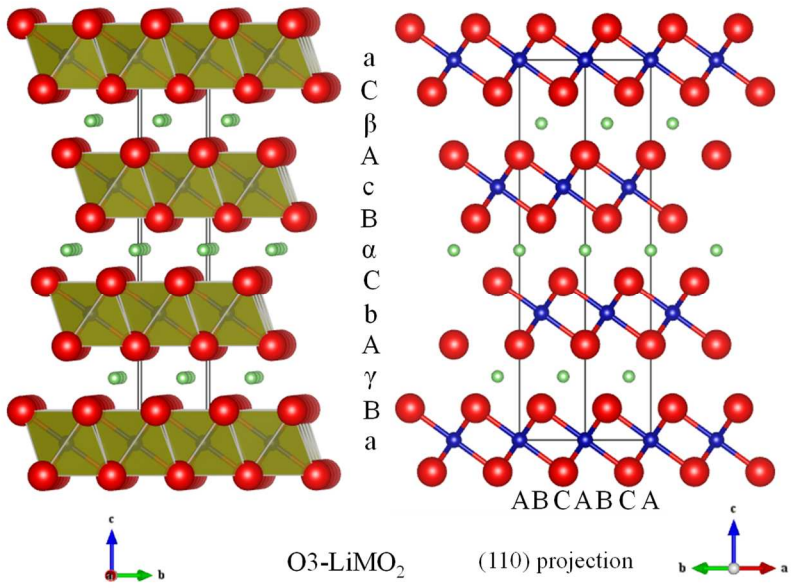

Figure 1.2 Crystallite structure of layered $LiMO_2$ (O3-type) and a (110) projection of the structure. The symbols in between the panels which align with either a transition metal atom layer (small letter), oxygen atom layer (capital letter) or lithium atom layer (Greek letter) show the stacking sequence. The blue, red and green balls show the M, O and Li atoms respectively.

The stacking sequence of the MO_2 (M for transition metal ions) slabs in the overall structure depends on the lithium site occupancy, especially in the case of Li_xCoO_2 when Li is partially removed from the host structure.[52,80] For instance, Figure 1.3 shows the structure of CoO_2 while all the lithium is removed. It adopts the O1 structure that has a unit cell that only contains one slab. Thus, there is a phase transition from O3 to O1 during the deintercalation process, while the transition metals change from 'abc' stacking to 'aa' stacking (Figure 1.2 and 1.3).

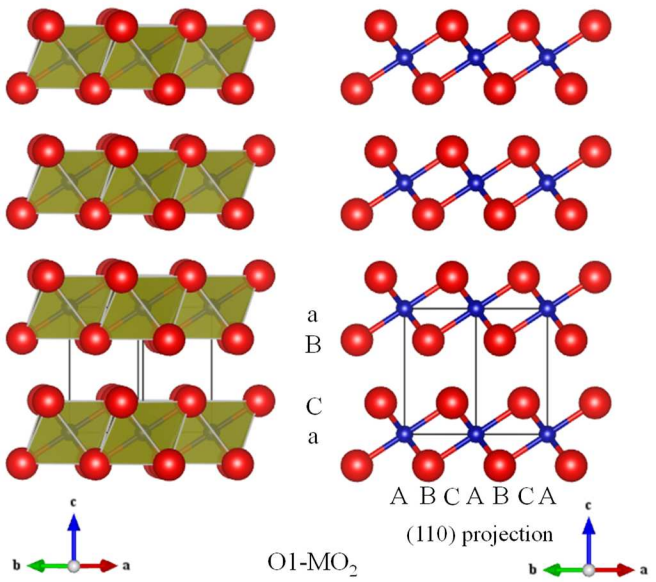

Figure 1.3 Crystallite structure of the layered MO_2 (O1-type) structure and a (110) projection. The symbols in between the panels which align with either a transition metal atom layer (small letter), oxygen atom layer (capital letter) or lithium atom layer (Greek letter) show the stacking sequence. The blue, red and green balls show the M, O and Li atoms respectively.

Another common layered structure for Li-rich and Mn-rich NMC such as $Li_{1+x}M_{1-x}O_2$ (M=Ni, Mn and Co) materials (e.g. $Li[Li_{1/3-2x/3}Ni_xMn_{2/3-x/3}]O_2$ ($0 \leq x \leq 0.5$))[79] is referred to as the M-layered structure by McCalla *et. al.* [6] This has a similar structure to Li_2MnO_3, which can be can be rewritten as $Li[Li_{1/3}Mn_{2/3}]O_2$ and indexed in a monoclinic space group (C_2/m), due to the cationic ordering in the transition metal (TM) layers. In these Li-rich and Mn-rich materials excess lithium partially replaces TM in the TM layers, as indicated in the hexagonal layered structured ($R\bar{3}m$) shown in Figure 1.2. The TM (Ni, Mn and Co)

and Li atoms tend to be ordered on a $\sqrt{3}a_{hex} \times \sqrt{3}a_{hex}$ superstructure in the transition-metal layer in order to minimize Coulomb repulsion.[5,6,81]

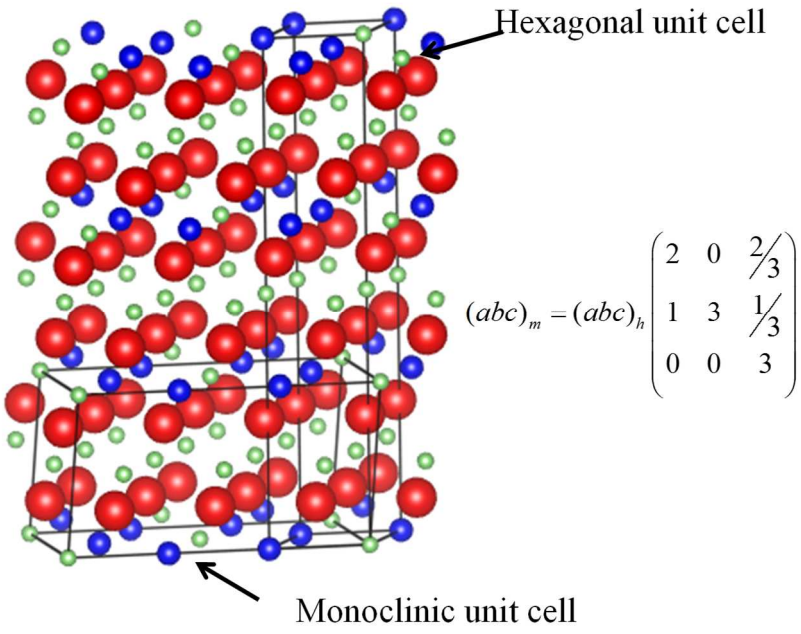

Figure 1.4 Monoclinic and hexagonal unit cells. The blue, red and green balls show the TM, oxygen and Li atoms respectively. The equation in the inset shows the structural relationship between a hexagonal and a monoclinic unit cell.

Figure 1.4 shows the ideal monoclinic and hexagonal unit cells together. The monoclinic cell has 1/3 of the layers of the original hexagonal cell. The relationship between the two unit cells is described in the figure, where *h* and *m* indicate the hexagonal and monoclinic settings respectively.[82] Figure 1.5 shows a projection along the C2/m (010) direction and the atoms in transition metal layer, where red and black lines show the monoclinic and hexagonal unit cells respectively. The blue dashed line shows the $\sqrt{3}a_{hex} \times \sqrt{3}a_{hex}$ super

lattice. Li and TM ions have an ideal ratio of 1:2. In the Li-rich and Mn-rich NMC materials, this ordering is formed between the weakly charged Li^{1+}, Ni^{2+} cations and the strongly charged Co^{3+}, Ni^{3+} and Mn^{4+} cations[6,29,66,83–89].

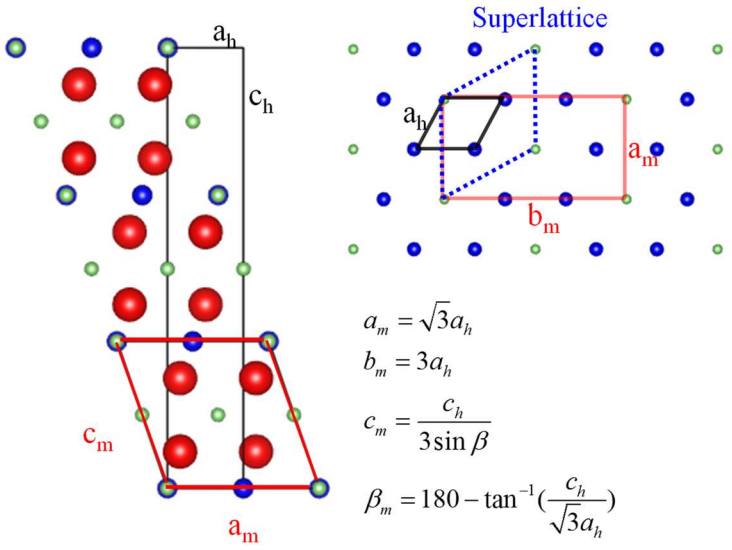

Figure 1.5 Monoclinic and hexagonal unit cell with a monoclinic (010) projection, and the transition metal layers respectively. The blue, red and green balls show the M, O and Li atoms respectively. The equations show the relationship between the monoclinic and hexagonal unit cell parameters.

Physical properties such as particle size distribution, particle shape, specific surface area and tap density are important factors for positive electrode materials. The particle shape, size and distribution will affect the solid state diffusion of lithium atoms from the surface to the bulk, especially when charging and discharging the cell at high rates.[2] A large gradient of lithium content from the surface to the bulk will be established when the diffusion length is long and the current is high.[90] The surface area is an important

parameter to minimize for improved safety and lifetime, due to reactions between the electrolyte and the charged electrode especially at elevated temperatures.[91–94] Hence, a minimum surface area is desired. For a cell to achieve high volumetric energy density, it requires a high density electrode. The tap density of powders can be used as an indicator of the density of a commercial, calendared electrode. These properties are usually affected by the synthesis procedure of positive electrode materials.

LCO is usually made by sintering a mixture of cobalt oxide or carbonate with lithium hydroxide or lithium carbonate at high temperatures. The achieved LCO particles are usually micron-scale single crystals.[80,95,96] Similarly, $LiMn_2O_4$ or $Li_{1+x}Mn_{2-x-y}Al_yO_4$ are normally synthesized by sintering a mixture of manganese dioxide, lithium carbonate and aluminum hydroxide. Boric acid can be added as flux to improve the degree of sintering and particle growth.[97] NMC and NCA require a uniform distribution of cations within the structure. As a result, a mixed metal hydroxide or carbonate precursor made by a co-precipitation method is normally made prior to sintering of the mixture with the lithium source. This results in spherical secondary-particles that consist of primary particles with a size around 200 nm.[98,99]

Normally, LCO, NMC and NCA electrode materials have a specific surface area around 0.1-0.9 m^2/g, a tap density of ~2 – 3 g/cc and a mean particle size of 5 – 20 μm, depending on the type of material and the manufacturer.[2] A specific surface area less than 0.5 m^2/g is preferred to minimize the reactions with electrolyte at the particle surfaces.[2] A detailed review of layered NMC materials including their electrochemical properties will be presented in the next chapter.

1.3 Negative Electrode Materials

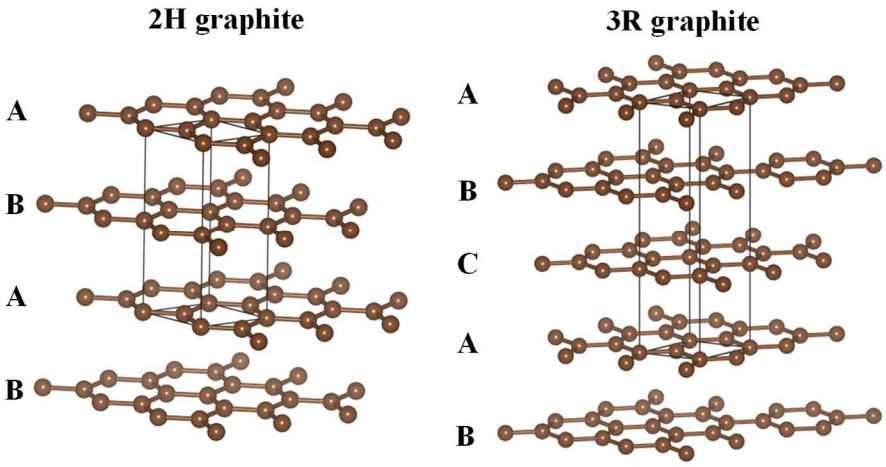

Figure 1.6 Structure of graphite.

Most Li-ion cells use graphitic carbons as negative electrode materials, such as mesocarbon microbead (MCMB) carbon, synthetic or natural graphite. These materials have high specific capacity, from 300 – 365 mAh/g, and a low specific surface area, which ensures low irreversible capacity and good safety properties.[2] Graphite has a highly ordered structure with an ABAB or ABCABC type of stacking along the c-axis, which yields hexagonal (2H) graphite or rhombohedral (3R) graphite respectively.

Figure 1.6 shows the structure of 2H and 3R graphite. 2H graphite can be indexed in the P6/mmc space group with a= 2.46 and c= 6.70 Å. The fractional atomic coordinates of the carbon atoms in layer A and in layer B are (0, 0, 0) (1/3, 2/3, 0) and (0, 0, 1/2) (2/3, 1/3, 1/2), respectively. 3R graphite can be indexed in the R-3m space group with a=2.46 and

c=10.05 Å. The fractional atomic coordinates of layer A, B and C atoms are (0, 0, 0) (1/3, 2/3, 0), (1/3, 2/3, 1/3) (2/3, 1/3, 1/3) and (0, 0, 2/3) (2/3, 1/3, 2/3), respectively.[100]

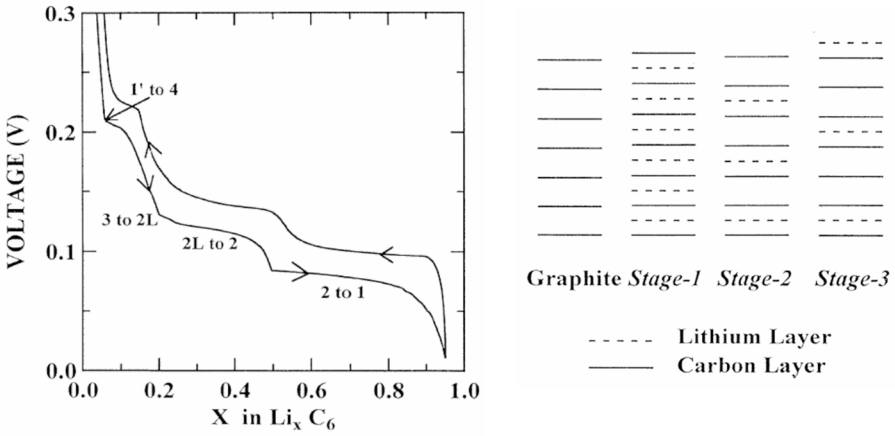

Figure 1.7 Staging of graphite during electrochemical intercalation, reprinted with permission.[102] Copyright (1995) The American Physical Society.

Figure 1.7 shows there are distinct voltage plateaus during the intercalation of lithium into graphite, which are associated with the formation of distinct phases (stages). Lithium atoms form 'islands' instead of a homogenous distribution.[51,101,102] In the coexistence region of two phases, the chemical potential of lithium in the two phases is equal, and as a result, plateaus in the voltage – composition curve are observed in the two phase region.[102]

It is important to use graphitic carbons with the highest degree of order for the highest specific capacity. [102–104] Other important selection factors for graphite powder to be used as negative electrode material for lithium ion batteries are specific surface area, particle

shape, tap density and impurity content.[2] Graphite with the smallest specific surface area is desirable for negative electrode materials to minimize the irreversible capacity and reactivity of the electrode surface with electrolyte.[105,106] A typical particle size of graphite in commercial cells is around 10 - 20 μm with a specific surface area less than 2 m^2/g.[2] Graphite normally has a flaky particle shape, however, spherical shaped graphite is also commonly found in lithium ion cells because the spherical shape minimizes the surface area per volume of material and minimizes the diffusion path length of lithium.[2]

1.4 Electrolyte, Solid Electrolyte Interphase and Additives

Non-aqueous liquid electrolytes are usually used in lithium ion cells, which are solutions of a lithium salt in organic solvents, typically carbonates.[24,107] Lithium hexafluorophosphate ($LiPF_6$) is typically used as the lithium salt due to its high ionic conductivity (10^{-2} S/cm)[108] in carbonate solvents, acceptable safety properties and ability to passivate the aluminum positive electrode current collector at high voltages.[24,107] Other salts are studied in the literature, notably lithium tetrafluoroborate ($LiBF_4$)[109], lithium bis-oxalato borate (LiBOB)[110], and $LiN(CF_3SO_2)_2$[2] usually have lower ionic conductivity in carbonate solvents. Typically, $LiPF_6$ has the highest conductivity with a salt concentration around 1 M at room temperature.[108] However, $LiPF_6$ is relatively costly, hygroscopic and produces hydrofluoric acid (HF) upon reaction with water, which requires handling in a dry environment.[2]

The solvents are usually a mixture of organic carbonates, typically ethylene carbonate (EC) which has a high dielectric constant, in combination with a linear carbonate, such as

dimethyl carbonate (DMC) or ethyl methyl carbonate (EMC), which have low viscosity.[111] This solvent mixture can provide high ion conductivity and high solubility for lithium salts ($\geq$ 1 M).[2] The choice of solvent is also influenced by the temperature range of the application. Low temperature performance requires using low viscosity solutions with low freezing points. [24,107]

Additionally, electrolyte must be stable within the potential window of a lithium cell. Normally, solvents are not thermodynamically stable with Li or Li_xC_6 near 0 V.[2,48,50] Most solvents react and form a passivation film, referred to as a solid electrolyte interphase (SEI), on the negative electrode surface which is ionically conductive and electronically insulating.[2] A stable passivation film can protect the electrolyte from further reaction near the electrode surface.[112] An unstable SEI can lead to capacity fade due to continuous formation and repair of the SEI that irreversibly consumes lithium within the cell.[113] Electrolyte can also be oxidized at the positive electrode surface at high voltages[2,48,50], which leads to production of gas and oxidized species that can migrate and interact with the negative electrode.[114] Furthermore, the presence of impurities, such as water and HF, could also lead to capacity loss as will be introduced in the positive electrode materials section.[2]

Electrolyte additives can significantly improve cell performance and extend the cell lifetime.[24,107] This is because appropriate electrolyte additives can improve the SEI stability, scavenge HF or water, form stable protecting films on the positive electrode, lower impedance growth and improve cell safety.[24,107] Vinylene carbonate[115] promotes the formation of a stable SEI for the negative electrode in lithium ion cells, and is used in many

commercial lithium ion cells. Heptamethyldisilazane[116] was found to be able to remove HF from $LiPF_6$-containing electrolytes. Epicyanohydrin[63], divinyl sulfone[64] and 1,3-propane sulfone[61] can be effective electrolyte additives to stabilize the interface between Ni-rich NMC positive electrodes and electrolyte. Many researchers are now focused on studying electrolyte additives (or combinations of additives) to extend the cell lifetime.

In summary, the cell performance and lifetime depend on the electrode materials, electrolyte and electrode-electrolyte interactions. Stabilizing the electrode/electrolyte interface is the key to extend cell lifetime.

CHAPTER 2. RECENT DEVELOPMENT OF LAYERED NMC BASED POSITIVE ELECTRODE MATERIALS

2.1 Background

Layered oxides such as LCO and NMC compose the majority of positive electrode materials used in LIB developed for mobile devices and power tools.[54] Layered NMC materials can be divided to two categories - regular NMC $LiNi_xMn_yCo_zO_2$ (x+y+z = 1) and lithium rich NMC $Li_{1+x}M_{1-x}O_2$ (M = Ni, Mn and Co). Regular NMC has a lithium to transition metal ratio of about 1:1 and usually has a Ni content that is equal or larger than the other transition metals. Lithium rich NMC usually contains a higher content of Mn than Ni and Co, and a Li/M ratio higher than 1. Regular NMC has a rhombohedral structure in the $R\bar{3}m$space group, and the lithium rich NMC adopts a monoclinic structure similar to Li_2MnO_3 in a C_2/m space group. The details of the two structures and their relationship were introduced in Figures 1.2, 1.4 and 1.5 in Chapter 1. Low cobalt content layered NMC materials will be the focus of this thesis. This chapter will start with a brief introduction to the phase diagram of Li-Ni-Mn-Co oxide, the concept of cation mixing, valence states of the transition metals in layered NMC and the band structure of the materials. It will then discuss the properties of regular NMC and Li-rich NMC materials.

2.1.1 Structure – Composition Diagram of Li-Ni-Mn-Co oxides

Figure 2.1a shows the structure - composition diagram of Li-Ni-Mn oxide for samples prepared at 900ºC in air with a regular cooling rate (5-10ºC/min), which was generated

based on the work of Aaron Rowe[117], Eric McCalla[10] and the work presented in Chapter 4[29].

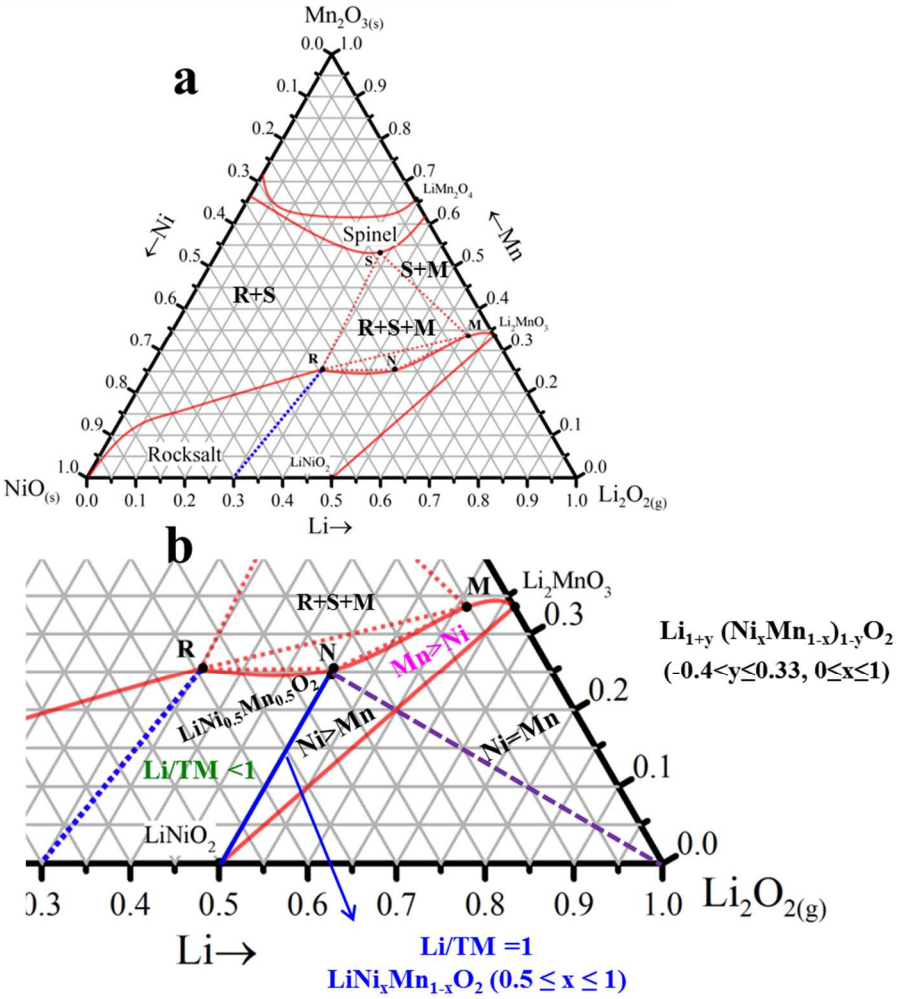

Figure 2.1 Structure - composition diagram of Li-Ni-Mn oxide for samples prepared at 900°C in air with a regular cooling rate (5-10°C/min) (a). The solid redlines borders the boundaries of the single phase layered region in the Li-Mn-Ni-Oxide pseudoternary phase diagram while red dashed lines are tie-lines at the outer edges of the 3-phase regions. S, R, M, N are the end members of the tie lines, representing the spinel, rocksalt, Mn-rich layered and Ni-rich layered phases, respectively. The extended view of the single –phase layered region (b). Copyright (2014) American Chemical Society Reproduced with permission.[29]

The solid redlines border the boundaries of the single phase regions in the Li-Mn-Ni-Oxide pseudoternary phase diagram while red dashed lines are tie-lines at the outer edges of the 3-phase regions. S, R, M, N are the end members of the tie lines, representing the spinel (Fd3m space group), disordered rocksalt ($Fm\bar{3}m$ space group), Mn-rich layered (C_2/m) and Ni-rich layered phases ($R\bar{3}m$), respectively. [10,29] The boundary of the single-phase regions change slightly with the synthesis conditions.[10]

Figure 2.1b shows an expanded view of the single – phase layered region. The materials in the single phase layered region can be denoted as $Li_{1+y}(Ni_xMn_{1-x})_{1-y}O_2$ ($-0.4 < y \leq 0.33$ and $0 \leq x \leq 1$). The solid blue line connecting $LiNiO_2$ and $LiNi_{0.5}Mn_{0.5}O_2$ describes the $LiNi_xMn_{1-x}O_2$ ($0.5 \leq x \leq 1$) series of materials ($y = 0$). On the left of this line (solid blue) in the layered region, the lithium to transition metal ratio is lower than 1 ($y < 0$). In such materials, some transition metals occupy sites in the lithium layer. The purple dashed line shows compositions with Ni to Mn ratio equal to 1 ($x = 0.5$). On the lower left of this line, the Ni to Mn ratio is higher than 1 ($0.5 < x \leq 1$) while to the upper right of this line, the Ni to Mn ratio is lower than 1 ($0 \leq x < 0.5$). A detailed study of Li-Ni-Mn oxides within the layered region will be presented in Chapter 4.

Figure 2.2 shows the composition - structure diagrams in the Li–Ni–Mn–Co–O pseudo-quaternary system at cobalt contents of 0% , 10%, 20% and 30% (among all the cations) for samples regular-cooled after heating to 800°C for 3 h in oxygen. Figure 2.2 shows the addition of cobalt to the Li–Ni–Mn–O pseudo-ternary system caused the single-phase layered region to decrease in size.[5]

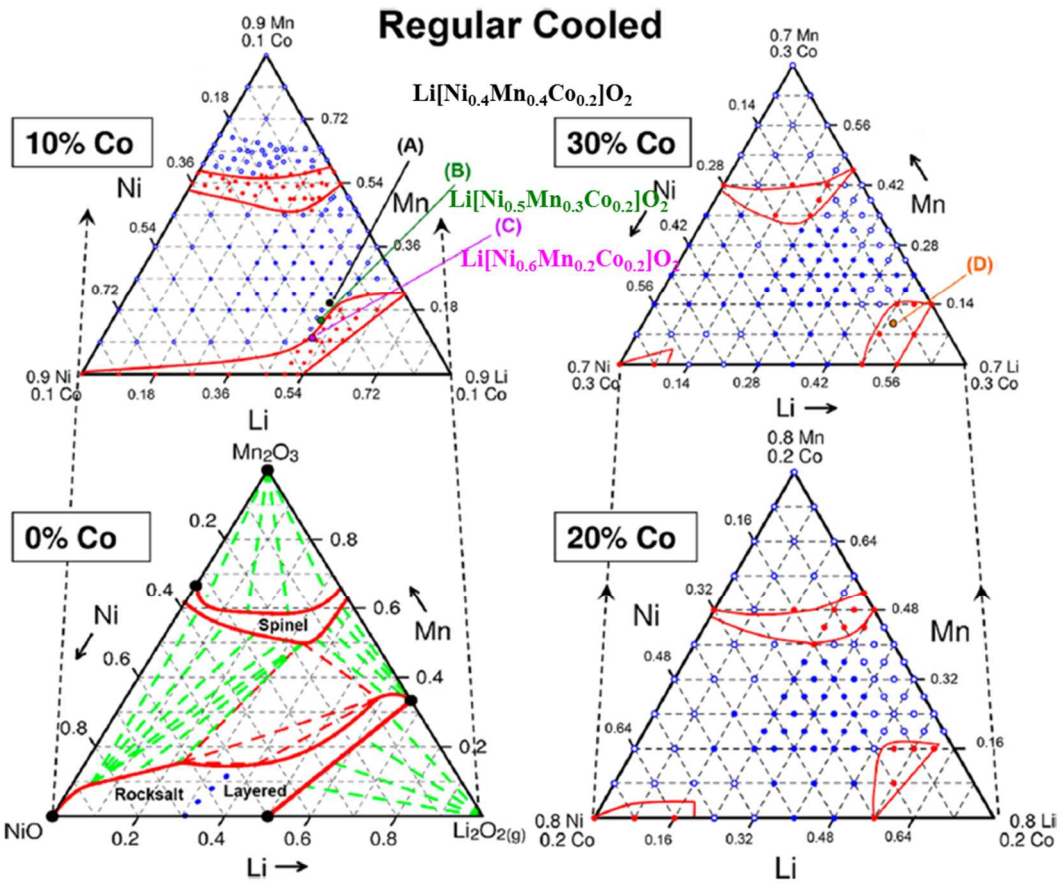

Figure 2.2 Composition – structure diagrams in the Li-Ni-Mn-Co-O pseudo-quaternary system at cobalt contents of 0%, 10%, 20%, and 30% for samples regular-cooled after heating to 800°C for 3 h in oxygen. Reproduced with permission.[5] Copyright (2015) American Chemical Society.

2.1.2 Cation Mixing and Impact

Figure 2.3a schematically shows the Li and Transition metal (TM) layeres in an ideal layered $LiMO_2$ structure, where lithium atoms only occupy the sites in lithium layer and

transition metal atoms stay in the transition metal layer. However, layered NMC materials usually have some nickel atoms present in in the lithium layer while an equivalent amount lithium atoms occupy sites in the transition metal layers.

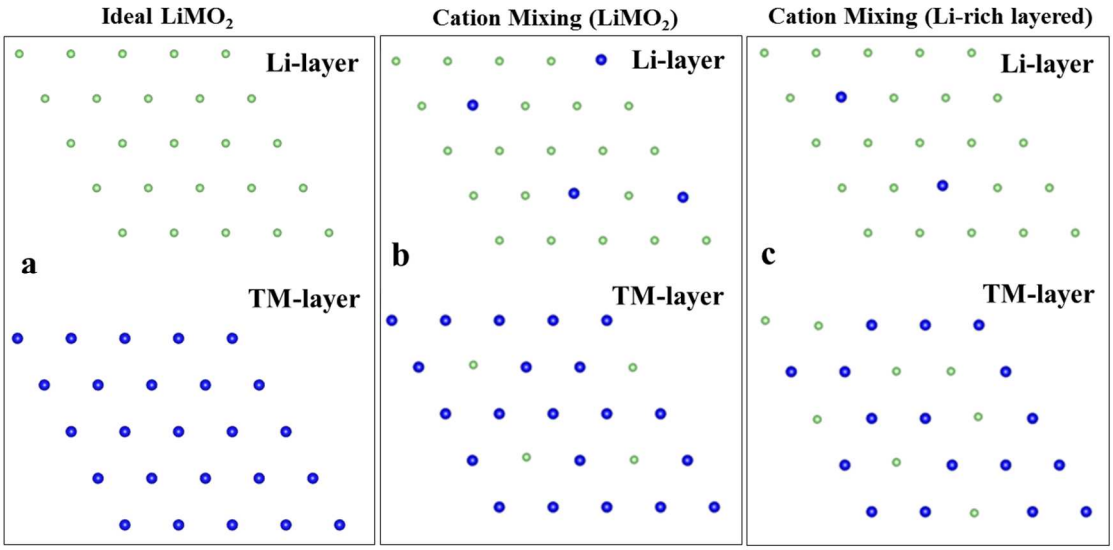

Figure 2.3 Li layer and transition metal layer in ideal layered $LiMO_2$ (M=Ni, Mn, and Co) (a). Li layer and transition metal layer in layered $LiMO_2$ with cation mixing (b). Li layer and transition metal layer in Li-rich layered structure with cation mixing (c). The green and blue balls indicate the lithium and transiton metal atoms respectively.

For instance, $LiNi_{0.5}Mn_{0.5}O_2$ has about 10% nickel atoms in the lithium layer.[118] Figure 2.3b schematically shows this phenomenon, which is termed cation mixing, where the nickel atoms in transition metal layer and lithium atoms in the lithium layer exchanges sites. Lithium-rich NMC materials usually have a very small degree of cation mixing, but have Li atoms in the TM layer by necessity as schematically shown in Figure 2.3c.[29]

The presence of nickel ions in the lithium layer can impede lithium diffusion, decrease reversible capacity and lower rate capability.[13] The degree of cation mixing can be affected by transition metal composition, lithium content, heating temperature *etc*. Z. Lu *et al.* showed that with the substitution of Co in $LiNi_{0.5}Mn_{0.5}O_2$ ($LiNi_xMn_xCo_{1-2x}O_2$ ($0 \leq x \leq 0.5$)), the amount of Ni in the lithium layer decreased as Co concentration increased.[119,120] With the increase of lithium content, excess lithium atoms substitute transition metal atoms in the transition metal layer which results in a decrease in the degree of cation mixing.[29] Additionally, it was shown by Whittingham that high temperature sintering increases the degree of cation mixing during the synthesis of regular NMC materials.[13] The degree of the cation mixing can be estimated from Rietveld refinement of x-ray diffraction data.[81]

2.1.3 Electronic Structure of Layered NMC Materials

In layered NMC materials, Mn is usually tetravalent, Co is trivalent, Ni can be divalent and/or trivalent.[121] During electrochemical intercalation of lithium, electrons are added/removed from the transition metal 3d band while lithium ions are insersted/removed from the host structure.[47] Figure 2.4a shows the schematic 3d electron levels of transition metals in NMC compounds, which split to a lower energy t_{2g} sub-band that contains six states and a higher energy e_g sub-band that has four states in an octahedral crystal field.[47,120,122] Figure 2.4a shows Mn^{4+} has three unpaired electrons occupying the t_{2g} band, which is usually electrochemically inactive. However, in lithium rich NMC materials, Mn^{4+} can sometimes be reduced to Mn^{3+} with one electron added to the Mn e_g sub-band.[122] Figure 2.4a shows Co^{3+} has six electrons filling the t_{2g} band. One electron is removed from the Co t_{2g} band for Co^{4+}.[122] Figure 2.4a also shows that Ni^{2+} has six electrons filling the

t_{2g} sub-band and two unpaired electrons in the e_g band. Electrons in the e_g band are removed when it is oxidized from2+ to 3+ or 4+ state.[47]

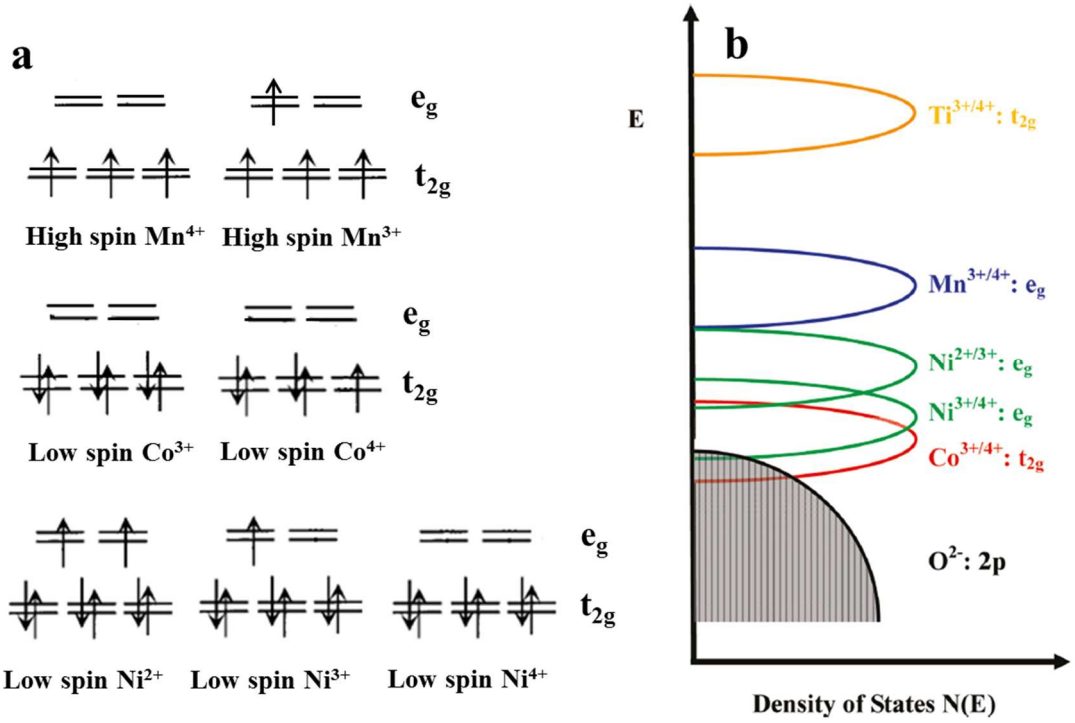

Figure 2.4 Schematic d electron levels of the transition metals in layered NMC compounds (a),[120,122] and qualitative energy vs electron density of states diagram of the transition metal 3d band and the oxygen 2p band of Ti doped $Li[Li_{0.2}Mn_{0.6}Ni_{0.2}]O_2$, reproduced with permission.[71] Copyright (2011) American Chemistry Society.

Figure 2.4b shows a qualitative energy vs. electron density of states diagram of the transition metal 3d band and the oxygen 2p band in a typical Li-rich compound. Figure 2.4b shows that $Co^{3+/4+}$ t_{2g} band overlaps the O 2p band, which increases the metal-oxygen covalence and decreases the electron localization. The overlap between the $Ni^{3+/4+}$ e_g band and the O 2p band is small.[71,123,124] Hence, Ni^{2+} can be fully oxidized to Ni^{4+}, but the

oxidation of Co^{3+} beyond $Co^{3.6+}$ involves the oxidation of O as suggested by A. Manthiram *et al.*.[14] Furthermore, the removal of lithium is accompanied by an increase of oxidation potential (lower Fermi level) of NMC, which is why NMC at higher states of charge (SOC) is more reactive with the electrolyte.[122]

2.2 Electrochemical Performance of Regular NMC

2.2.1 Impact of Upper Cut-off Voltage

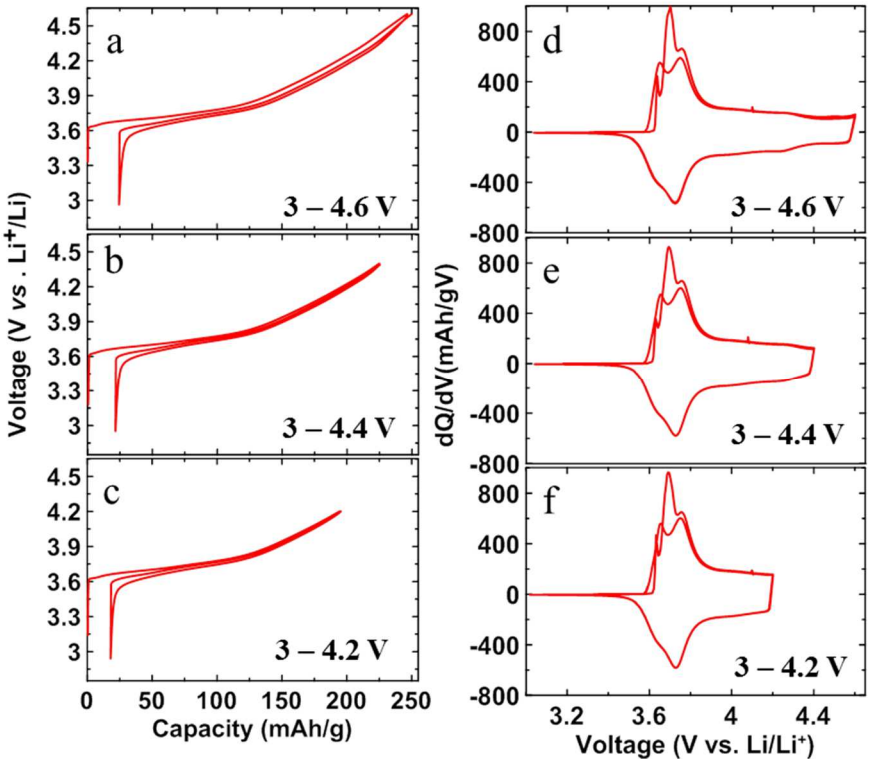

Figure 2.5 Voltage as a function of capacity between 3 – 4.6 V (a), 3 – 4.4 V (b) and 3 – 4.2 V (c). Differential capacity curve of NMC622 with C/20 current 3 – 4.6 V (d), 3 – 4.4 V (e) and 3 – 4.6 2 (f). The electrolyte is 1M $LiPF_6$ in EC:DEC electrolyte at 30 °C.

The reversible capacity of regular NMC materials $LiNi_xMn_yCo_zO_2$ (x+y+z = 1) depends on the composition and upper cut-off voltage.[2,14] For instance, $LiNi_{0.6}Mn_{0.2}Co_{0.2}O_2$ (NMC622) is a single phase material in the layered region as shown in Figure 2.2. Figure 2.5 shows the voltage as a function of specific capacity and differential capacity curve of $LiNi_{0.6}Mn_{0.2}Co_{0.2}O_2$ (NMC622) cells charged to 4.2, 4.4 and 4.6 V (*vs.* Li). Figure 2.5 shows that NMC622 can deliver a reversible capacity of ~175, 200 and 220 mAh/g when tested between 3 – 4.2, 4.4 and 4.6 V, respectively. Figure 2.5 shows that the energy density of NMC622 cells can be increased by increasing the upper cut-off voltage.

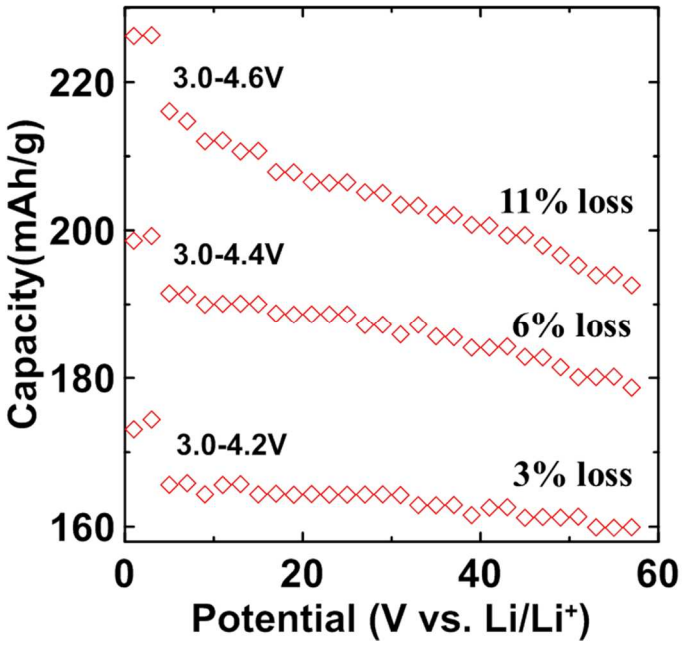

Figure 2.6 Specific capacity of NMC622 at 30 °C as a function of cycle number for cells charged to 4.2, 4.4 and 4.6 V (*vs.* Li), respectively. The electrolyte was 1M $LiPF_6$ in EC:DEC. Currents of 10 mA/g for the first 2 cycles and 40 mA/g in the following cycles were used. The numbers in the graph show the percentage of capacity loss from the 3rd cycle to the 58th cycle for cells with different upper – cut off voltages.

Figure 2.6 shows the specific capacity of NMC622 at 30ºC as a function of cycle number for cells charged to 4.2, 4.4 and 4.6 V (*vs.* Li), respectively. The electrolyte was 1M $LiPF_6$ in EC:DEC electrolyte. Currents of 10 mA/g for the first 2 cycles and 40 mA/g in the following cycles were used. Figure 2.6 shows that cells with higher upper-cut off voltages had worse capacity retention. This is associated with the decreased electrolyte stability and the increased reactivity of the delithiated positive electrode materials at high voltages, which reduces lifetime.[2,14]

2.2.2 Impact of Transition Metal Composition

The electrochemical performance of regular NMC materials is highly dependent on the transition metal composition. For instance, $LiNi_{0.42}Mn_{0.42}Co_{0.16}O_2$ (NMC442) can deliver a capacity of ~160, 180, and 210 mAh/g between 3 - 4.3, 4.5 and 4.7 V (*vs.* Li) respectively.[125] NMC811 can deliver a capacity of ~160, 180, 200, and 210 mAh/g between 3.0–4.1, 4.2, 4.3 and 4.4 V (*vs.* Li), respectively.[12,126,127] This suggests that regular NMC materials with higher nickel content can deliver higher capacity at lower voltages. Additionally, Y. K Sun *et al.*[128] found that increasing the Co to Mn ratio while maintaining the Ni content in layered $LiNi_xMn_yCo_zO_2$ (x+y+z = 1) can increase the reversible capacity due to the contribution of the $Co^{3+/4+}$ redox. On the other hand, an increase of Ni content can affect the lifetime and safety of a cell.[54,127,129]

Figure 2.7 shows a map of relationship between discharge capacity, thermal stability and capacity retention of $Li/Li[Ni_xCo_yMn_z]O_2$ (x= 1/3, 0.5, 0.6, 0.7, 0.8 and 0.85). [127] The capacity was tested between 3 – 4.3 V (vs. Li) at 25ºC with a current of 0.5 C in coin cells. The capacity retention was determined after 100 cycles. The thermal stability of the

charged electrode powders at 4.3 V without addition of electrolyte was measured with differential scanning calorimetry.

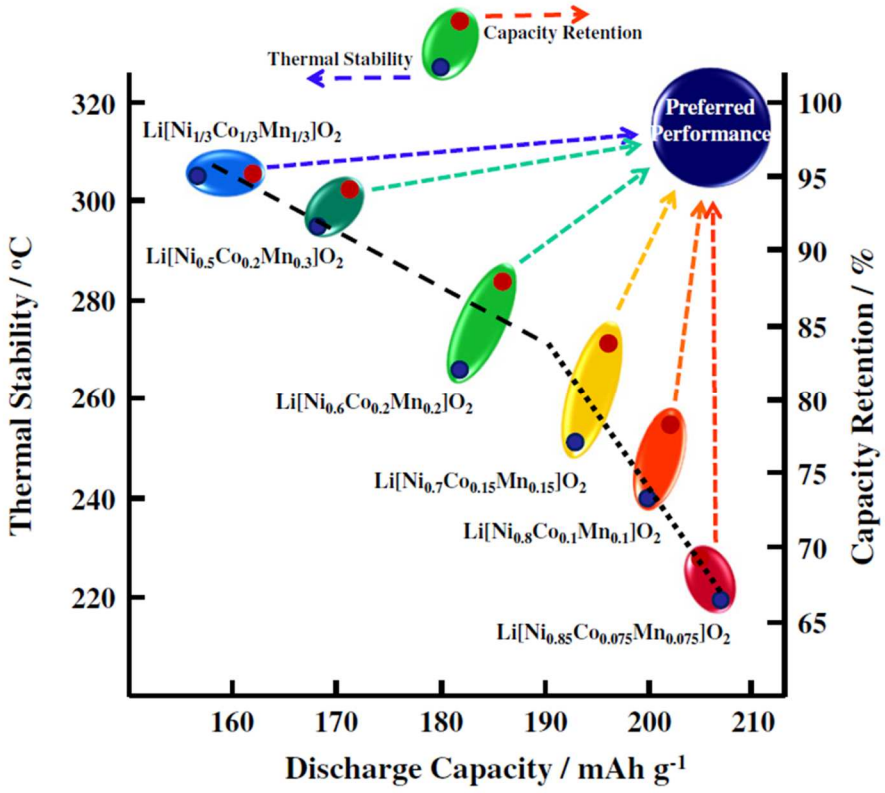

Figure 2.7 Map of relationship between discharge capacity, thermal stability and capacity retention of Li/Li[$Ni_xCo_yMn_z$]O_2 (x= 1/3, 0.5, 0.6, 0.7, 0.8 and 0.85), reprinted with permission.[127] Copyright (2016) Elsevier.

Figure 2.7 shows that $LiNi_{1/3}Mn_{1/3}Co_{1/3}O_2$ (NMC111) has the lowest specific capacity of ~ 150 mAh/g with best capacity retention (~95%) and the highest exothermic reaction peak temperature (~300°C) in the delithiated state (4.3 V). NMC811 has the highest specific capacity of ~200 mAh/g but the worst capacity retention (~73%) and lowest exothermic reaction peak temperature (~215 °C) in the delithiated state (4.3 V). The specific capacity

of $Li[Ni_xCo_yMn_z]O_2$, with compositions shown in the figure, between 3 – 4.3 V increases with increasing nickel content, while the capacity retention and exothermic reaction peak temperature decrease, which indicates worse lifetime and safety.

2.2.3 Challenges for Ni-rich NMC

NMC materials with a Ni content higher than 60% are referred to as Ni-rich NMC. They can deliver high capacities over a narrow potential range as well as excellent rate capability as shown in the last section.[54,55,59,127] However, they have challenges in terms of synthesis, storage, lifetime and safety.

The main difficulty in the synthesis of Ni-rich NMC is to minimize the degree of cation mixing which requires an excess of the lithium source prior to sintering, while also minimizing residual compounds left at the surface. To fully oxidize Ni to 3+ while obtaining a minimal degree of cation mixing, heating in dry air or in oxygen at lower temperatures is preferred[127], which could increase the cost of synthesis.

Lithium compounds like Li_2O, Li_2CO_3 and LiOH remain on the surface after synthesis or from the reaction of the nickel-rich surface with moist air during storage.[130,131] These have a negative impact on cell performance.[59] One study shows that reheating $LiNi_{0.7}Mn_{0.3}O_2$ at 200°C can help remove water molecules trapped at the surface and can partially remove the surface residuals without affecting structural integrity.[132] Y. K. Sun's group showed that modifying the surface of NMC622 with H_3PO_4 in anhydrous ethanol can remove the residual surface compounds. H_3PO_4 changes to Li_3PO_4 coated on the particle surface after reaction with residual LiOH and Li_2CO_3 during heating at 500°C.[55]

Figure 2.7 shows that Ni-rich materials have poor capacity retention, which worsens with higher Ni content when charged to the same voltage. It is also interesting that some electrolyte additives in NMC622/graphite, NMC442/graphite and NMC111/graphite cells, such as prop-1-ene-1,3-sultone (PES), can significantly improve the cell performance compared to cells with only control electrolyte (1 M $LiPF_6$ in EC:EMC 3:7).[33,133] Conversely, NMC811/graphite cells show worse performance with PES compared to cells with only control electrolyte, which indicates the importance of positive electrode Ni content on additive functionality.[33,34] Manthiram's group showed the effect of Ni/Mn ratio in compositions of $LiNi_{0.8-x}Co_{0.1}Mn_{0.1+x}O_2$ ($0.0 \leq x \leq 0.08$) around NMC811.[60] $LiNi_{0.72}Co_{0.10}Mn_{0.18}O_2$ showed 70.2% capacity retention after 100 cycles between 2.7 – 4.5 V (vs. Li) at 55°C (C/2 rate which indicates a full charge and discharge in 2h respectively), while $LiNi_{0.76}Co_{0.10}Mn_{0.14}O_2$ and NNMC811 showed only 56% and 34% capacity retention, respectively. This suggests that significant changes occur when the nickel content is larger than 72%.

Besides poor capacity retention, safety is another major concern for Ni-rich NMC materials.[12,127,134] The thermal decomposition of the delithiated NMC materials is associated with O_2 release from the lattice and migration of transition metal ions, while the amount the O_2 release from the lattice increases with increasing Ni content.[134]

2.2.4 Failure Mechanisms of Regular NMC Based Lithium-ion Cells

The failure of regular NMC materials is mainly related to the undesired reaction between the electrolyte and delithiated electrode surface such as electrolyte oxidation.[14,60,127,135] Regular NMC materials with higher nickel content show higher capacity when compared

in the same voltage ranges, which means more lithium is extracted from the host structure Li_xMO_2, resulting in a more reactive surface. Additionally, the decrease of capacity retention with the increase of Ni/Mn ratio may relate to the catalytic role of Ni that also increases the reactivity of electrolyte at the positive electrode surface[91,107,136], while Mn shows the opposite function. Manthiram's group stated that "Mn ions as incorporated into the Ni-rich cathodes, especially those existing at the particle surface, significantly reduce the irreversible side reactions between the electrode surface and the electrolyte and improve the surface structural stability."[60]

Besides electrolyte oxidation at the positive electrode surface, researchers also claim that the volume expansion of NMC materials[137], and the surface structural reconstruction from layered to rocksalt structure[125,136,138–143] are other major contributors to the failure of NMC, especially Ni-rich NMC materials. E.J. Lee *et al*[137] showed that volume expansion could lead to the build-up of macrostrain, eventually causing cracking of particles. The measurement of macrostrains of the cycled electrode using XRD in this paper[137] did not report the state of charge of each sample, and seems to be different due to the obvious shifting of the (003) peak. This could significantly affect the peak width observed, which is troublesome. The volume change of the NMC lattice is less than 6% even with more than 75% lithium extraction (~200 mAh/g capacity).[12,144–146] NMC442 experiences a volume change of less than 3% with an upper-cut off of 4.4 V.[145,146] The volume expansion in NMC materials doesn't seem to be as problematic compared to Si based anode materials which have a volume expansion as large as of ~280%.[147]

Some researchers believe the formation of a rock salt phase at the NMC surface would block the lithium diffusion path and cause impedance growth and capacity fade.[140,141] Other researchers think this rocksalt surface layer can act as a layer which protects the bulk material from further structural degradation and hinders electrolyte decomposition at the positive electrode surface.[143] Sasaki *et al.*[148] and Muto *et al.*[149] think the appearance of Li-deficiencies and inactive Ni^{3+} which are distributed throughout the entire particles are a major contributor to the failure of Ni-rich materials. The impact of the surface rocksalt layer will be discussed in Chapter 7.

2.2.5 Methods for Improvement of Cell Performance

Electrolyte additives[61–64] and surface modifications such as coatings on the positive electrode material surfaces[39,40,150,151] have been clearly shown to significantly extend the lifetime of regular NMC based cells. Electrolyte additives can help to form a stable protective layer on the positive electrode side, while coatings can protect the positive electrode surface from undesired reactions with the electrolyte and scavenge trace amounts of HF in the electrolyte.[14] Coating materials include metal oxides, metal phosphates, metal fluorides and polymers, *etc*.[39,40,55,56,150,152–156] Combining electrolyte additives and coatings can lead to improvements in cell performance. Recently, fluorine doping, which partially replaces oxygen in the lattice at the surface was also shown to be effective.[157,158]

Thick coatings (greater than 3 wt.%) of inactive materials on NMC materials significantly decrease the energy density and rate capability of the cells, and thus these coatings are usually incomplete with nano-particles scattered on the NMC surface.[39,40] Core-shell or gradient $LiNi_xMn_yCo_zO_2$ ($x + y + z = 1$) materials were first developed by Y. K. Sun's

group, which use active layered NMC materials with high Mn content as coating layers[27,44,45,159–161]. Thus a high energy core material with poor stability against the electrolyte can be protected by a thin layer of a stable and active shell material with lower Ni and higher Mn content.[26] Typically, the full concentration gradient (FCG) NMC materials have a high Ni content (~80 - 90%) in the core with increasing Mn content and decreasing Ni content from the core to the surface, with a maximum Mn content on the surface of ~50%.[44,45,159–161] The FCG NMC material with an average composition of $LiNi_{0.75}Co_{0.10}Mn_{0.15}O_2$ showed 95% capacity retention over 1000 cycles in a FCG/graphite cell between 3 – 4.2 V with a constant current of 1 C at room temperature.[45]

2.3 Properties of Li and Mn-rich NMC Materials

2.3.1 Debate about the Structure of Li and Mn-rich NMC Materials

The layered lithium rich NMC system has received lots of attention due to its high specific capacity after a first charge to above 4.6 V (*vs.* Li) and excellent capacity retention at high voltage as compared to other layered oxides.[65,66,73,74,77–79,123,162–168] These materials can be written as $Li_{1+x}M_{1-x}O_2$ or sometimes denoted as (1-x) $Li_2MnO_3 \cdot xLiMO_2$, and have been described as a solid solution of monoclinic Li_2MnO_3 and rhombohedral $LiMO_2$.[5–8,10,81,85–89,169] Conversely, Thackeray *et. al.* have incorrectly described the Li and Mn-rich materials as a nano-composite of Li_2MnO_3 and $LiMO_2$ [170–185]

Numerous studies have found that lithium rich NMC materials display solid solution behavior since the lattice parameters change linearly with composition. K. Jarvis *et al.*[66,69], C. Genevois *et al.*[85], H. Koga *et al.*[87] and A. K. Shukla *et al.*[186] (Ni^{3+}, Co^{3+}, Mn^{4+}) have

shown these materials have a single phase structure at the atomic level. In the Li and Mn-rich materials, low charge (Li^+ and Ni^{2+}) (bigger ionic radii) and high charge (smaller ionic radii) cations tend to be ordered (long range) on a $\sqrt{3}a_{hex} \times \sqrt{3}a_{hex}$ superstructure in the transition-metal layer (TM) in order to minimize Coulomb repulsion. As a result, superlattice peaks in x-ray diffraction patterns (XRD) can be often be observed between 20-30° (Cu $K\alpha$).

Studies of the structure - composition diagram of Li-Ni-Mn oxides and Li-Mn-Co oxides using combinatorial methods showed that the structure of these materials are highly dependent on the composition and synthesis conditions.[5–8,10,81] Figure 2.8 shows the partial Li-Mn-Ni oxide structure - composition diagram and the boundaries to the single phase layered region. The insert shows the approximate boundaries (upper boundary between the two-phase and one-phase region) to the layered region with different synthesis conditions. The solid black line shows the boundary for samples synthesized at 900°C in air with quenching. The solid and dashed green lines show the boundaries for samples synthesized at 800°C in 2% oxygen with quenching and regular cooling (5–10°C/min), respectively. The solid and dashed blue lines show the boundaries for samples synthesized at 800°C in air with quenching and regular cooling, respectively. Figure 2.8 shows sample B, which has a composition of $LiNi_{0.5}Mn_{0.5}O_2$, phase separates to a layered-layered nano-composite when made at 800°C in air with regular cooling, and is, otherwise, single phase layered. Monte Carlo simulation results showed that this phase separation can occur on a 2 – 10 nm length scale with both domains (Li_2Mn and $Ni_{0.5}Mn_{0.5}$ in the transition metal layer) on the same lattice.[8] This kind of short range ordering was observed using extended

x-ray absorption fine structure (EXAFS) on a non-quenched sample of $Li_{1.2}Co_{0.4}Mn_{0.4}O_2$ by J. Bareno *et al.*.[176]

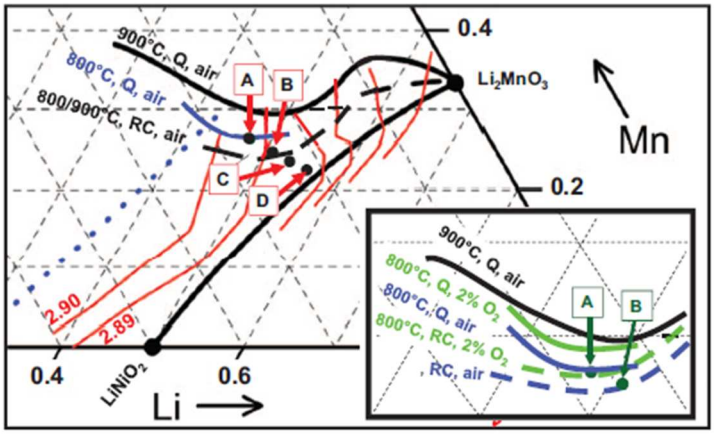

Figure 2.8 Partial Li-Mn-Ni oxide composition - structure diagram showing the boundaries to the single phase layered region. The lower boundary is shown connecting $LiNiO_2$ to Li_2MnO_3. The insert shows approximate boundaries to the layered region with different synthesis conditions. The red lines are *a* lattice parameter contours, reprinted with permission.[81] Copyright (2014) The Electrochemical Society.

2.3.2 Electrochemical Performance of Li-Rich NMC

Lithium-rich NMC materials can have extraordinary high specific capacity of more than 250 mAh/g with an average potential of ~3.6 V (vs. Li) after an irreversible oxygen release activation process at ~4.5 V (vs. Li). Major issues such as large irreversible capacity (IRC),[69,72,187] voltage fade upon cycling [67,68,74,88,162,188,189] and poor rate capability[74,127,166] have hindered the application of these materials.

Figure 2.9a shows the voltage as a function of capacity for $Li_{1.26}(Ni_{0.2}Mn_{0.8})_{0.74}O_2$. The cells were first tested between 2.5 – 4.4 V for four cycles, then charged to 4.8 V for one cycle and followed by cycling between 2.5 – 4.6 V. A reversible capacity of ~70 mAh/g was observed between 2.5 – 4.4 V, which arises from the oxidation of Ni^{2+} to Ni^{4+} during lithium extraction. A prolonged plateau at 4.5 V was observed and a reversislbe capacity of ~200 mAh/g was delivered when cells were tested between 2.5 – 4.8 V. This is associated with about 28% irreversible capcity. During the first charge to 4.8 V, the prolonged plateau at 4.5 V is thought to be associated with the removal of oxygen from the lattice while lithium being extracted.[14] After this process, some Mn^{4+} is reduced to Mn^{3+} during discharge which partially contributes to the high capacity (~200 mAh/g) observed in the following cycles.[78]

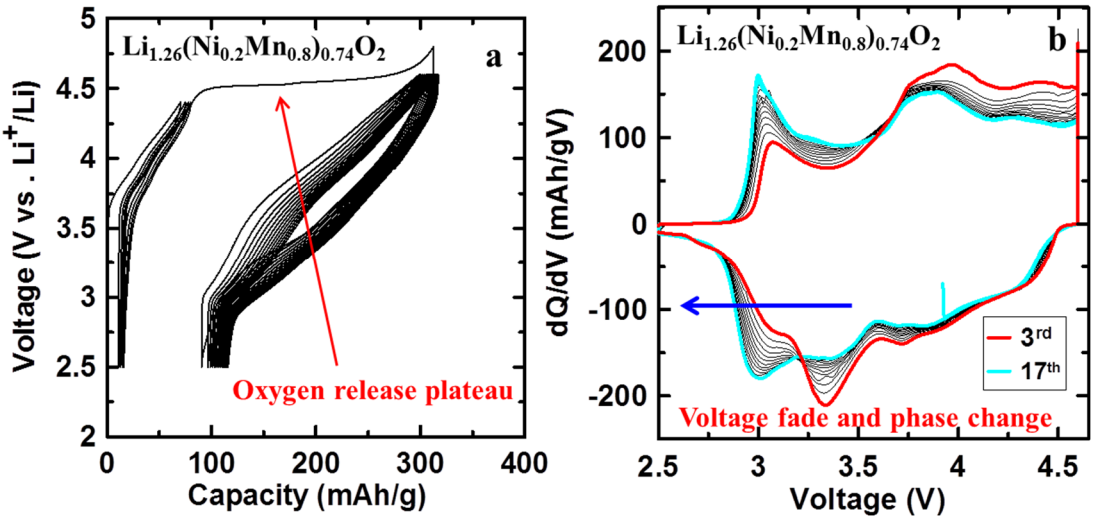

Figure 2.9 Voltage (a) and differential capacity (b) curve for $Li_{1.26}(Ni_{0.2}Mn_{0.8})_{0.74}O_2$. The cells were first tested between 2.5 – 4.4 V for four cycles, then charged to 4.8 V for one cycle and followed by cycling between 2.5 – 4.6 V.

The Mn-rich materials also have serious voltage fade issues during cycling. Figure 2.9b shows the differential capacity as function of voltage for $Li_{1.26}(Ni_{0.2}Mn_{0.8})_{0.74}O_2$ when cycled between 2.5 – 4.6 V after the first charge to 4.8 V. Figure 2.9b shows that, during discharge, the main feature at ~3.3 V at the beginning gradually disappeared while the feature at ~3.0 V is pronounced during cycling. The voltage decay significantly decreases the energy density of the lithium-rich NMC materials.

2.3.2.1 **Mechanism of Extraordinary High Capacity and Voltage Fade**

Tremendous work has focused on understanding the extraordinary high capacity of the lithim rich NMC materials and voltage fade mechanism.[74,75,85,162] A reversible anion redox of O^{2-}/ O^{-} was proposed by M. Sathiya *et al.*[190] and K. Luo *et al.*[191] which can be explained through the generation of localized electron holes on oxygen through the transition metal 3d and oxygen 2p hybridization. M. Sathiya *et al.*[190] proposed that the formation of oxygen vacancies which appear during the first charge is triggered by the destabilization of the oxidized O 2p level. The voltage fade is due to a cycling-driven phase conversion from layered to a spinel-like or "splayered" phase.[67,68,74,88,162,188,189] This phase transformation could be due to the migration of transition metals and oxygen vacancies trigered by the anionic redox process during cycling.

Manthiram's group showed that the substitution of Co^{3+} for equal amounts of Mn^{4+} and Ni^{2+} in $Li[Li_{0.2}Ni_{0.2-x/2}Mn_{0.6-x/2}Co_x]O_2$ can extend the oxygen release plateau and aggravate the voltage decay.[72] This is associated with the increased metal–oxygen covalence and electron delocalization due to the overlap of $Co^{3+/4+}$ t_{2g} band with the top of the O^{2-} 2p band, and severe migration of Li and TM ions caused by the lengthened plateau region.[14,72] Quian

et al. proposed the activation barriers for transition metal diffusion in the presence of oxygen vacancies are drastically reduced. The migration of transition metals to the lithium layer and the formation of tetrahedral Li–Li dumbbells induced by oxygen vancancies leads to the local structural transformation from layered phase to spinel-like phase.[75]

Koga *et al.* found co-existence of two phases at the top of charge (4.8 V) of the lithium-rich NMC materials which were maintained in the following cycles.[88] Based on the two-phase observation, it was proposed that oxygen loss occured at the surface of the particles with a corresponding densification of the host structure, while reversible oxygen redox occurs within the bulk without major modification of the structure. The two phases were referred to as the surface and bulk phases respectively. During the following cycling process, it was proposed that the surface phase transforms to the spinel-like structure and the active redox couples involve Ni^{4+}/Ni^{2+}, Co^{4+}/Co^{3+} and Mn^{4+}/Mn^{3+}, whereas the bulk phase involves redox couples of Ni^{4+}/Ni^{2+}, Co^{4+}/Co^{3+} and O^{2-d}/O^{2-} with a similar structure to the pristine material.[85,86,88,162,169,190]

2.3.2.2 **Methods for Improvement of Cell Performance**

Optimizing the nickel, manganese and cobalt composition such as increasing Ni content is one way to improve the performance of lithium rich NMC materials.[72,164,192] Other methods such as applying dopants like Al, Cr and F *etc.*[189,193–197], coatings such as AlF_3, Al_2O_3, $AlPO_4$ *etc.*[41–43,153,154,198–200], and surface treatments with NH_4SO_4 and persulfates *etc.*[201,202] were introduced to improve the performance of lithium-rich NMC materials. Additionally, blending lithium-rich NMC materials with lithium insertion hosts likeV_2O_5, LiV_3O_8 *etc.*[203–205] that can take the 'irreversible' lithium extracted in the first charge reduced the

irreversible capacity. Besides the above mentioned methods, electrolyte additives were also heavily studied in cells made from lithium-rich NMC materials.[206–209] Most of these works showed improved rate capability and less irreversible capacity due to minimized internal impendence growth and the formation of thinner and more stable SEI layers, possibility because of reduced surface/electrolyte reactivity.[14] However, the impact on voltage fade due to the structural transformation was not significant.

2.3.2.3 **Lithium-rich Core-shell Materials**

Li-rich and Mn-rich positive electrode materials were shown, using high precision coulometry studies, to have minimal reactivity with electrolyte even when charged to 4.6 V (*vs.* Li).[20] They were proposed as shell materials for high voltage core-shell structured NMC materials by J. Camardese *et al.*.[26] Lithium-rich core-shell materials have similar structure to the core-shell/gradient materials developed by Y. K. Sun's group.[27,45,210] They have a nickel-rich material as core, and use a lithium and manganese-rich material as the shell in a hybrid system for cells charged to above 4.5 V. R. Shunmugasundaram *et al.* showed that some compositions with metal site vacancies and no lithium in the transition metal layer, $Li[\square_q M_{(1-q)}]O_2$, have oxygen release plateaus but extremely low irreversible capacity (as low as 4%).[211] These materials could also be interesting shell materials. The last three chapters of this thesis focus on the development and understanding of lithium-rich core-shell materials.

2.3.2.4 **Volumetric Energy Density of Li-rich NMC**

Lithium-rich materials have a low crystallite density, which is ~ 4.18 g/cc for $Li_{1.2}Ni_{0.2}Mn_{0.6}O_2$, compared to LCO (~5.08 g/cc) and NMC622 (~4.77 g/cc). The stable capacity of $Li_{1.2}Ni_{0.2}Mn_{0.6}O_2$ reported varies from 200 – 250 mAh/g depending on the synthesis methods, while average voltage decreases from 3.7 to 3.5 V at C/20 in about 30 cycles.[65,66,70,72,212–217] Assuming a stable capacity of ~220 mAh/g and an average voltage of 3.6 V from 2.5 – 4.6 V (vs. Li) for $Li_{1.2}Ni_{0.2}Mn_{0.6}O_2$ gives an energy density of 4.18 g/cc ×225 mAh/g × 3.6 V =3.38 Wh/cc (assuming no electrode porosity). Assuming a capacity of ~ 155 mAh/g and an average voltage of 3.9 V from 3 – 4.2 V for LCO[218], and a capacity of ~185 mAh/g and an average voltage of 3.8 V between 3 – 4.3 V for NMC622 (Figure 2.5), one can calculate volumetric energy densities of ~3.07 and 3.35 Wh/cc respectively. This shows NMC622 between 3 – 4.3 V has almost the same volumetric energy density as $Li_{1.2}Ni_{0.2}Mn_{0.6}O_2$ has between 2.5 – 4.6 V.

If the voltage window of LCO and NMC622 is increased, a capacity of 175 mAh/g and an average voltage of 3.95 V for high voltage LCO between 3 – 4.45 V (vs. Li)[218] and 210 mAh/g and an average voltage of 3.9 V for NMC622 between 3 – 4.5 V (vs. Li) (Figure 2.5) can be achieved. This will then give energy densities of 3.51 and 3.91 Wh/cc for LCO and NMC622 respectively. NMC622 can deliver a much higher volumetric energy density between 3 – 4.5 V compared to that of $Li_{1.2}Ni_{0.2}Mn_{0.6}O_2$ between 2.5 – 4.6 V.

Lithium-rich NMC materials usually have low tap density, lower than 1.8 g/cc, with only a few papers reported to densify around 1.9 – 2.0 g/cc.[65,212–217] Regular NMC and LCO

usually have tap densities higher than 2.5 g/cc.[2] With this consideration, lithium-rich NMC materials do not have advantages in volumetric energy density compared to high voltage LCO and NMC622 (4.5 V *vs.* Li). Additionally, to obtain the high capacity of lithium-rich NMC, these materials must be cycled over a wide potential range of 2.5-4.6 V (vs. Li), which may be challenging for the current carbonate-based electrolytes. This shows that NMC622 can be a promising core material for core-shell materials.

CHAPTER 3. EXPERIMENTAL AND THEORETICAL CONSIDERATIONS

3.1 Sample Preparation

3.1.1 Synthesis of NMC Hydroxide Precursors

Metal hydroxide precursors $Ni_xMn_yCo_z(OH)_2$ were prepared *via* co-precipitation in a continuously stirred tank reactor (CSTR) using a method similar to that described by Van Bommel *et al.*[98]

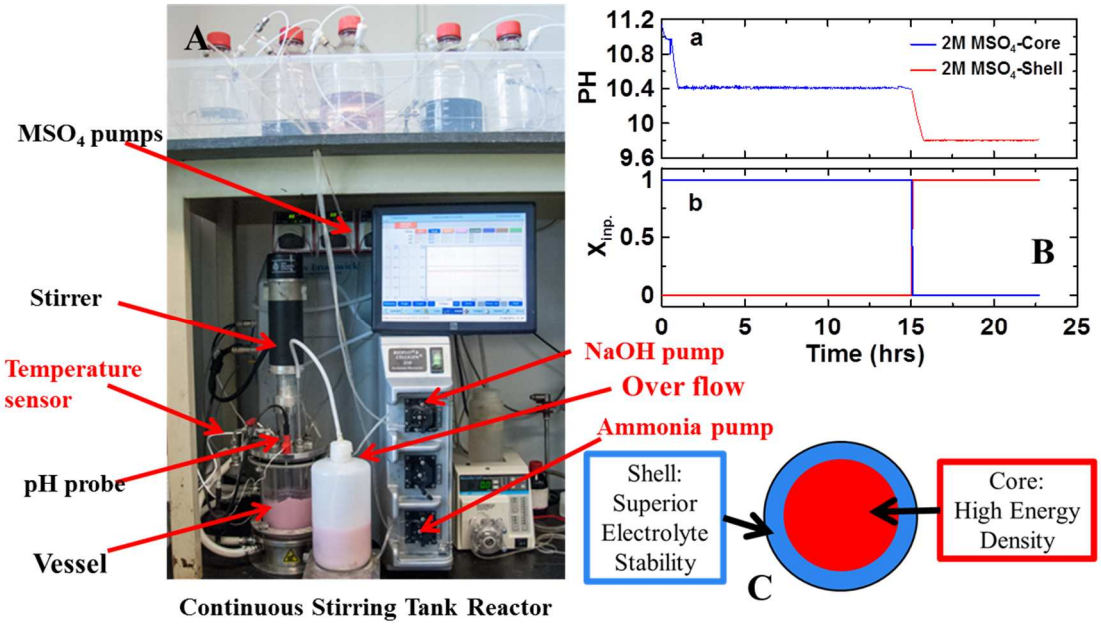

Figure 3.1 Continuously Stirred Tank Reactor (A); example of pH (a) and pumping rate of the core/shell solution for a core-shell sample (b) change as a function of time, where 1 indicates 100% of default pumping speed (B). A schematic diagram of core-shell particles (C).

Aqueous solutions of $NiSO_4$, $MnSO_4$ and $CoSO_4$ were prepared with Ni:Mn:Co molar ratios of x:y:z. The total metal ion concentration of each solution was 2.0 M. A 10.0 M $NaOH_{(aq)}$ solution was used as the source of base for the reaction, while a 5.0 M $NH_{3(aq)}$ solution was used for metal ion coordination with ammonia to facilitate spherical and dense particle growth during the reaction.[98]

Figure 3.1A shows a continuously stirred tank reactor used for the synthesis of precursors. It has a main reaction vessel, internal pumps for NaOH and ammonia solutions, external pumps for metal sulfate (MSO_4) solutions, a pH controller, a temperature controller, an over-head stirring controller, a gas flow controller and an over-flow container. During the reaction, reagents were added using digital peristaltic pumps (Masterflex L/S 07524). Sodium hydroxide addition was automatically controlled by the pH controller and added as required by a peristaltic pump on the reactor. The vessel was maintained at a temperature of 60°C and the contents of the reactor were stirred by an overhead stirrer at 800-1000 rpm. Nitrogen was bubbled (60 sccm (standard cubic centimeter per minute)) into the reactor throughout the reaction to create an inert reaction atmosphere in order to minimize the oxidation of Mn rich hydroxides. The pH electrode (Mettler-Toledo InLab 424) was calibrated at room temperature using buffer solutions. The pH values of the buffer solutions were 4.0 and 10.0 at 20°C (Fisher Scientific).

For each precursor, a volume of 1 L of a 1 M $NH_{3(aq)}$ solution was first heated to 60°C. The reaction proceeded with the addition of 5.0 M $NH_{3(aq)}$ at 0.14 ml/min and 2.0 M MSO_4 at 0.5 ml/min. The morphology and tap density of the precursors depend on the pH, concentration of ammonia and transition metal composition which was demonstrated by

Van Bommel *et al.*[98] A pH of around 10.2 – 10.6 was used for the Ni-rich core hydroxides and a lower pH of 9.6 – 10.1 was usually used for the Mn-rich shell precursors. After 20 hours of reaction time, the hydroxide precursor was rinsed with 4.0 L of deionized water, and then dried at 120°C overnight.

3.1.2 Synthesis of Core-Shell Hydroxide Precursors

For the CS precursors[26], aqueous solutions with a desired ratio of $NiSO_4$, $MnSO_4$ and $CoSO_4$ for the core and shell were first made separately. The total metal ion concentration of each solution was 2.0 M. The volume of the core solution and shell solution was calculated based on the pre-designed core to shell ratio with a total volume of 600 mL. For instance, if the target core to shell ratio was 2:1, the core solution would be 600 mL*2/3= 400 mL, and the shell solution wouldbe 600 mL* 1/3 = 200 mL. Thus, the core solution was pumped for ~15 hours (400 mL) and then pumping switched to the shell solution for ~8 hours (200 mL), which yielded about 33 mol% shell (molar ratio). The desired pH values were changed accordingly when the solutions were switched from core to shell. Figure 3.1B shows an example of the change of pH, and the pumping rate of the core and shell metal sulfate solution for a CS precursor as a function of time. The CS precursor has 33 mol% $Ni_{0.2}Mn_{0.6}Co_{0.2}(OH)_2$ shell and 67 mol% $Ni_{0.67}Mn_{0.33}(OH)_2$ core.

3.1.3 Lithiation of Precusors

Each dried precursor was recovered, ground, and mixed with a stoichiometric equivalent of Li_2CO_3 (Umicore) by mechanical grinding until a homogenous consistency was achieved; about 10-15 minutes. The powder mixtures were sintered in a box furnace at

temperatures around 900°C for 10 hours, with an initial heating rate of 20°C/min and a final cooling rate of 20°C/min for all samples. The final products were mechanically ground and passed through a 45 micron sieve prior to characterization.

3.2 Powder Characterization Techniques

3.2.1 X-ray Diffraction

3.2.1.1 Bragg's Law

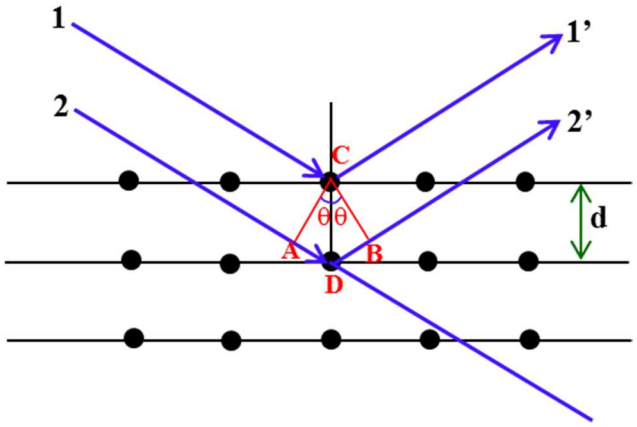

Figure 3.2 Diffraction of x-rays by a crystal.

Figure 3.2 shows the diffraction of x-rays by a crystal. The parallel beams 1 and 2 represent the incident waves, and beams 1' and 2' represent the diffracted waves by the atoms in the lattice. The incident beam angle is θ and the perpendicular distance between adjacent planes is d. The path difference of the scattered waves is AD+BD = 2dsinθ. If the scattered waves are to be in phase then

$$2d\sin\theta = n\lambda \quad (3.1)$$

where n is an integer and λ is the wavelength. Equation 3.1 is known as Bragg's law.[219]

3.2.1.2 **Geometrical Structure Factor**

The absolute intensity of the x-rays scattered by a single electron is given by the Thomson equation:

$$I = I_o \frac{K}{r^2}\left(\frac{1+cos^2 2\theta}{2}\right) \quad (3.2)$$

where I_o is the intensity of the incident beam, K is a constant ($7.94 * 10^{-30}$ m^2), and r is the distance from the electron to the detector.[219]

When the x-ray beam encounters an atom with Z electrons, if the atomic number is Z, each electron in the atom scatters part of the radiation coherently.[219] If the scattering is in the forward direction ($\theta=0^o$), the waves scattered by all electrons are in phase which results in constructive interference. The amplitude of the scattered wave is then Z times the wave scattered by a single electron. If the scattering is in the other directions, the path length of the waves scattered by different electrons could be different, which results in partial interference of the scattered waves. Hence, the net amplitude is less than Z times the wave scattered by a single electron. The atomic scattering factor *f* is then defined as the ratio of the amplitude of the wave scattered by an atom and the amplitude of the wave scattered by one electron.[219,220] As a result, the atomic scattering factor equals the number of electrons

in an atom when $2\theta = 0$. Generally, the atomic scattering factor decreases as $\sin\theta/\lambda$ increases.[219]

The intensity of Bragg peaks scattered by a crystal can be estimated from the scattering from the unit cell. Assuming the Bragg's law is satisfied, the intensity of the diffracted beam is then affected by the types and positions of the atoms in the unit cell. Similar to the waves diffracted by electrons, the diffracted waves may have phase differences when scattered by individual atoms in the unit cell. This effect is taken into account by the geometrical structure factor, which is given by[219]:

$$F_{hkl} = \sum_{j=1}^{N} n_j f_j \; e^{2\pi i(hu_j + kv_j + lw_j)} \tag{3.3}$$

where the summation extends over all N atoms of the unit cell, *hkl* are the Miller indices for a specific set of lattice planes, (u_j, v_j ,w_j) are the fractional atomic coordinates of individual atom j, and n_j is the site occupancy factor indicating what fraction of a site is occupied by an atom. The intensity of the *hkl* reflection measured in XRD is then proportional to $|F_{hkl}|^2$.[219]

3.2.1.3 **Rietveld Refinement**

The x-ray diffraction patterns can be fitted with the Rietveld method, which minimizes the weighted least square difference between the calculated intensity and observed intensity.[221] Useful information about the sample such as lattice parameters, fractional atomic coordinates and site occupancies, and phase content *etc.* can be extracted. In the Rietveld

method, the intensity of each individual data point is calculated with a Pseudo-Voight peak profile function as[221]:

$$I_c\,(2\theta) = I_b\,(2\theta) + \sum_{k=k1}^{k2} I_k^o\,(2\theta)\,[\gamma C(2\theta, 2\theta_k, H_k) + (1-\gamma)G(2\theta, 2\theta_k, H_k)] \qquad (3.4)$$

where $I_c(2\theta)$ is the calculated intensity at the scattering angle of 2θ. $I_b(2\theta)$ is the intensity of the background, $I_k^o\,(2\theta)$ is the contribution from the k^{th} Bragg reflection and k_1 to k_2 are the reflections contributing the intensity at 2θ.[221,222]

The component $[\gamma C(2\theta, 2\theta_k, H_k) + (1-\gamma)G(2\theta, 2\theta_k, H_k)]$ is the Pseudo -Voight peak profile function, where C and G are the Lorentzian and Gaussian functions, respectively.[221,222] γ is a refinable mixing parameter which is in the range between 0 and 1. H_k is the full width half maximum (FWHM) of the k^{th} reflection which is described by the Cagliotti equation that is treated as a convolution between instrument and sample broadening functions:[221]

$$H_k = (Utan^2\theta + Vtan\theta + W)^{1/2}. \qquad (3.5)$$

The parameters U, V and W are refinable parameters for the peak width.

The intensity of the k^{th} reflection is calculated as:

$$I_k^o = SM_k|F|^2 L_k P_k \qquad (3.6)$$

where the S is an arbitrary scale factor, M is the multiplicity of the k^{th} reflection, L_k is the Lorentz-Polarization factor, and P_k is a possible modification of intensity due to preferred

orientation. F is the structure factor, which is affected by the atom positions, atom types and site occupancy. Absorption and extinction corrections can also be applied.[221]

Besides the *in-situ* XRD patterns, the patterns in this thesis were fitted with Rietveld refinement using the Rietica program.[221] The space group $P\bar{3}m1$ was used for metal hydroxide precursors. For single phase NMC materials, the scans were fitted assuming a single hexagonal layered structure ($R\bar{3}m$ space group). For Li-rich and Mn-rich NMC samples, the superlattice peaks in the region between 20 and 35° were excluded. It was assumed that Li was on the 3a sites (lithium layer), excess lithium and transition metals were on the 3b sites (transition metal layer), and oxygen was on the 6c sites. The exchange of Ni and Li atoms between 3a and 3b sites was allowed with constraints that the stoichiometry of the samples was fixed to the values obtained with elemental analysis.[77] For layered-layred composite samples (Chapter 4) or core-shell samples (Chapter 8), Rietveld refinements were applied to the data assuming two hexagonal layered phases. The errors in the lattice constants reported in the thesis were generated through the Rietveld refinement software.

3.2.1.4 **Bragg-Brentano Diffractometer**

Powder X-ray diffraction (XRD) in this thesis was carried out using a Siemens D5000 diffractometer equipped with a Cu target X-ray tube and a diffracted beam monochromator. Figure 3.3 shows a schematic of the Bragg-Brentano diffractometer.[223] The x-ray beam from the X-ray tube passes through a divergence slit and then interacts with the sample. The diffracted beam leaves the sample, passes through an anti-scatter slit and then a receiving slit. The beam eventually reaches a diffracted beam monochromator to filter out

Cu-K_β and fluorescence radiation before detected by the detector.[223] As a result of beam divergence, the length of the beam illuminating the sample becomes smaller as the incident angle becomes larger. With smaller slits, peaks become sharper which gives better resolution to separate overlapping peaks, however, with a sacrifice of intensity counts.[223]

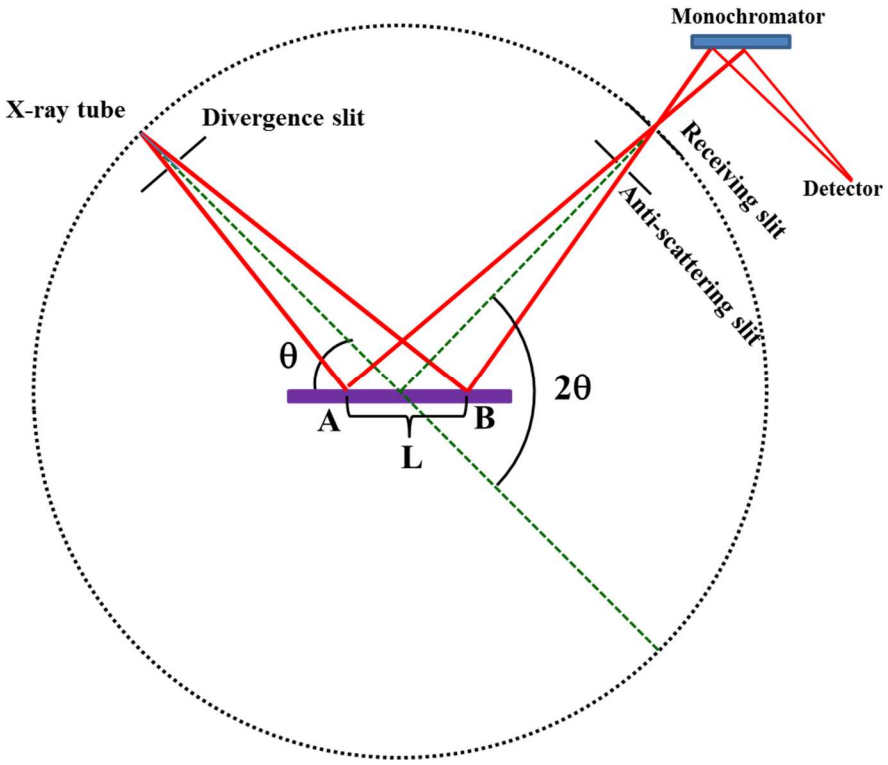

Figure 3.3 Schematic of the Bragg-Brentano diffractometer.

3.2.1.5 **XRD Data Collection**

For most of the samples, XRD patterns were collected in the scattering angle (2θ) range of 15 – 70° at 0.05° intervals with a dwell time of 3 s, a 1° divergence slit, a 1° antiscattering slit and a 0.2 mm receiving slit. For the CS samples (Chapter 8), a 0.5° divergence slit, 0.5° antiscattering slit and a 0.1 mm receiving slit were used, with data collection at 0.02° intervals and a dwell time of 10 s to ensure high resolution to help resolve the overlapping peaks of the core and shell phases.

3.2.1.6 ***In-situ* X-ray Diffraction**

A slurry containing active materials (see section 3.3.1), which was purposely made more viscous with less N-methyl-pyrrolidone (NMP, 99.5%, Sigma-Aldrich), was cast using a 260 µm notch bar directly onto a 2.0 cm diameter beryllium window. The electrodes were dried overnight at 120°C in a vacuum oven before use. The beryllium window was attached using Roscobond pressure sensitive adhesive to the positive electrode side of the cell case that had a pre-cut 1.5 cm diameter hole. The *in-situ* cell was then assembled in the same way as normal coin cells (see section 3.3.1). A small bead of Torr-Seal ultra-high vacuum epoxy was applied to the beryllium-cell case joint to eliminate the possibility of leaks. The *in-situ* cells were cycled at a rate of either C/100 or C/50 in the desired voltage range for two cycles using the E-One Moli charger system. Diffraction patterns were collected in scattering angle (2θ) ranges of 17 – 20°, 35 – 50°, 57 – 60° and 62 – 70° at 0.05° intervals with a dwell time of 15 s. The ranges may be slightly different depending on the sample. Each scan took approximately 2.5 h. As the beam width at lower angle was slightly larger than the size of the electrode, the detected intensity of the peak near 19°

was lower than expected. Rietveld refinement was carried out using GSAS with an EXPGUI user interface, which has an automated sequential fitting function.[224]

3.2.1.7 *Ex-situ* X-ray Diffraction

Charged electrodes were rinsed with dimethyl carbonate (DMC) (99%, Sigma) to remove any residual electrolyte. The electrodes were mounted on a zero-background silicon wafer in an air-sensitive holder in a helium filled glove box. Diffraction patterns were collected using the same Siemens D5000 diffractometer discussed above, in the scattering angle (2θ) range of 15 – 70° at 0.05° intervals with a dwell time of 5 s.

3.2.2 Scanning Electron Microscope and Energy Dispersive X-ray Spectroscopy

When a high energy electron beam interacts with the specimen in the scanning electron microscope (SEM), both elastic scattering and inelastic scattering can occur. Elastic scattering occurs when the incident electron is deflected by atomic nuclei in the specimen with negligible energy loss.[225] Backscattered electrons (BSE) are incident electrons elastically scattered through an angle of more than 90°.[225] More electrons can be back scattered from an element with higher atomic number. Thus, SEM images produced from BSEs can provide compositional information or atomic contrast.[225,226]

When an electron beam strikes a sample, energy can be transferred from the primary beam electron to the atom in inelastic scattering. Specimen electrons can be excited during ionization of the specimen atoms. This will lead to the generation of secondary electrons (SE), which possess low energies of less than 50 eV.[225,226] Secondary electrons are used principally for topographic contrast in the SEM images such as surface texture and

roughness.[225,226] SE are mostly generated from regions near the surface of a specimen and BSE are generated from regions that are generally deeper.[225] Thus, SE images can provide better lateral resolution than BSE images. [225]

Besides the generation of SE, characteristic x-rays can also be produced during the interaction between the primary electron beam and the specimen.[225,227] This happens when an inner shell electron of the specimen atom is excited by a primary electron and ejected from the atom. Then, an outer shell electron may fall into the empty inner shell level with corresponding emission of an x-ray photon.[225,227] Since each element has unique atomic structure, the x-rays generated are characteristic for each element. This allows the unique set of peaks in the x-ray emission spectrum to be used for both quantitative and qualitative elemental analysis in energy dispersive x-ray spectroscopy (EDS).[225,227]

Three different SEM instruments were used throughout this thesis. A NanoScience Phenom Pro G2 Desktop Scanning Electron Microscopy (SEM) was used to study the morphology of precursors and sintered samples in Chapter 4. This is equipped with a backscattered electron detector and a fixed acceleration voltage of 5 kV. Samples were prepared by mounting the powder on adhesive carbon tape prior to imaging.

EDS mapping measurements shown in Chapter 8 and point compositional analysis shown in Chapter 9 required special samples. These were prepared by first encasing powder in epoxy (CrystalBond 555, SPI Supplies/Structure Probe Inc.). The particles encased in epoxy were cut with sandpaper and then polished to a mirror finish with alumina paste. The stubs were then coated with amorphous carbon (~40 nm thick) using magnetron

sputtering. The mapping was carried out using a Hitachi S-4700 SEM equipped with an 80 mm^2 silicon drifted detector (Oxford Instruments). Elemental maps of samples were collected in 300 seconds with an accelerating voltage of 20 kV and a current of 15 μA.

In Chapter 10, samples for cross-sectional SEM imaging and EDS mapping measurements were prepared at the Canadian Centre for Electron Microscopy by argon milling the samples embedded in a graphite block with carbon paint (PELCO®) to achieve a smooth cross-section surface. The mapping was carried out using a JEOL JSM-7000F SEM at CCEM. Elemental maps of samples were collected in 300 seconds with an accelerating voltage of 10 kV and a current of 10 μA. This instrument has both backscattered and secondary electron detectors.

3.2.3 Scanning Transmission Electron Microscope and Electron Energy Loss Spectroscopy

The scanning transmission electron microscope (STEM) works similarly to a normal SEM in that the desired signal is collected to form an image while a focused beam of electrons is scanned over the sample.[225,227] The difference with SEM is that thin specimens and high accelerating voltage (200 – 300 kV) are used so that transmission modes of imaging with high spatial resolution are available.[225] This can allow the actual atomic configuration within the nanostructure to be observed. In STEM, a dark field (DF) detector excludes the transmitted beam.[225,227] An annular dark field detector collects electrons from an annulus around the beam, thus detects mostly scattered electrons.[225,227] A high angle annular dark field (HAADF) image is formed only by incoherently scattered electrons at very high

angle, which is different to Bragg scattered electrons. STEM-HAADF images have a high sensitivity to the atomic numbers of the elements in the sample (Z-contrast).[228]

As discussed in section 3.2.2 the electron beam can lose energy during the interaction with the specimen undergoing inelastic scattering. Similar to the generation of characteristic x-rays, the energy loss of the incident electrons, such as due to inner shell ionization, is also a characteristic feature for each atom.[229] Energy-loss spectroscopy (EELS) measures the change in kinetic energy of electrons after they have interacted with a specimen, which can be used to give structural and chemical information.[229]

In this thesis, STEM/EELS results are discussed in Chapter 7, which were carried out at CCEM. The STEM samples were prepared using a dual beam focused ion beam/scanning electron microscope (FIB/SEM) (Zeiss NVision 40). The sampling location on each electrode was randomly selected prior to TEM sample preparation. Protection layers of tungsten and/or carbon were then pre-deposited to the selected region before beam milling. The TEM samples were mounted onto a FIB lift-out grid (PELCO®) and eventually thinned down to ~ 70 nm prior to the analysis.

Scanning transmission electron microscopy and electron energy loss spectroscopy (EELS) were carried out using an aberration-corrected (image and probe-forming lenses) FEI Titan Cubed 80-300 HB scanning/transmission electron microscope (S/TEM) operated in STEM mode with an acceleration voltage of 200 keV. EELS spectra were collected using a Gatan Image Filter Quantum-965 spectrometer with 0.25 eV/channel dispersion. The high-angle annular dark field (HAADF) STEM images were obtained using HAADF detector. The

total cost of all experiments at CCEM was about $40,000 CAD, not including living and travel expense for four months of experiments.

3.2.4 Elemental Analysis

Elemental analysis (EA) was completed using inductively coupled plasma optical emission spectrometry (ICP-OES) to determine the Li, Mn, Ni and Co ratio of each sample. Approximately 10 mg of each sample was dissolved in a 2:1 reagent grade HCl:HNO_3 aqua regia solution which was then diluted prior to measurement.

3.3 Cell Construction

3.3.1 Coin Cells

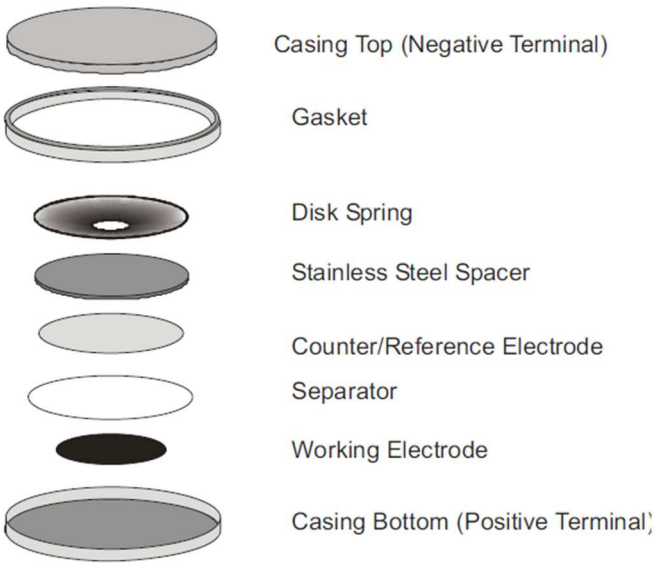

Figure 3.4 A schematic of components in making a coin cell, reprinted from reference[279].

A slurry with a mixture of 92 wt. % active material, 4 wt.% Super-S carbon black as conductive additive and 4 wt.% poly(vinylidene) fluoride (PVDF, Kynar 301F, Arkema), with N-methyl-pyrrolidone (NMP, 99.5%, Sigma-Aldrich) as the solvent was first prepared. Electrodes were made by coating the slurry on an Al foil with a 150 µm notch bar spreader. The electrode was first dried at 80°C in air for three hours, then pressed with a pressure of ~1000 atmosphere**.** The electrodes were eventually dried overnight at 120 °C in a vacuum oven before use. Figure 3.4 shows a schematic of components used in making a coin cell.[117,223] The counter electrode was lithium metal or graphite. The electrolyte used was 1.0 M $LiPF_6$ in 1:2 v/v ethylene carbonate : diethyl carbonate (EC:DEC). The separators used were one Celgard 2320 (Celgard) on the lithium electrode and one polypropylene blown-microfiber separator (3M) adjacent to the positive electrode.

3.3.2 Pouch Cells

Machine-made NMC811/graphite pouch cells (220 mAh) were obtained dry (no electrolyte) from LiFun Technology (Xinma Industry Zone, Golden Dragon Road, Tianyuan District, Zhuzhou City, Hunan Province, PRC, 412000). The cells were vacuum sealed in a dry room in China before they were shipped to Canada. The cells were balanced so that they could be charged to 4.7 V without any lithium plating. The cells were cut open below the heat seal and placed in a heated vacuum oven at 80°C overnight (approximately 14 hours) to remove residual water. After drying, the cells were directly transferred to an argon-filled glove box without exposure to ambient air, where they were filled with 0.90 g electrolyte. The electrolyte used differed from experiment to experiment which will be stated explicitly in the results section. Once cells were filled with electrolyte, they were

sealed with a compact vacuum sealer (MSK-115V, MTI Corp.) to 94% of full vacuum (-95.2 kPa gauge pressure or 6.1 kPa absolute pressure) with a 6 second sealing time at 150°C.

All cells were placed in a temperature-controlled box at 40. ± 0.1°C and held at 1.5 V for 24 hours to ensure complete wetting. Then cells were charged at C/20 to 3.8 V using a Maccor series 4000 automated test system (Maccor Inc.), where C/20 is the current required to complete a full charge (to 4.2 V) or discharge in 20 hours. The cells were transferred back to an argon-filled glove box and cut open under the previous seal to release any gas that was produced. The cells were then vacuum sealed again as previously described. For cells with an upper cut-off voltage of 4.1 V, there was only one degassing procedure performed at 3.8 V as described before. For cells with an upper cut-off voltage of 4.3 V, a second degas was performed after the charge to 4.3 V based on the work by Aiken *et al*.[230,231]

3.4 Electrochemical Measurements

3.4.1 Galvanostatic Cycling

Galvanostatic charge and discharge cycling was used to analyze coin cells and pouch cells. The cells were charged and discharged with a constant current until the upper cut-off voltage (charge) or lower cut-off voltage limit (discharge) was reached. The capacity of the each charge and discharge is:

$$Q=It \tag{3.7}$$

where Q is the capacity in mAh or mAh/g, I is the current in mA or mA/g and t is the time the current has been applied on in h.

Usually, the cell capacity is plotted as a function of cell voltage and the average voltage of each cycle can be calculated by:

$$\bar{V} = \frac{\int_{Q_1}^{Q_2} V(Q)dQ}{Q(V_2) - Q(V_1)} \tag{3.8}$$

where V_1 and V_2 are the lower and upper cut-off voltages respectively.

3.4.2 Electrochemical Impedance Spectroscopy

Electrochemical impedance spectroscopy (EIS) measurements were conducted on NMC811/graphite pouch cells after formation and after cycling using a Biologic VMP-3 instrument. Cells were charged or discharged to 3.80 V before they were moved to a 10. ± 0.1°C temperature box for EIS measurements. Alternating current (AC) impedance spectra were collected with ten points per decade from 100 kHz to 10 mHz with a signal amplitude of 10.0 mV. The experimental setup did not allow for reproducible solution resistance measurements due to cable and connector impedance. Therefore, all impedance spectra were manually shifted to zero on the real axis at the highest frequency measured.

3.5 Gas Measurement

The gas produced in cells due to electrolyte decomposition during cycling was measured using Archimedes's principle[230]. The pouch cells after cycling were first discharged to 3.8 V. *Ex-situ* gas measurements were carried out by suspending pouch cells from a fine wire

"hook" attached under a Shimadzu balance (AUW200D) and then immersing them in a beaker of de-ionized "nanopure" water (18 MΩ) that was at 20. ± 1°C for measurement. The change in the weight of the cell suspended in fluid, before and after testing is directly related to the volume changes by the change in the buoyant force. The change in weight of a cell, Δw, suspended in a fluid of density, ρ, is related to the change in cell volume, Δv, in mL by:

$$\Delta v = -\Delta w/(\rho\, g) \tag{3.9}$$

where the weight was measured in milliNewtons, the density in g/cc and g is the acceleration due to gravity in m/sec^2. It is important to realize that w/g is what a balance reports as the mass in grams.

The errors of capacity, R_{ct} and gas volume of cells shown in the thesis are measured from the range of data from pair cells and not a standard deviation.

3.6 Interdiffusion of Transition Metals During Sintering

3.6.1 Preparation of Laminar Pellets for the Interdiffusion Studies

The use of laminar pellets for the study of transition metal interdiffusion in core-shell materials is discussed in Chapters 9 and 10. Powders samples such as $Li_{1.09}(Ni_{0.8}Mn_{0.2})_{0.91}O_2$ (Mn^{4+} and Ni^{3+}) and Li_2MnO_3 (Mn^{4+}) were synthesized by first mixing $LiOH{\cdot}H_2O$, $Ni(OH)_2$, and MnO powders in a stoichiometric ratio. The mixtures were then heated at 900°C in oxygen for 10 h, while Li_2MnO_3 was made in air. In Chapter 10, powder samples were achieved using co-precipitation method as introduced in section

3.1. The Ni-rich compounds showed significant grain size growth and continued sintering during heating at high temperatures, which caused pellets made subsequently to shrink. Hence, all the powders were heated to 1000°C in air for 10 h, for subsequent use in pellets to be heated at 1000°C, in order to eliminate shrinkage and ensure intimate contact between the two pellets for the diffusion couple experiments.

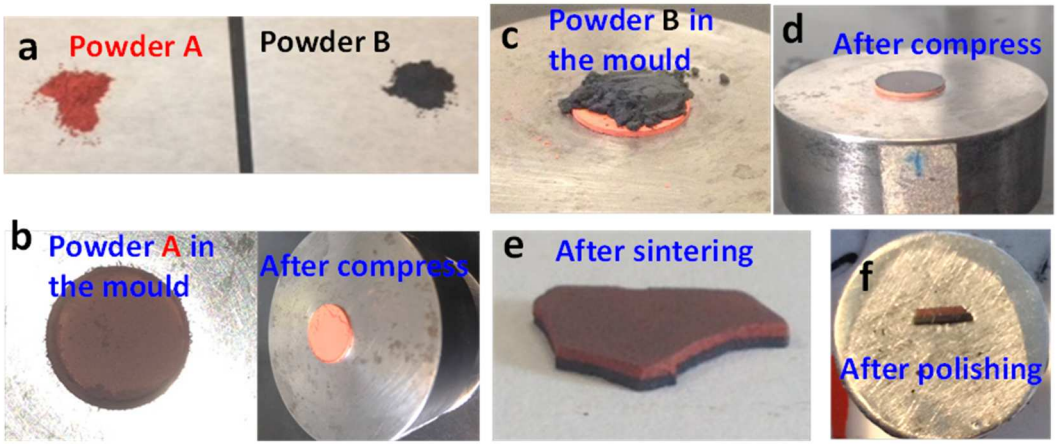

Figure 3.5 Procedure for assembling the composite pellets. Powder A and powder B (a), powder A in mold (c), and pellet after the first compression to 15 MPa (c). Pellet A with powder B on top (d) and the combined pellet after the second compression (e). The composite pellet after sintering (f) and the fractured pellet in the cross section, held in Crystalbond after polishing (g). Reprinted with permission.[271] Copyright (2015) American Chemistry Society.

The powders were mixed with 2 wt.% of $LiOH \cdot H_2O$ as a "binder" prior to making the pellets and to compensate for possible lithium loss during heating. For each pellet, powder A was first compressed to 15 MPa for 5 minutes, then powder B was added to the pellet mould on top of the pellet A. The powders were compressed again to 55 MPa for 10 minutes to ensure good contact at the interface. The pellets were heated to 800, 900 or

1000ºC for 10 h and then cooled slowly. The heated pellets were purposely fractured into smaller pieces, which were subsequently embedded into Crystal BondTM (CrystalBond 555, SPI Supplies/Structure Probe Inc.) and polished to a mirror surface finish for SEM and EDS experiments. Transition metal concentration profiles were measured on the cross sections of the diffusion couple pellets. Figure 3.5 shows photographs of the synthesis path. Figure 3.5a shows powder A and powder B. Figure 3.5b shows powder A in the mould and Figure 3.5c shows pellet A after the first compression to 15 MPa. Figure 3.5d shows pellet A with powder B on top, and Figure 3.5e shows the composite pellet after the second compression. Figure 3.5f shows the combined pellet after sintering and Figure 3.5g shows the fractured pellet in cross section held in crystal bond after polishing.

3.6.2 Interdiffusion Model in Binary Systems

3.6.2.1 Linear flow for laminar pellets

A linear flow model was used for the least square fitting of the measured concentration profile in order to obtain the interdiffusivity, $\tilde{D}$, which was assumed to be independent of concentration.[232–234] The diffusion equation defined by Fick's law, [233]:

$$\frac{\partial C}{\partial t} = \widetilde{D}\,\frac{\partial^2 C}{\partial x^2} \tag{3.10}$$

was used for the modelling. In equation (10), C is concentration at time, t, and position, x, of one of the elements (since $C_A + C_B = 1$), where t is the time since the beginning of heating and x is the direction perpendicular to the interface between the two pellets. The concentration profile and heating time can be discretized by equidistant segments of size

Δx and Δt respectively. The concentration gradient at point x_i can be determined from the concentrations of the neighbouring points x_{i-1} and x_{i+1} as :

$$\left(\frac{\partial C}{\partial x}\right)_{x=x_i} = \frac{C_{i+1} - C_{i-1}}{2\Delta x} \tag{3.11}$$

Equation (10) can then be discretized in time and space as:

$$\frac{C_{i,t+\Delta t} - C_{i,t}}{\Delta t} = \widetilde{D}\,\frac{C_{i+1,t} - 2C_{i,t} + C_{i-1,t}}{\Delta x^2} \tag{3.12}$$

Concentrations at the next time step can be determined from the initial concentrations with Euler forward integration:

$$C_{i,t+\Delta t} = \widetilde{D}\,\frac{C_{i+1,t} - 2C_{i,t} + C_{i-1,t}}{\Delta x^2}\Delta t + C_{i,t} \tag{3.13}$$

Additionally, symmetric boundary conditions were assumed with the introduction of hypothetical points x_{-1} and x_{n+1} at both ends of the sample, which were set to have the same values as the points at positions x_2 and x_{n-1}, respectively. [233]

3.6.2.2 **Radial Flow for Spherical CS Particles**

A radial flow model was used for the simulation of interdiffusion in the spherical CS particles. Fick's law can be written as[232]:

$$\frac{\partial C}{\partial t} = \widetilde{D}\left(\frac{\partial^2 C}{\partial r^2} + \frac{2}{r}\cdot\frac{\partial C}{\partial r}\right) \tag{3.14}$$

Similarly, equation (14) can be discretized in time and space and the concentrations at time t+Δt can be determined from the concentration at time *t* with:

$$C_{i,t+\Delta t} = \widetilde{D}\left[\frac{C_{i+1,t}-2C_{i,t}+C_{i-1,t}}{\Delta r^2} + \frac{2}{r}\cdot\frac{C_{i+1,t}-C_{i-1,t}}{2\Delta r}\right]\Delta t + C_{i,t} \tag{3.15}$$

Symmetric boundary conditions in the radial flow model were applied.

At r=0 :

$$C_{0,t+\Delta t} = \widetilde{D}\left[\frac{C_{1,t}-2C_{0,t}+C_{-1,t}}{\Delta r^2} + \frac{2}{r}\cdot\frac{C_{1,t}-C_{0,t}}{\Delta r}\right]\Delta t + C_{0,t} \tag{3.16}$$

and at r=r_n :

$$C_{n,t+\Delta t} = \widetilde{D}\left[\frac{C_{n-1,t}-2C_{n,t}+C_{n+1,t}}{\Delta r^2} + \frac{2}{r}\cdot\frac{C_{n,t}-C_{n-1,t}}{\Delta r}\right]\Delta t + C_{n,t} \tag{3.17}$$

3.6.3 Interdiffusion in a Ternary System

In a ternary system, the flux of one component can be expressed in terms of two independent fluxes, which means the concentration change of one component with time is dependent on the concentration gradient of the element itself and another independent element. Fick's law can be expressed as[232–234]:

$$\frac{\delta C_i}{\delta t} = \tilde{D}_{i1}^3 \frac{\partial^2 C_1}{\partial x^2} + \tilde{D}_{i2}^3 \frac{\partial^2 C_2}{\partial x^2} (i = 1, 2) \tag{3.18}$$

Hence, there are four independent interdiffusion coefficients, and two independent concentration profiles. The superscript "3" in the notation of the interdiffusion coefficient indicates that the 3rd element is dependent on the other two. The equation can be discretized by equidistant segments of size Δx and Δt, and solved numerically using the same method introduced in the binary system. The average effective interdifusion coefficient that includes all of the diffusional interactions among the components over the specified ranges is defined as below[234]:

$$\tilde{D}_{i,\Delta c}^{eff} = \frac{\sum_{j=1}^{n-1} \tilde{D}_{ij}^{n}[C_j(x_1) - C_j(x_2)]}{C_i(x_1) - C_i(x_2)} \tag{3.19}$$

3.6.4 Least Square Fitting

Least square fitting was performed using the linear flow model for the data collected in the pellet interdiffusion experiments in Chapter 9 and Chapter 10. The step size, Δx, was set to be that of the experimental concentration profile, while the sinter time was set to match that of the experiments. The interdiffusivity, the initial position of the interface, and the initial concentrations at the left and right side were refined during the fitting.

The experimental techniques and theories introduced in this chapter were used for the work conducted in this thesis. Results will be discussed in the following chapters.

CHAPTER 4. STUDY OF THE LI-MN-NI OXIDE SYSTEM WITHIN THE LAYERED SINGLE PHASE REGION

Specific compositions in the lithium rich layered material $Li_{1+x}M_{1-x}O_2$ systems (M = Mn, Ni and/or Co) have been carefully studied.[123,165,166,215] However, no systematic structural **and** electrochemical study in the layered region of the Li-Mn-Ni oxide system with varied lithium and transition metal content had been reported until this work. In this Chapter, bulk samples with compositions $Li_{1+x}(Ni_yMn_{1-y})_{1-x}O_2$ (y = 0.2, 0.33, 0.4, 0.5, 0.6 and 0.7, $0 \leq x \leq 0.34$) were synthesized in order to understand the influence of the transition metal composition and lithium content on the electrochemical performance. Contour plots of the lattice constants versus composition in the single phase region were generated, which should be of great value to future workers. The electrochemical results are summarized and correlated to the lithium content and transition metal composition. The majority of this Chapter was published in Chemistry of Materials.[29] Permission has been granted by the American Chemical Society for the reuse of the complete article.

4.1 Experimental Design

Metal hydroxide precursors $Ni_yMn_{1-y}(OH)_2$ (y = 0.2, 0.33, 0.4, 0.5, 0.6 and 0.7) were prepared *via* the co-precipitation method that was introduced in Chapter 3. Three grams of precursor were used for the synthesis of each sample. The powder mixtures were sintered in a box furnace at 900°C for 10 hours. The target stoichiometries are shown in Tables 4.1, 4.2 and A.1 in Appendix A. Electrochemical measurements were carried out *via* galvanostatic charge/discharge cycling using standard 2325 coin cells with lithium metal as the anode on an E-One Moli Energy Canada battery testing system. All the cells

were tested with a current density of 10 mA/g at 30°C. Cells were first charged and discharged between 2.5 – 4.4 V for four cycles, then charged to 4.8 V for one cycle and further cycled between 2.5 – 4.6 V vs. Li/Li^+.

Table 4.1 The target chemical composition and the elemental analysis results from ICP-OES for the precursors assuming the chemical formula $M(OH)_2$ where M represents the transition metal atoms.

Precursor	
Sample	Elemental Analysis
$Ni_{0.6}Mn_{0.4}(OH)_2$	$Ni_{0.6}Mn_{0.4}(OH)_2$
$Ni_{0.7}Mn_{0.3}(OH)_2$	$Ni_{0.703}Mn_{0.297}(OH)_2$
$Ni_{0.5}Mn_{0.5}(OH)_2$	$Ni_{0.496}Mn_{0.504}(OH)_2$
$Ni_{0.4}Mn_{0.6}(OH)_2$	$Ni_{0.408}Mn_{0.592}(OH)_2$
$Ni_{0.2}Mn_{0.8}(OH)_2$	$Ni_{0.167}Mn_{0.833}(OH)_2$

Table 4.2 The target chemical composition and the elemental analysis results from ICP-OES for samples of the composition series $Li_{1+x}(Ni_{0.4}Mn_{0.6})_{1-x}O_2$ ($0 \leq x \leq 0.24$) assuming the chemical formula $Li_{1+x}M_{1-x}O_2$

$Li_{1+x}(Ni_{0.4}Mn_{0.6})_{1-x}O_2$			
ID	Sample	x	Elemental Analysis
1A	$Li_{1.00}Ni_{0.400}Mn_{0.600}O_2$	0.00	$Li_{0.969}Ni_{0.418}Mn_{0.613}O_2$
1B	$Li_{1.04}Ni_{0.384}Mn_{0.576}O_2$	0.04	$Li_{1.011}Ni_{0.403}Mn_{0.585}O_2$
1C	$Li_{1.08}Ni_{0.368}Mn_{0.552}O_2$	0.08	$Li_{1.078}Ni_{0.371}Mn_{0.551}O_2$
1D	$Li_{1.12}Ni_{0.352}Mn_{0.528}O_2$	0.12	$Li_{1.093}Ni_{0.361}Mn_{0.546}O_2$
1E	$Li_{1.16}Ni_{0.336}Mn_{0.504}O_2$	0.16	$Li_{1.129}Ni_{0.355}Mn_{0.516}O_2$
1F	$Li_{1.20}Ni_{0.320}Mn_{0.480}O_2$	0.20	$Li_{1.175}Ni_{0.331}Mn_{0.493}O_2$
1G	$Li_{1.24}Ni_{0.304}Mn_{0.456}O_2$	0.24	$Li_{1.207}Ni_{0.318}Mn_{0.475}O_2$

4.2 Results and Discussion

4.2.1 Elemental Analysis Results

Tables 4.1 and 4.2 show the elemental analysis results for the precursors and samples of the composition series $Li_{1+x}(Ni_{0.4}Mn_{0.6})_{1-x}O_2$ ($0 \leq x \leq 0.24$) respectively. The actual stoichiometry of the samples was very close to the target value. The same results for other compositions are shown in Table A.1 in Appendix A. It was noted that the actual lithium stoichiometry in the samples of the composition series $Li_{1+x}(Ni_{0.7}Mn_{0.3})_{1-x}O_2$ approached close to 1 ($x = 0$) even when $x = 0.08$ was targeted. This indicates that that it is difficult to incorporate excess lithium in the layered structure of samples with higher nickel ratio ($y = 0.7$). In fact it is not possible to make $Li_{1+x}Ni_{1-x}O_2$ with $x > 0$ in an atmosphere containing oxygen, which is consistent with the above finding.[9]

4.2.2 SEM Images of the Lithiated Samples

Figure 4.1 shows SEM images of samples of the composition series $Li_{1+x}(Ni_{0.5}Mn_{0.5})_{1-x}O_2$ ($0 \leq x \leq 0.24$)**.** The dark spots on the particles which are highlighted with red circles in Figure 4.1 are suspected to be Li_2CO_3 or Li_2O and represent unreacted lithium after sintering. Li_2CO_3 and Li_2O contain lighter elements (smaller atomic number) than Li-Ni-Mn-O phases so they appear relatively dark in electron backscatter SEM images. Residual Li_2CO_3 was observed in samples with higher lithium content ($x = 0.16, 0.20, 0.24$). Similar results were found for $Li_{1+x}(Ni_{0.7}Mn_{0.3})_{1-x}O_2$ with $x = 0.06$ and 0.08, which are shown in Figure A.1. This further confirms that it is difficult to incorporate excess lithium in the layered structure of samples with higher nickel ratio ($y = 0.7$). The observation of residual Li_2CO_3 in each series indicates the saturation of the **local** lithium content, however, the stabilization of the lattice constants should be used to define the boundary between the

single layered hexagonal phase and the two-phase region between the layered hexagonal phase and Li_2O_2 as presented by McCalla *et al.*[10]

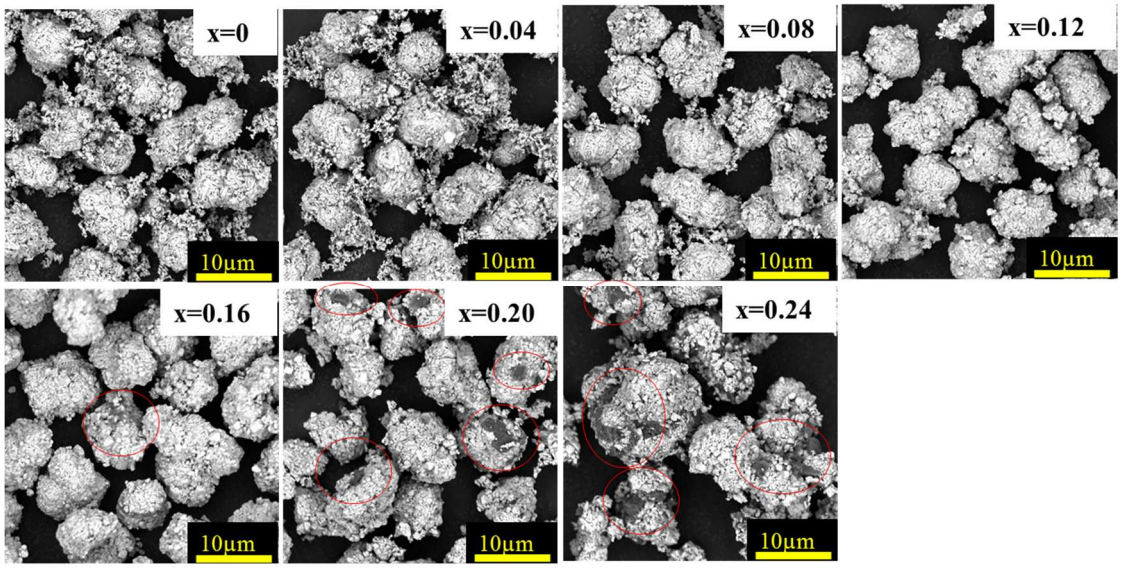

Figure 4.1 SEM images for samples of the composition series $Li_{1+x}(Ni_{0.5}Mn_{0.5})_{1-x}O_2$ ($0 \leq x \leq 0.24$). The red circles highlight the residual Li_2CO_3.

4.2.3 XRD and Rietveld Refinement Results

Figure 4.2a shows the XRD patterns of samples along the composition line $Li_{1+x}(Ni_{0.4}Mn_{0.6})_{1-x}O_2$ ($0 \leq x \leq 0.24$) with exception of peaks between 20° - 35°. The region of the XRD patterns near 44° for $Li_{1+x}(Ni_{0.4}Mn_{0.6})_{1-x}O_2$ ($0 \leq x \leq 0.24$) samples is shown in Figure 4.2b. Samples 1A and 1B with the lowest lithium content (x) show three phases (three peaks visible near 44°), which are consistent with **three of** the Rocksalt (R), Spinel(S), Nickel-rich layered (N) and Manganese-rich layered (M) phases discussed by McCalla *et al.*[10,81]

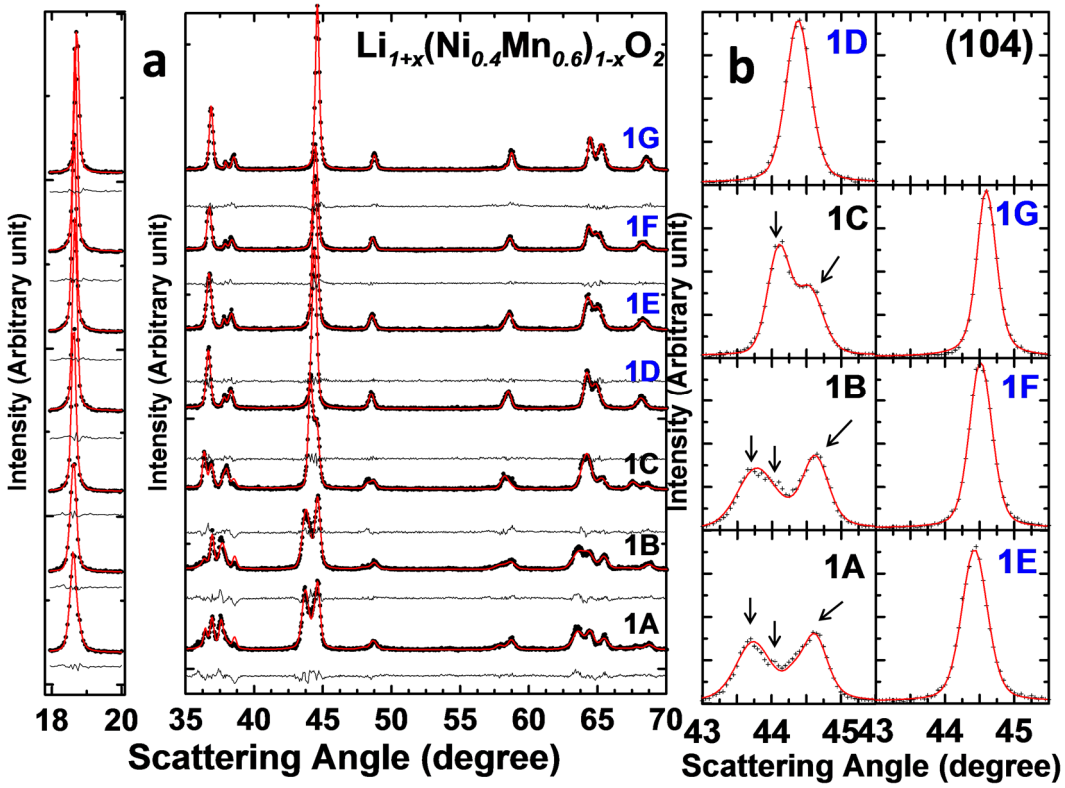

Figure 4.2 (a) XRD patterns for samples of the composition series $Li_{1+x}(Ni_{0.4}Mn_{0.6})_{1-x}O_2$ ($0 \leq x \leq 0.24$). (b) Expanded view of the (104) reflection indexed in the R-3m space group. The arrow indicates the presence of a 2nd or 3rd peak in sample 1A, 1B and 1C. The red lines are multiphase or single layered fits to the data. The cross symbols are the original data points.

As suggested by the phase diagram created by McCalla *et al.*[10], sample 1A has the R-S-M phases, and sample 1B has the R-N-M phases. As x increases up to 0.08, only two peaks near 44° were observed indicating the sample is a layered-layered (MN) nanocomposite.[81] When x increases to 0.12 and 0.16, there is no second peak observed in samples 1D and 1E, indicating they are in the single phase layered region. When x further increases to 0.20 and 0.24, the XRD results do not show evidence for a second phase in samples 1E, 1F and 1G. However, residual lithium carbonate was observed in the SEM images suggesting that

samples 1E, 1F and 1G are approaching the lower boundary (the most lithium) of the single phase layered region.

To more carefully quantify the changes taking place with increasing lithium content, the scans were fitted using Rietveld refinement assuming a single hexagonal layered structure for samples 1D to 1G, and two layered phases for samples 1A to 1C except for extra peaks associated with the superlattice structure observed between 20 and 35°.[77] The results of the refinement (only showing the main phase for samples 1A to 1C) are presented in Table 4.3. Table 4.3 shows that both the a and c lattice parameters decreased with the addition of lithium (increasing x) while the nickel content in the lithium layer decreased. Within the single phase layered region, the change in the c axis is much more significant (0.013 Å from x = 0.12 to x = 0.16) while the a lattice parameter has very little change (0.006 Å). The lattice constants of samples 1F and 1G did not show any sign of saturation even though residual Li_2CO_3 were observed. Samples 1F and 1G were ground with a mortar and pestle and then reheated to 900°C for 10 hours in an attempt to remove the Li_2CO_3. No evidence of Li_2CO_3 was found after the second heating. The refinement results show that the lattice constants of reheated samples 1F and 1G increased from (2.8631 Å, 14.254 Å) to (2.8719 Å, 14.272 Å) and from (2.8601 Å, 14.245 Å) to (2.8699 Å, 14.274 Å), respectively, indicating lithium loss during the reheating process. This is probably due to the removal of lithium peroxide vapor by evaporation during reheating of samples 1F and 1G in air.[9,235,236] This implies that it is possible to make samples close to the lower boundary of the single phase region (the largest lithium content) where all the nickel ions are 3+ if a high partial pressure of lithium peroxide is available as apparently is the case when excess Li_2CO_3 is present.

Table 4.3 The target chemical composition and the elemental analysis results for samples of the composition series $Li_{1+x}(Ni_{0.4}Mn_{0.6})_{1-x}O_2$ ($0 \leq x \leq 0.24$).

$Li_{1+x}(Ni_{0.4}Mn_{0.6})_{1-x}O_2$							
ID	Sample	x	a(Å) (± 0.0004 Å)	c (Å) (± 0.002 Å)	$^{\bullet}Ni_{Li}$ (%)	Single phase	R-factor
A	$Li_{1.00}Ni_{0.400}Mn_{0.600}O_2$	0.00	2.9427	14.373	40	No	3.98
B	$Li_{1.04}Ni_{0.384}Mn_{0.576}O_2$	0.04	2.9233	14.343	38.4	No	3.15
C	$Li_{1.08}Ni_{0.368}Mn_{0.552}O_2$	0.08	2.8987	14.310	10.2	No	2.14
D	$Li_{1.12}Ni_{0.352}Mn_{0.528}O_2$	0.12	2.8754	14.285	5.4	Yes	1.06
E	$Li_{1.16}Ni_{0.336}Mn_{0.504}O_2$	0.16	2.8692	14.272	4.3	Yes	1.35
F	$Li_{1.2}Ni_{0.32}Mn_{0.0.48}O_2$	0.20	2.8631	14.254	2.6	No*	1.69
G	$Li_{1.24}Ni_{0.304}Mn_{0.456}O_2$	0.24	2.8601	14.245	2.7	No*	3.88
F+	$Li_{1.2}Ni_{0.32}Mn_{0.0.48}O_2$	0.20	2.8719	14.272	3.6	yes	3.88
G+	$Li_{1.24}Ni_{0.304}Mn_{0.456}O_2$	0.24	2.8699	14.274	3.5	yes	4.85

* This co-existence is between the layered material and un-reacted Li_2CO_3.

+ Samples were reheated to 900 °C for 10 hours to remove the un-reacted Li_2CO_3.

The XRD patterns and refinement results for the other compositions are shown in Figures A.2 – A.5 and Tables A.2 – A.5. Similar trends in the changes in structures and lattice parameters with increasing x were observed.

Figure 4.3 shows partial XRD patterns from 20 to 35° for $Li_{1+x}(Ni_yMn_{1-y})_{1-x}O_2$ (y = 0.2, 0.4, 0.5, 0.6 and 0.7, with varied x) samples. Some of these samples show superstructure peaks which can be indexed on a monoclinic unit cell described in the C_2/m space group. This $\sqrt{3}a_{hex} \times \sqrt{3}a_{hex}$ superstructure derives from the ordering between the Li^{+1}, Ni^{+2} cations and the Ni^{+3}, Mn^{+4} cations with an ideal ratio of 1:2 in the transition metal layer (TM) as shown in Figure 1.5.[9,66,69,81,88,89,187]

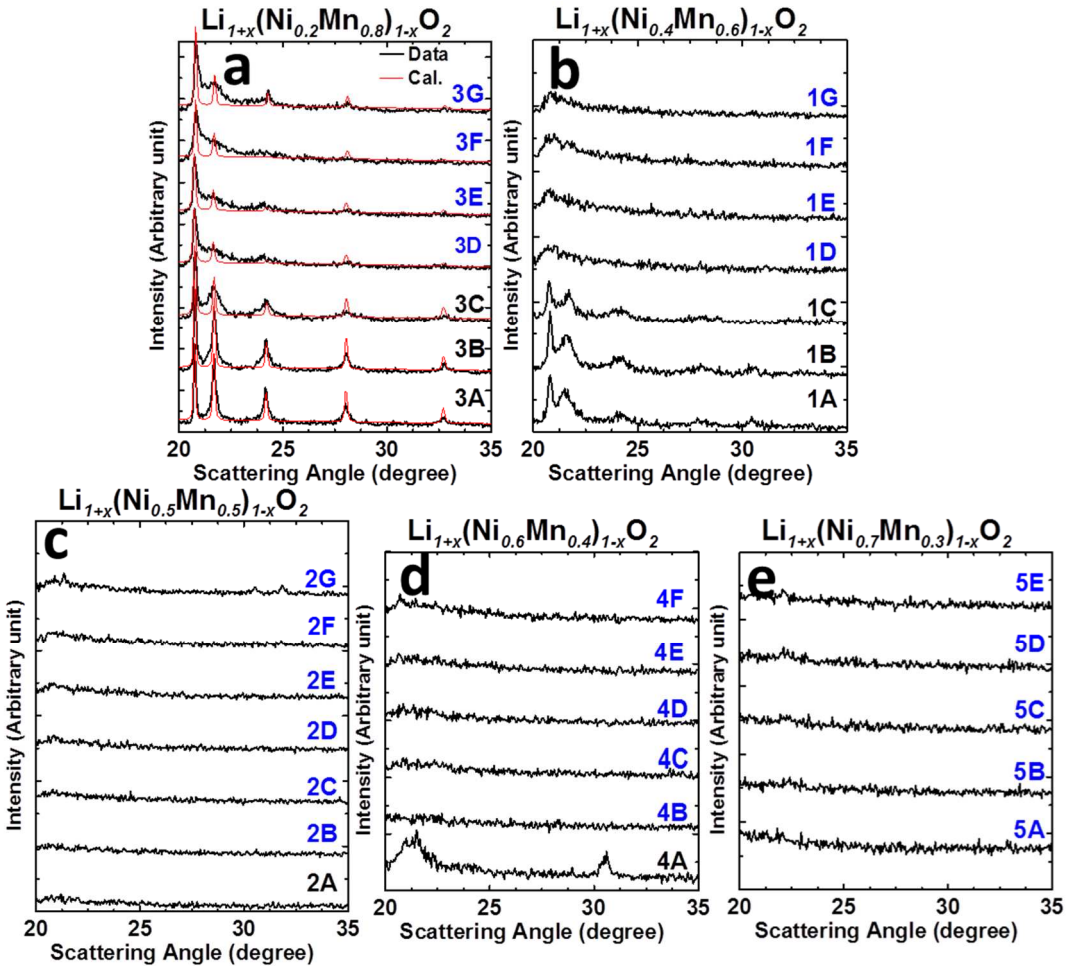

Figure 4.3 Partial XRD patterns (20-35°) for samples of the composition series $Li_{1+x}(Ni_y Mn_{1-y})_{1-x}O_2$ (y=0.2, 0.4, 0.5, 0.6 and 0.7) showing the superlattice peaks. The red lines in (a) are monoclinic fits to the data in the C_2/m space group. The blue labels indicate the samples in the single phase region.

When y = 0.2 (Figure 4.3a), there are sufficient Mn atoms and obvious superlattice peaks were observed which match the expected positions in the C2/m space group as shown by the red lines. The peak widths of all the superstructure peaks cannot be fit well indicating that the superstructure ordering has stacking faults along the c-axis.[83,237–239] The peaks

became broader when x increased suggesting an increase in the probability of stacking faults when more Li replaces Mn in the TM layer.[237] When y = 0.4 (Figure 4.3b), relatively intense superlattice peaks in samples 1A, 1B and 1C were observed, which are due to the presence of the M-layered phase as mentioned before that has ordering in the TM layer.[10] The peaks were very broad for samples in the single phase region compared to y = 0.2. Although when y = 0.5 the superlattice peaks were very weak in XRD patterns, weak superlattice spots were observed by Makimura *et al.* in electron diffraction.[240] The superlattice peaks became almost invisible when y > 0.5 (Figures 4.3c – 3e). This indicates the loss of the ordering in the TM layer and along the c-axis when there is more Ni replacing Mn. There is not enough Mn^{+4} to maintain this long range superstructure as the ratio between the weakly charged large cations (Li^{+1} and Ni^{+2}) and the strongly charged cations (Mn^{+4}) departs from the ideal 1:2 ratio. However, short range ordering over short distance may be detected by other techniques. Then the Li^{+1} and Ni^{+2} ions become randomly distributed in the TM layer leading to the transfer of the Li_2MnO_3-like structure (C_2/m) to the $LiCoO_2$-like structure ($R\bar{3}m$). It should be mentioned that the peaks observed in sample 2G in Figure 4.3c are from Li_2CO_3.

4.2.4 Contour Plots of the Lattice Parameters in the Single Phase Layered Region

Figure 4.4 shows the boundaries (solid red lines) of the single phase layered region in the Li-Mn-Ni-Oxide pseudoternary phase diagram which were carefully determined from the XRD and EA data. The lower right corner of the triangle is listed as Li_2O_2 in accordance with the work in reference 10 which captures the fact that Li_2O reacts in air to form Li_2O_2 vapor.

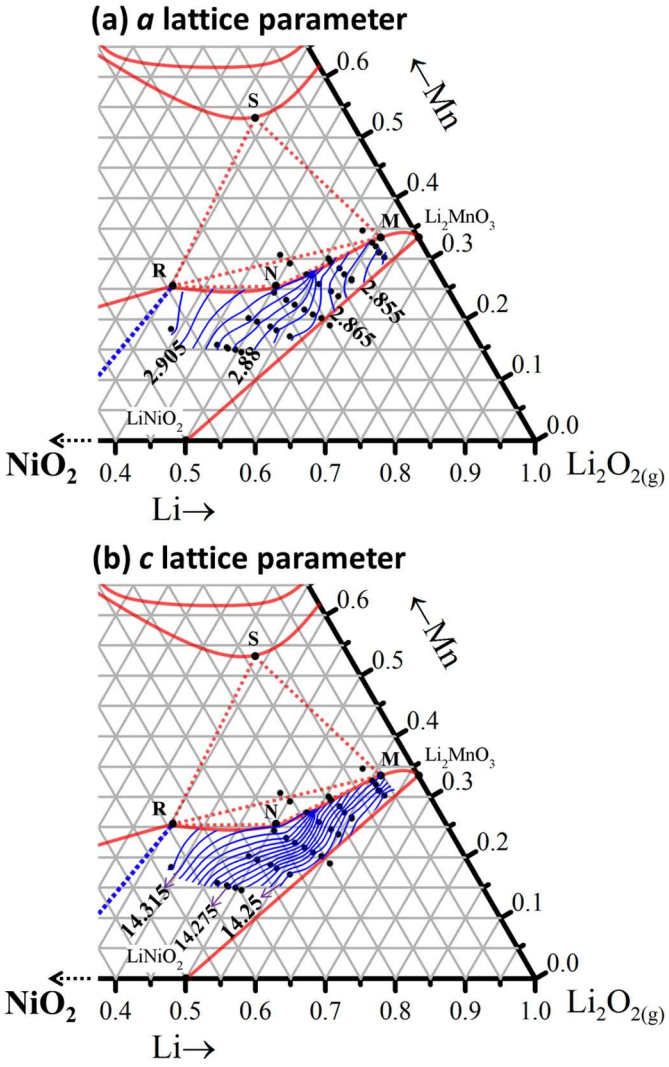

Figure 4.4 Contour plots of the a and c lattice parameters obtained by fitting all regular cooled layered structures as hexagonal. The solid red lines border the boundaries of the single phase layered region in the Li-Mn-Ni-Oxide pseudoternary phase diagram while red dashed lines are tie-lines at the outer edges of the 3-phase regions. S, R, M, N are the end members of the tie lines, representing the spinel, rocksalt, Mn-rich layered and Ni-rich layered phases, respectively. The solid black dots represent the actual composition of all the samples made. Only the samples in the layered region were used to generate the contour plots. An extra series of y=0.33 were added for the generation of the contour plots.

The lower boundary line is defined as a straight line drawn from $LiNiO_2$ to Li_2MnO_3 where nickel ions are 3+ according to McCalla *et al.*[10], which agrees well with the XRD data available. The red dashed lines are tielines at the outer edges of the 3-phase regions. The solid black dots represent the actual compositions of all the samples made. The contour plots of a and c lattice parameters in the single phase region were generated when the structures were fitted in the $R\bar{3}m$ space group. The addition of lithium resulted in a reduction of the c axis but very little change in the a lattice parameter. This trend is in good agreement with McCalla *et.al.*[10]

4.2.5 Electrochemical Testing Results

4.2.5.1 Voltage as a Function of Specific Capacity

Figure 4.5 shows the voltage versus specific capacity curves of samples of the composition series $Li_{1+x}(Ni_{0.4}Mn_{0.6})_{1-x}O_2$ ($0 \leq x \leq 0.24$). The cells were first tested between 2.5 – 4.4 V for four cycles, then charged to 4.8 V for one cycle and followed by cycling between 2.5 – 4.6 V. Samples at x = 0 showed a plateau at ~2.75 V, which suggests the existence of a spinel phase.[86,187] This plateau is no longer observed at x=0.04 in agreement with the XRD results. Samples at x = 0 and x = 0.04, which are in the three-phase region, show very poor electrochemical activity. With the further increase of lithium content, the sample at x = 0.08, which has a two phase layered-layered structure, shows improved performance, with a plateau at ~ 3.6 V, but large polarization existed. When samples were in the single phase layered region, larger capacity and smaller polarization were observed for x = 0.12 to x = 0.24**.** There was a major reversible plateau at ~ 3.6 V and a prolonged irreversible plateau at ~ 4.5 V when cells were charged to 4.8 V. This prolonged plateau was associated with

the oxygen release from the surface and bulk removal of Li^+ as well as electrons from energy levels derived from transtion metal 3d and oxygen 2p.[86,88,187,190,191] Additionally, the length of the plateau increases as *x* increases. A small plateau at ~ 3.3 V was also observed for samples with higher lithium content (x = 0.20 and 0.24).

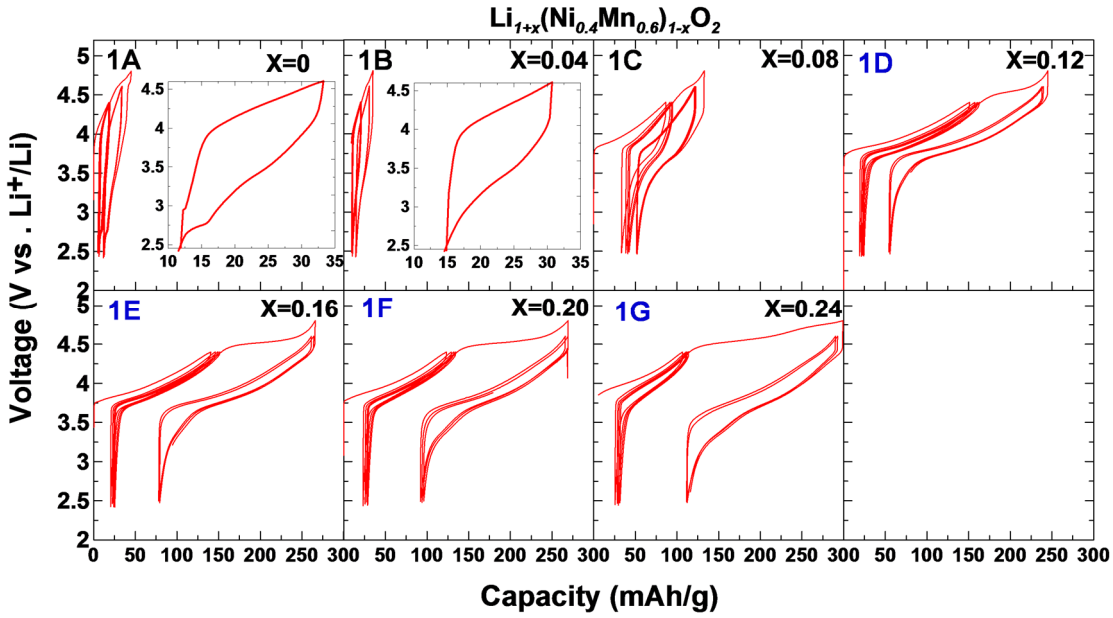

Figure 4.5 The voltage of samples along the composition series $Li_{1+x}(Ni_{0.4}Mn_{0.6})_{1-x}O_2$ ($0 \leq x \leq 0.24$). The cells were first tested between 2.5–4.4 V for four cycles, then charged to 4.8 V for one cycle and followed by cycling between 2.5–4.6 V.

Figure 4.6 shows the voltage versus specific capacity plots of samples in the composition series $Li_{1+x}(Ni_{0.7}Mn_{0.3})_{1-x}O_2$ ($0 \leq x \leq 0.08$). There was no oxygen-release plateau at 4.5 V when cells were charged to 4.8 V for all the samples, indicating there may be no excess lithium in any of the samples, which agrees well with the elemental analysis data presented in Table A.1. Additionally, a small charge–discharge polarization was observed during the second cycle suggesting good electronic and ionic conductivity of the samples. Figures

A.6 – A.8 show the voltage curves for the other compositions. The electrochemical properties of $Li_{1+x}(Ni_yMn_{1-y})_{1-x}O_2$ materials are clearly strongly dependent on their composition.

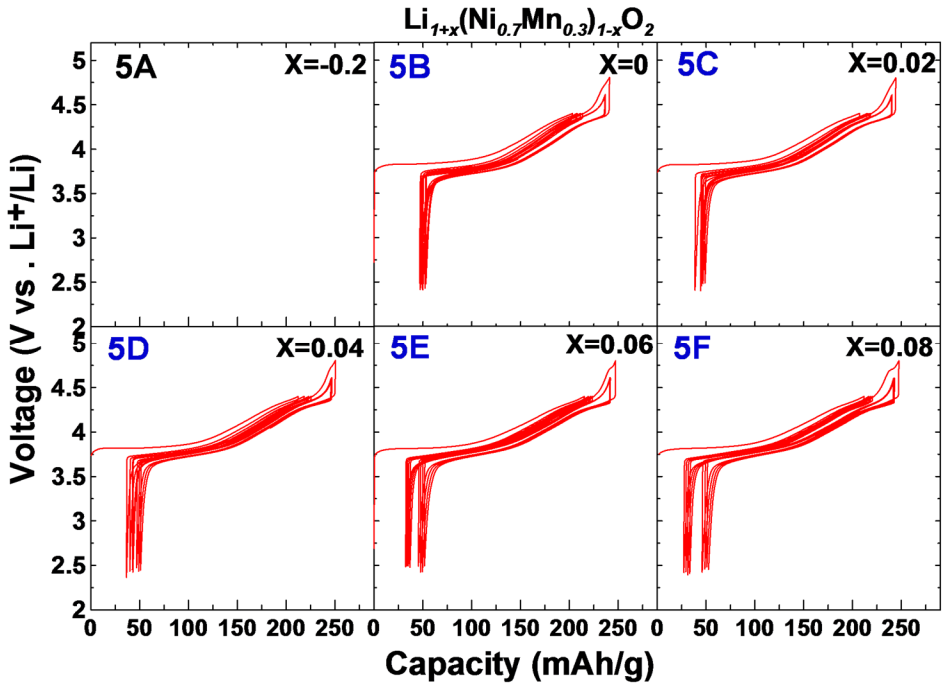

Figure 4.6 The voltage curves of samples along the composition series Li_{1+x} $(Ni_{0.3}$ $Mn_{0.7})_{1-x}$ O_2 ($0 \leq$ x ≤ 0.08). The cells were first tested between 2.5–4.4 V for four cycles, then charged to 4.8 V for one cycle and followed by cycling between 2.5–4.6 V.

4.2.5.2 **Differential Capacity Versus Potential (dQ/dV vs. V)**

Figure 4.7a shows the differential capacity versus potential (dQ/dV vs. V) plot between 2.5 – 4.6 V for the $Li_{1+x}(Ni_{0.4}Mn_{0.6})_{1-x}O_2$ ($0 \leq x \leq 0.24$) series after the first charge to 4.8 V. When x = 0, a discharge peak at ~ 2.75 V was observed and this peak disappeared when x = 0.04 while the other features were maintained.

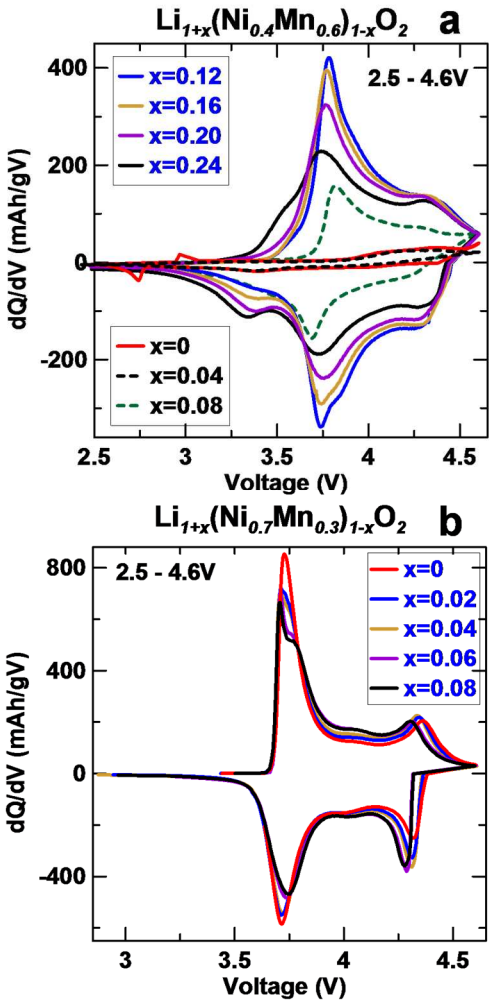

Figure 4.7 Differential capacity (dQ/dV) vs potential (the 5th cycle after charging to 4.8 V) for the series (a) $Li_{1+x}(Ni_{0.4}Mn_{0.6})_{1-x}O_2$ ($0 \leq x \leq 0.24$) and (b) $Li_{1+x}(Ni_{0.3}Mn_{0.7})_{1-x}O_2$ ($0 \leq x \leq 0.08$) between 2.5 – 4.6V.

When x = 0.08, a main feature at ~ 3.75 V appeared which typically corresponds to the redox couple Ni^{2+}/Ni^{4+} in the layered materials. For the samples in the single phase region, the main feature at ~ 3.75 V became pronouced and the area of this peak decreased as x increased. This can be attributed to a decrease in the amount of Ni^{2+} and an increase in the amount of Ni^{3+} which reduces the amount of capacity available due to Ni during

electrochemical cycling as excess lithium is added. Additionaly, a new peak at ~ 3.3 V arose as x was increased to 0.16 and higher, which could be associated to the Mn^{4+}/Mn^{3+} redox couple in the layered stacking after traversing the 4.5 V plateau.[77–79]

Figure 4.7b shows dQ/dV plots for the series of samples with y = 0.7. The peak at about 4.3 V became prominent and a fairly small polarization was observed. However, there were no peaks detected at ~ 3.3 V indicating that no manganese took part in the redox reaction. The dQ/dV curves for the other compositions are shown in Figure A.9. Figures 4.7 and A.10 show that the composition of manganese and nickel can significantly affect the electrochemical performance of the materials.

4.2.5.3 **Capacity Versus Cycle Number**

Figure 4.8 shows the capacity versus cycle number plots for samples of the composition series $Li_{1+x}(Ni_{0.4}Mn_{0.6})_{1-x}O_2$ ($0 \leq x \leq 0.24$). Samples with x = 0 and 0.04, which exhibited a three-phase structure, showed an extremely low discharge capacity of ~ 23.4 and ~ 16.6 mAh/g between 2.5 – 4.6 V after the charge to 4.8 V, respectively. The sample with x = 0.08, which had a two phase layered-layered structure, delivered a capacity of ~ 69.5 mAh/g when cycled between 2.5 – 4.6 V. The electrodes with x = 0.12, 0.16, 0.20 and 0.24, which had single phase layered structures (with/without Li_2CO_3), showed stable capacities of about 182.5, 180.1, 171.5 and 163.6 mAh/g between 2.5 – 4.6 V, respectively. These results clearly show that phase separation into layered-layered and multiphase composites should be avoided in order to deliver the highest capcity and that single phase samples should be prepared, at least at this Ni:Mn ratio.

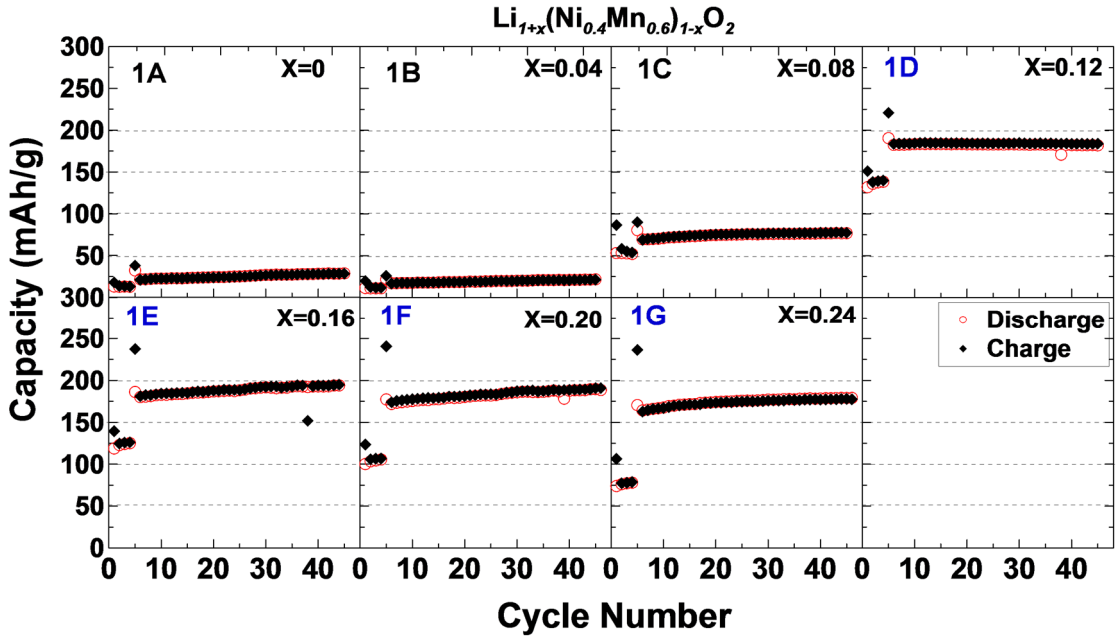

Figure 4.8 Cycling performance of samples along the composition series Li_{1+x} ($Ni_{0.4}$ $Mn_{0.6}$)$_{1-x}$ O_2 ($0 \leq x \leq 0.24$). The cells were first tested between 2.5–4.4 V for four cycles, then charged to 4.8 V for one cycle and followed by cycling between 2.5–4.6 V.

Figure 4.9 shows the the capacity versus cycle number plots for samples in the composition series $Li_{1+x}(Ni_{0.7}Mn_{0.3})_{1-x}O_2$ ($0 \leq x \leq 0.08$). The electrodes with x = 0, 0.02, 0.04, 0.06 and 0.08 showed stable capacities of about 189.1, 193.7, 196.4 and 193.6 mAh/g between 2.5 – 4.6 V, respectively. The nearly linear increase in capacity for $x < 0.08$ can be attributed to a decrease in the amount of Ni ions in the Li layer as shown in Table A.5.

Rapid capacity fading was shown in all the nickel rich samples, which could be due to serious electrolyte oxidation, maybe accompanied by the structural change from H_2 to H_3.[54,241] The capacity versus cycle number data for the other compositions are shown in Figures A.6 – A.9.

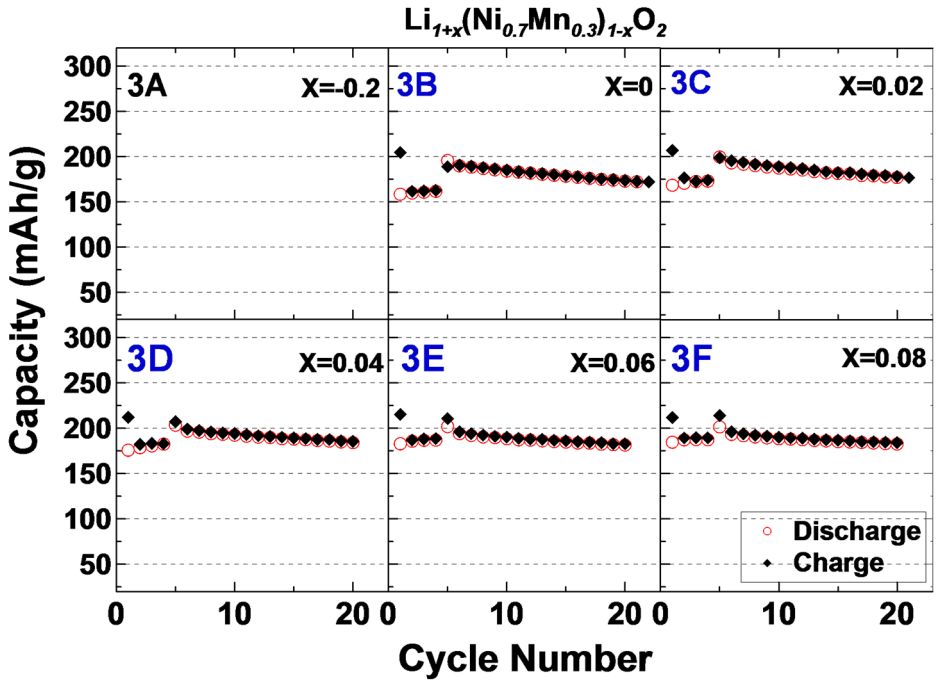

Figure 4.9 Cycling performance of samples along the composition series Li_{1+x} ($Ni_{0.3}$ $Mn_{0.7}$)$_{1-x}$ O_2 ($0 \leq x \leq 0.08$). The cells were first tested between 2.5–4.4 V for four cycles, then charged to 4.8 V for one cycle and followed by cycling between 2.5–4.6 V.

4.2.6 Summary of Reversible Capacity in Terms of Li and TM Composition

4.2.6.1 Reversible Capacity between 2.5 – 4.4 V

Figure 4.10 shows a summary of the reversible capacities of the series $Li_{1+x}(Ni_yMn_{1-y})_{1-x}O_2$ with y = 0.2, 0.4, 0.5, 0.6 and 0.7 between 2.5 – 4.4 V. The rectangular boxes indicate the single phase ranges (for samples without Li_2CO_3). Figure 4.10 shows that the maximum discharge capacity to 4.4 V in each series was found in the sample that is closest to the top of the single phase boundary (smallest x) in the phase diagram when $y \leq 0.5$, and x is closet to 1 when $y > 0.5$.

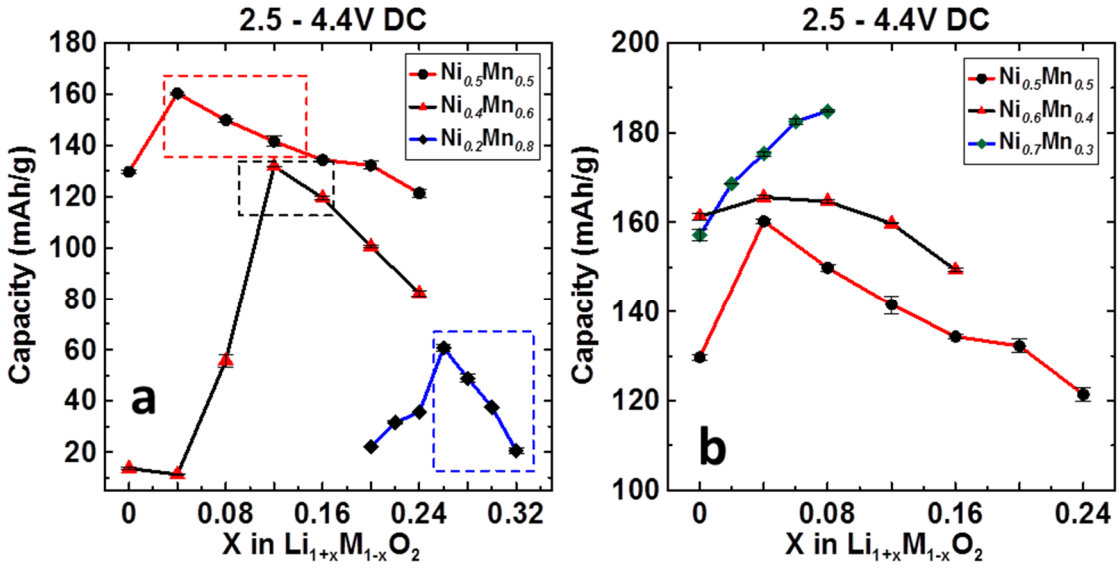

Figure 4.10 Summary of the reversible discharge capacity (the first discharge capacity) of the series $Li_{1+x}(Ni_y\ Mn_{1-y})_{1-x}O_2$ with y=0.2, 0.4 and 0.5 (a) and y=0.5, 0.6 and 0.7 (b) between 2.5 – 4.4 V. The boxes show the single phase regions (without Li_2CO_3).

There is a nearly linear decrease of capacity in the single phase region of each series when x increased except for y = 0.7 as mentioned previously. This can be attributed to an increase in Ni^{3+} (compared to Ni^{2+}) as excess lithium was added, which decreased the amount of nickel redox available. Additionaly, an increase of the amount of Ni (y) resulted in an increase of the specific discharge capacity. The best capacities for y = 0.2, 0.4, 0.5, 0.6 and 0.7 were about 60.7, 150.7, 160.2, 165.6 and 175.3 mAh/g between 2.5 and 4.4 V,respectivly. Above all, Figure 10 shows that phase separation should be avoided and single phase samples with a nickel to manganese ratio of at least 3:2 should be prepared in order to obtain the highest capacity and stable cycling performance between 2.5 and 4.4 V.

4.2.6.2 **Reversible Capacity between 2.5 – 4.6 V**

Figure 4.11 shows a summary of the reversible capacity of the series $Li_{1+x}(Ni_yMn_{1-y})_{1-x}O_2$ with y = 0.2, 0.4, 0.5, 0.6 and 0.7 between 2.5 – 4.6 V.

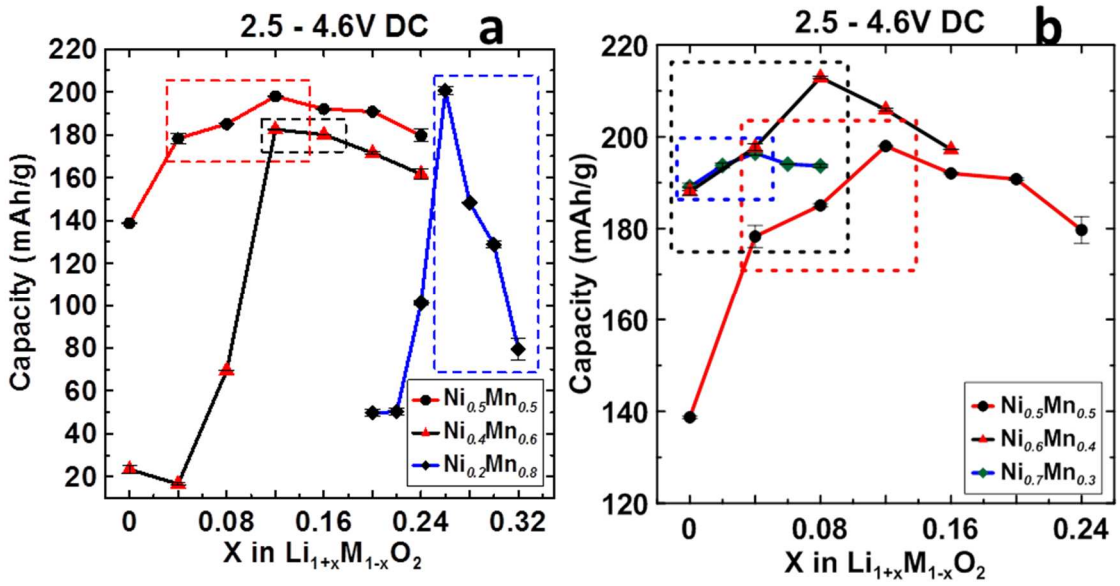

Figure 4.11 Summary of the reversible discharge capacity (the first discharge capacity) of the series $Li_{1+x}(Ni_y\ Mn_{1-y})_{1-x}O_2$ with y=0.2, 0.4 and 0.5 (a) and y=0.5, 0.6 and 0.7 (b) between 2.5 – 4.6 V. The boxes show the single phase regions (without Li_2CO_3).

The rectangular boxes highlight the single phase ranges for samples that do not contain Li_2CO_3. When y > 0.5 (Figure 4.11a), the highest discharge capacity (2.8 – 4.6 V) was obtained at the top (smallest lithium content) of the single phase region in the phase diagram.

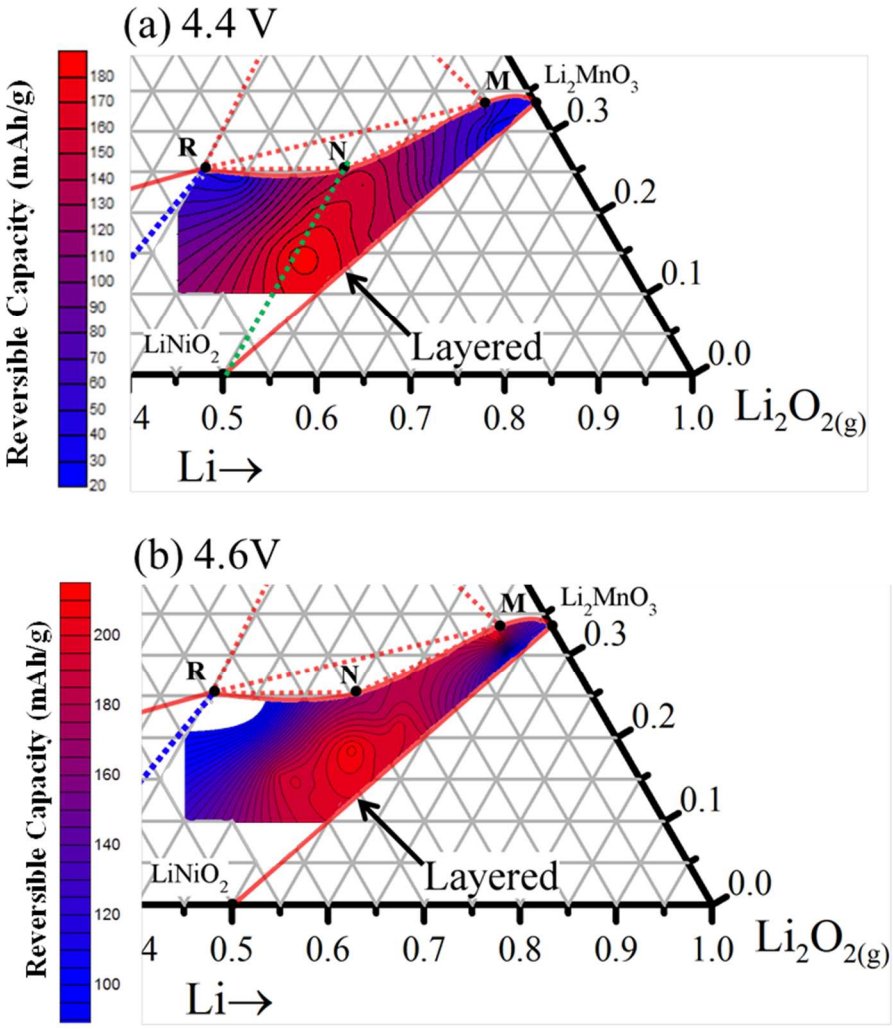

Figure 4.12 Contour plots of the reversible discharge capacity (the first discharge capacity) of the series $Li_{1+x}(Ni_y\ Mn_{1-y})_{1-x}O_2$ between 2.5 – 4.4 V and 2.5 – 4.6 V in the single phase layered region.

The specific capacity decreased as x increased in each series due to a decrease in the amount of Ni^{2+} ions availible as excess lithium was added. When $y \geq 0.5$ (Figure 11b), the samples in the middle of the single phase region gave the highest capacity when cycled to

4.6 V, since these samples have the least Ni in the Li layer and the least Ni^{3+} as excess lithium was added.

4.2.6.1 Contuor Plot of Reversible Capacity in the Single Phase Layered Region

Figures 4.12a and b summarize Figures 4.10 and 4.11 and show contour plots of the reversible discharge capacity (the first discharge capacity) of the series $Li_{1+x}(Ni_yMn_{1-y})_{1-x}O_2$ between 2.5 – 4.4 V and 2.5 – 4.6 V in the single phase layered region, respectively. Figure 4.12b shows the largest capacity between 2.5 – 4.6 V is achieved near the middle of the single phase region when Ni > Mn ($y \leq 0.5$), while it is at the upper boundary (smallest lithium content) when Ni < Mn ($y>0.5$).

4.3 Conclusions

In summary, a series of bulk samples in the layered region of the Li-Mn-Ni oxide system with varied lithium content and transition metal composition ($Li_{1+x}(Ni_y\ Mn_{1-y})_{1-x}O_2$ with y = 0.2, 0.4, 0.5, 0.6 and 0.7) were synthesized in order to understand the influence of the transition metal composition and lithium content on the electrochemichal and structural properties. The boundaries of the single layered phase region along with contour plots of the lattice constants versus composition in the single phase region were generated. The electrochemical results showed that phase separation should be avoided and single phase samples should be prepared in order to obtain the highest capacity. An increase of nickel ratio (y) lead to an increase in the specific discharge capacity when cycled to 4.4 V. The maximum reversible capacity to 4.6 V was found near the middle of the single phase region

when $y > 0.5$ while it was at the top (smallest lithium content) of the single phase region when $y \leq 0.5$. This work provides a careful baseline study for the rational selection of core and shell compositions for core-shell materials.

CHAPTER 5. IN-SITU X-RAY DIFFRACTION STUDY OF LAYERED LI-NI-MN-CO OXIDES

There are debates in the literature about whether Li-rich and Mn-rich materials show a two-phase reaction or single-phase reaction at the top of charge during the oxygen release plateau.[73,74,78,88]

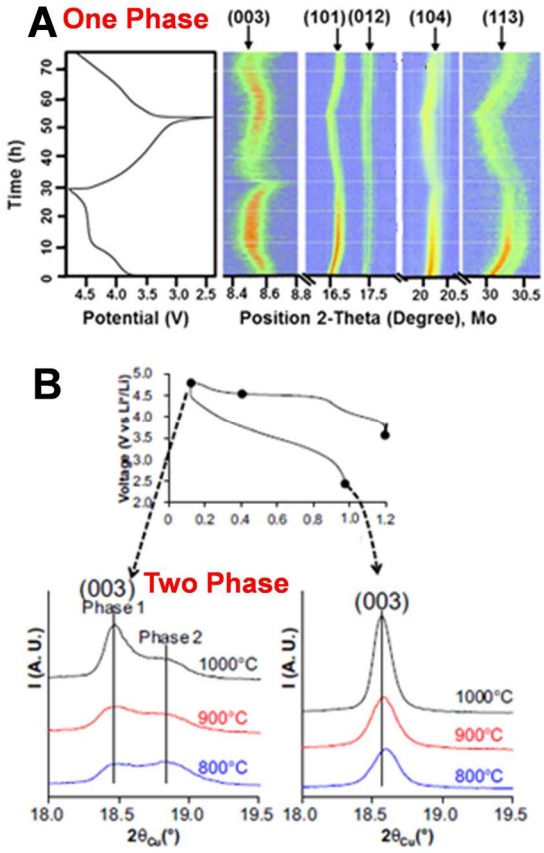

Figure 5.1An example of single-phase reaction throughout the first cycle by Mahonty et al (A), reprinted with permission.[165] Copyright (2013) Elsevier . An example of two-phase reaction by Koga et al (B), reprinted with permission.[88] Copyright (2013) Elsevier.

Figure 5.1 shows *in-situ* and *ex-situ* XRD results for Li and Mn-rich NMC materials from the literature. Figure 5.1A shows a single-phase reaction throughout the first cycle as reported by Mahonty *et al.*[165] Figure 5.1B shows there was a splitting of the (003) reflection at the top of charge indicating a two-phase reaction in the materials studied by Koga *et al.*.[87,88] Based on the two-phase observation, it was proposed that oxygen loss occurred at the surface of the particles with a corresponding densification of the host structure, while reversible oxygen redox occurs within the bulk without major modification of the structure. The two phases were then referred to as the surface and bulk phases respectively.[86–88190]

5.1 Experimental Design

In order to clarify the confusion about the one-phase/two-phase view of the Li and Mn-rich materials during the first cycle and further understand the voltage fading mechanism, materials with same composition but different particle size (secondary particles) were synthesized for *in-situ* XRD experiments. The particle sizes were selected in the hope that the particles in the small particle sample were small enough that they would be all surface phase, while the large particle samples were so large they would have both surface and bulk phases. Figure 5.2 shows the compositions of samples A and B on the Li-Ni-Mn oxide pseudoternary phase diagram. Both samples A and B are on the green line in Figure 5.2 that yields compositions with the best capacity at 4.6 V.[29] The structural and electrochemical properties of these materials were discussed in Chapter 4. Samples A and B have target compositions of $Li[Li_{0.12}(Ni_{0.5}Mn_{0.5})_{0.88}]O_2$ ($Li_{1.12}Ni_{0.44}Mn_{0.44}O_2$), and $Li[Li_{0.23}(Ni_{0.2}Mn_{0.8})_{0.77}]O_2$ ($Li_{1.23}Ni_{0.154}Mn_{0.616}O_2$), respectively.

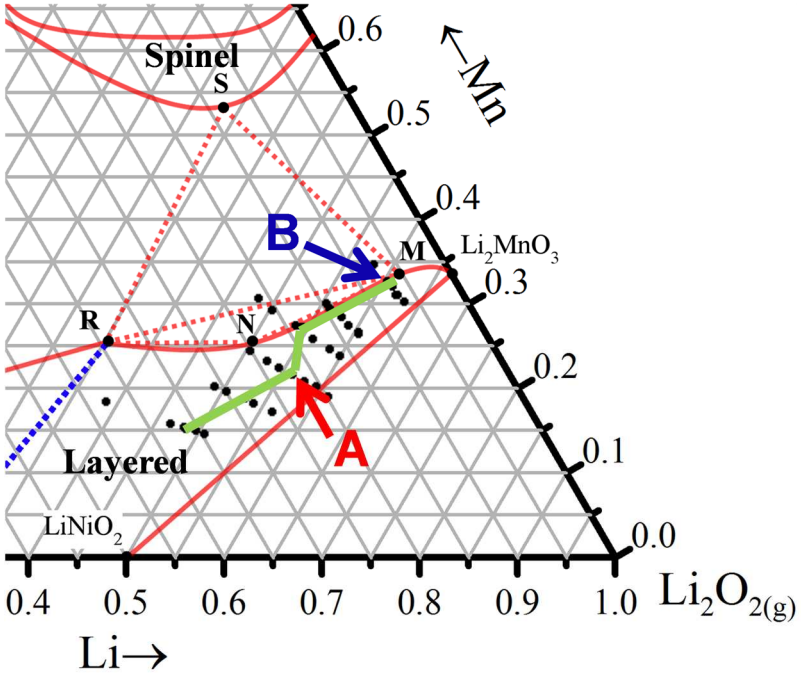

Figure 5.2 The composition of samples A and B on the Li-Ni-Mn oxide pseudoternary phase diagram. Samples on the green line show the highest capacity at 4.6 V.[29]

The detailed synthesis procedures of samples A and B can be found in Chapter 3. When synthesizing sample B with a small particle size, a higher pH of 10.5, a faster stirring rate of 1000 rpm and shorter reaction time of 5 h was used. These samples will be called B(BP) (large particles) and B(SP) (small particles). NMC811 powders and NMC442 pouch cells were obtained from LiFun Technology (Zhuzhou, PRC).

All the cells were tested with a current density of 10 mA/g (~C/20). Cells were tested between 2.5 – 4.8 V for one cycle and between 2.5 - 4.6 V for 20 cycles at 30°C. The in-situ cells were cycled at a rate of ~C/100 during the first charge between 2.5 - 4.8 V and at

a rate either C/100 or C/50 between 2.5 - 4.6 V during the following cycle when Li and Mn-rich materials were tested using the E-one Moli charger system.

In-situ XRD measurements were also performed on layered Li-Ni-Mn-Co oxides with varied nickel content to examine the possibility of volume mismatch between the Ni-rich (core material) and Mn-rich (shell material) materials in the core shell structure.[26,242] The samples studied include NMC811 ($LiNi_{0.8}Mn_{0.1}Co_{0.1}O_2$) and NMC442 ($LiNi_{0.42}Mn_{0.42}Co_{0.16}O_2$) in addition to samples A and B. The results for NMC442 were measured using *in-situ* neutron diffraction, as discussed by Li *et al*.[243].

The majority of this Chapter was published in Chemistry of Materials.[146] Permission has been granted by the American Chemical Society for the reuse of the complete article.

5.2 Results and Discussion

5.2.1 SEM Images of Samples A and B

Figure 5.3 shows SEM images of sample A (e, f) and sample B with small particles (SP) (a, b) and large particles (BP) (c, d)**.** The particle size of sample A and sample B(BP) is around 10 µm, whereas the particle size of sample B(SP) with small particles is less than 1 µm. The sample B(BP) particles are made up of small primary particles which have been sintered into a polycrystalline monolith. SEM cross sections of particles made by these methods (for example see Figure 3 in reference[242]) show the particles to be nearly free of interior voids. The sample B(BP) particles have high tap density and low specific surface

area. Therefore the electrolyte does not have significant access to the interior of the sample B(BP) particles.

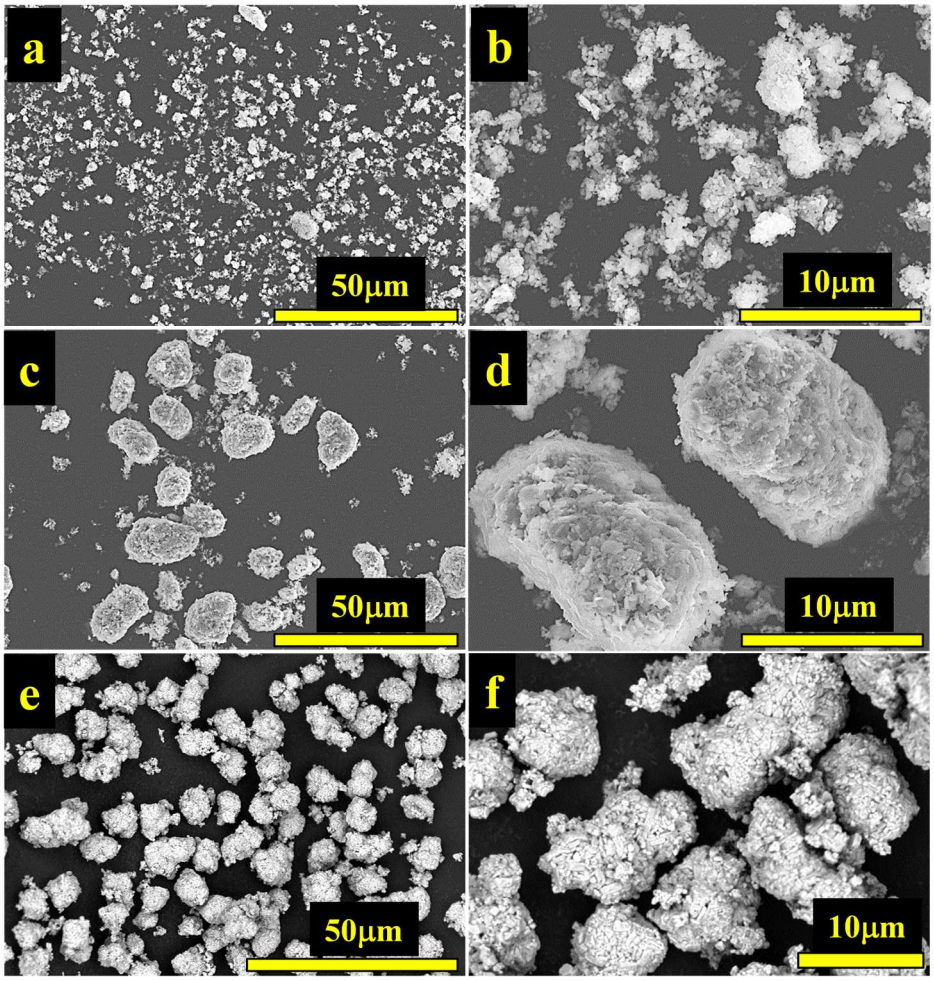

Figure 5.3 SEM images of sample A (e, f) and B with small particles (a, b) and large particles (c, d).

5.2.2 XRD Results for Samples B(SP) and B(BP).

Figure 5.4a shows the XRD patterns of samples B(SP) and B(BP).

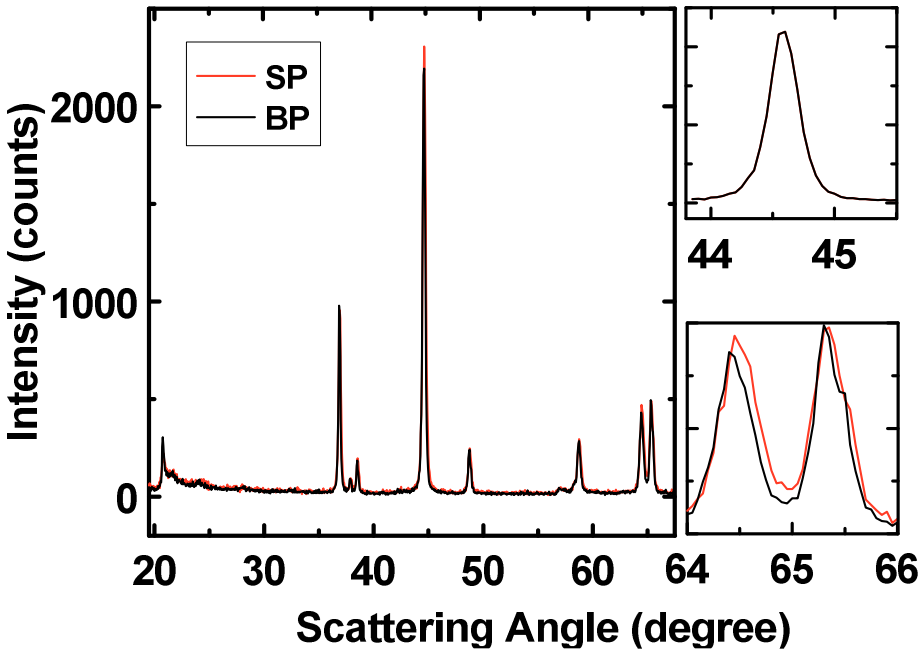

Figure 5.4 XRD patterns of samples B(SP) with small particles and B(BP) with large particles (a) and expanded views of the (104) (b), and (018/110) (c) peaks as indexed in the $R\bar{3}m$ space group for both samples.

Figures 5.4b and 5.4c show expanded views of the (104) and (018/110) peaks as indexed in the $R\bar{3}m$ space group for both samples. The peak positions in the two patterns are virtually identical suggesting similar lattice constants, while the increased breadth of the peaks in Figures 5.4b and 5.4c for the B(SP) sample are due to the reduced particle size. Rietveld refinements were performed in the $R\bar{3}m$ space group with exclusion of the superlattice peak region (20 - 30^{o}).

Table 5.1 shows the Rietveld refinement results for samples B(BP) and B(SP). The lattice parameters of B(BP) and B(SP) are (a = 2.8557(4) Å, c = 14.251(2) Å) and (a = 2.8574(4)

Å, c = 14.249(2) Å), respectively, which are almost identical within uncertainty. This indicates the composition of the B(BP) and B(SP) samples are very close.

Table 5.1 Rietveld refinement results of samples B(BP) and B(SP).

Sample B. $Li[Li_{0.23}(Ni_{0.2}Mn_{0.8})_{0.77}]O_2$				
Sample	a(Å) (± 0.0004 Å)	c (Å) (± 0.002 Å)	Ni_{Li} (%)	FWHM (44.8^{o})
SP	2.8557	14.2515	1.8	0.21
BP	2.8574	14.2490	2.2	0.26

5.2.3 Electrochemical Testing Results

Figure 5.5 shows the electrochemical testing results of samples A, B(BP) and B(SP). Figures 5.5a1, 5a2 and 5a3 show cell voltage as a function of specific capacity for each sample, respectively. The cells with samples A and B(BP) were first tested between 2.5 – 4.4 V for four cycles, then charged to 4.8 V for one cycle and followed by cycling between 2.5 – 4.6 V with a specific current of 10 mAh/g. The cells for sample B(SP) were charged to 4.8 V for one cycle and then tested between 2.5 – 4.6 V directly. A prolonged irreversible plateau at ~ 4.5 V was observed when cells were charged to 4.8 V, which is associated with oxygen release from the lattice and/or oxygen redox.[77] The charge capacities to 4.8 V for samples A, B(BP) and B(SP) were ~245, 296, and 382 mAh/g respectively, whereas the corresponding discharge capacities were ~204, 222 and 218 mAh/g, resepectively.

Figures 5.5b1, 5b2 and 5b3 shows the charge and discharge capacity as a function of cycle number for each sample respectively. Samples A and B(BP) showed stable discharge capacity of ~200 mAh/g for over 20 cycles, while sample B(SP) showed dramatic capacity fading from ~218 to ~100 mAh/g over 17 cycles. Additionally, sample B(BP) shows much smaller irreversible capacity than sample B(SP).

Figures 5.5c1, 5c2 and 5c3 show the differential capacity as a function of voltage (dQ/dV *vs*. V) for each sample respectively, where the red line shows the third cycle, the cyan line shows the 20^{th} cycle and the black lines show the intervening cycles. Figure 5.5c1 shows results for sample A having two main features at ~ 3.75 V and ~ 4.3 V, which typically correspond to the redox couple Ni^{2+}/Ni^{4+} in the layered materials and a weak peak at ~3.3 V which could be associated with the Mn^{4+}/Mn^{3+}redox couple after traversing the 4.5 V plateau.[77–79] Additionally, the area of the 3.3 V peak gradually increased with cycling. Figure 5.5c2 shows sample B(BP) had a strong discharge peak at ~3.3 V, and two weak peaks at ~3.0 V and ~3.75 V respectively at the third cycle. The peak at ~3.0 V could be related to the Mn^{4+}/Mn^{3+} redox in domains with transition metals in the lithium sites (interslab).[88] The area of the peaks at 3.3 V and 3.75 V continously decreased during cycling while the 3.0 V peak increased dramatically, becoming the strongest peak at cycle 20. The continous voltage fading indicates a gradual structural transformation of the material over 20 cycles.

Figure 5.5c3 shows that during the discharge of cycle 2, sample B(SP) had similar features to sample B(BP) at approximately cycle 10 suggesting that the major structural change to the spinel-like phase may be completed after the first cycle for sample B(SP).

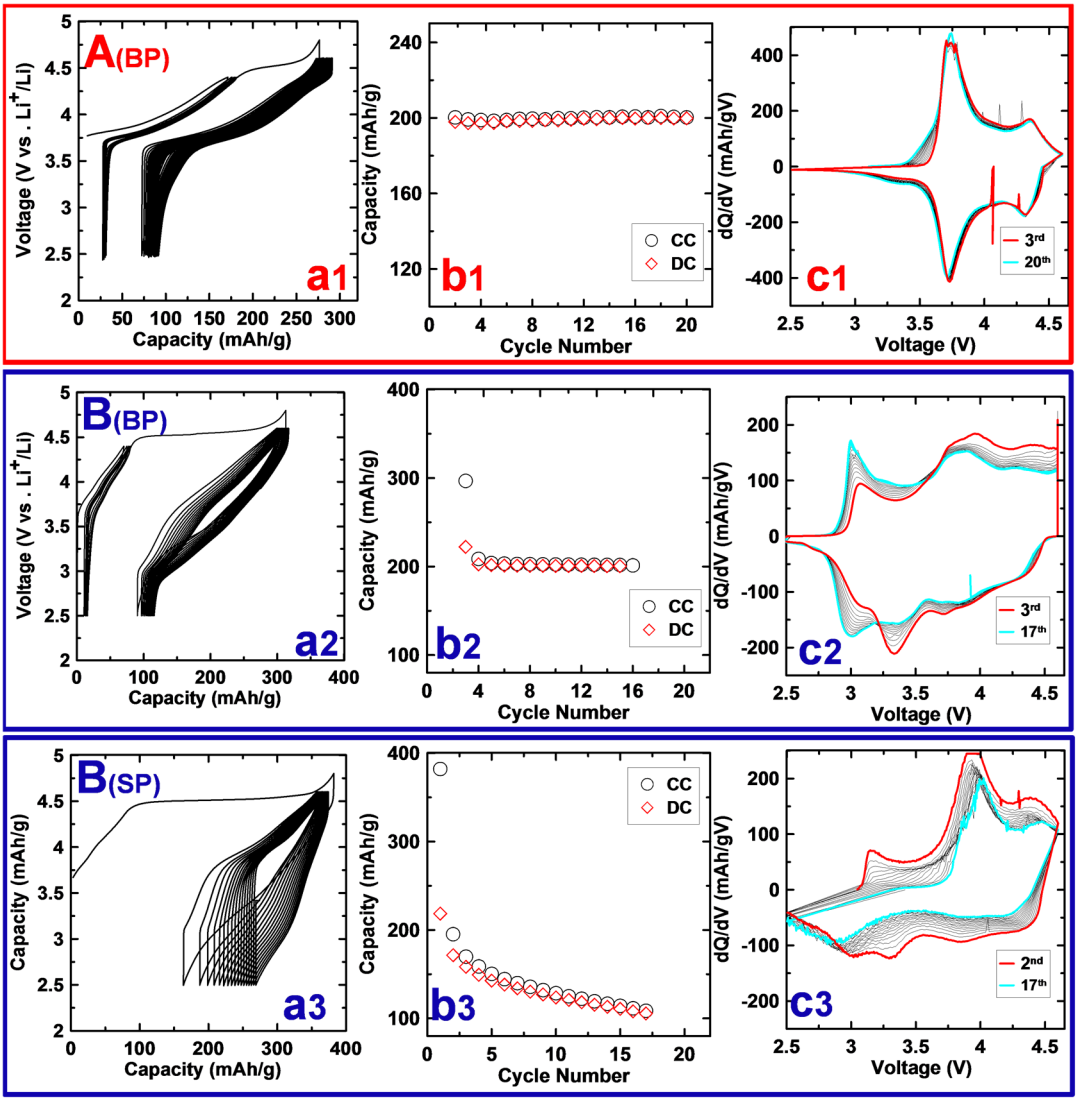

Figure 5.5 Cell voltage as a function of capacity for sample A (5a1), and sample B(BP) (5a2) and SP (5a3). Charge and discharge capacity as a function of cycle number for sample A (5b1), sample B(BP) (5b2) and B(SP) (5b3). Differential capacity as a function of voltage (dQ/dV) for sample A (5c1), sample B(BP) (5c2) and sample B(SP) (5c3), respectively. The red line shows the third cycle, the cyan line shows the 20th cycle and the black lines show the cycles in between.

Sample B(SP) displayed very poor capacity retention. Figures 5.5b and 5.5c clearly demonstrate that the size of the particles of Li and Mn-rich layered oxides can **dramatically** affect the electrochemical performance of the materials, even though the starting materials have the exact same composition and the exact same structure. This suggests that samples with different particle size may experience different structural evolution during cyling. In-situ XRD experiments were initiated to probe this possibility.

5.2.4 In-Situ XRD Results for Sample A

Figure 5.6 shows the *in-situ* cell voltage and XRD patterns of sample A as a function of time. The cell was first charged to 4.8 V at a rate of C/150 and then cycled between 2.5 – 4.6 V at C/50. The cell was held at the top of each charge until the current was lower than 0.03 mA (C/2). Only every fourth diffraction pattern is shown in Figure 5.6 to prevent confusion. Figure 5.6b shows an expanded view of the (003) reflection at the top of charge to 4.8 V (blue lines) and after the second charge to 4.6 V (red line), as indicated by the blue and red circles/arrows in Figure 5.6a, respectively.

Figure 5.6a shows that the (003) peak at ~19^{o} continuously shifted to the left (lower scattering angle) and then to the right (higher scattering angle) as the cell voltage increased, indicating an expansion and then contraction of the c-lattice upon the removal of lithium atoms. Meanwhile, a new peak at higher angle (~19.2^{o}) appeared when the oxygen release plateau began, and became pronounced at the end of first charge. This new peak indicates a coexistence of two phases during the oxygen release plateau. The new phase has a much smaller c- lattice constant. This agrees well with the observations from Koga *et al*.[88] where a surface phase (new phase) and a bulk phase were proposed. As the discharge continued,

the two peaks shifted to lower angle and became difficult to resolve. The (003) peak splitting was also observed at the top of the second charge.

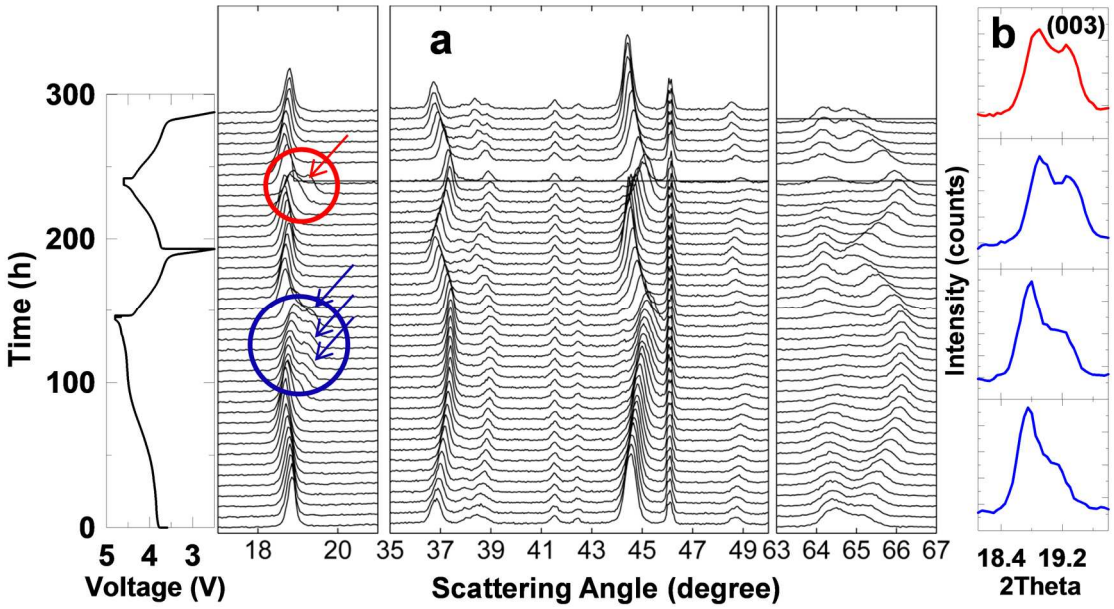

Figure 5.6 *In-situ* cell voltage and XRD patterns of sample A as a function of time (a). An expanded view of the (003) reflection (~19°) at the top of charge to 4.8 V (blue lines) and the second charge to 4.6 V (red line), as indicated by the blue and red circles/arrows in (a) respectively. The cell was first charged to 4.8 V at a rate of C/150 and then cycled between 2.5 – 4.6 V at C/50. The cell was held at the top of each charge until the current was lower than 0.03 mA (C/2). Every fourth pattern is shown.

Figure 5.6b clearly shows the coexistence of the two phases at the top of charge. The new peak at higher angle and the peak at lower angle originate from the surface phase and from the bulk phase, respectively.[88] The peak positions of the two phases both changed during charge and discharge, which indicates a change of composition (lithium content) in both phases. This is different from the staged phases observed in Li_xCoO_2 [52] and in Li_xC_6 [51,244]

that display a coexistence of two phases with changing phase fraction but which have fixed compositions.

5.2.5 Rietveld Refinement Results for Sample A

Rietveld refinements were performed on the *in-situ* XRD data assuming one/two hexagonal layered phases in the $R\bar{3}m$ space group to extract the lattice information. Figure B.1 in Appendix B shows examples of the two-phase fitting for Sample A and Sample B(BP) at the top of charge (4.8 V).

Figures 5.7a, 7b and 7c show the c-lattice constant, a-lattice constant and the *in-situ* cell voltage as a function of the lithium content (x in Li_xMO_2) during the first cycle, respectively. The capacity at the middle of each scan was used to determine the value of x. The red and blue symbols indicate the charge and discharge processes, respectively, while open circles show results for phase 1 (bulk phase) and closed triangles show results for phase 2 (surface phase). A two-phase fitting was performed on patterns that had a clear (003) peak splitting during the oxygen release plateau and at the top of discharge.

As charging started, the c-lattice constant continuously increased from 14.272 Å at x = 1.11 to 14.395 Å at x = 0.67 until phase coexistence began, while the according a-lattice constant continuously decreased from 2.877 Å to 2.837 Å. The c-lattice constants of the two phases decreased with the further decrease of x (charging), whereas the a-lattice constants changed very little. The lattice constants at the end of charge of the bulk and surface phases were (2.835, 14.212) Å and (2.832, 13.931) Å respectively. The c-lattice of the surface phase showed a much larger contraction than that of the bulk phase. During discharge, the lattice

constants of the two phases first increased, and converged closely at x=0.33. The c-lattice constant then continuously decreased to ~14.326 Å at x=0.76 at the end of the first discharge, whereas the a-lattice constant gradually increased to ~2.878 Å.

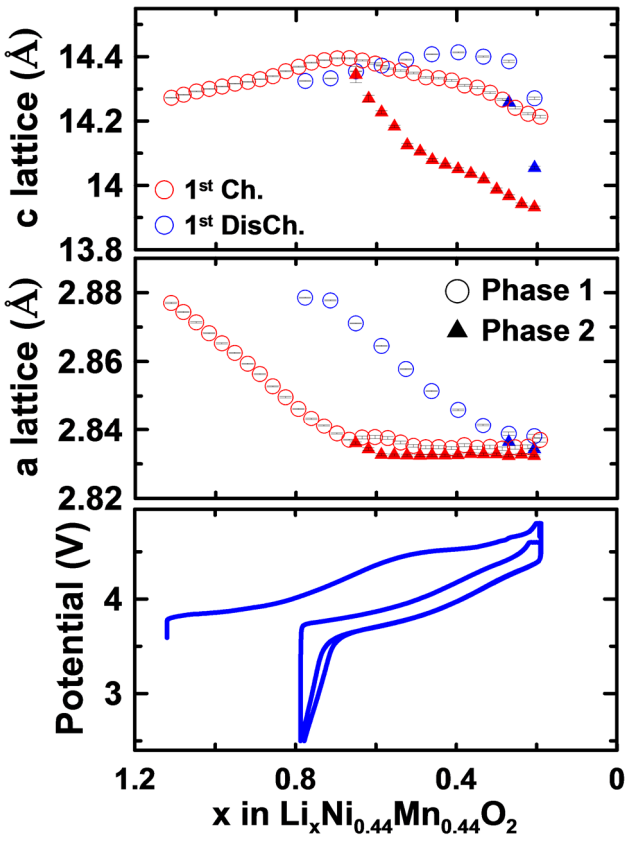

Figure 5.7 The c-lattice (a) and a-lattice (b) constants as well as the *in-situ* cell voltage (c) as a function of the lithium content (x in $Li_xNi_{0.44}Mn_{0.44}O_2$) during the first cycle, respectively. The capacity at the middle of each scan was used to determine x. The red and blue colours indicate the charge and discharge, respectively, while the open circles show phase 1 (bulk phase) and the closed triangles show phase 2 (surface phase). A two-phase fitting was performed on patterns that had clear (003) peak splitting during the oxygen release plateau and at the top of discharge.

Figure B.2 in Appendix B shows that the c/3a ratio of the two phases formed during the first cycle was always larger than the ideal cubic closed packed (ccp) value of 1.633 that is

expected for long-range spinel ordering. The c/3a ratio is a direct measure of the deviation of the lattice from a ccp lattice. According to Whittingham *et al.*[13] , the closer the value is to 1.6333, the greater the transition-metal content in the lithium layer. Figure B.2 indicates that there was no spinel phase formed as claimed in the literature[68,189], however, local domains can have transition metals ions in the lithium layer, and the spinel phase may form after long term cycling. The c/3a ratio of the surface phase was ~1.640, close to 1.6333, which is much smaller than the bulk phase, indicating there might be relatively a large amount of transition metals in the lithium layer. The transition metal ions in the surface phase are unstable in a MO_5 environment after oxygen loss, thus migration of transition metals to the vacant lithium sites are reasonable.[85,86,162]

5.2.6 In-Situ XRD Results for Samples B(BP) and B(SP)

Figures 5.8a1 and 8b1 show the *in-situ* cell voltage and XRD patterns of sample B(BP) and B(SP) as a function of time respectively. The cells were tested between 2.5 – 4.8 V with a current of ~C/100. Every fourth pattern has been plotted to avoid confusion. Figures 5.8a2 and 8b2 show an expanded view of the (003) reflection at the top of the charge to 4.8 V for B(BP) (8a2) and B(SP) (8b2) as indicated by the red circles in Figures 8a1 and a2 respectively. Figure B.3 in Appendix B shows the *in-situ* cell voltage and XRD patterns of sample B(BP) during the second cycle.

Figure 5.8a1 shows that the (003) peak (~19^o) of sample B(BP) shifted to the left (lower angle), and remained almost unchanged as the voltage increased, until a new peak at higher angle (~19.2^o) appeared, which is the similar to the bulk and surface phases observed for sample A (Figure 5.6).

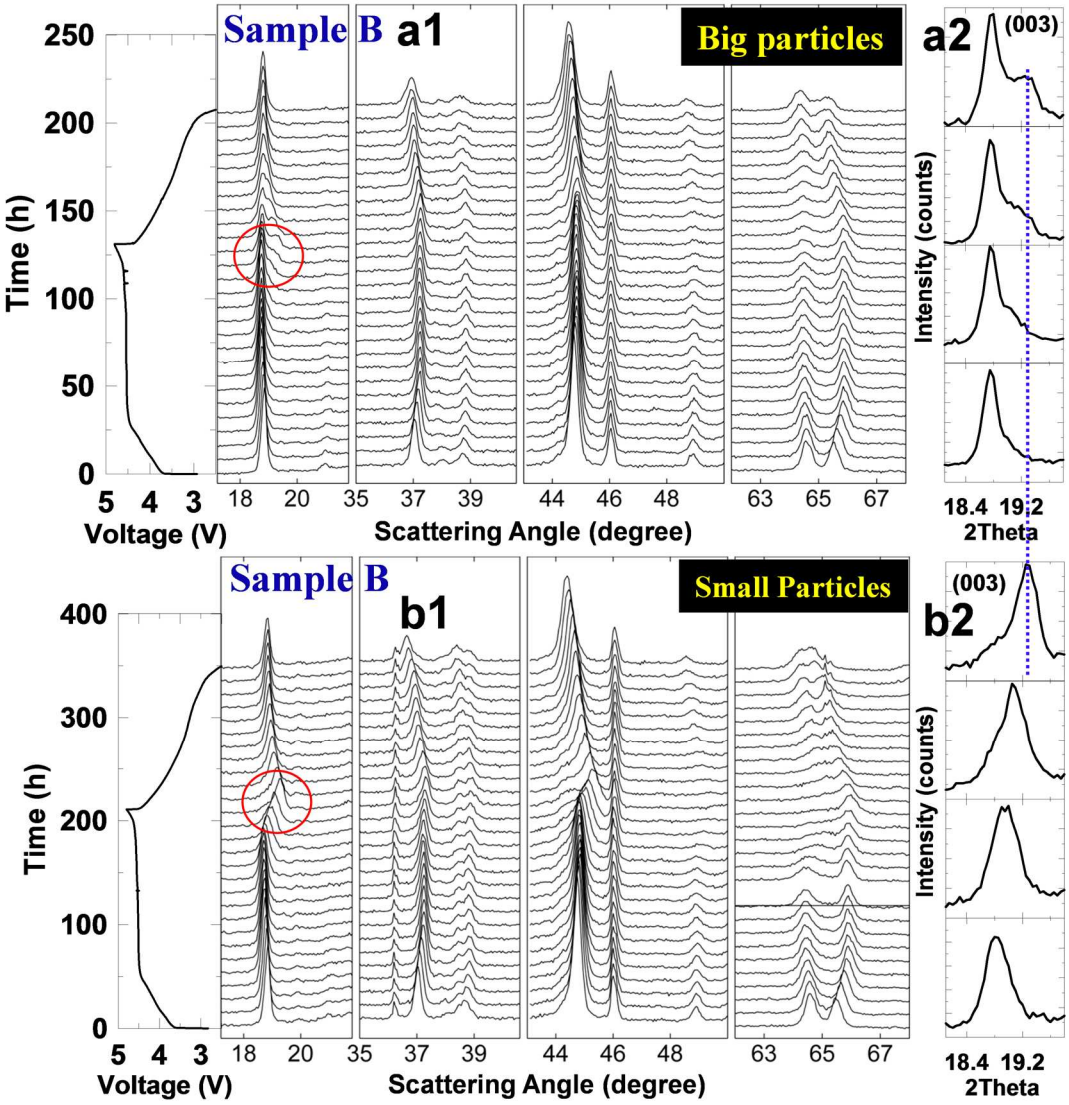

Figure 5.8 The *in-situ* cell voltage and XRD patterns of sample B(BP) (a1) and sample B(SP) (b1) as a function of time, respectively. An expanded view of the (003) reflection at the top of the charge to 4.8 V for B(BP) (a2) and B(SP) (b2) as indicated by the red circles in (a1) and (b1), respectively. The cells were tested between 2.5 – 4.8 V with a current of ~C/100. Every fourth pattern is shown.

Figure 5.8a2 shows the separation of the two peaks became more obvious as voltage further

increased. The (003) peak of the surface phase continuously shifted to higher angle, whereas the (003) peak of the bulk phase changed very little as the charge continued. The two-phase observation for sample B(BP) agrees well with the results for sample A and the results from Koga. *et al*.[88].

Figure 5.8b1 shows the (003) peak of sample B(SP) first shifted to a lower angle and then remained almost unchanged until dramatic shifts to higher angle, indicating a large contraction of the c-lattice when most of the lithium was removed. Figure 5.8b2 shows there was **no splitting of the (003) peak** during the charge and discharge process, indicating there was no phase separation, which matches the results reported by Mohanty *et al*.[165]. This suggests that the particles are small enough that they behave as the "surface phase" of the large particles throughout their entire volume.

The results in Figure 5.8 strongly suggest that the size of particles significantly affects the structural evolution of the Li and Mn-rich materials during electrochemical testing. The blue dashed line in Figures 5.8a2 and 8b2 shows that the (003) peak for the B(SP) sample and the surface phase of the B(BP) sample have the same peak position, and hence similar structure at the end of charge. This suggests that oxygen loss occurred throughout the entire B(SP) sample, instead of just on the surface. The phase separation in the B(BP) sample could therefore be caused by the limited ability of oxygen atoms to diffuse from the bulk to the surface, or alternatively, by the limited ability of cations surrounded by insufficient oxygen, to diffuse into the bulk. Combined with the dQ/dV results shown in Figure 5.3, it is proposed that the extent of the surface phase continuously grows with cycling in the B(BP) samples, leading to the voltage fade. Samples with large particle size

should be prepared for the best electrochemical performance but this will come at the cost of decreased rate capability.

5.2.7 Rietveld Refinement Results for Samples B(BP) and B(SP)

Figures 5.9a1, 9a2 and 9a3 show the c-lattice constant, a-lattice constant and the *in-situ* cell voltage as a function of the lithium content (x in Li_xMO_2) during the first cycle for sample B(BP), respectively. The red and blue symbols indicate the data collected during charge and discharge, respectively, while the open circles show phase 1 (bulk phase) and the closed triangles show phase 2 (surface phase).

Figure 5.9a1 shows that the c-lattice constant continuously increased from 14.262 Å at x=1.22 to 14.327 Å at x =0.91 until phase separation occurred during the first charge, while the corresponding a-lattice constant continuously decreased from 2.856 Å to 2.842 Å. The c-lattice constant of phase 1 (bulk phase) decreased very little as x decreased further and reached ~14.308 Å at the end of the first charge when x = 0.24. The c-lattice constant of phase 2 (surface phase) continuously decreased to ~13.961 Å at 4.8 V. The c-axis lattice constant of the bulk phase at 4.8 V was larger than that of the surface phase suggesting that not all the lithium atoms were removed from the bulk phase.

The a-lattice constant is directly related to the ionic radii, hence, the average valence state of the transition metals in the TM layer. The a-lattice constants of both phases changed very little during the plateau, suggesting there was oxygen loss/redox occurring in the sample. During discharge, the a-axis lattice constants of both phases continuously increased, suggesting Mn was activated and was reduced to Mn^{3+}.

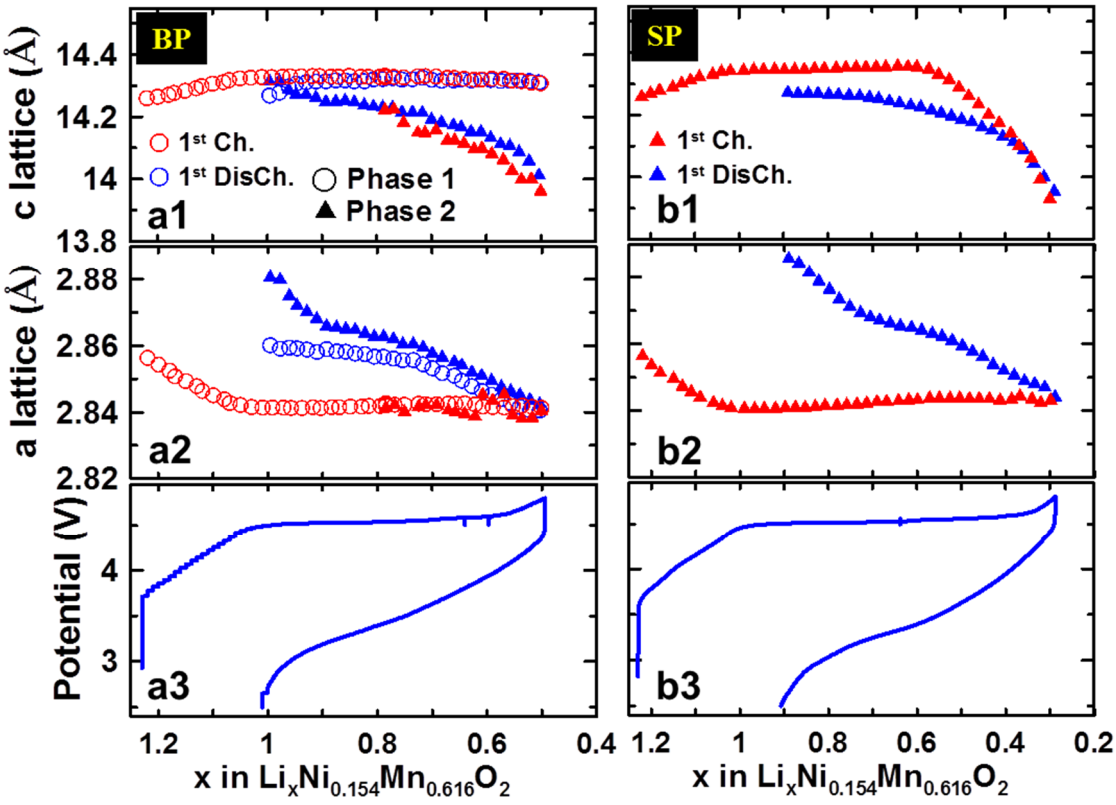

Figure 5.9 The c-lattice (a1) and a-lattice (a2) constants as well as the *in-situ* cell voltage (a3) as a function of the lithium content (x in $Li_xNi_{0.154}Mn_{0.616}O_2$) during the first cycle for sample B(BP), respectively. The c-lattice (b1) and a-lattice (b2) constants as well as the *in-situ* cell voltage (b3) as a function of the lithium content (x in $Li_xNi_{0.154}Mn_{0.616}O_2$) during the first cycle for sample B(SP), respectively. The red and blue symbols indicate the charge and discharge, respectively, while the open circles show phase 1 (bulk phase) and the closed triangles show phase 2 (surface phase).

The maximum charge that can be transferred by Ni^{4+}/Ni^{2+} redox in sample B is about x=0.30, which is much smaller than the total charge transferred during the discharge process (x = 0.71) (x = 1 corresponds to a capacity of ~320 mAh/g), suggesting Mn must be reduced.

Figures 5.9b1, 9b2 and 9b3 show the Rietveld refinement results for the *in-situ* XRD studies of sample B(SP) having small particles. The a-lattice and c-lattice constants of sample B(SP) changed in the very similar way to those of the surface phase of the B(BP) sample. The lattice parameters of sample B(SP) at 4.8 V were (2.843 Å, 13.930 Å), which were very similar to the corresponding lattice parameters of the surface phase of B(BP) (2.841 Å, 13.961 Å). This strongly suggests that the surface phase of sample B(BP) has a very similar structure to the B(SP) sample.

5.2.8 Unit Cell Change as a Function of Cell Voltage for Different Compositions

Figure 5.10 shows the c-lattice constant as a function of cell voltage for NMC811 ($LiNi_{0.8}Mn_{0.1}Co_{0.1}O_2$) (3.0 - 4.4 V), sample A ($Li_{1.12}Ni_{0.44}Mn_{0.44}O_2$) (3.0 to 4.6 V), NMC442 ($LiNi_{0.42}Mn_{0.42}Co_{0.16}O_2$) (3.0 - 4.8 V), and sample B(BP) ($Li_{1.23}Ni_{0.154}Mn_{0.616}O_2$) (3.0 to 4.6 V) during the second charge. The c-lattice constant first increased than decreased in all samples with increasing of cell potential. The maximum change of the c-lattice constant for each sample was 0.51 Å, 0.42 Å, 0.36 Å and 0.24 Å respectively, which suggests that the higher the nickel content of the sample, the larger the c-axis contraction during charge. It should be noted that for sample A and sample B(BP) the largest c-lattice change was for the surface phase.

Figure 5.11 shows the normalized and absolute unit cell volume change as a function of cell voltage during the second charge for the same samples described by Figure 5.10. In Figure 5.11, the black circles are for NMC811 (3.0 - 4.4 V), the blue diamonds are for sample A ($Li_{1.12}Ni_{0.44}Mn_{0.44}O_2$) (3.0 – 4.6 V) (surface phase), the green crosses are for NMC442 (3.0 -4.8 V), and the red triangles are for sample B(BP) ($Li_{1.23}Ni_{0.154}Mn_{0.616}O_2$)

(3.0 to 4.6 V) (surface phase). Figure 5.11a shows that the normalized unit cell volumes follow a very similar path at the beginning of charge when the potential is below ~4.0 V.

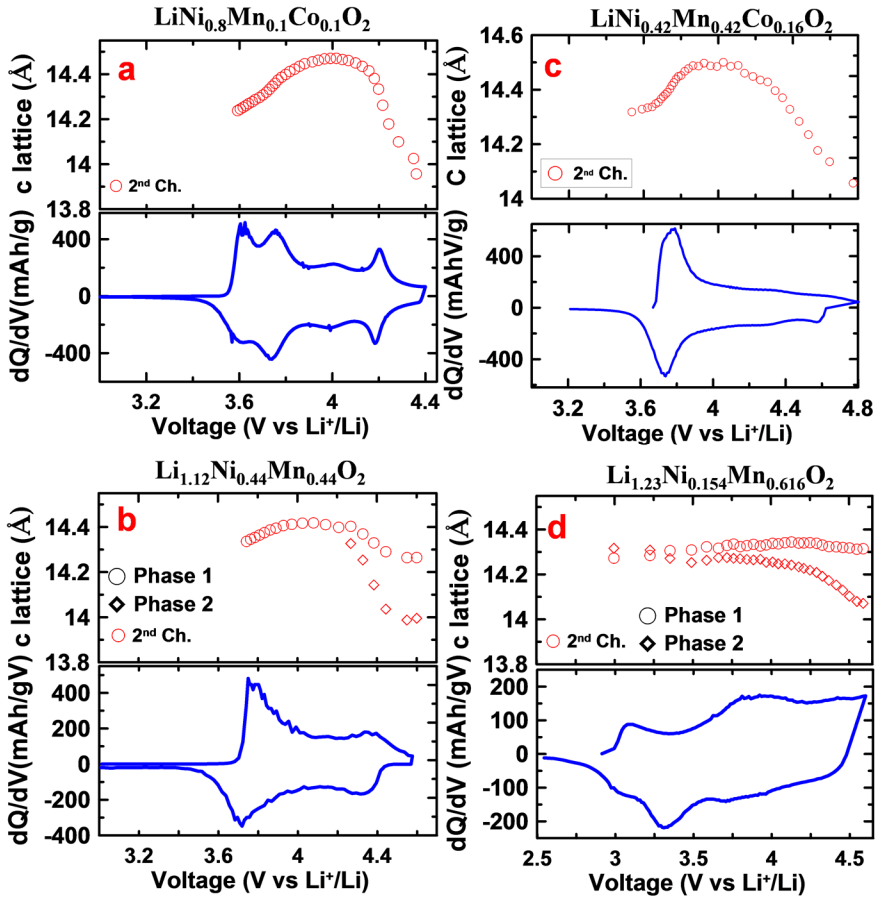

Figure 5.10 The c-lattice constant as a function of cell voltage for NMC811 ($LiNi_{0.8}Mn_{0.1}Co_{0.1}O_2$) (3-4.4 V) (a), sample A ($Li_{1.12}Ni_{0.44}Mn_{0.44}O_2$) (b), NMC442 ($LiNi_{0.42}Mn_{0.42}Co_{0.16}O_2$) (3-4.8 V) (c), and sample B(BP) ($Li_{1.23}Ni_{0.154}Mn_{0.616}O_2$) (d) during the second charge.

As the cell potential increases further, a dramatic volume contraction was observed, especially for samples with high nickel content such as NMC811, due to the removal of most of the lithium atoms from the lattice. The detailed discussion regarding NMC811 is presented in Chapter 5.

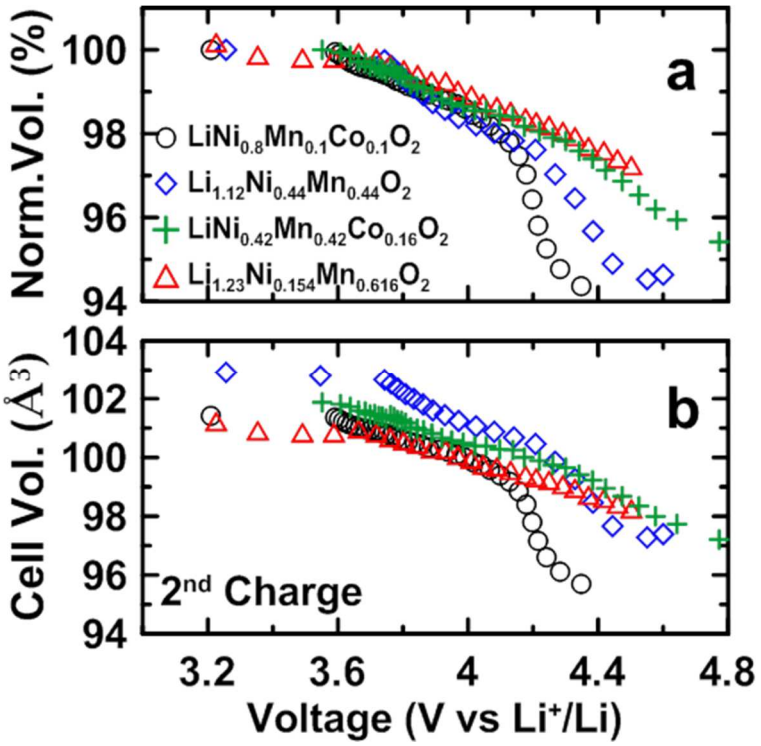

Figure 5.11 The normalized and absolute unit cell volume change as a function of cell voltage during the second charge, where the black circles are for NMC811 (3 - 4.4 V), the blue diamonds are for sample A ($Li_{1.12}Ni_{0.44}Mn_{0.44}O_2$) (surface phase), the green crosses are for NMC442 (3 - 4.8 V), and the red triangles are for sample B(BP) ($Li_{1.23}Ni_{0.154}Mn_{0.616}O_2$).

Samples with larger nickel content showed a much faster contraction of unit cell volume as a function of cell potential. This suggests that there should not be compressive stress on the core nor tensile stress on the shell in core-shell materials (same potential) during cycling, provided the core is Ni-rich (e.g. NMC811) and the shell is Mn-rich (e.g. sample B). Figure B.5 in Appendix B shows a schematic of such a scenario, suggesting the shell layer should not crack due to the "volume mismatch" between the core and shell.

5.3 Conclusions

In-situ XRD measurements revealed a two-phase behavior for sample B(BP) sample at high potential, and a one-phase behaviour for sample B(SP). The surface phase of sample B(BP) had a similar structure to the B(SP) sample at the end of the first charge. This suggests that oxygen loss occurred throughout the entire particle of sample B(SP) while only of the surface of the large particle sample B(BP). The low c/3a ratio of the surface phase suggests there might be a relatively large fraction of transition metals in the lithium layer in the surface phase at the top of charge.

These results demonstrate that the particle size of the Li and Mn-rich materials can significantly affect the structural evolution during electrochemical testing and the corresponding electrochemical performance. These results help explain some of the conflicting results in the literature. The phase separation in sample B(BP) could be a result of the limited ability of oxygen atoms to diffuse from the bulk to the surface or, alternatively of cations surrounded by insufficient oxygen to diffuse into the bulk. Samples with of Li and Mn-rich layered oxides with large particle size should have smaller irreversible capacity and better cycle life and hence should be prepared for the best electrochemical performance at the possible sacrifice of high rate performance.

Additionally, samples with higher nickel content showed much faster contraction of unit cell volume as a function of increasing cell potential. This suggests that the core-shell structure in particles with a nickel rich core (e.g. NMC811) and a Mn-rich shell (e.g. $Li_{1.23}Ni_{0.154}Mn_{0.616}O_2$) should be stable during extended charge-discharge cycling as was observed in Appendix B.

CHAPTER 6. FAILURE MECHANISMS OF $LiNi_{0.8}Mn_{0.1}Co_{0.1}O_2$ AS A POSITIVE ELECTRODE MATERIAL

Chapter 2 briefly reviewed the failure mechanisms of Ni-rich NMC in the literature. It was shown that Ni-rich materials have poor charge-discharge capacity retention, which could be related to the electrolyte oxidization at the positive electrode surface[21,23,24,31,107,133] and/or structural changes of the material, such as large c-axis shrinkage[241,245], at high potentials. This work is therefore aimed at determining the failure mechanism of NMC811/graphite cells as a function of the potential range chosen for cycle testing, the results of which will aid in further developments. The majority of this Chapter was published in Journal of the Electrochemical Society.[12] Permission has been granted by The Electrochemical Society for the reuse of the complete article.

6.1 Experimental Design

Half cells (coin cells) with control electrolyte, and full cells (pouch cells) with control electrolyte plus additives such as vinylene carbonate (VC) and a prop-1-ene-1,3-sultone (PES) based blend were tested over four different upper cut-off potential ranges. In coin cells, the control electrolyte was 1.0 M $LiPF_6$ in 1:2 v/v ethylene carbonate:diethyl carbonate (EC:DEC). All the coin cells were tested with a current density of 10 mA/g (~C/20) for two cycles and 40 mAh/g (~C/5) for the following cycles. Cells were tested between 3.0 – 4.1, 4.2, 4.3 or 4.4 V (vs. Li/Li^+) at 30°C, respectively. In pouch cells, the control electrolyte was 1M $LiPF_6$ in 3:7 v:v ethylene carbonate (EC):ethylmethyl carbonate

(EMC). Electrolyte additives used were VC, PES, tris(trimethylsilyl)phophite (TTSPi) and methylene methanedisulfonate (MMDS). The combinations of the above additives studied were 2 wt.% VC and 2 wt.% PES + 1 wt.% MMDS + 1 wt.% TTSPi (PES211). Details about the NMC811 used in the pouch cells from Li-Fun can be found in Figure C.1 and Table C.1 in Appendix C. *In-situ* and *ex-situ* X-ray diffraction (XRD) and scanning electron microscopy (SEM) were used to investigate the structural degradation of the materials during cycling.

Isothermal microcalorimetry was used to explore the parasitic reactions and their potential dependence in collaboration with Laura E. Downie.[94,246] Heat flow measurements were performed using a TAM III isothermal microcalorimeter (TA Instruments) as described by Downie et al.[246]. All data were collected at 40.00°C with a heat flow measurement uncertainty of $< \pm 1.0$ µW, a noise level of about 100 nW, and a baseline drift from 0.00 µW to less than 500 nW over the experimental time frame. While inside the calorimeter, cells were charged and discharged using a Maccor series 4000 automated test system (Maccor Inc.). The NMC811/graphite cells were first left under open circuit conditions for 24 hours to allow for complete thermal equilibration. These cells were then charged and discharged between 2.8 – 4.1 V four times at 10 mA (C/20) to allow for partial stabilization of the SEI layers. The cells were then charged to 4.0 V at 10 mA, then proceeded through a charge-discharge segment between 4.0 – 4.1 V at 10 mA, then 5 mA, then 2 mA, then finally 1 mA. The cells were charged to 4.1 V at 10 mA, then proceeded through four charge-discharge segments between 4.1 – 4.2 V at 10 mA for partial SEI stabilization in that voltage range, then were cycled between the same voltage limits for 10 mA, 5 mA, 2 mA,

then finally 1 mA. This variable rate procedure was repeated for 4.2 – 4.3 V and 4.3 – 4.4 V.

Safety issues associated with the reactivity of the charged electrode material and electrolyte at elevated temperature were studied using accelerating rate calorimetry (ARC) in collaboration with Lin Ma.[93] The single-point BET surface areas of NMC811 and NMC111 ($LiNi_{1/3}Mn_{1/3}Co_{1/3}O_2$) powders were measured with a Micromeritics Flowsorb 2300 instrument and were found to be 0.38 ± 0.01 m^2/g and 0.48 ± 0.01 m^2/g, respectively. Pellet-type electrodes were made with a weight ratio of active material: Super-S carbon black: PVDF binder of 92:4:4. Pellet-type electrode coin cells were made using control electrolyte and charged to 4.2 V using a "signature charge" protocol.[92,93] At 4.2 V the specific capacity of the NMC811 and NMC111 electrodes were 185 ± 5 mAh/g and 160 ± 5 mAh/g, respectively. The coin cells were then opened in an argon-filled glove box. The electrode was ground lightly and rinsed four times using DMC to remove any residual electrolyte. The powder was then dried overnight in the vacuum antechamber of a glove box before being used for the ARC tests. 94 mg of delithiated NMC111 and 30 mg of electrolyte were used for the ARC tests. To keep the same capacity as NMC111 and the same ratio between electrode material and electrolyte, 81 mg delithiated NMC811 and 26 mg electrolyte were used during the ARC test. The ARC starting temperature was set at 70°C. ARC tests were tracked under adiabatic conditions when the sample self-heating rate (SHR) exceeded 0.03°C/min. Experiments were stopped at 350°C or when the SHR exceeded 20°C /min. To test the reproducibility of the ARC sample construction and measurements, two identical ARC samples were made and tested for every condition.

6.2 Results and Discussion

6.2.1 Half Cell Results

6.2.1.1 Voltage vs Capacity and dQ/dV Results

Figure 6.1a shows the voltage versus capacity curves of Li/NMC811 coin cells with an upper cut-off potential of 4.1 V (vs. Li/Li^+) in red, 4.2 V in blue, 4.3 V in yellow and 4.4 V in black. The first charge curves in the range of 3.0 – 3.9 V show a different pathway than the second charge, whereas there is good overlap between the first and second charge pathways in the 3.9 – 4.4 V region. Irreversible capacities of about 20 – 25 mAh/g were observed and reversible capacities of 159, 178, 195 and 203 mAh/g from 3.0 – 4.1 V, 4.2 V, 4.3 V and 4.4 V (vs. Li/Li+), respectively, were measured. The potential increased very rapidly between 4.3 V and 4.4 V such that the capacity in this range is only ~10 mAh/g.

Figure 6.1b shows the corresponding differential capacity (dQ/dV) as a function of cell potential for the first cycle for each of the four upper cut-off potentials. A weak charge peak at ~3.65 V and an intense charge peak at ~3.75 V, together with two charge peaks at ~ 3.95 V and ~ 4.2 V were observed. There were no obvious peaks between 4.3 and 4.4 V, which agrees well with the small capacity observed in this region.

Figure 6.1c shows the dQ/dV curves of the second cycle for each of the four upper cut-off potentials. A relatively more intense charge peak at ~3.65 V and a relatively weaker peak at ~ 3.75 V were measured when compared with the first charge. Conversely, there were no significant differences of the peaks at ~ 3.95 V and ~ 4.2 V between the first and second

charge in the 3.9 – 4.4 V region. The corresponding discharge peaks at ~ 3.65 V, 3.75 V, 3.9 V, and 4.2 V match well with those observed for the first discharge.

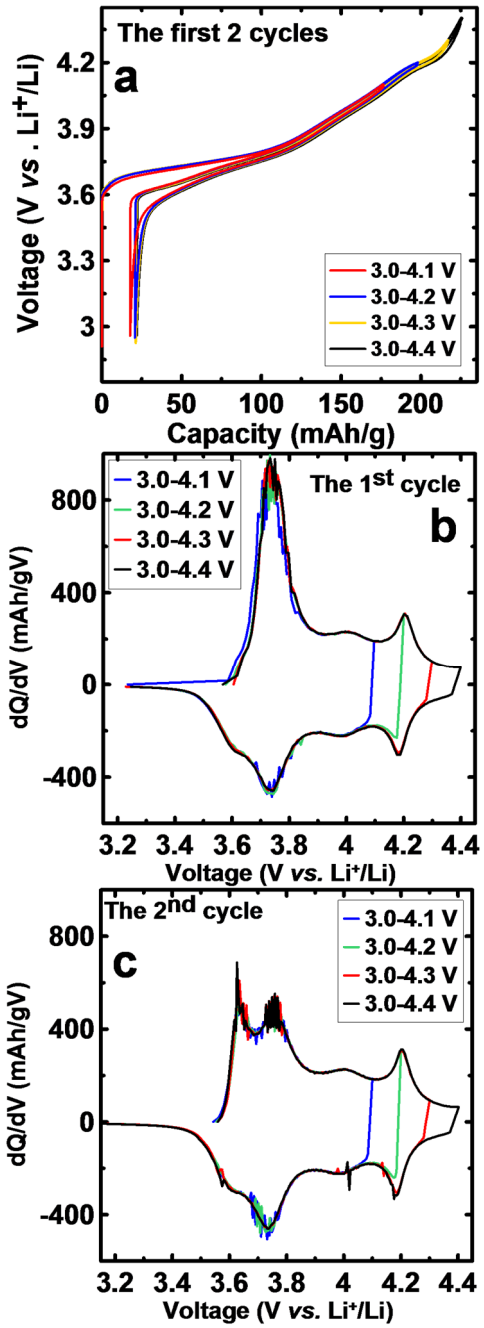

Figure 6.1 (a) The voltage versus capacity curves of NMC811/Li coin cells with an upper cut-off potential of 4.1 V, 4.2 V, 4.3 V and 4.4 V (vs. Li+/Li) respectively. (b) Differential capacity (dQ/dV) as a function of cell potential for the first cycle with the four upper cut-off potentials respectively. (c) Differential capacity (dQ/dV) as a function of cell potential for the second cycle with the four upper cut-off potentials respectively. The cells were tested at a rate of C/20 for 2 cycles and then cycled at a rate of C/5 at a constant temperature of 30ºC.

6.2.1.2 **Capacity Retention for Cells with Different Upper Cut-off Voltage**

Figure 6.2 shows the measured discharge capacity of the Li/NMC811 coin cells as a function of cycle number. The cells tested with an upper cut-off potential of 4.1 V, 4.2 V, 4.3 V and 4.4 V (vs. Li/Li^+) are shown in green inverted triangles, black triangles, blue circles and red diamonds, respectively. Second discharge capacities of ~161, 180, 198, and 207 mAh/g at C/20 were measured from 3.0 – 4.1 V, 4.2 V, 4.3 V and 4.4 V, respectively, whereas the second discharge capacities at C/5 within the same potential ranges were ~150, 169, 188 and 197 mAh/g respectively.

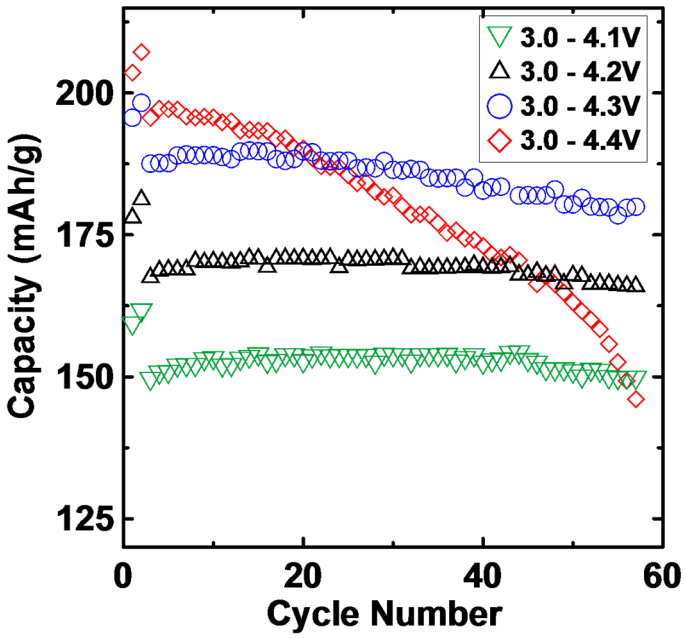

Figure 6.2 Discharge capacity of NMC811/Li coin cells with control electrolyte as a function of cycle number for four different potential ranges. All the coin cells were tested with a current density of 10 mA/g (~C/20) for two cycles and 40 mAh/g (~C/5) for the following cycles at 30ºC.

After 57 cycles, measured capacities were 149, 166, 180, and 146 mAh/g with corresponding capacity retentions of 99%, 98%, 95% and 74% (comparing to the second discharge at C/5), respectively. Cells that cycled above 4.2 V showed poor capacity retention. Moreover, a very significant increase in capacity fade rate was observed between cells that were cycled between 3.0 – 4.3 V and 3.0 – 4.4 V, despite a small 0.1 V difference in upper cut-off potential.

6.2.2 Pouch Cell Results

6.2.2.1 Capacity Retention for Cells with Different Upper Cut-off Voltage

Figure 6.3 shows the discharge capacity as a function of cycle number for NMC811 pouch cells (full cells) containing control electrolyte with 2% VC in red symbols and with PES211 in blue and black symbols. The cells were tested with a lower cut-off potential of 3.0 V for the 2% VC cells and 2.8 V for PES211 cells, while the upper cut-off potentials were 4.1 V, 4.2 V, 4.3 V and 4.4 V, respectively. The cells were cycled at C/20 for two cycles and then cycled at C/5 at 30^{o}C for the duration of the experiment. Cells containing 2% VC had capacities of 167, 186, 177, and 161 mAh after 70 cycles, with corresponding capacity retentions of 98%, 98%, 91%, and 88% compared to the third cycle at 4.1 V, 4.2 V, 4.3 V and 4.4 V respectively.

Cells containing PES211 had capacities of 154, 156, 163 and 148 mAh after only 40 cycles with capacity retentions of 91%, 82%, 82% and 74% at 4.1 V, 4.2 V, 4.3 V and 4.4 V respectively. PES211 cells showed worse capacity retention compared with 2% VC cells cycled to the same potential.

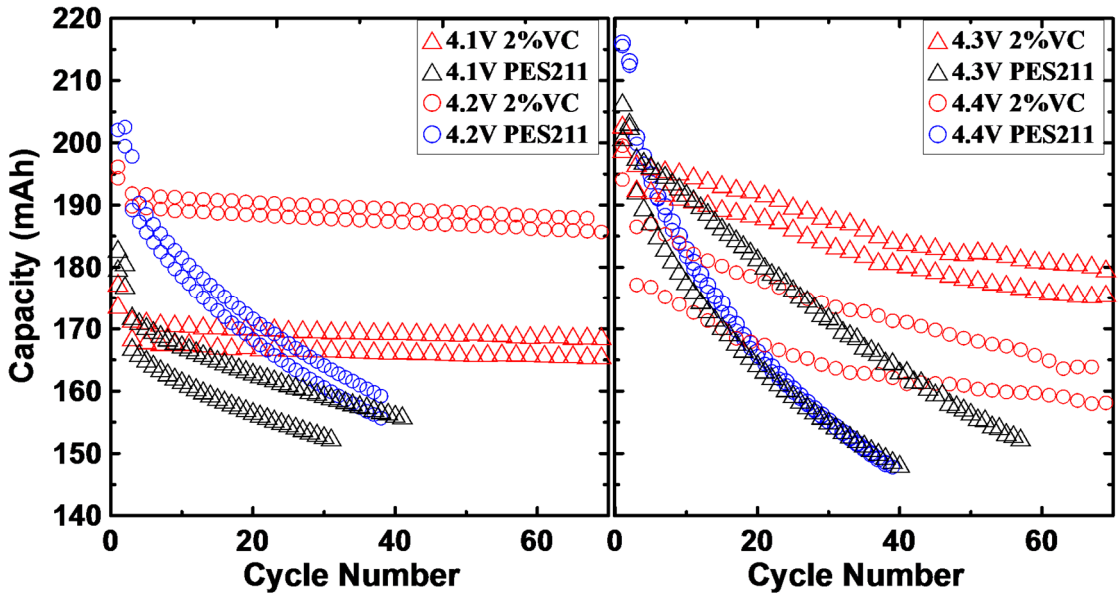

Figure 6.3 Discharge capacity of NMC811/graphite pouch cells with electrolyte additives in the control electrolyte as a function of cycle number. The cells were tested with a lower cut-off potential of 3.0 V for 2% VC cells and 2.8 V for PES211 cells, while the upper cut-off potentials were 4.1 V, 4.2 V, 4.3 V and 4.4 V for both electrolytes. The cells were cycled at a rate of C/20 for two cycles and then cycled at a rate of C/5 in a temperature box at 30°C.

This surprised us because NMC442/graphite and NMC111/graphite cells with PES211 electrolyte show significantly **better** performance than cells with 2% VC,[133] suggesting the Ni-rich surface of NMC811 behaves differently. Cells containing 2% VC cycled to and above 4.3 V showed much worse capacity retention performance compared to cells cycled to and below 4.2 V.

6.2.2.2 **Delta V Analysis**

In order to explore what was happening inside the cells, the average polarization, ΔV, was calculated by subtracting the average charge potential and the average discharge potential.

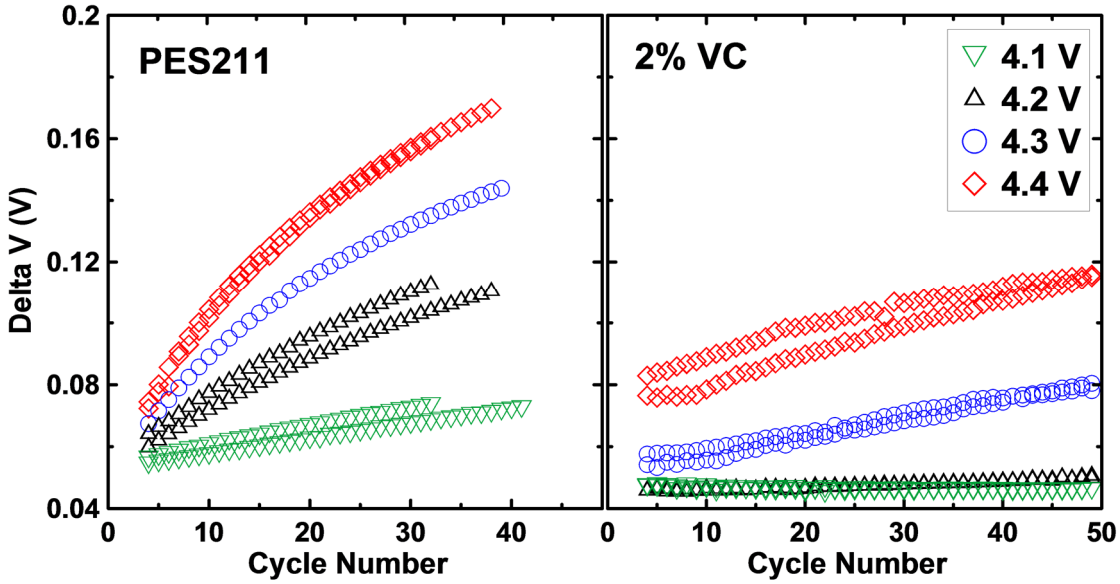

Figure 6.4 ΔV of the pouch cells as a function of cycle number. Cells with PES211 are shown in the left panel and cells with 2% VC are shown in the right panel.

Figure 6.4 shows ΔV as a function of cycle number, which tracks the increase in the polarization of the cells. Cells cycled at lower potentials showed smaller initial ΔV, beginning at the fourth cycle. ΔV was found to be 0.046 V at 4.1 V, 0.046 V at 4.2 V, 0.056 V at 4.3 V and 0.079 V at 4.4 V for 2% VC cells, while it was 0.055 V at 4.1 V, 0.062 V at 4.2 V, 0.067 V at 4.3 V and 0.073 V at 4.4 V for PES211 cells. Cells containing PES211 showed larger initial ΔV when cycled to a potential lower than 4.4 V compared to 2% VC cells, indicating larger cell impedance. After 50 cycles, 2% VC cells at 4.1 V showed very stable ΔV of 0.045 V, while a small increase to ~0.051 V was observed for cells cycled to 4.2 V. Meanwhile, the Δ V increased rapidly to 0.086 V and 0.116 V for cells cycled at 4.3 V and 4.4 V respectively, suggesting significant impedance growth for cells cycled to higher potentials. Conversely, PES211 cells in general showed much larger

increases in polarization with continued cycling. ΔV was 0.072 V, 0.114 V, 0.145 V, and 0.169 V after 40 cycles at 4.1 V, 4.2 V, 4.3 V, and 4.4 V respectively.

The observed impedance growth upon cycling could explain the poor cycling performance of 2% VC cells at higher potentials, as well as PES211 cells even at 4.1 V. The difference in the impedance growth rates shows that different electrolyte additives have different parasitic reaction rates and products which can significantly impact the cell performance.

6.2.3 Isothermal Microcalorimetry Results

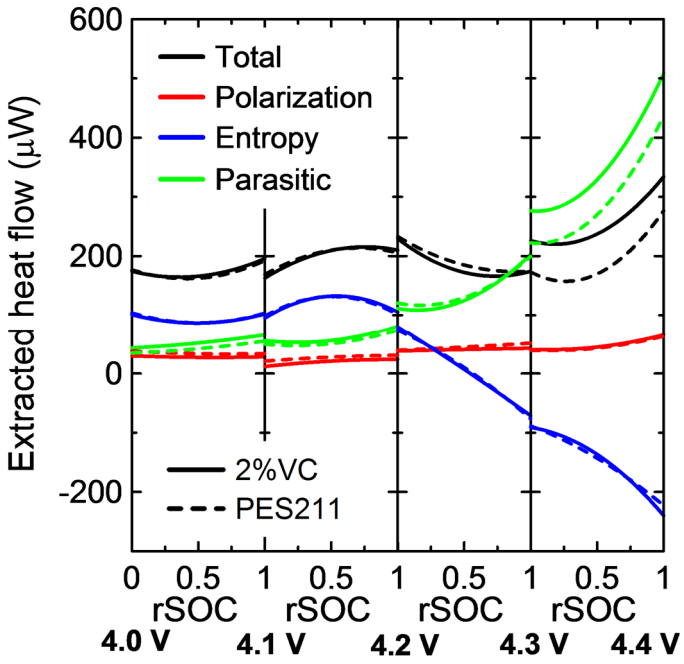

Figure 6.5 The extracted polarization (red), entropic (blue), and parasitic (green) heat flow components of the total heat flow (black) as a function of the relative state of charge (rSOC) for 2% VC (solid lines) and PES211 (dashed lines) cells for a 5 mA charge segment. Courtesy of Laura E. Downie.

In order to further examine the parasitic reaction rate of the cells with different electrolyte additives, cells with PES211 and 2% VC were tested with isothermal microcalorimetry by Laura Downie and the data were analyzed. Figure 6.5 shows the extracted polarization, entropic, and parasitic heat flow components of the total heat flow as a function of the relative state of charge (rSOC) for 2% VC and PES211 pouch cells operating during charge at 5 mA. rSOC is defined as running from 0 to 1 over each potential range studied. For each of the four potential ranges explored, 4.0 – 4.1 V, 4.1 – 4.2 V, 4.2 – 4.3 V, and 4.3 – 4.4 V, the total measured heat flow was collected for four currents (charge and discharge), 10 mA, 5 mA, 2 mA, and 1 mA. The total measured heat flow for all currents was fit using a three-component model described by Downie *et al.*[94,246] that included the irreversible heat flow due to polarization, the reversible heat flow due to changes in entropy as a function of lithium content, and the time-dependent heat flow resulting from the sum of all parasitic reactions occurring in the cell. In this model, each contribution was described using a simple polynomial function of rSOC. The extracted fitting parameters then gave the relative contributions of each term as a function of rSOC. This method is described in detail by Downie *et al.*[94,246]

Figure 6.5 shows the extracted results for cells containing 2% VC in solid lines and PES211 in dashed lines for a 5 mA charge segment in each potential range. Both cells have similar heat flows due to polarization throughout the entire potential range examined during these early cycles. At 5 mA (C/40) the cell polarization is small, which is reflected in the magnitude of polarization heat flow. The heat flow associated with changes in entropy was found to be nearly identical for both electrolyte blends, as would be expected since the electrode materials are nominally identical for machine-made pouch cells. Both cells show

a large entropic heat flow beginning above 4.2 V. This can be understood with a simple lattice gas model[247–250] of the positive electrode materials, where the configurational entropy decreases dramatically as small amounts of lithium are removed from the already highly delithiated positive electrode material (the rate of change of lithium content is negative, resulting in an endothermic heat flow).

Figure 6.5 also shows that below 4.2 V, cells containing 2%VC and PES211 have very similar parasitic heat flows that increase minimally as a function of potential. Between 4.2 V and 4.3 V, the heat flow due to parasitic reactions begins to increase dramatically for both electrolytes. As an order of magnitude reference point, a sustained parasitic heat flow of 100 μW/Wh would consume all the electrolyte in these cells within one year.[246] Above 4.3 V, the parasitic heat flow continues to increase very rapidly, but the addition of the PES211 additive blend reduces the parasitic heat flow as compared to the cell containing 2% VC. The rapid increase in parasitic heat flow above 4.2 V suggests that the highly delithiated positive electrode material surface becomes very reactive towards the electrolyte at high potentials. This is one reason why cells cycled above 4.2 V showed worse capacity retention than those cycled to lower upper cut-off potentials. It is not easy to explain why the cells with PES211 show worse capacity retention than those with 2% VC based on the microcalorimetry results alone, which predict the opposite. Detailed knowledge of the reaction products, in addition to the rate of parasitic heat generation is required.

6.2.4 Analysis of Structural Stability

In order to explore if there is any serious structural change of NMC811 during charge/discharge and whether this change has a significant impact on the cells for long term cycling at the rates tested, a series of *in-situ* and *ex-situ* experiments were performed.

6.2.4.1 *In-Situ* XRD Results

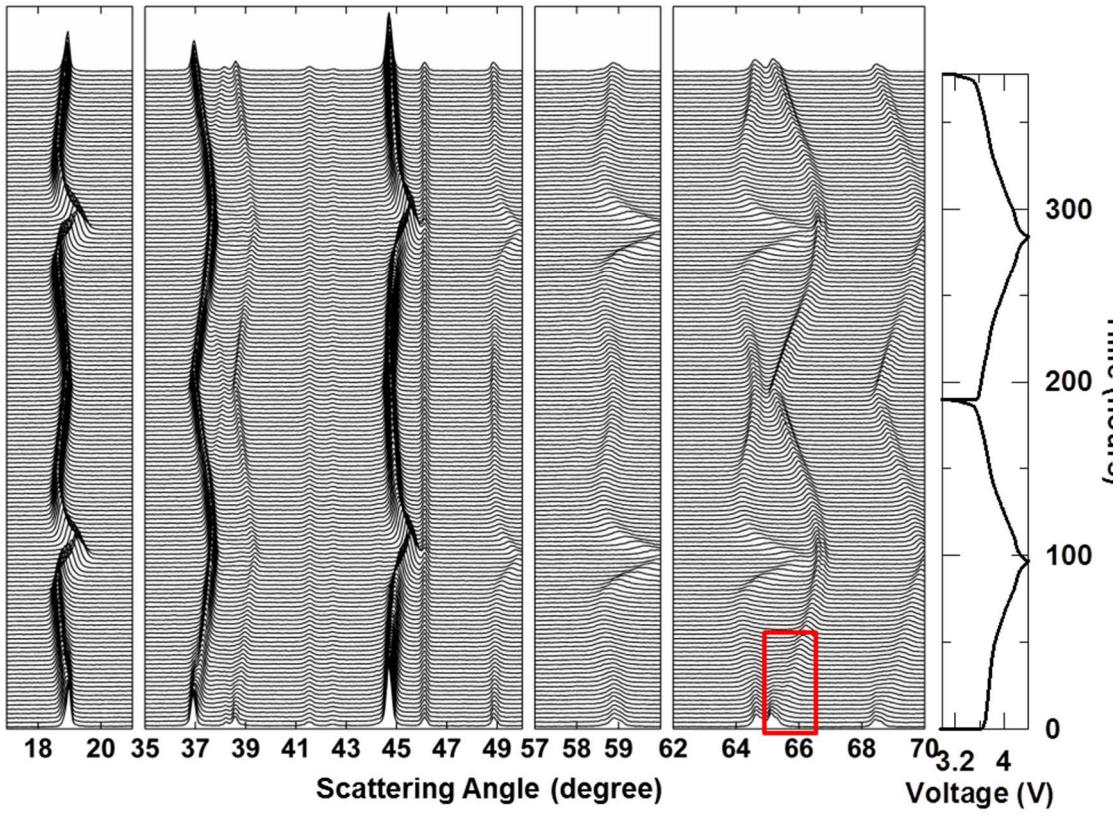

Figure 6.6 Diffraction patterns from *in-situ* XRD experiments, displayed with a sequential offset in intensity for clarity. The right panel shows the voltage curve of the cell as a function of time, which is aligned with the diffraction patterns. The cells were cycled between 3.0 – 4.4 V at a rate of C/100 for two cycles. Each XRD scan took about 2.5 h.

Figure 6.6 shows the diffraction patterns from the *in-situ* XRD experiments with a sequential offset in intensity for clarity. The right panel shows the voltage curve of the cell

as a function of time, which is aligned with the diffraction patterns. The cells were charged and discharged between 3.0 – 4.4 V at a rate of C/100 for two cycles, while each XRD scan was about 2.5 h. As the diameter of the active material coated on the beryllium window was smaller than the beam width at lower angles, the intensity of the detected (003) peak was much lower than expected. The (003) reflection at about 18.96^{o} continually shifted to lower scattering angle during the first charge, however, it began to shift rapidly to higher scattering angle after the cell reached ~4.0 V. The scattering angle was ~19.09^{o} when the cell eventually reached 4.4 V, indicating a significant decrease in the c-axis of the hexagonal structure between 4.0 V and 4.4 V. Moreover, the scattering angle decreased rapidly at the beginning of discharge to ~4.0 V and then gradually increased to ~18.93^{o} when the cell was eventually discharged to 3.2 V. This process was mostly reversible during the second cycle. A similar trend was observed for the (104) peak at ~44.5^{o}, the (015) peak at ~48.8^{o} and (108) reflection at ~64.6^{o}. The (110) peak at ~65.12 ^{o}, as highlighted in the red box, gradually disappeared at the beginning of the first charge, which cannot be observed in the same position after the cell was discharged to 3.2 V, nor in subsequent cycles. Meanwhile, a new peak at a higher angle (near 65.3^{o}) appeared at the beginning of the first charge and a new (110) peak at ~65.19^{o} was detected at the end of the first and second discharges. This indicates that there was a two hexagonal phase co-existence region at the beginning of the first charge. Figure C.2 in Appendix C shows a two-phase Rietveld refinement during this coexistence region during the first charge. The structure changed in a different way at the beginning of the second charge where only single phase behavior was observed. This agrees well the electrochemical results of the

half cells shown in Figure 6.1, where the voltage and dQ/dV curves were different for the first charge and second charge in the 3.0 – 3.9 V region.

6.2.4.2 **Rietveld Refinement Results for *in-situ* XRD Patterns**

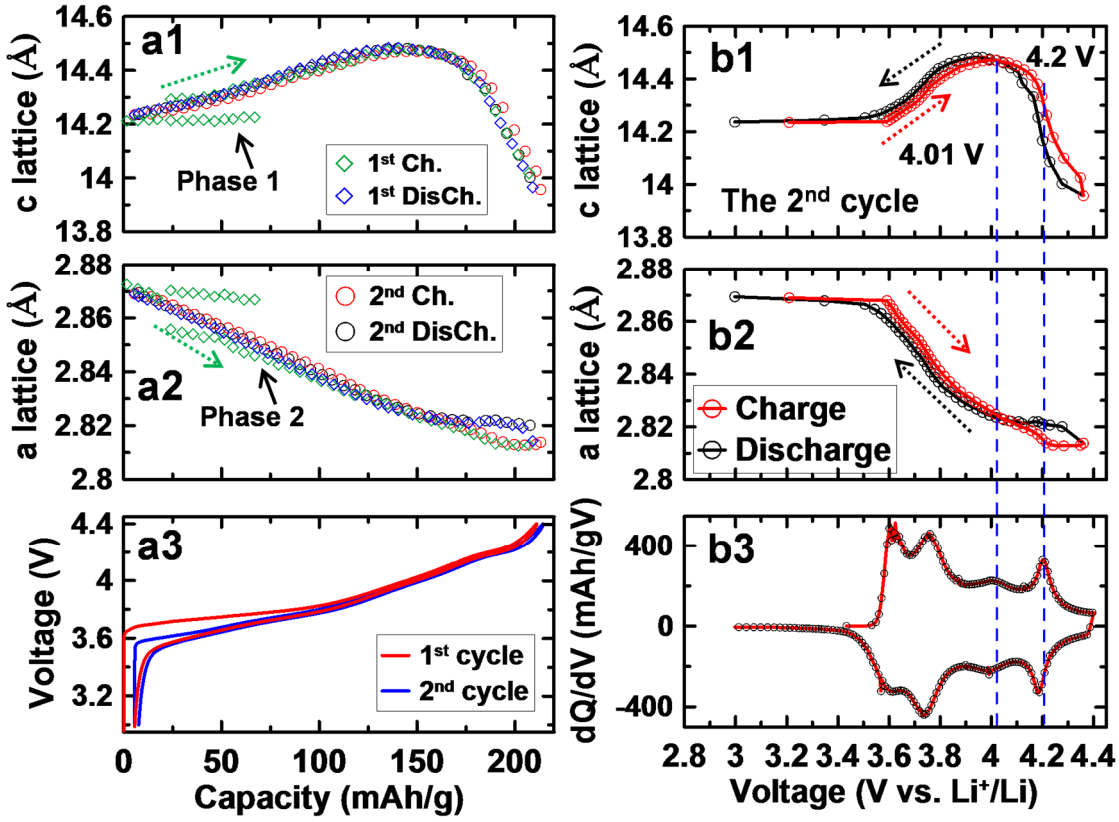

Figure 6.7 The c-axis (a1), a-axis (a2) and the potential of the *in-situ* cell (a3) as a function of specific capacity. The c-axis (b1) and a-axis (b2) as a function of cell potential during the second cycle, and dQ/dV of the second cycle as a function of cell potential (b3).

Figures 6.7a1 and 7a2 show the c-axis and a-axis lattice constants as a function of the specific capacity, respectively, while Figure 6.7a3 shows the voltage of the *in-situ* cell as a function of the specific capacity of the cell. The green diamonds show the first charge

and the blue diamonds show the first discharge, while the red circles show the second charge and the black circles show the second discharge. The green dashed arrow indicates the direction of the change starting from the first charge. It shows that the initial c and a lattice constants were ~14.21 Å and 2.873 Å, respectively, which were slightly different than the lattice constants (14.20, 2.871) Å that were directly obtained from the powder samples due to the off-axis displacement of the *in-situ* electrode.

There was a two phase co-existance region at the beginning of the first charge, which has been discussed in the previous sections, where the two phases called phase 1 and phase 2 are identified with black arrows in Figures 6.7a1 and 7a2, respectively. At the beginning of charge, phase 1 showed a relatively larger a-axis lattice constant than that for phase 2. With further charging of the cell, phase 1 disappeared while the c-axis of phase 2 kept increasing to ~14.49 Å when the capacity reached ~150 mAh/g. However, upon further charging of the cell, it began to dramatically decrease. The c-axis was ~13.96 Å at the end of the first charge when the capacity was ~ 210 mAh/g. The a-axis of phase 2 smoothly decreased during the whole charge process. The change of the lattice constants for phase 2 was reversible in the following cycles. The lattice constants of the active material at the end of the first discharge were about (2.870, 14.23) Å.

Figures 6.7b1 and 7b2 show the c and a - axes as a function of cell potential for the second cycle, while Figure 6.7b3 shows dQ/dV of the second cycle as a function of cell potential. The red circles show the data for the second charge and the black circles show the data for the second discharge. The color-matched arrows indicate the direction of change for the charge and discharge processes. The c-axis continually increased from 14.23 Å to 14.47

Å until the cell potential reached 4.01 V (first vertical blue dashed line). It then started to smoothly decrease with further increase of cell potential. However, a rapid drop in the c-axis (13.96 Å at 4.4 V) was observed after the cell potential reached 4.2 V (second vertical blue dashed line). The a-axis gradually decreased with increasing potential throughout the charge process. This change in the lattice parameters with potential was mostly reversible, though a small hysteresis was detected between charge and discharge above 4.2 V. Figure C.3 in Appendix C shows the percentage changes of the lattice constants as a function of voltage during the second cycle.

The dramatic change of the c-axis at higher potential could lead to the cracking of particles and poor connections between particles as well as macrostrains[137] in the electrode after extensive cycling, which might be one of the reasons for the poor cycling performance of cells that cycled to a potential higher than 4.2 V. In order to confirm if this could be the case for the NMC811cells, pouch cells with 2% VC were cycled for 200 cycles. The active materials were carefully recovered after discharging the cell to ~0 V for *ex-situ* experiments. This is very important, as it is meaningless for comparison if the cells were at different states of charge.

6.2.4.3 **SEM Images of the Electrode after Cycling**

Figure C.4 in Appendix C shows (a) the capacity and (b) ΔV of the 2% VC pouch cells as a function of cycle number for 200 cycles at a rate of C/5 for tests at 30ºC. Cells were cycled to varying upper cut-off potentials of 4.1 V, 4.2 V, 4.3 V, and 4.4 V, which are shown with green inverted triangles, black triangles, blue circles and red diamonds respectively.

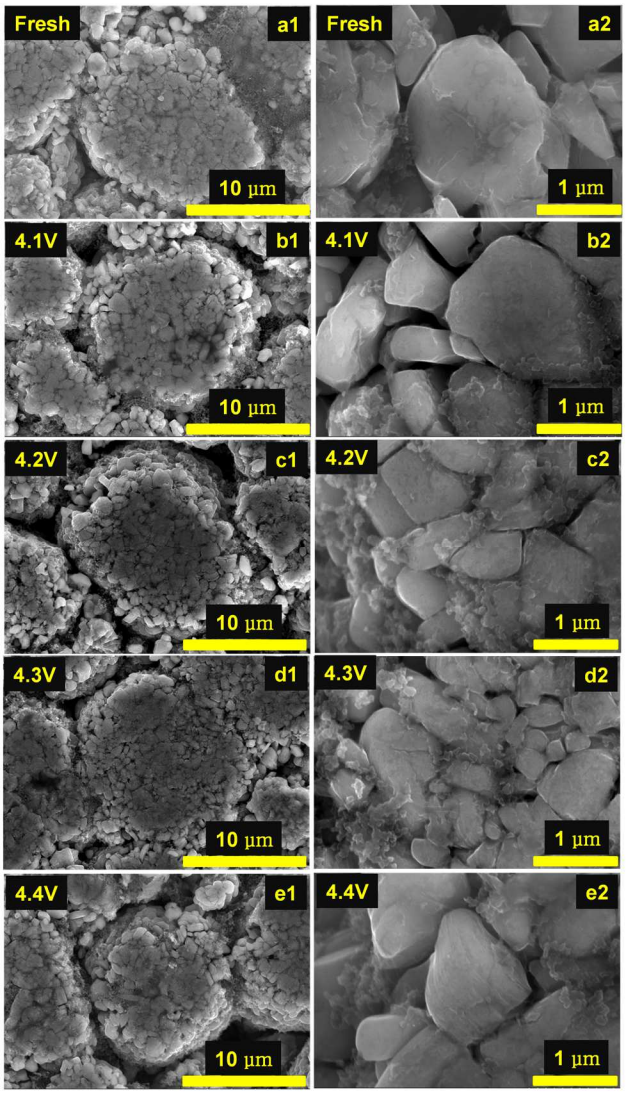

Figure 6.8 SEM images of the fresh NMC811 electrode (a1, a2), and recovered electrodes that were cycled to 4.1 V (b1, b2), 4.2 V (c1, c2), 4.3 V (d1, d2) and 4.4 V (e1, e2).

Figure 8a shows that the capacity for cells cycled to 4.1 V, 4.2 V, 4.3 V and 4.4 V after 200 cycles was 163 mAh, 175 mAh, 162 mAh, and 146 mAh corresponding to a capacity retention of 96%, 91%, 83% and 80%, respectively, compared to the second discharge capacity at C/5. Figure 8b shows that ΔV for cells cycled to 4.1 V, 4.2 V, 4.3 V and 4.4 V

after 200 cycles was ~0.052 V, 0.077 V, 0.126 V and 0.184 V respectively. A larger value and more rapid increase in ΔV were detected for the cells that cycled to a higher potential.

Figure 6.8 shows SEM images of the fresh electrode (a1, a2), and recovered electrodes that were cycled to upper cut-off potentials of 4.1 V (b1, b2), 4.2 V (c1, c2), 4.3 V (d1, d2) and 4.4 V (e1, e2) after 200 cycles at a rate of C/5. Images of the NMC811 positive electrode material particles with lower magnification are shown on the left and images with higher magnification are shown on the right. The images of the electrodes cycled to 4.1 V, 4.2 V, 4.3 V and 4.4 V were very similar to those of the fresh electrodes. No significant damage to either electrode, such as particle cracking or disconnections between particles, was observed from these top-view SEM results

6.2.4.4 *Ex-situ* XRD Results

Figure 6.9 shows XRD patterns of the fresh electrode (A) and the recovered electrodes that were cycled to 4.1 V (B), 4.2 V (C), 4.3 V (D) and 4.4 V (E), respectively. The black symbols show the collected data and the red lines are the fits to the data for a R-3m space group. The right panel shows an expanded view of the (104) reflections. There were no observable differences in either the peak shape or position between electrodes which were cycled to different upper cut-off potentials. The results of the refinements are presented in Table 6.1. The fresh electrode had lattice constants of (2.8710, 14.204) Å, which were the same as those measured from the NMC811 powder within uncertainty. The recovered electrode that was cycled to 4.1 V (A) had lattice constants of (2.8711, 14.216) Å. There was slight increase in the c-axis compared to that of the fresh electrode due to the change that occurs after the first charge that was observed in the *in-situ* results.

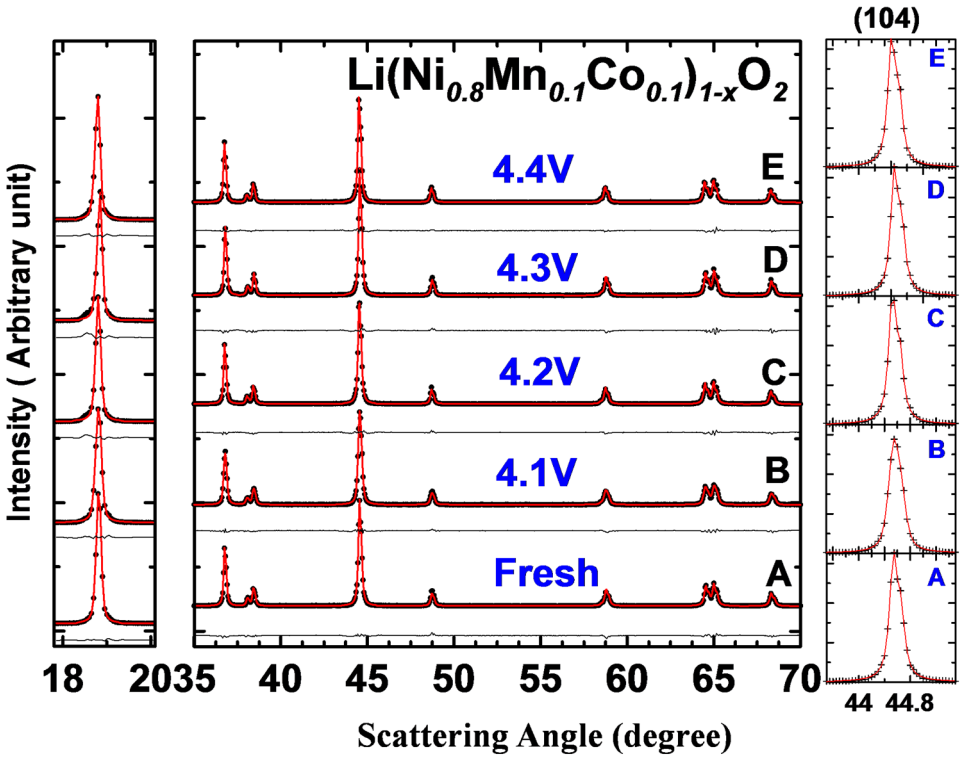

Figure 6.9 XRD patterns of the fresh NMC811 electrode (A) and the recovered electrodes that were cycled 200 times to 4.1 V (B), 4.2 V (C), 4.3 V (D) and 4.4 V (E), respectively. The right panel shows an expanded view of the (104) reflection.

The c-axes of the recovered electrodes that were cycled to 4.2 V, 4.3 V and 4.4 V were 14.217 Å, 14.217 Å, and 14.221 Å, respectively, which are consistent with that of electrode A (4.1V) within uncertainty (0.004 Å). The a-axes increased slightly for the recovered electrodes that were cycled to higher potentials (4.3 and 4.4 V). Additionally, there was no significant difference in the Ni content in the lithium layer. Electrode A (4.1 V) showed a slightly larger full width at half maximum (FWHM) at 44.5°, while it was very close for the other electrodes (C, D and E). The recovered electrodes that were cycled to higher

potentials (4.3 and 4.4 V) did not show any significant structural differences compared to the recovered electrodes that were cycled to lower potentials (4.1 and 4.2 V).

Table 6.1 Rietveld refinement results of the recovered electrodes

NMC811						
ID	Sample	a(Å) (± 0.0001)	c (Å) (± 0.004)	Ni_{Li} (%)	FWHM (44.5^{o})	Bragg R-factor
	Powder sample	2.8708	14.202	3.0	0.128	3.01
A	Fresh electrode	2.8710	14.204	1.1	0.139	2.14
B	4.1V (200 cycles)	2.8711	14.216	0.76	0.188	3.15
C	4.2V (200 cycles)	2.8717	14.217	1.26	0.128	2.46
D	4.3V (200 cycles)	2.8722	14.217	0.94	0.122	3.34
E	4.4V (200 cycles)	2.8721	14.221	1.26	0.125	1.79

Previous results showed that there was a large c axis contraction and expansion at high potentials during charge and discharge processes. However, the results presented in Figures 6.8, 6.9 and Table 6.1 show that this did not cause any significant morphological changes to the electrodes or the atomic structure of the recovered active material after extensive cycling at a rate of C/5 and temperature of 30.0°C. The structural changes in the active material during charge and discharge may not the major contributor to the poor cycling performance of the cells cycled at high potentials. Instead, we suggest it is the onset of severe parasitic reactions between electrode material and electrolyte above 4.2 V (as shown by Figure 6.5) that is responsible for the poor capacity retention for cells cycled to 4.3 or 4.4 V

6.2.5 ARC Results

Figure 6.10 shows the self-heating rate (SHR) versus temperature for charged NMC811 (4.2 V) and charged NMC111 (4.2 V) with control electrolyte tested between 70°C and

350°C, which are shown in blue and black lines respectively. The dashed lines show results from duplicate samples. An exothermic onset was detected at around 105°C for NMC811 samples, while it was not observed for NMC111 samples up to about 200°C.

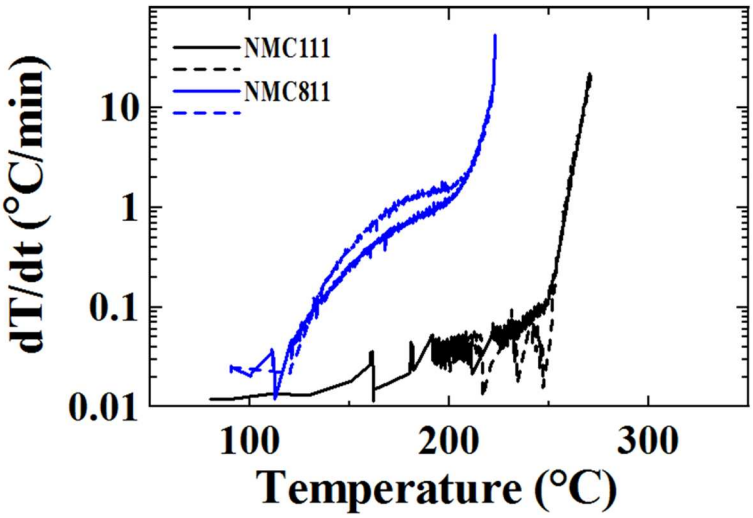

Figure 6.10 Self-heating rate (SHR) versus temperature for delithiated NMC811 (blue) and NMC111 (black) with control electrolyte tested between 70 °C and 350 °C. Courtesy of Lin Ma.

Additionally, the SHR for NMC811 samples increased rapidly after about 120°C, which was much higher than that for NMC111 at the same temperature. The SHR at 200°C was about 1°C/min for NMC811 whereas it was ~0.05 °C/min for NMC111. The delithiated NMC811 samples showed severe reactivity with the control electrolyte at elevated temperature. This suggests that NMC811/graphite cells may be very difficult to design to pass mandatory Li-ion cell safety tests such as the oven exposure test, among others. It will probably be necessary to modify the positive electrode material surface and/or identify and use electrolyte blends to dramatically improve the safety of NMC811 electrodes.

6.3 **Conclusions**

Electrochemical tests from NMC811/Li coin cells and NMC811/graphite pouch cells showed poor cycling performance for cells that were cycled to potentials greater than 4.2 V. Pouch cells containing control electrolyte with 2% VC showed much better capacity retention and lower ΔV than cells with PES211when cycled to the same upper cut-off potentials. However, severe impedance growth was observed for all the cells that cycled to above 4.2 V. Isothermal micro-calorimetry results showed that the parasitic heat flow increased as a function of potential, dramatically so above 4.2 V, for both 2% VC and PES211 cells. A significant c-axis contraction from ~14.47 Å to ~13.96 Å during charging between 4.0 – 4.4 V was measured using *in-situ* XRD. However, no significant changes of the morphology of the electrodes or the atomic structure of the recovered active materials after 200 cycles at a rate of C/5 were observed from the top-view *ex-situ* SEM, and *ex-situ* XRD results. The dramatic structural change of the active material during charge and discharge may not be the major contributor to the poor cycling performance of the cells that cycled to higher potentials. The parasitic reactions that arise from the interactions between the electrolytes and the highly reactive delithiated positive electrode material surface at high potentials are suggested to be responsible for the failure of cells cycled to above 4.2 V. Charged NMC811 showed much stronger reactivity with electrolyte than NMC111 at elevated temperatures suggesting it may be difficult to prepare NMC811 Li-ion cells that can pass mandatory safety tests such as the oven exposure test. It is essential to improve the performance of NMC811 at high potentials by modifying the positive

electrode material surface such as a core-shell or coating strategy, and/or identifying and using electrolyte blends which reduce parasitic reactions and improve safety.

CHAPTER 7. FAILURE MECHANISM OF $LiNi_{0.8}Mn_{0.1}Co_{0.1}O_2$ AS POSITIVE ELECTRODE MATERIAL – SURFACE RECONSTRUCTION

The last Chapter showed that there were no significant irreversible structural changes in the bulk of $LiNi_{0.8}Mn_{0.1}Co_{0.1}O_2$ during charge-discharge cycling. Instead, the parasitic reactions between the electrolyte and the surface of the positive electrode particles at high voltages were suggested to be the cause of the failure of cells cycled above 4.2 V.[12] Recently, Lin *et al*[141] showed that the surface of $LiNi_{0.42}Mn_{0.42}Co_{0.16}O_2$ (NMC442) went through a structural reconstruction from layered ($R\bar{3}m$) to rocksalt (Fm3m). In that transition, transition metal ions migrated to the lithium layers with a possible loss of Li and O from the surface of the structure. This was cited as the cause of a significant increase in cell impedance under high voltage cycling conditions. This surface reconstruction phenomenon was also observed in many other reports about NMC and $Li[Ni_{0.80}Co_{0.15}Al_{0.05}]O_2$ (NCA) positive electrode materials where the surface reconstruction was ascribed to be a result of interactions between the positive electrode surface and the electrolyte.[125,136,138–143,149,251–257]

The thickness of the observed rock salt surface layer varies in the literature. T. Hayashi *et al.*[140] found it was about 5 nm in the positive electrode material from a NCA/graphite 18650 cell after 1000 cycles at room temperature between 2.5 – 4.2 V using currents corresponding to 0.3 C. F. Lin *et al.*[141] showed that the thickness of the surface layer was about 4 nm in the positive electrode material from a NMC442/Li cell after 20 cycles

between 2.5 – 4.7 V at room temperature using current corresponding to C/20. However, **convincing** electrochemical results used to prove that the failure of the Li-ion cells is caused by rocksalt layer growth are not available. Figure 2 in Reference[140] shows that the recovered positive electrode from a cycled NCA/graphite 18650 cell had more than 50% capacity loss while the 18650 cell itself had about 70% capacity retention after 1000 cycles. These two measurements contradict one another. Figure 2c in Reference[141] showed that the capacity of a NMC442/Li half cell was ~150 mAh/g after 20 cycles between 2.5 – 4.7 V at room temperature using currents corresponding to C/20. After the electrolyte was refreshed in the cell, Figure 15c in the supporting information of Reference[141] shows that the same cell had a capacity of only 120 mAh/g (can be counted as the 21st cycle) at the same rate. This is also very troublesome because one would expect the positive electrode to have a capacity of at least about 150 mAh/g even without refreshed electrolyte. It is very important to combine careful electrochemical results with structural observations to actually understand the failure in Ni-rich layered lithium metal oxides.

Many studies show that the rock salt layer is much thicker than those reported above and that it can be beneficial to cell performance. Y. Makimura *et al.*[143] found that the surface layer on NCA grew most dramatically during the first cycle (2.5 - 4.2 V with a C/40 rate at room temperature). They reported a surface layer thickness of about 20 nm including the partially layered region. They reported that this layer did not thicken appreciably in the following cycles. Similar results were also found by N. Y. Kim *et al*.[139]. Makimura *et al.* claimed that this reconstructed surface layer can be a lithium ion conductor due to its nanometer-scale, and can act as a layer which protects the bulk material from further structural degradation and hinders electrolyte decomposition at the positive electrode

surface.[143] Tarascon's group.[258,259] found that thin-films of rocksalt structure oxides exhibited reversible electrochemical reactions in lithium cells while these materials were inactive on a macroscopic scale. Recently, it was also found that disordered rocksalt materials can exhibit high capacities, even on macroscopic scales, if excess lithium is added to the structure [168,260–262]. Y. Cho *et al.*[136] reported that a fresh NMC material ($LiNi_{0.62}Co_{0.14}Mn_{0.24}O_2$) that had a thick surface rocksalt layer (10 nm) displayed better charge-discharge capacity retention than a fresh NMC material ($LiNi_{0.7}Co_{0.15}Mn_{0.15}O_2$) that had a thin surface layer (3 nm). Sasaki *et al.*[148] and Muto *et al*[149] showed that NCA/graphite cells could cycle more than 500 cycles at 60ºC. They found that the degradation of the NCA positive electrode material could not only be attributed to the NiO (Ni^{2+}) type rock salt surface. They claimed the appearance of Li-deficiencies and inactive Ni^{3+} which were distributed throughout the entire particles was also a major contributor.

The literature results certainly leave a careful reader in a confused state. One must ask: Is the nanometer scale (less than 30 nm after aggressive cycling conditions, and less than 10 nm under regular cycling condition) surface rocksalt layer **really** a major contributor to the failure of NMC/NCA based cells? In addition, can this surface layer be suppressed using electrolyte additives or by surface coatings on the positive electrode materials? Takamatsu *et al*[263] recently reported that Co^{3+} at the surface of $LiCoO_2$ was reduced to Co^{2+} after soaking in the electrolyte, however, the reduction of Co was suppressed by the presence of a small amount of vinylene carbonate (VC) additive. This suggests that appropriate electrolyte additives might be able to suppress surface reconstructions of NMC materials.

7.1 Experimental Design

In order to answer these questions, the impact of electrolyte additives and cell upper cut-off potential on the formation of a rocksalt surface layer was studied using STEM. NMC811/graphite pouch cells (220 mAh) were cycled between 2.8 to 4.1 V or between 2.8 to 4.3 V with control electrolyte (control), control electrolyte plus 2% VC (2% VC) and control electrolyte plus 2% PES (2% PES). The control electrolyte was 1M $LiPF_6$ in 3:7 w:w EC:EMC (BASF, max < 20 ppm water). The cells were tested at C/20 for two cycles and then at C/2 for 2 cycles and C/5 for 2 cycles repeatedly for a total of 83 cycles. The tests were made at 40. ± 0.1°C in temperature-controlled boxes. The pouch cells after cycling were discharged to 3.8 V before shipping to the Canadian Centre for Electron Microscopy (CCEM). The cells were discharged to 3.0 V and held for 24 h at CCEM. The cells were then disassembled in an argon-filled glove box, and the recovered positive electrodes were thoroughly rinsed with dimethyl carbonate (DMC). The discharged electrode was transferred to the focused ion beam milling station in air for the preparation of STEM sample. The maximum exposure time was about 2 – 5 mins.

7.2 Determining the Boundary of the Surface Layer

The boundary of the surface layer was determined using two different methods. One method was to visually observe in the image where the surface layer stopped by tracking the presence of transition metal atoms along the lithium layer. The second method was to use image processing software Image J[264,265] to measure the intensity ratio between the Li layers and the TM layers[143]. First, the gray scale value (intensity) was measured along the Li layers and TM layers, respectively, from the original images. At least 20 lines, which mean 10 pairs of Li and TM layers, were measured from each image. The gray-scale

intensities from every Li layer and TM layer were summed and averaged, respectively. Then that data was smoothed using the running average method. The intensity ratio of the Li layers over the TM metal layers was calculated and subsequently re-scaled by defining the minimum intensity ratio point as 0 and the average of the first 10 data points at the sample surface as 1. The thickness of the surface layer can, hence, be determined by the point where the intensity ratio reaches zero (no transition metals in the Li layer). The thickness value determined using this method is already averaged over the whole image. This is the thickness of the surface layer parallel to the lithium and transition metal layers which is called the 'parallel' thickness here. The thickness of the surface layer perpendicular to the surface was calculated by multiplying the 'parallel thickness' by sin(θ) where θ is the angle between the particle surface and the layers in each image. This calculation was performed on 3-5 images from each sample. Then the average surface thickness and its standard deviation was then calculated. This method requires high quality images to be reliable.

7.3 Results and Discussion

7.3.1 Electrochemical Testing Results of Pouch Cells

7.3.1.1 Capacity and ΔV as a Function of Cycle Number

Figures 7.1a and 1c show the capacity and ΔV (difference between average charge and discharge voltage) as a function of cycle number, respectively, for cells with an upper cut-off voltage of 4.1 V, while Figures 7.1b and 1d show the capacity and ΔV as a function of cycle number, respectively, for cells with an upper cut-off voltage of 4.3 V. Figure 7.1a

shows that cells with an upper cut-off voltage of 4.1 V have a relatively stable capacity during cycling.

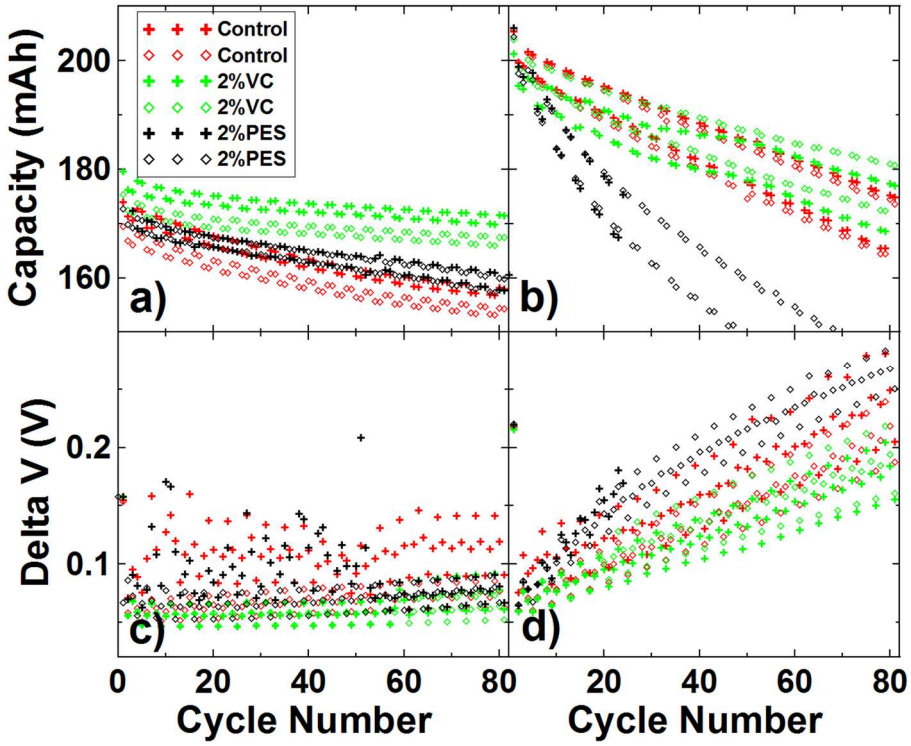

Figure 7.1 Capacity as a function of cycle number for cells with an upper cut-off voltage of 4.1 V (a) and 4.3 V (b). ΔV (difference between average charge and discharge voltage) as a function of cycle number for cells with upper cut-off voltage of 4.1 V (c) and 4.3 V (d). The cells were tested at 40°C with 2 cycles of C/2 followed by 2 cycles of C/5. Two cells for each electrolyte were prepared and tested.

Cells with 2% VC have the best capacity retention whereas cells with control electrolyte and cells with 2% PES have worse. Data for six cells are given in Figure 7.1a but it may appear to the reader that there are 12 distinct sets of data. The reader is reminded that the cycling consists of two cycles at C/2 (slightly lower capacity) followed by two cycles of

C/5 (slightly higher capacity) which explains why there may appear to be two traces for each symbol type. Figure 7.1c shows that there is no significant increase in ΔV with cycle number for the cells charged to 4.1 V. Figure 7.1b shows that cells with an upper cut-off voltage of 4.3 V have much worse capacity retention compared to cells with an upper cut-off voltage of 4.1 V. At 4.3 V cells with 2% PES perform worst while cells with 2% VC perform best. It is worth pointing out that NMC442/graphite and NMC111/graphite cells with 2% PES electrolyte show significantly **better** performance than cells with 2% VC and control electrolyte, which indicates the importance of positive electrode Ni content on additive functionality.[33,34] Figure 7.1d shows that cells with an upper cut-off voltage of 4.3 V have a significant ΔV increase, indicating serious polarization growth within the cells.

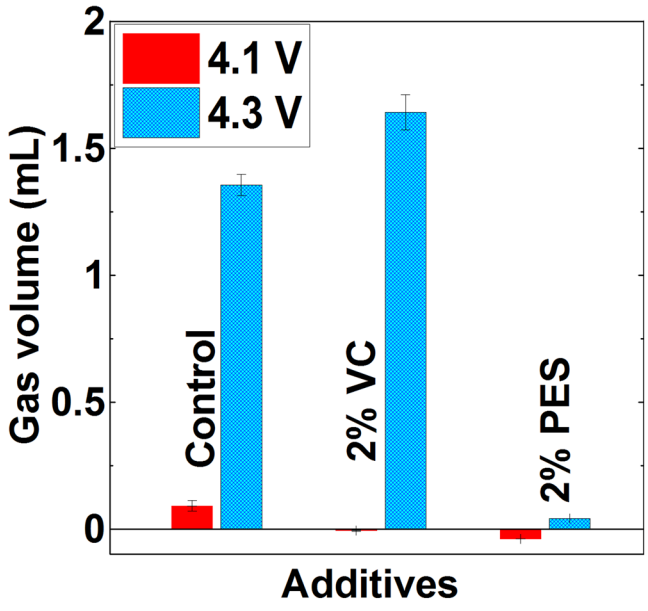

Figure 7.2 The volume of gas produced in the pouch cells during cycling as a function of electrolyte type. The original pouch cell volume was about 2.5 mL.

7.3.1.2 **Gas Produced During Cycling in the Pouch Cells**

Figure 7.2 shows the volume of gas produced in the pouch cells (original volume of the cells was about 2.5 mL) during cycling as a function of the additive used. Figure 7.2 shows that the amount of gas produced in cells with an upper cut-off voltage of 4.1 V was minimal. For cells with an upper cut-off voltage of 4.3 V, cells with control and 2% VC showed a large amount of gas (~1.5 mL) due to electrolyte decomposition while cells with 2% PES had minimal gas production during cycling. Therefore, although the reader might have guessed that extensive gassing for the cells with 2% PES caused the rapid capacity fade, this guess would be wrong.

7.3.1.3 **AC Impedance Results**

Figures 7.3a and 3c show the AC impedance spectra of cells after degassing at 3.8 V and after cycling to 4.1 V for 83 cycles respectively. Figure 7.3c shows that the impedance of cells with an upper cut-off voltage of 4.1 V remained quite small after cycling, which suggests that impedance growth is not a major contribution to the capacity fade of the 4.1 V cells.

Figures 7.3b and 3d show the impedance spectra for cells after degassing at 4.3 V (impedance spectrum was measured at 3.8 V after a partial discharge) and after cycling to 4.3 V for 83 cycles, respectively. Figures 7.3b and 3d show there was a large impedance growth in cells with control and 2% VC electrolytes after cycling. However, cells with 2% PES showed almost no impedance growth during cycling. The reader is cautioned that cells with 2% PES showed an impedance **decrease** when tested to 4.1 V (Figures 7.3a and

7.3c) so the data in Figure 7.3d represent an impedance increase compared to cells tested to 4.1 V.

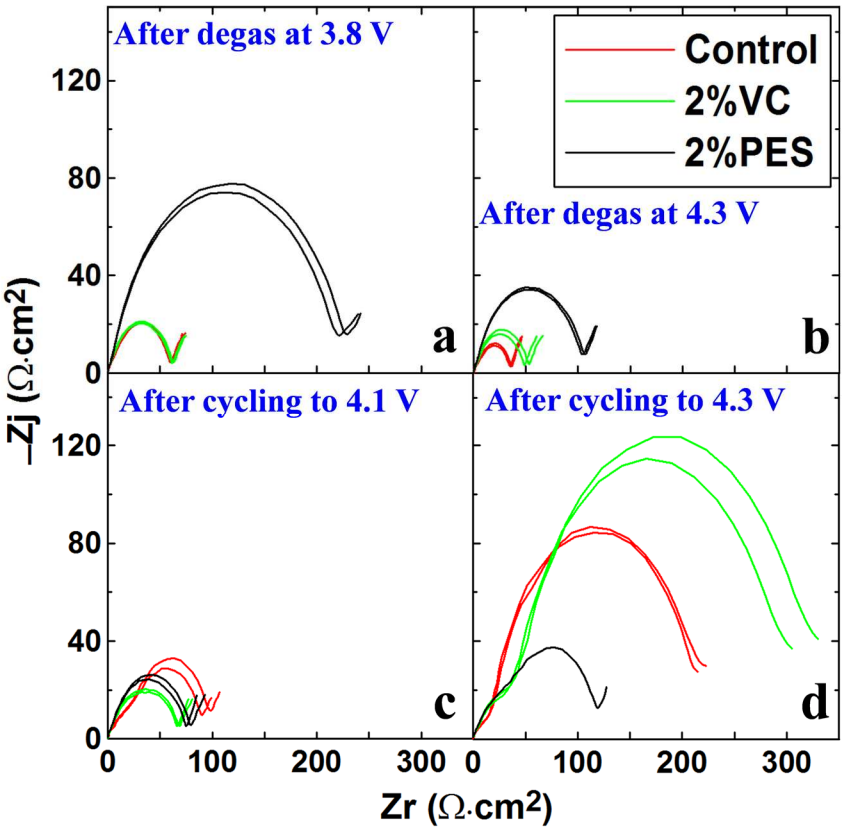

Figure 7.3 Impedance spectra for cells after degassing at 3.8 V during the formation cycle (a), after degassing at 4.3 V and discharge to 3.8 V during the formation cycle (b), after cycling to 4.1 V for 83 cycles (See Figure 7.1) (c) and 4.3 V (d) for 83 cycles respectively. All impedance spectra were measured at 10°C.

In any event, the data in Figure 7.1d and Figure 7.3d suggest that the polarization growth during cycling for the cells with 2% PES is not due to a dramatic increase in the resistance associated with the transport of Li ions or electrons through surface layers on either electrode, since the diameter of the impedance semicircle does not increase dramatically.

7.3.2 SEM Image of a Typical Electrode

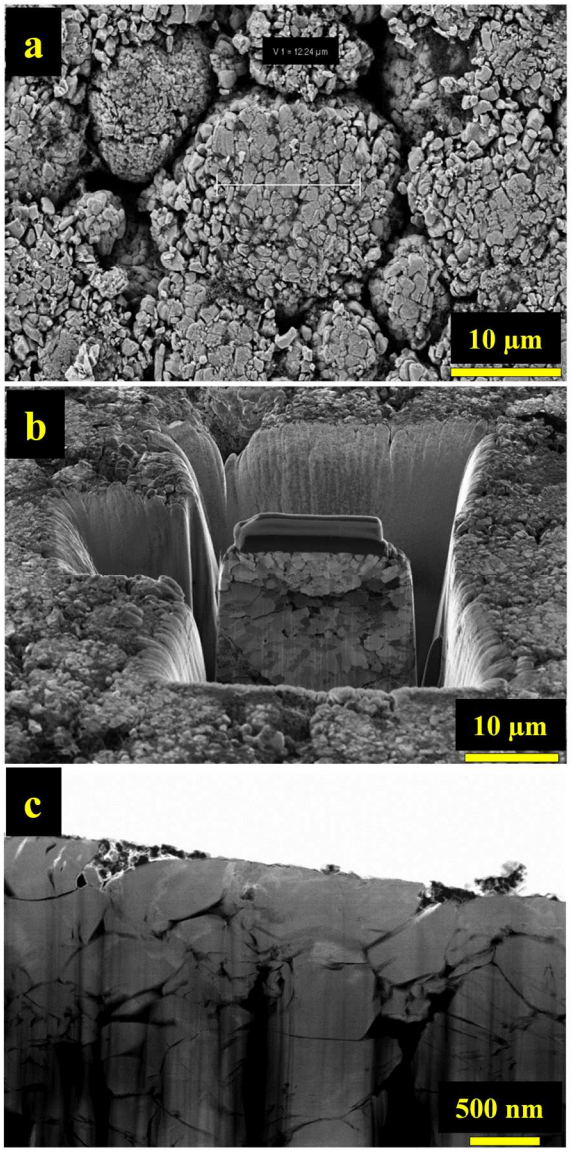

Figure 7.4 A typical electrode surface and a selected particle. (a) Image of the particle after a primary FIB step with carbon and tungsten deposited on top of the particle surface. (b) A typical HAADF-STEM image of an electrode sample prepared using FIB (c).

Figure 7.4a shows an SEM image of a typical electrode surface after 83 cycles and a selected particle with a size of around 15 μm. Figure 7.4b shows a view of the particle after the primary FIB step showing the carbon and tungsten deposited on top of the particle surface. Figure 7.4c shows a typical HAADF-STEM image of an electrode sample prepared using the FIB.

7.3.3 EELS of the Surface and Bulk

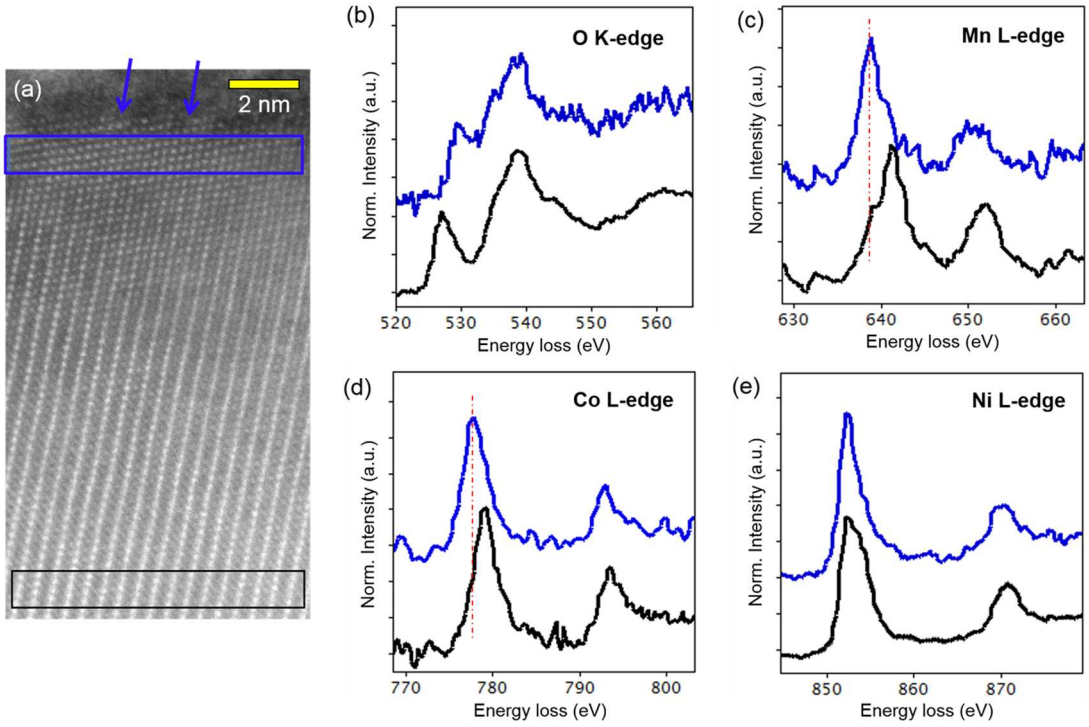

Figure 7.5 HAADF-STEM images near the surface of an NMC811 particle from an electrode from a cell with control electrolyte that had been charged to 4.3 V for 83 cycles (a). EELS spectra of the oxygen K edge (b), manganese L-edge (c), cobalt L-edge (d), nickel L-edge, respectively, from the surface to the bulk.

Figure 7.5a shows a HAADF-STEM image of a NMC811 sample taken from a cell with control electrolyte that was charged to 4.3 V for 83 cycles. The image was taken near the particle surface Every other column of the transition metal atoms, as indicated by the blue arrows, observed at the surface disappeared when moving into the bulk region, indicating a reconstructed surface layer.[141,162,251,266] Figures 7.5b – 5e show the EELS spectra of the oxygen K edge, manganese L-edge, cobalt L-edge andnickel L-edge, respectively. The spectra were taken from the surface and the bulk as indicated in Figure 5a with the blue and the black boxes, respectively. Figures 7.5c and 5d show that the Mn-L and Co-L edges, respectively, slightly shift to a lower energy loss from the bulk to the surface indicating a decreased oxidation state of Mn and Co at the surface.[142,251,267] Figure 7.5e shows it is difficult to observe changes in the Ni-L edge at this resolution, other than the broadening of the peaks in the bulk which suggests there might be an oxidation state change of Ni as well. The pre-peak of the O–K edge, which is attributed to the hybridization of TM3d–O2p orbitals, shifts to higher energy and shows a significant decrease in intensity from the bulk to the surface indicating a modification of the unoccupied TM-3d states and TM-TM bond lengths.[142,251,267]

7.3.4 Nano-Beam Diffraction from the Surface to the Bulk

Figures 7.6a – 6c show nano-beam electron diffraction patterns (NBED) at the surface, near the transition from surface to bulk (called 'middle') and within the bulk for the control electrode cycled to 4.3 V. The inset in each figure shows an extended view of the STEM image in the region where the NBD was performed. The red dashed lines show the

remaining diffraction spots while the blue dashed lines show the diffraction spots that appeared when the beam moved from surface to bulk.

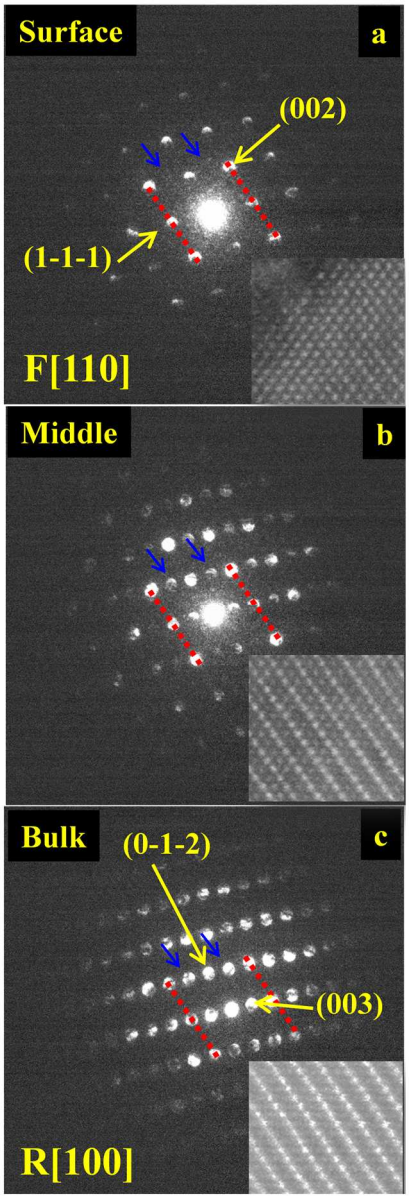

Figure 7.6 Nano-beam diffraction (NBD) at the surface (a), an intermediate region (b) and in the bulk (c) of the a particle taken from an electrode from a control cell cycled to 4.3 V.

Figure 7.6a shows that the diffraction spots from the surface can be indexed to a rocksalt structure in the Fm3m space group with a [110] zone axis. Conversely, the diffraction spots from the bulk can only be indexed to a layered $R\bar{3}m$ space group. This result confirms the observation in the HAADF STEM images that the surface structure is reconstructed from a layered structure to a rocksalt structure.

7.3.5 HAADF-STEM Images

Figures 7.7a – 7d show the HAADF-STEM images near the surface of a particle taken from a pristine NMC811 electrode and from particles taken from electrodes from cells after 83 cycles between 2.8 – 4.1 V with control, 2% VC and 2% PES electrolytes respectively. The transparent yellow lines show the approximate boundary of the surface layer identified visually. The distance to the surface from the yellow line has been roughly measured and is labelled on each image. Figure 7.7a shows that a reconstructed surface layer of about 3 nm thickness was observed on the fresh electrode before contacting any electrolyte. Such a surface layer is common on high Ni content NMC materials which have been exposed to air.[136,139,143] Figures 7.7b - 7d show that the thickness of the surface layer on electrodes from cells with control, 2% VC and PES 211 electrolyte was about 2 – 4 nm, which was almost the same as that on the pristine electrode.

Figures 7.8a – 8d show the HAADF-STEM images near the surface of a particle taken from the pristine NMC811 electrode and for particles taken from electrodes from cells after 83 cycles between 2.8 – 4.3 V with control, 2% VC and 2% PES electrolyte, respectively. The thickness of the surface layer on particles from the electrode from cells with control

electrolyte was ~6 nm, while the thickness of the surface layer on the electrodes from cells with 2% VC and 2% PES was about ~3 nm, almost the same as the pristine electrode.

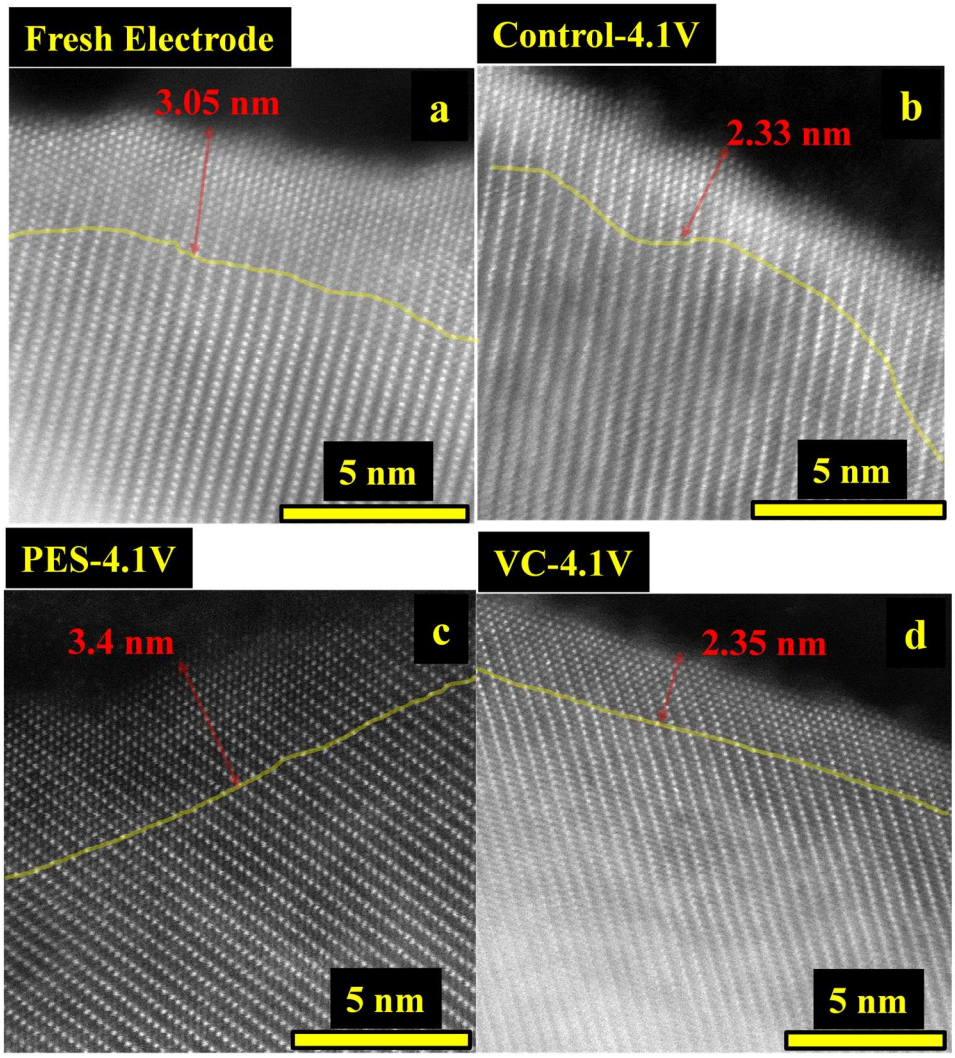

Figure 7.7 HAADF-STEM images of a particle from a pristine NMC811 electrode near the surface before contacting any electrolyte (a). HAADF-STEM images of particles from electrodes after 83 cycles between 2.8 – 4.1 V with control (b), 2% VC (c) and 2% PES (d) electrolyte in the cells, respectively.

To more accurately determine the surface layer thickness, the intensity ratio between the Li layer and neighbouring TM layer was calculated.

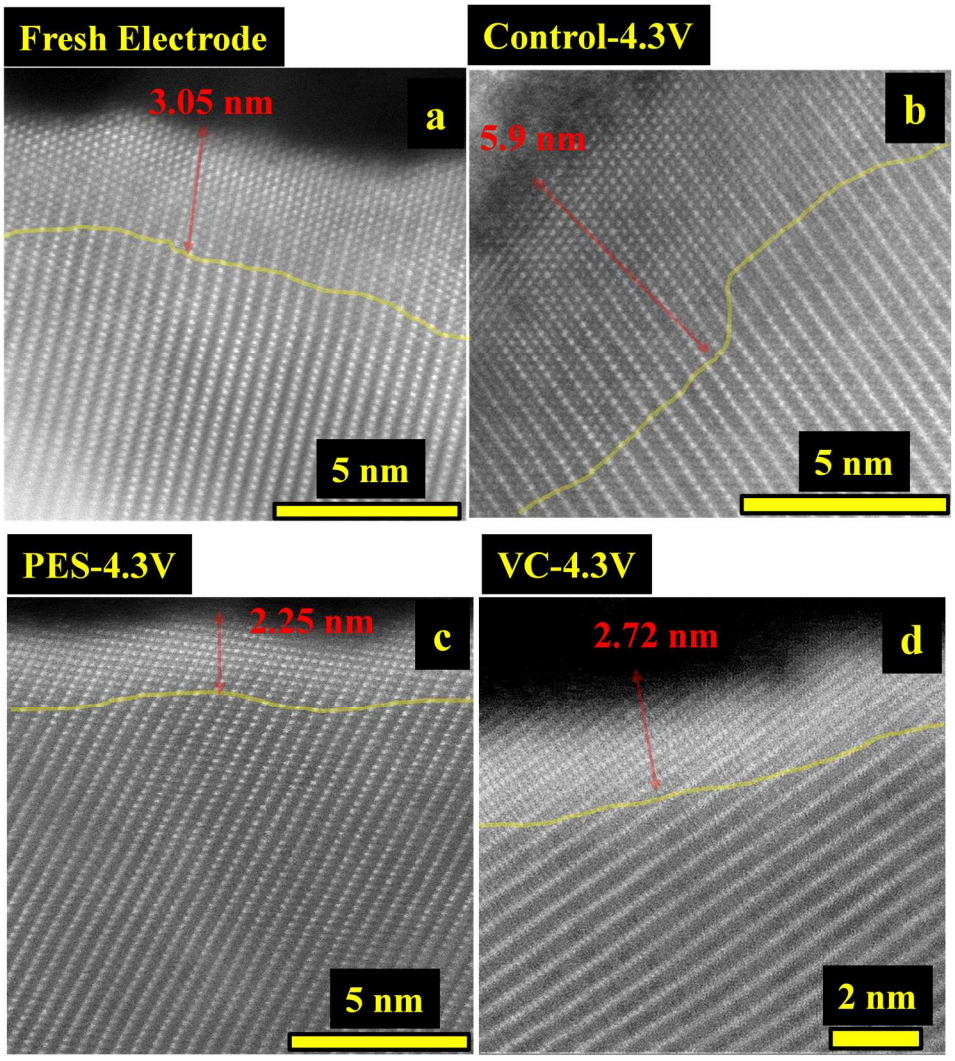

Figure 7.8 HAADF-STEM image of a particle from a pristine NMC811 electrode near the surface before contacting any electrolyte (a). HAADF-STEM images of particles from electrodes after 83 cycles between 2.8 – 4.3 V with control (b), 2% VC (c) and 2% PES (d) electrolyte in the cells respectively.

Theoretically, this ratio would be 1 at the top of the surface layer where TM metals fully

occupy the Li layer, and decrease to 0 when there are no TM atoms in the Li layer. The point where the intensity ratio reaches zero is therefore a measure of the surface layer thickness, parallel to the Li layers.

7.3.6 Calculation of the Surface Layer Thickness

Figures 7.9a and 9c show the intensity ratio as a function of parallel distance and surface distance, respectively, determined from images shown in Figure 7.7, for the fresh electrode, and electrodes from cells cycled between 2.8 – 4.1 V. Figures 7.9a and 9c show that the intensity ratio decreases from the surface to the bulk and that there are no significant differences between all the electrodes. The thickness of the surface layer can be estimated from the distance where the intensity first reaches zero. The surface layer thickness for the fresh electrode is ~4 nm and is also about 3 – 4 nm for control, 2% PES and 2% VC electrodes, respectively. This result agrees well with the results from visual examination of the images shown in Figure 7.7. For these images, where the Li layers were nearly perpendicular to the surface, the difference between the surface distance and the parallel distance is small.

Figures 7.9b and 9d show the intensity ratio as a function of parallel distance and surface distance, respectively, determined from the images shown in Figure 7.8, for the fresh electrode, and electrodes from cells cycled between 2.8 – 4.3 V. Figure 7.9b shows that parallel thickness of the fresh, control, 2% PES and 2% VC electrodes are ~4.2, 7.5, 3.8 and 10.5 nm, respectively. Figure 7.9d shows the surface thickness of the fresh, control, 2% PES and 2% VC electrodes are ~4.0, 6.8, 3.5 and 4.5 nm, respectively, which agree with the visual results as shown in Figure 7.8. The surface thickness is much smaller than

the parallel thickness for the 2% VC sample due the small angle between the layers and the surface (~25^{o}) as shown in Figure 7.8d.

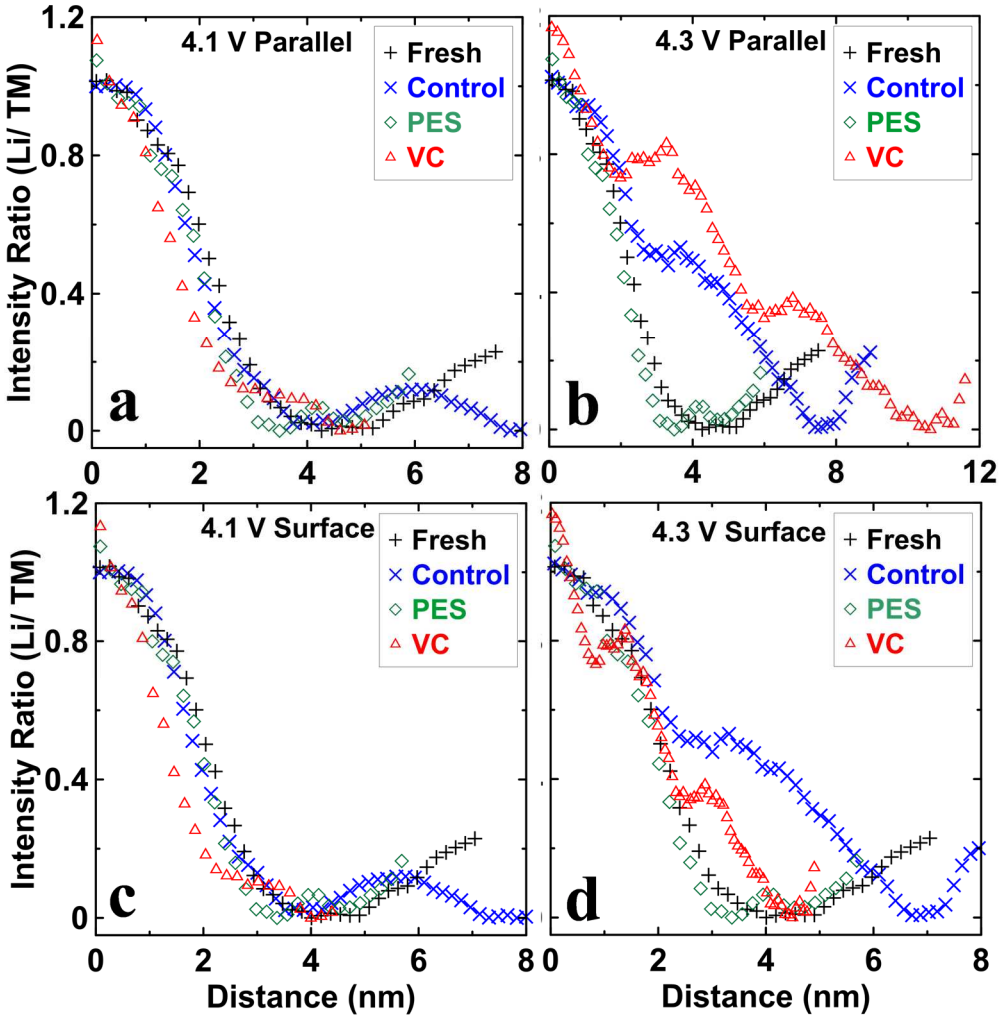

Figure 7.9 The intensity ratio as a function of parallel distance (a) and surface distance (b), respectively, determined from images shown in Figure 7.7, for the fresh electrode and electrodes from cells cycled between 2.8 – 4.1 V. The intensity ratio as a function of parallel distance (c) and surface distance (d), respectively, determined from images shown in Figure 8, for the fresh electrode and electrodes from cells cycled between 2.8 – 4.3 V.

The parallel thickness is dependent on the alignment of the crystal surface with respect to Li layers, hence, only the surface thickness is used for comparison between the samples.

7.3.7 Summary of the Surface Layer Thickness

In order to better quantify the thickness of the surface layer with more statistical meaning, 3 - 5 images of particles from each electrode were measured using the two different methods, respectively. Error bars were calculated from the standard deviation of the measurements. Figures 7.10a and 10b show a summary of surface thickness of the surface rocksalt layer determined visually and using image analysis, respectively.

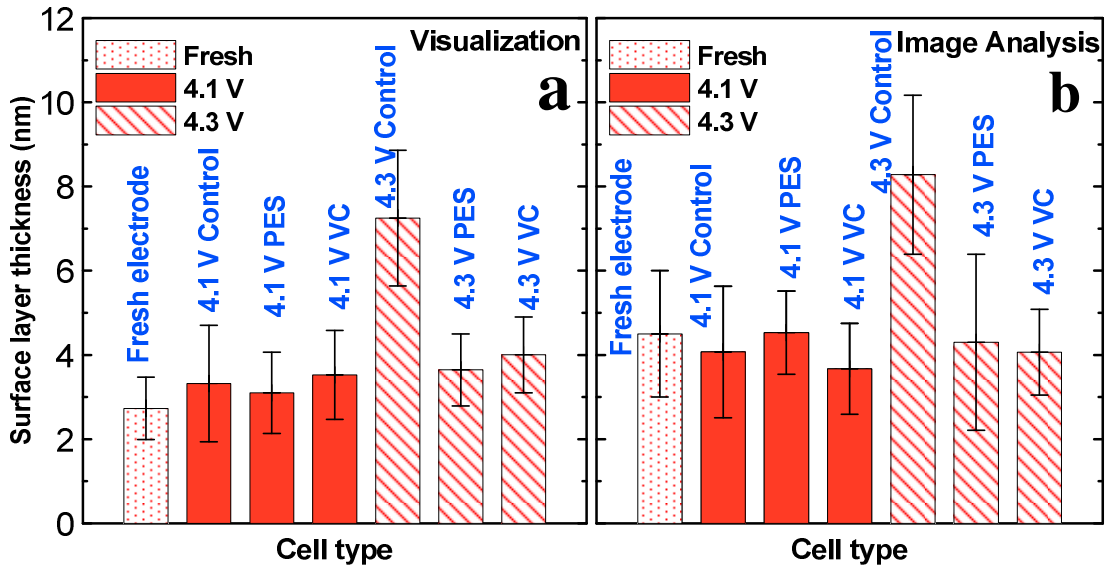

Figure 7.10 Summary of the surface thickness of the rocksalt surface layer determined visually (a) and by image analysis (b), respectively.

Figure 7.10a shows that the thickness of the surface layer on particles from electrodes taken from cells with an upper cut-off voltage of 4.1 V is ~3(1) nm, regardless of the type of

electrolyte used, which is almost the same as the pristine electrode. As comparison, Figure 7.10b shows the surface layer thickness is ~ 4(2) nm for the particles from the fresh, control, 2% PES and 2% VC electrodes respectively. Figures 7.10a and 10b show that there is no significant surface layer growth during cycling on particles of the positive electrodes taken from cells with an upper cut-off voltage of 4.1 V. This agrees well with the impedance results shown in Figure 7.3.

Figure 7.10a also shows that particles from electrodes from control cells tested to 4.3 V have the thickest surface layer of ~7(2) nm while the surface layer is about 3(1) and 4(1) nm for particles from electrodes from cells that contained 2% PES and 2% VC, respectively. As a comparison, Figure 7.10b shows the surface layer thicknesses from image analysis for particles from electrodes taken from cells cycled to 4.3 V. The surface layer thicknesses for particles taken from cells with control, 2% PES and 2% VC electrolyte are ~ 8(2), 4(2) and 4(1) nm, respectively. The thickness of the surface layer on the particles from electrodes from 2% VC and 2% PES cells tested to 4.3 V is almost the same as the pristine electrode indicating there was no significant surface layer growth in the VC and PES cells. Hence, the electrolyte additives VC and PES can suppress the surface layer growth for NMC811 cells with an upper cut-off voltage of 4.3 V.

7.3.8 Discussion

The results of the work presented here strongly suggests that the impedance growth in the 2% VC cells cycled to 4.3 V (Figures 7.3b and 7.3d) is not due to growth of a rocksalt surface layer. In addition, cells with 2% PES showed dramatic capacity fade when cycled to 4.3 V (Figure 7.1b), did not show a dramatically increased diameter in the impedance

spectrum and also did not show a thick rocksalt surface layer. Hence, at least for NMC811 cells with PES or VC additives tested to 4.3 V, failure cannot only be ascribed to a growing rocksalt surface layer. Instead, other processes, for example associated with electrolyte oxidation, must be responsible for failure.

Many researchers showed that electrolyte additives can supress the internal impedance growth in Ni-rich NMC based cells and significantly extend the cell lifetime by forming protective layers on the positive electrode surface. Y. K. Sun's group[63] showed that adding 0.1% epicyanohydrin to $LiNi_{0.6}Co_{0.2}Mn_{0.2}O_2$/Li cells as an electrolyte additive can suppress the growth of interfacial impedance and protect the positive electrode surface from further reaction with the electrolyte when cycled between 2.5 to 4.6 V at 60 ºC. Won Jong Lee *et al*[62] showed that NMC532/Li and NMC622/Li cells using VC as an electrolyte additive exhibited superior electrochemical and thermal behavior through the formation of a stable SEI on the positive electrode. Additionally, it was shown by T. Yim *et al.*[64] that divinyl sulfone can be a very effective electrolyte additive to stabilize the interface between Ni-rich NMC positive electrodes and electrolyte, hence improving the cycle life of Ni-rich NMC based cells. Similar effects of 1,3-propane sulfone as an electrolyte additive were also found by K. S. Kang *et al.*[61] for Ni-rich NMC materials. These results indirectly support our results that appropriate electrolyte additives can suppress the growth of the surface rock salt layer.

7.4 Conclusions

In order to further explore the failure mechanism in NMC811/graphite cells, the impact of electrolyte additives and cell upper cut-off voltage on the formation of a rocksalt surface layer in NMC811 cells was studied. The NMC811 in all cells tested to 4.1 V showed almost no growth in rocksalt surface layer thickness after 83 cycles at 40°C. By contrast, in cells tested to 4.3 V with control electrolyte, the rocksalt surface layer on the NMC811 particles doubled compared to the pristine material. However, when 2% PES or 2% VC was used in the cells the rocksalt surface layer did not increase in thickness compared to the pristine sample, even though dramatic capacity fade, worse than control cells, was observed in the case of cells with 2% PES. In addition, although the polarization of the cells with 2% PES cycled to 4.3 V increased dramatically with cycle number, the diameter of the impedance semi-circle did not. Thus, polarization growth in such cells was certainly not due to surface layer growth. In cells with 2% VC tested to 4.3 V, there was significant polarization growth and a dramatic increase in the diameter of the impedance semicircle, but no increase in the thickness of the rocksalt surface layer. Hence, at least for NMC811/graphite cells with PES or VC additives, failure cannot only be ascribed to a growing rocksalt surface layer on the NMC811 particles. Instead, other processes, for example associated with electrolyte oxidation, are probably responsible for failure.

CHAPTER 8. SYNTHESIS AND CHARACTERIZATION OF THE LITHIUM-RICH CORE-SHELL MATERIALS

Based on the study of Ni-rich and Mn-rich materials in Chapters 4 - 7, the following Chapters focus on the synthesis, testing and understanding of lithium rich core-shell (CS) NMC materials. A CS structure with a Ni-rich material as the core and a Mn-rich material as the shell can balance the pros and cons of the materials in a hybrid system. The Ni-rich core contributes high energy density as well as good rate capability and the Mn-rich shell provides a surface which hinders electrolyte oxidation. J. Camardese *et al.* have described the synthesis and characterization of CS materials in the Li-Ni-Mn Oxide system based on the studies in Chapter 4.[26] It's difficult to predict the lithium content in the core and shell phases of the CS materials and to ensure both phases have the optimal lithium content. However, it is possible to calculate an approximate range of the amount of lithium needed prior to sintering based on the layered phase boundaries determined in Chapter 4. Recently, Shunmugasundaram *et.al* have shown that some compositions derived from carbonate precursors deliver extremely small irreversible capacities.[211]

8.1 Experimental Design

In this work, CS samples with 67 mol% of core with the composition $Li_{1+x}(Ni_{0.67}Mn_{0.33})_{1-x}O_2$ (**C**) and 33 mol% of shell with the compositions $Li_{1+x}(Ni_{0.2}Mn_{0.6}Co_{0.2})_{1-x}O_2$ (**S1**) or $Li_{1+x}(Ni_{0.4}Mn_{0.5}Co_{0.1})_{1-x}O_2$ (**S2**) were synthesized and studied. The structural and electrochemical properties of the core, shell and CS materials were carefully measured and summarized. The majority of this Chapter was published in Chemistry of Materials.[242]

Permission has been granted by the American Chemistry Society for the reuse of the complete article.

Table 8.1 The lithium content used for the calculation of the amount of Li_2CO_3 needed for the core, shell and CS samples.

Sample	1	2	3	4	5	6
C	0[a]	0.02	0.04	0.06	0.08	0.12
S1	0.12	0.16	0.20	0.24	0.28	0.32
S2	0	0.04	0.08	0.12	0.16	0.20
CS1	0,0.08[b]	0.02,0.12	0.04,0.16	0.06,0.20	0.08,0.24	0.10,0.28
CS2	0,0	0.02,0.04	0.04,0.08	0.06,0.12	0.08,0.16	0.10,0.20

[a] The values in the table are x in $Li_{1+x}(Ni_{0.67}Mn_{0.33})_{1-x}O_2$ for the core (C), x in $Li_{1+x}(Ni_{0.2}Mn_{0.6}Co_{0.2})_{1-x}O_2$ for S1, and x in $Li_{1+x}(Ni_{0.4}Mn_{0.5}Co_{0.1})_{1-x}O_2$ for S2. [b] (x,y) in 0.67 $Li_{1+x}(Ni_{0.67}Mn_{0.33})_{1-x}O_2$●0.33$Li_{1+y}(Ni_{0.2}Mn_{0.6}Co_{0.2})_{1-y}O_2$, 0.67$Li_{1+x}(Ni_{0.67}Mn_{0.33})_{1-x}O_2$●0.33 $Li_{1+y}(Ni_{0.4}Mn_{0.5}Co_{0.1})_{1-y}O_2$ for CS1 and CS2 respectively.

Metal hydroxide precursors $M(OH)_2$ (M = Ni, Mn or Co) were prepared *via* co-precipitation in a continuously stirred tank reactor (CSTR) using the method described in Chapter 3. The core has a Ni:Mn molar ratio of 2:1, and the shell has Ni:Mn:Co molar ratios of 1:3:1 for shell S1, and 4:5:1 for shell S2. During the synthesis of CS precursors, the core solution was pumped for ~15 hours (400 mL) and then pumping switched to the shell solution for ~8 hours (200 mL), which yields about 33 mol% shell (molar ratio). CS precursors with 33 mol% S1 and 33 mol% S2 as the shell are referred to here as CS1 (0.67

$Ni_{0.67}Mn_{0.33}(OH)_2$ • 0.33 $Ni_{0.2}Mn_{0.6}Co_{0.2}(OH)_2$) and CS2 (0.67 $Ni_{0.67}Mn_{0.33}(OH)_2$ • 0.33 $Ni_{0.4}Mn_{0.5}Co_{0.1}(OH)_2$), respectively.

The target stoichiometries for the lithiation process are shown in Table 8.1. For CS samples, the amount of Li_2CO_3 was calculated by a simple linear combination of the amount for core-only (67%) and shell-only (33%) phases. The stoichiometries used for calculating the amount of Li_2CO_3 for the CS samples may not be the same as the final compositions due to diffusion during heating. The powder mixtures were sintered in a box furnace at 900°C for 10 hours, with an initial heating rate of 10°C/min and a final cooling rate of 20°C/min for all samples.

EDS mapping measurements of the polished CS samples were carried out using a Hitachi S-4700 SEM. Elemental maps of samples were collected in 300 seconds with an accelerating voltage of 20 kV and a current of 15 μA.

Electrochemical measurements were carried out *via* galvanostatic charge-discharge cycling using standard 2325 coin cells with lithium metal negative electrodes on an E-One Moli Energy Canada battery testing system. The electrolyte was 1.0 M $LiPF_6$ in 1:2 v/v ethylene carbonate:diethyl carbonate (EC:DEC) (BASF). All the cells were tested with a specific current of 10 mA/g at 30°C. Cells were charged to 4.8 V for two cycles and further cycled between 2.5 and 4.6 V *vs.* Li/Li^+.

8.2 Results and Discussion

8.2.1 Elemental Analysis Results

Tables 8.2 and 8.3 show average compositions determined using elemental analysis (EA) for the precursors and the CS1 series, respectively. The actual stoichiometry of the samples was close to the target values.

Table 8.2 Elemental analysis of the hydroxide precursor to obtain an average transition metal composition.

Precursor		
	Sample	Elemental Analysis
C	$Ni_{0.67}Mn_{0.33}(OH)_2$	$Ni_{0.648}Mn_{0.352}(OH)_2$
S1	$Ni_{0.2}Mn_{0.6}Co_{0.2}(OH)_2$	$Ni_{0.189}Mn_{0.611}Co_{0.2}(OH)_2$
S2	$Ni_{0.4}Mn_{0.5}Co_{0.1}(OH)_2$	$Ni_{0.374}Mn_{0.523}Co_{0.102}(OH)_2$
CS1	$Ni_{0.51}Mn_{0.42}Co_{0.06}(OH)_2$	$Ni_{0.484}Mn_{0.441}Co_{0.075}(OH)_2$
CS2	$Ni_{0.58}Mn_{0.39}Co_{0.03}(OH)_2$	$Ni_{0.562}Mn_{0.403}Co_{0.035}(OH)_2$

Table 8.3 Elemental analysis of the $0.67Li_{1+x}(Ni_{0.67}Mn_{0.33})_{1-x}O_2 \cdot 0.33\ Li_{1+y}(Ni_{0.4}Mn_{0.5}Co_{0.1})_{1-y}O_2$ CS1 series. The average composition is shown. Equal numbers of metal atoms and oxygen atoms are assumed.

CS1 Average Composition			
ID	Sample	(x,y)	Elemental Analysis
1	$Li_{1.026}Ni_{0.507}Mn_{0.405}Co_{0.061}O_2$	(0, 0.08)	$Li_{0.988}Ni_{0.486}Mn_{0.448}Co_{0.077}O_2$
2	$Li_{1.053}Ni_{0.496}Mn_{0.393}Co_{0.058}O_2$	(0.02, 0.12)	$Li_{1.013}Ni_{0.474}Mn_{0.439}Co_{0.074}O_2$
3	$Li_{1.079}Ni_{0.484}Mn_{0.381}Co_{0.055}O_2$	(0.04, 0.16)	$Li_{1.043}Ni_{0.462}Mn_{0.423}Co_{0.071}O_2$
4	$Li_{1.106}Ni_{0.473}Mn_{0.368}Co_{0.053}O_2$	(0.06, 0.20)	$Li_{1.060}Ni_{0.452}Mn_{0.417}Co_{0.071}O_2$
5	$Li_{1.133}Ni_{0.461}Mn_{0.356}Co_{0.050}O_2$	(0.08, 0.24)	$Li_{1.076}Ni_{0.440}Mn_{0.414}Co_{0.070}O_2$

Samples in the CS1 series had systematically lower Ni contents and higher Mn contents than targeted. Elemental analysis results for the other series are shown in Table D.1 in Appendix D.

8.2.2 XRD Results for the Precursors

Figure 8.1 shows the XRD patterns of the core, shell and CS precursors. The black, green and blue dashed lines on the right panel show the Bragg peaks around 38° from the C, S1 and S2 precursors as well as those of the CS1 and CS2 precursors. CS1 and CS2 show two peaks in the 37 – 40° range indicating a co-existence of two phases.

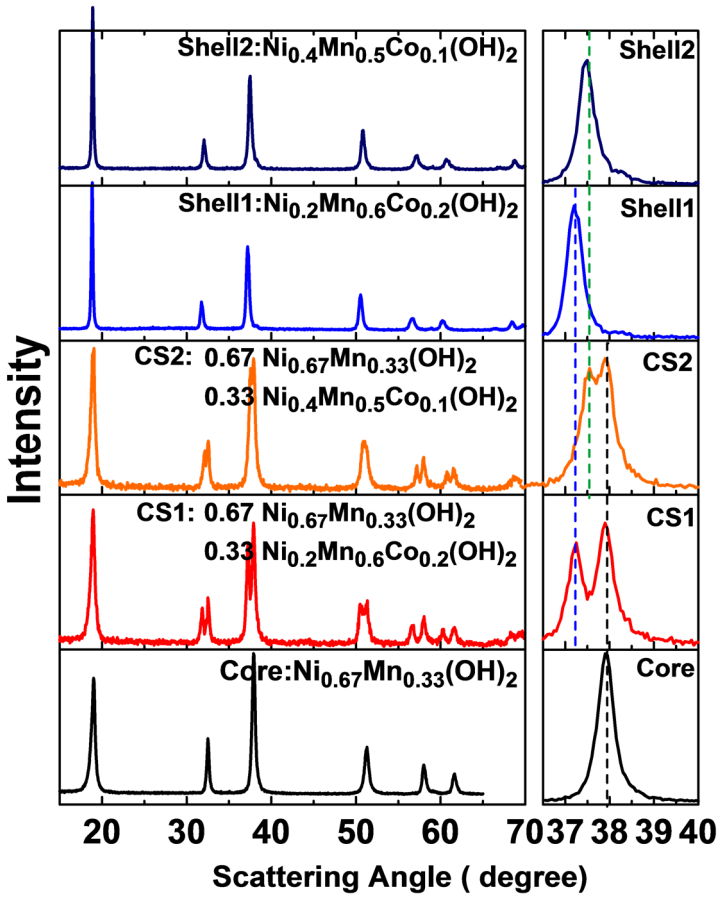

Figure 8.1 XRD patterns of the core, shell, and CS hydroxide precursors. The right panel shows an expanded view of the peak near 37° – 40°. The black, green and blue dashed lines show the alignment of the peak at around 38° from the C, S1and S2 phases with those in the in the CS1 and CS2 precursors, respectively.

The position of the Bragg peak from the core phase matches extremely well in the C, CS1 and CS2 precursors. The position of the Bragg peaks in the shell phase in S1 and CS1 match very well as do the corresponding peaks in the S2 and CS2 precursors. The patterns were fitted with Rietveld refinement using the $P\bar{3}m1$ structure and the results are presented in Table 8.4. The lattice constants of core and shell phases in the C, S1 and S2 precursors match with the corresponding phases in the CS1 and CS2 precursors, respectively, indicating that the transition metal compositions of the core phase and the shell phase in the CS precursors are very close to those in the C, S1 and S2, precursors, as expected.[98]

Table 8.4 Lattice constant of the as prepared precursors.

Sample	Composition	Core phase		Shell phase	
		a(Å) (± 0.0004)	**c(Å) (± 0.002)**	**a(Å) (± 0.0004)**	**c(Å) (± 0.002)**
Core (C)	$Ni_{0.67}Mn_{0.33}(OH)_2$	3.1849	4.678	-	-
CS1	0.67 $Ni_{0.67}Mn_{0.33}(OH)_2$ ● 0. $Ni_{0.2}Mn_{0.6}Co_{0.2}(OH)_2$	3.1852	4.678	3.2492	4.715
Shell1 (S1)	$Ni_{0.2}Mn_{0.6}Co_{0.2}(OH)_2$	-	-	3.2487	4.706
CS2	0.67 $Ni_{0.67}Mn_{0.33}(OH)_2$ ●0.33$Ni_{0.4}Mn_{0.5}Co_{0.1}(OH)_2$	3.1878	4.681	3.2161	4.729
Shell2 (S2)	$Ni_{0.4}Mn_{0.5}Co_{0.1}(OH)_2$	-	-	3.2270	4.702

8.2.3 SEM Images of the Precursors and Lithiated Samples

Figure 8.2 shows the SEM images of the precursors (left panels) and the lithiated samples (the third sample from each series is shown) (right panels). The particle size of the precursors was around 10 µm.

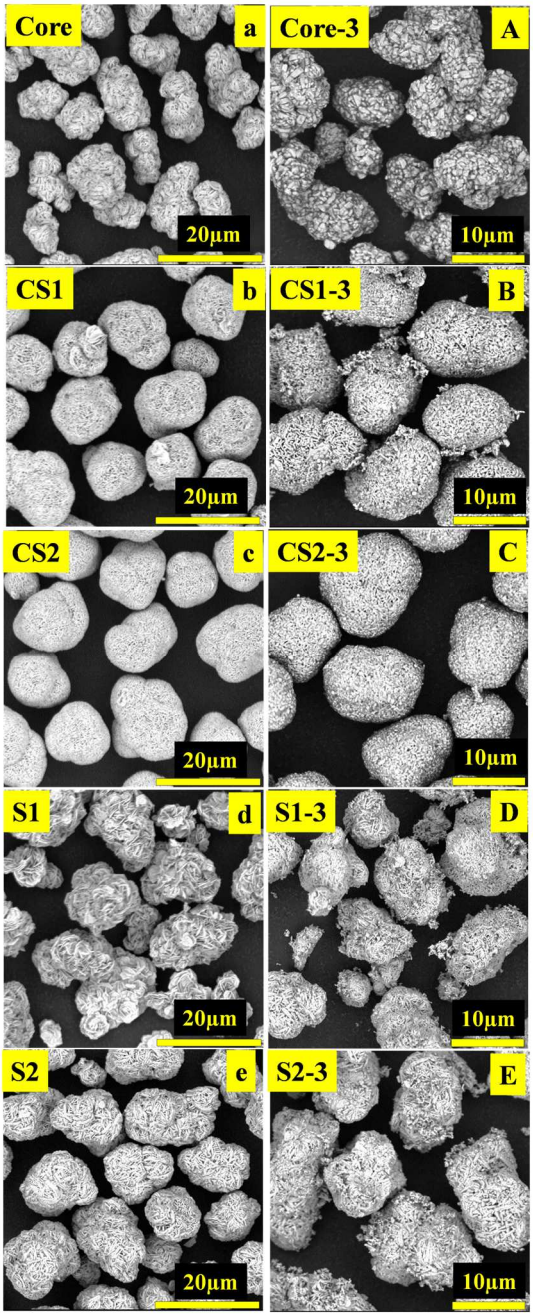

Figure 8.2 SEM images of the precursors (**a-e**) in the left panel and the lithiated samples (**A-E**) in the right panels. The third sample from each series is shown.

The nearly mono-disperse and dense particles of the CS1 (Figure 8.2b) and CS2 (Figure 8.2c) indicates the successful coating of the shell on the core in the CS precursors. After the lithiation process, the particle shapes and sizes (Figures 8.2A – 2E) were well maintained.

8.2.4 Cross-sectional EDS Mapping of the CS samples

Figure 8.3 shows cross-sectional SEM images and EDS maps of the CS precursors and lithiated samples, where Mn is shown as red, Ni as blue and Co as green.

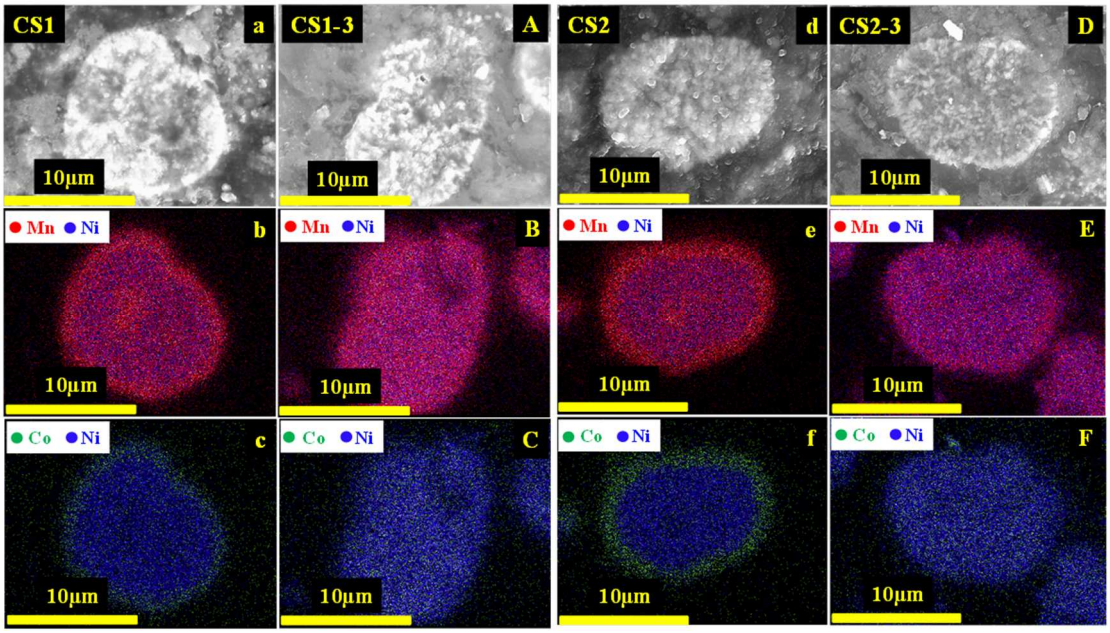

Figure 8.3 Cross-sectional SEM image of CS1 precursor (a) and the corresponding EDS mapping (b, c). Cross-sectional SEM image of the lithiated sample CS1-3 (A) and the corresponding EDS mapping (B, C). Cross-sectional SEM image and corresponding EDS mapping of CS2 precursor (d – f) and the lithiated sample CS2-3 (D – F).

Figures 8.3a-3c for the CS1 precursor and Figures 8.3d-3f for the CS2 precursor show a clear manganese and cobalt-rich shell and a nickel-rich core. This is consistent with the compositions of the target CS precursors which have high Mn and Co in the shell. However, after sintering at 900°C, the cobalt rich shell disappeared (Figures 8.3C, 8.3F) and an approximately uniform distribution of cobalt across the particles was observed. The manganese-rich shell was still maintained, however the relatively weak contrast between manganese and nickel in the shell indicated some diffusion of nickel and manganese between the core and shell phases, due to the concentration gradient of transition metals during heating. Further detailed studies reported in Chapters 9 and 10 were made to determine the relative diffusion rates of Ni, Co and Mn in these materials.

8.2.5 XRD Results of CS Samples

Figure 8.4 shows the XRD patterns of the lithiated CS1 series as the lithium content increases from the bottom to the top of the figure. Rietveld refinements were applied to the data assuming two hexagonal layered phases in the $R\bar{3}m$ space group. In order to fit the intensity well, the cobalt content of each phase was adjusted at the very end. In Figure 8.4a, the black dots are the data points, the red line is the fit to the data, and the black solid line shows the difference between the data and calculated results. Figure 8.4b shows part the CS1-2 data with the calculated core and shell phases shown as blue and green solid lines, respectively. The fit matches very well with the raw data and clearly shows the core phase at lower angles and the shell phase at higher angles when comparing the same diffraction peak. Figure 8.4c shows a blow-up of the region between 36-38° corresponding to the (101) reflections of core and shell phases.

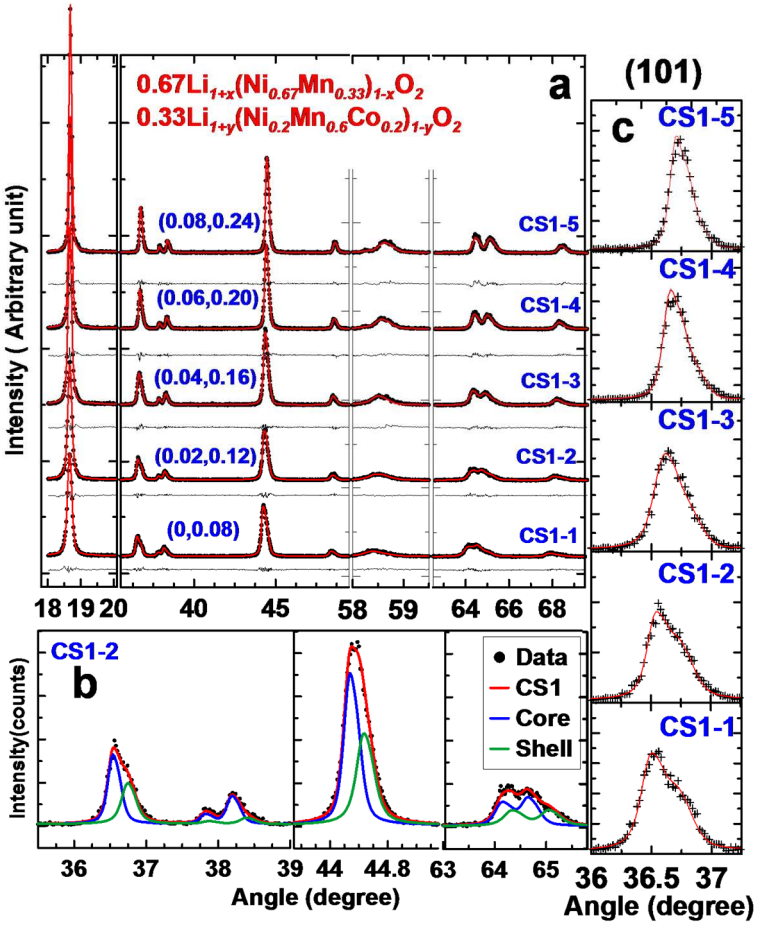

Figure 8.4 XRD patterns for the lithiated CS1 series (a), the black dots are the data points, the red line is the fit to the data with two $R\bar{3}m$ phases. Part of the fit to the CS1-2 sample with the calculated patterns from the two phases shown as blue and green lines, respectively (b). An expanded view of the region between 36-38° corresponding to the (101) Bragg peak (c).

In sample CS1-1, two peaks at 36.48° and 36.69° were observed, which are the core and shell phases, respectively. The two peaks can still be distinguished in sample CS1-2. As the lithium content increases further in samples CS-1 to CS-5, the two peaks are difficult to resolve but a clear asymmetry in the peaks is observed. Meanwhile, the scattering angles of the two peaks shift to the right (increase of scattering angle), that is from (36.48°, 36.69°)

at CS1-1 to (36.71°, 36.86°) at CS1-5, respectively. The Rietveld refinement results are shown in Table 8.5. The lattice constants of the core phase decrease from (2.8871, 14.289) Å in CS1-1 to (2.8685, 14.243) Å in CS1-5 with the increase of lithium content, whereas the lattice constants of the shell phase changed from (2.8701, 14.256) Å in CS1-1 to (2.8566, 14.252) Å in CS1-5. It is noted that the c-axis of the shell phase was almost invariant as the total lithium content of the materials increased.

Table 8.5 Rietveld refinement results for the $Li_{1+x}(Ni_{0.67}Mn_{0.33})_{1-x}O_2 \bullet 0.33Li_{1+y}(Ni_{0.2}Mn_{0.6}Co_{0.2})_{1-y}O_2$ CS1 series.

Sample	(x,y)	Phase 1 (core)		Phase 2 (Shell)		
		a(Å) (± 0.0004)	c(Å) (± 0.002)	a(Å) (± 0.0004)	c(Å) (± 0.002)	Bragg R-factor
CS1-1	(0,0.08)	2.8871	14.289	2.8701	14.256	2.62
CS1-2	(0.02,0.12)	2.8828	14.273	2.8673	14.256	2.28
CS1-3	(0.04,0.16)	2.8774	14.262	2.8617	14.257	3.62
CS1-4	(0.06,0.20)	2.8729	14.252	2.8595	14.253	3.17
CS1-5	(0.08,0.24)	2.8685	14.243	2.8566	14.252	3.0

Figure 8.5 shows the same plot (as Figure 8.4) of XRD results for the CS2 series. Figure 8.5b presents part of the data for the CS2-2 sample with the calculated core and shell phases shown as blue and green solid lines, respectively. Figure 8.5c shows an expanded view of the (101) reflections from the core and shell phases. The two (101) peaks for samples CS2-1 and CS2-2 do not split as obviously when compared to CS1-1 and CS1-2 (Figure 8.4c), instead, a clear asymmetry for all the lithiated CS2 samples was observed. The composition difference between the core and shell phase in CS2 was relatively smaller compared to that in the CS1 series, as a result, the differences in the lattice constants of the two phases were not as large.

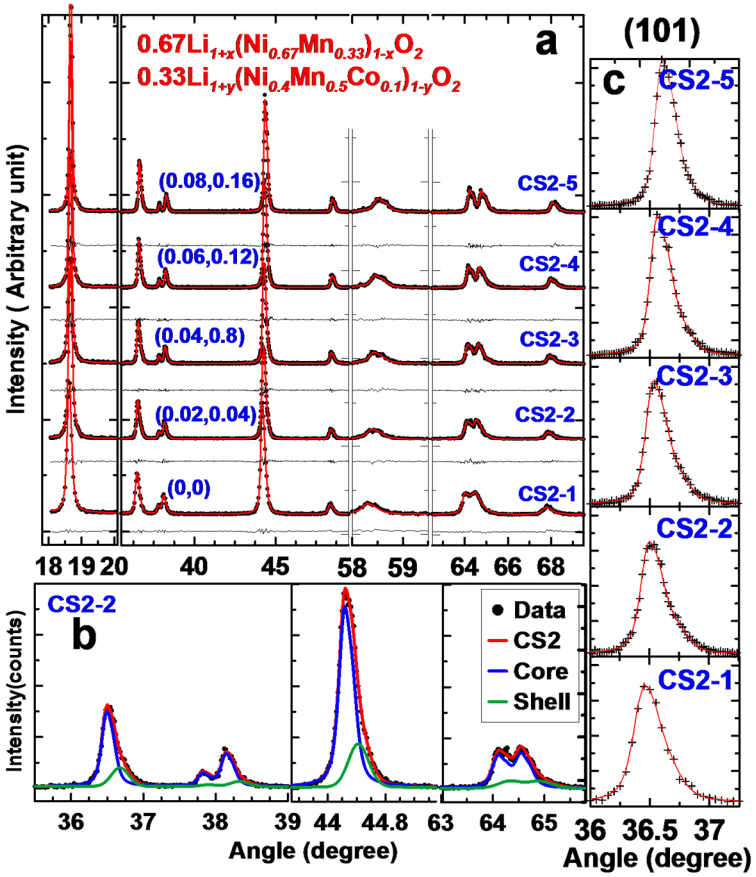

Figure 8.5 XRD patterns for the lithiated CS2 series (a), the black dots is are data points, the red line is the fit to the data with two R$\bar{3}$m phases. Part of the fit to the CS2-2 sample with the calculated patterns from the two phases shown as blue and green lines, respectively (b). An expanded view of the region between 36-38^{o} corresponding to the (101) Bragg peak (c).

Table 8.6 shows the Rietveld refinement results. With increasing lithium content, the lattice constants of the core phase decreased from (2.8902, 14.293) Å in CS2-1 to (2.873, 14.258) Å in CS2-5, whereas the lattice constants of the shell phase changed from (2.8774, 14.252) Å in CS1-1 to (2.8664, 14.248) Å in CS2-5. Similarly, the c-axis of the shell phase was almost constant. The XRD data and refinement results for the core, S1 and S2 series are presented in Figures D.1 – D.3 and Tables D.2 – D.4 in the supporting information.

Table 8.6 Rietveld refinement results for the $0.67Li_{1+x}(Ni_{0.67}Mn_{0.33})_{1-x}O_2 \bullet 0$. $Li_{1+y}(Ni_{0.4}Mn_{0.5}Co_{0.1})_{1-y}O_2$ CS2 series.

Sample	(x,y)	Phase 1 (core)		Phase 2 (Shell)		
		a(Å) (± 0.0004)	c(Å) (± 0.002)	a(Å) (± 0.0004)	c(Å) (± 0.002)	R-factor
CS2-1	(0,0.08)	2.8902	14.293	2.8774	14.252	3.08
CS2-2	(0.02,0.12)	2.8868	14.274	2.8740	14.251	2.53
CS2-3	(0.04,0.16)	2.8829	14.268	2.8699	14.251	2.14
CS2-4	(0.06,0.20)	2.8808	14.267	2.8687	14.251	2.69
CS2-5	(0.08,0.24)	2.873	14.258	2.8664	14.248	1.92

Figure 8.6 shows the lattice constants of the core series, the S1 series and the S2 series as well as the core and shell phases in the CS samples as a function of the total lithium content. The black lines and symbols show the core-only and the core-phase in the core-shell samples whereas the blue lines and symbols show the shell-only and the shell-phase. For CS1, the c-axis (Figure 8.6a) of the CS1 shell phase remained almost constant while those of the shell-only samples changed normally as discussed in Chapter 4. Meanwhile, the a-axis (Figure 8.6b) of the CS1 shell phase changed at a similar rate as that of the shell-only samples. Additionally, the c-axis (Figure 8.6a) and a-axis (Figure 8.6b) of the CS1 core phase changed much faster with lithium content than that of the core-only samples. Similar results were observed for CS2 as shown in Figures 8.6c and 6d. The lattice constants of the core and shell phases in the core-shell materials changed at different rates with lithium content than the core-only and shell-only samples due to interdiffusion between the core and shell phases.

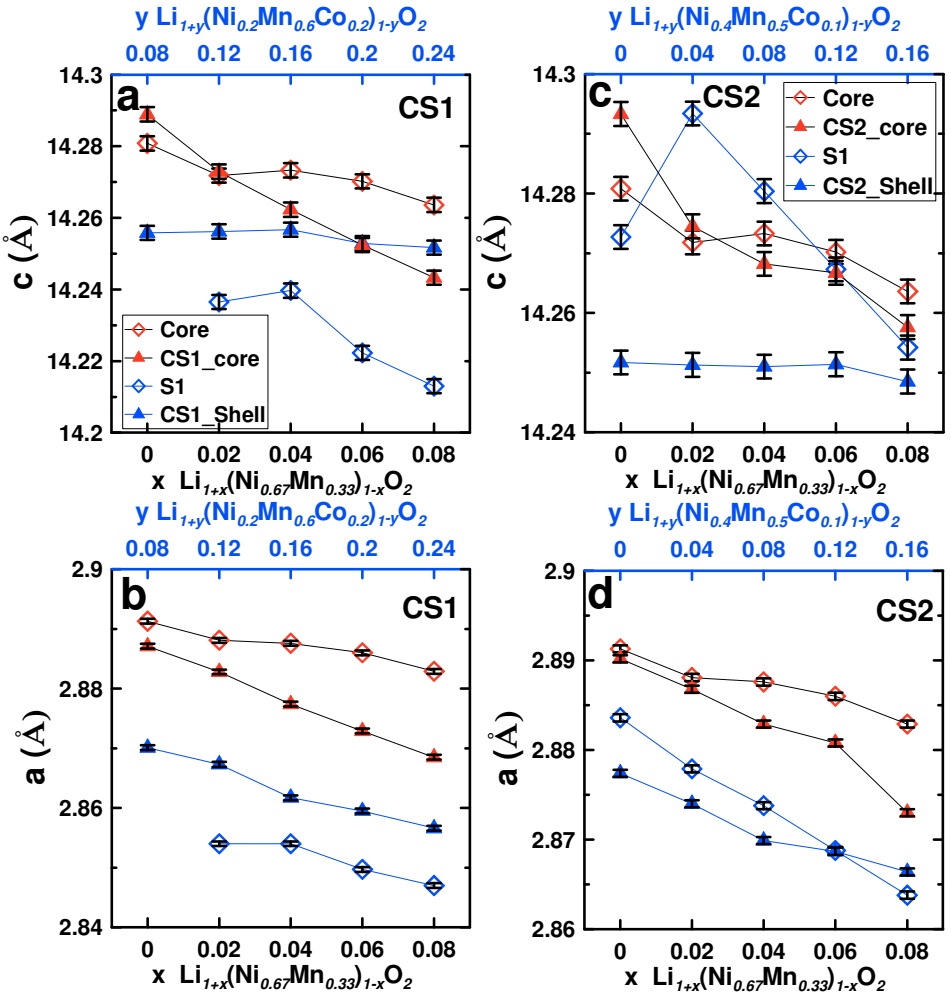

Figure 8.6 Lattice constants as a function of lithium content for the C, S1, and CS1 series (a, b), lattice constants as a function of lithium content for the C, S2, and CS2 series (c, d).

8.2.6 Electrochemical Testing Results

8.2.6.1 Voltage vs Capacity and Capacity vs Cycle Number

Figure 8.7 shows the voltage versus specific capacity curves and the capacity versus cycle number plots for the core, shell and CS samples. The cells were first tested between 2.5 –

4.8 V (*vs.* Li^+/Li) for two cycles and subsequently cycled at 2.5 – 4.6 V for about 50 cycles with a specific current of 10 mA/g. For the core composition series $Li_{1+x}(Ni_{0.67}Mn_{0.33})_{1-x}O_2$ $(0.02 \leq x \leq 0.12)$ as shown in Figure 8.7a, there was no obvious oxygen release plateau observed at around 4.5 V for all the samples during the first charge. This can be gleaned by comparing the shape of the first charge curve to the subsequent charge curves. There was, however, a small plateau that appears above 4.6 V in all the core samples which grows with lithium content. The origin of this small plateau is unknown.

The electrodes with x = 0.02, 0.04, 0.06, 0.08 and 0.12 showed a reversible capacity of 177 , 186, 189, 191 and 188 mAh/g between 2.5 – 4.6 V, with a capacity retention of ~76.9%, 84.6%, 89.1%, 89.3% and 93.8% after 40 cycles, respectively. The core materials showed poor cycling stability. All the samples had irreversible capacities near 50 mAh/g.

For the CS1 composition series $0.67Li_{1+x}(Ni_{0.67}Mn_{0.33})_{1-x}O_2 \bullet 0.33Li_{1+y}(Ni_{0.2}Mn_{0.6}Co_{0.2})_{1-y}O_2$ $(0.02 \leq x \leq 0.12, 0.08 \leq y \leq 0.24)$ as shown in Figure 8.7b, a prolonged oxygen release plateau was observed for every lithium content, which could be due to the contribution of the Mn-rich shell. This plateau increased with the increase of lithium content from CS1-1 to CS1-5. The electrodes from CS1-1 to CS1-5 showed reversible capacities of 206, 218, 218, 217 and 211 mAh/g between 2.5 – 4.6 V, with capacity retentions of ~93.8%, 98.2%, 98.9%, 98.5% and 96.5% after 40 cycles, respectively. The CS1 series showed much improved capacity and cycling stability compared to the core-only samples. For the CS2 composition series, $0.67Li_{1+x}(Ni_{0.67}Mn_{0.33})_{1-x}O_2 \bullet 0.33Li_{1+y}(Ni_{0.4}Mn_{0.5}Co_{0.1})_{1-y}O_2$ $(0 \leq x \leq 0.08, 0 \leq y \leq 0.16)$, as shown in Figure 8.7c, there was only a small oxygen release plateau in CS2-1 which increases with further increase of lithium content.

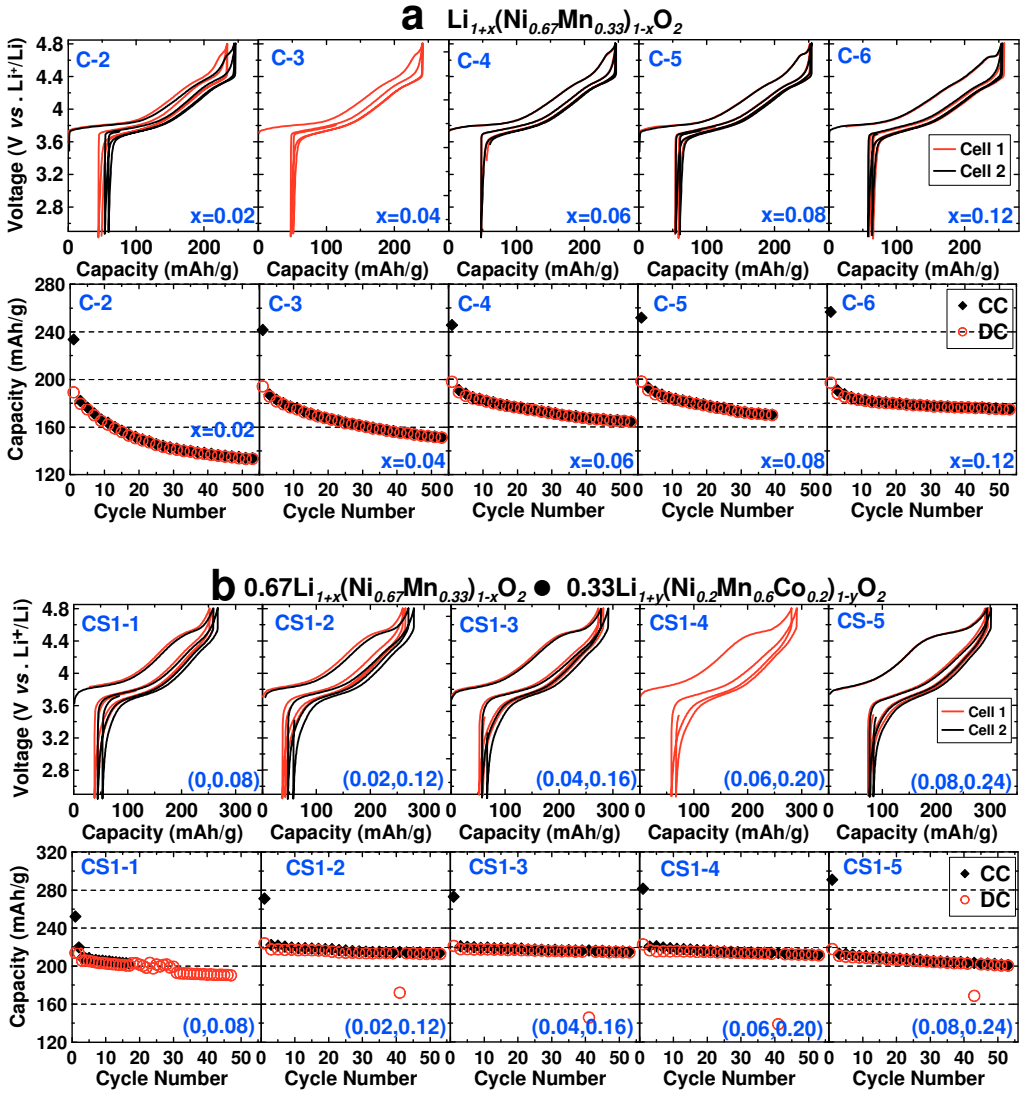

Figure 8.7 Voltage versus capacity curves and capacity as a function of cycle number for the core series as a function of the composition, x in $Li_{1+x}(Ni_{0.67}Mn_{0.33})_{1-x}O_2$ (a), Voltage versus capacity curves and capacity as a function of cycle number for the CS1 series as a function of the composition, x and y, in 0.67 $Li_{1+x}(Ni_{0.67}Mn_{0.33})_{1-x}O_2$•0.33$Li_{1+y}(Ni_{0.2}Mn_{0.6}Co_{0.2})_{1-y}O_2$ (b), Voltage versus capacity curves and capacity as a function of cycle number for the CS2 series as a function of the composition, x and y, in 0.67$Li_{1+x}(Ni_{0.67}Mn_{0.33})_{1-x}O_2$•0.33$Li_{1+y}(Ni_{0.4}Mn_{0.5}Co_{0.1})_{1-y}O_2$ (c).

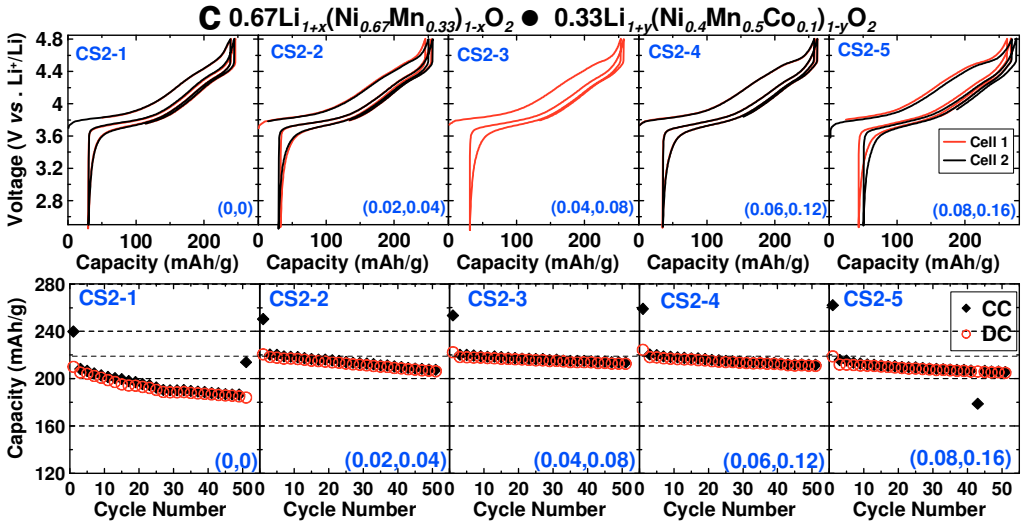

Figure 8.7 Voltage versus capacity curves and capacity as a function of cycle number for the core series as a function of the composition, x in $Li_{1+x}(Ni_{0.67}Mn_{0.33})_{1-x}O_2$ (a), Voltage versus capacity curves and capacity as a function of cycle number for the CS1 series as a function of the composition, x and y, in 0.67 $Li_{1+x}(Ni_{0.67}Mn_{0.33})_{1-x}O_2$•0.33$Li_{1+y}(Ni_{0.2}Mn_{0.6}Co_{0.2})_{1-y}O_2$ (b), Voltage versus capacity curves and capacity as a function of cycle number for the CS2 series as a function of the composition, x and y, in 0.67$Li_{1+x}(Ni_{0.67}Mn_{0.33})_{1-x}O_2$•0.33$Li_{1+y}(Ni_{0.4}Mn_{0.5}Co_{0.1})_{1-y}O_2$ (c).

The electrodes from CS2-1 to CS2-5 showed reversible capacities of 205, 218, 218, 218 and 212 mAh/g at 2.5 – 4.6 V, with capacity retentions of ~91.4% , 95.7 %, 98.0%, 97.4% and 97.5% after 40 cycles, respectively. The CS2 series also showed much improved cycling stability in comparison with the core-only materials. The electrochemical performance of the S1 series, $Li_{1+y}(Ni_{0.2}Mn_{0.6}Co_{0.2})_{1-y}O_2$, and S2 series, $Li_{1+y}(Ni_{0.4}Mn_{0.5}Co_{0.1})_{1-y}O_2$, are shown in Figures D.4 and D.5 in Appendix D.

The electrochemical performance of the CS samples as shown is dependent on the lithium content and the composition of the transition metals in the shell phase. It is possible to

achieve an optimal performance by effectively selecting the right shell despite the minor diffusion of transition metals between the core and shell.

8.2.6.2 **dQ/dV at the Third Cycle**

Figure 8.8 shows the differential capacity (dQ/dV) as a function of the cell potential (vs Li+/Li) between 2.5 – 4.6 V for the core series (Figure 8.8a), CS1 series (Figure 8.8b) and CS2 series (Figure 8.8c) after the cycles to 4.8 V had been completed (the third cycle).

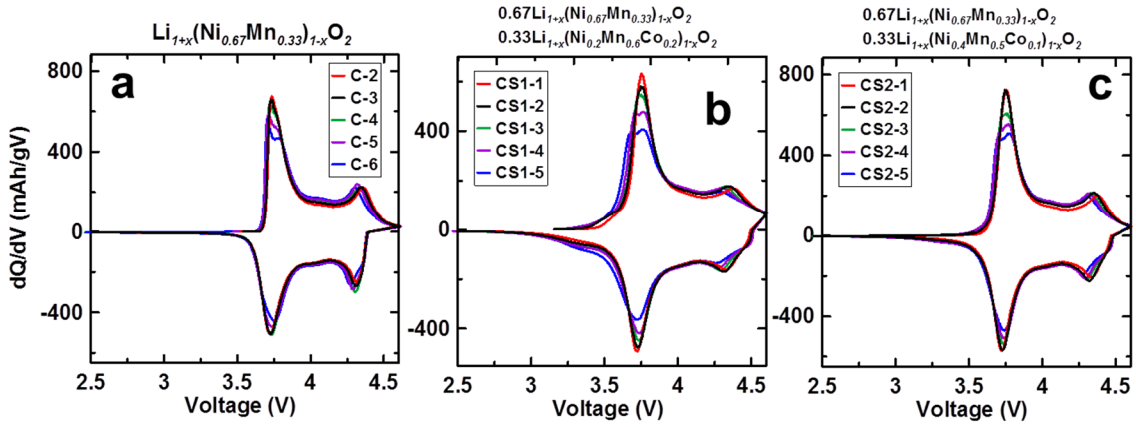

Figure 8.8 The differential capacity as a function of the cell potential (vs Li/Li^+) (dQ/dV vs. V) between 2.5 – 4.6 V for the core series (8a), CS1 series (8b) and CS2 series (8c) after the charge to 4.8 V (the third cycle).

Two major discharge peaks at ~3.75 V and ~4.3 V were observed for all the samples. Additionally, a small peak at ~3.3 V arose as lithium content increased for the CS1 series (Figure 8.8b), which could be associated with the Mn^{4+}/Mn^{3+} redox couple in the layered structure from the shell phase after the activation at 4.5 V.[88] There was a much smaller feature at ~ 3.3 V for the CS2 series (Figure 8.8c), indicating a small amount of Mn was reduced in the CS2 series that could also be derived from the shell. The same plots for the

S1 and S2 series are shown in Figure D.6 in Appendix D. dQ/dV versus V of the CS samples cannot be modeled by a simple linear combination of dQ/dV vs V of the core and shell phases, which is consistent with the observation of diffusion of the transition metals between the core and shell phases from the EDS mapping and XRD results.

8.2.6.3 **Reversible Capacity**

Figure 8.9a shows the first charge capacity (CC) of the core, shell and CS series as a function of lithium content.

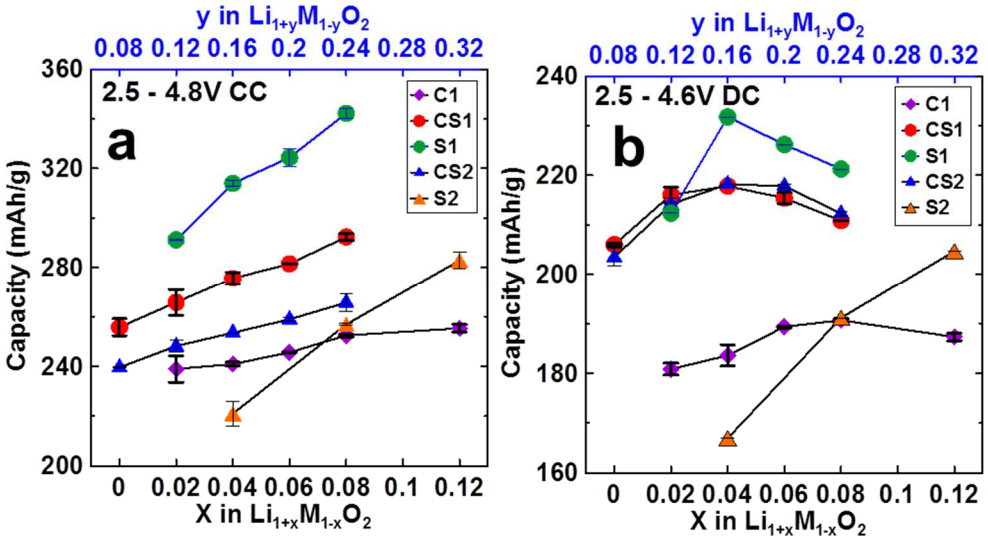

Figure 8.9 The first charge capacity of the core, shell and CS series as a function of lithium content (a), a summary of the first reversible discharge capacity (the third cycle) of the core, shell and CS series as a function of the lithium content between 2.5 – 4.6 V (b).

The S1 series is plotted against the top axis (blue) and the other series are plotted against the bottom axis (black). The same trend is observed for each series. The first charge capacity increased with increasing of lithium content, which is related to the length of

oxygen release plateau.[29] The rate of capacity increase with lithium content for the core-only phase was very small and was caused by the small feature at 4.6 V as shown in Figure 8.7a. It was noticed that the sample at x = 0.04 in S2 and the sample at y = 0.12 in S1 were not single phase as shown in Figures D.2 and D.3 in Appendix D. Figure 8.9b shows a summary of the first reversible discharge capacity between 2.5 – 4.6 V (DC) (the third cycle) of the core, shell and CS series as a function of the lithium content. The best capacity in the S1 series was ~232 mAh/g at y = 0.16 (single phase, least lithium content), while the best capacity in the S2 series in the cells tested was ~207 mAh/g at x = 0.12 that is near the middle of the single phase region. The capacity of the cells with S2 series electrodes increased somewhat with cycling as shown in Figure D.5. The best capacity of the core, CS1 and CS2 series were found to be in the middle of the series at about 190, 218 and 218 mAh/g, respectively. The CS samples show excellent reversible capacity, however, the capacity of the CS samples cannot be predicted as a linear combination of the capacity of the core and shell phases due to diffusion between the core and shell phases during sintering.

8.2.6.4 **Irreversible Capacity**

Figure 8.10a shows the specific irreversible capacity (1^{st} CC – 1^{st} DC) of the core, shell, and CS series as a function of lithium content. The IRC increased with lithium content for each series. The core series showed a minimum IRC of ~ 47.1 mAh/g and the S1 series showed the largest IRC of more than 80 mAh/g. However, the CS2 series showed the smallest IRCs of ~ 30, 31, 31, 35 and 47 mAh/g from CS2-1 to CS2-5, respectively, while they were ~41, 42, 54, 59 and 75 mAh/g for CS1-1 to CS1-5, respectively. Figure 10b shows the percentage IRC (IRC/1^{st} CC x 100%) versus the Li content. The S1 and S2

series showed a minimum IRC of 26.2% and 24.4%, respectively, while those for the core series were around 20.5 – 22.9%.

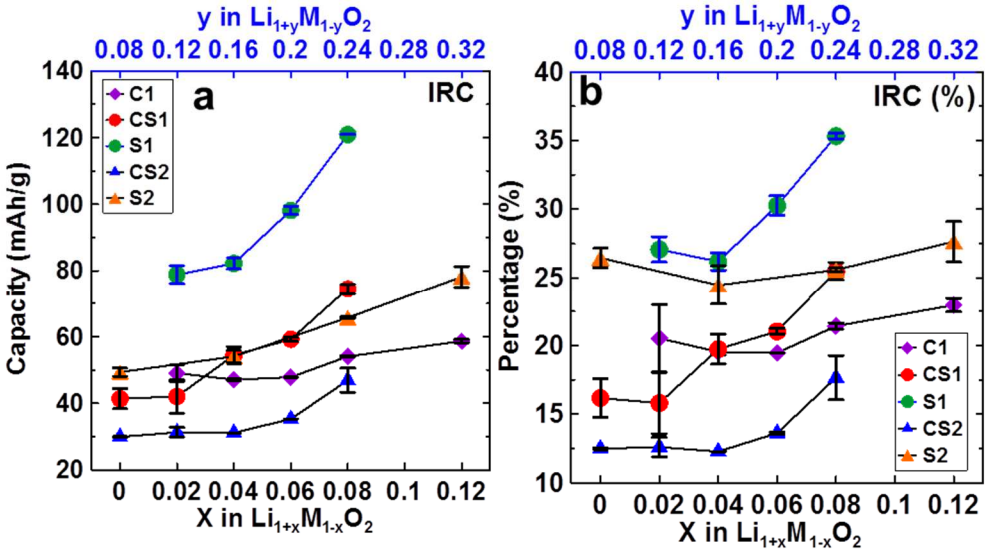

Figure 8.10 The specific irreversible capacity (IRC) (1^{st} CC – 1^{st} DC) (a) and percentage IRC (IRC/1^{st} CC x 100%) (b) of the core, shell, and CS series as a function of the lithium content.

The CS2 series showed the best IRCs of ~12.5%, 12.6%, 12.3%, 13.6% and 17.6% from CS2-1 to CS2-5 respectively, whereas the CS1-1 to CS1-5 samples showed IRCs of ~16.2%, 15.8%, 19.7%, 21.1% and 25.5%.

The CS samples with optimal lithium content not only show extremely low IRC, but also high capacity and stable capacity retention. In order to further explore the changes within the cells upon cycling, the dQ/dV vs. V data for samples with the best capacity and capacity retention for the core-only, shell-only as well as the CS samples were selected and analyzed.

8.2.6.5 **dQ/dV Analysis during Cycling**

Figure 8.11 shows dQ/dV vs. V for the C-4 (Figure 8.11a), CS1-2 (Figure 8.11b) and S2-3 (Figure 8.11c) samples between 2.5 – 4.6 V for the 3rd cycle to the 40th cycle in black lines.

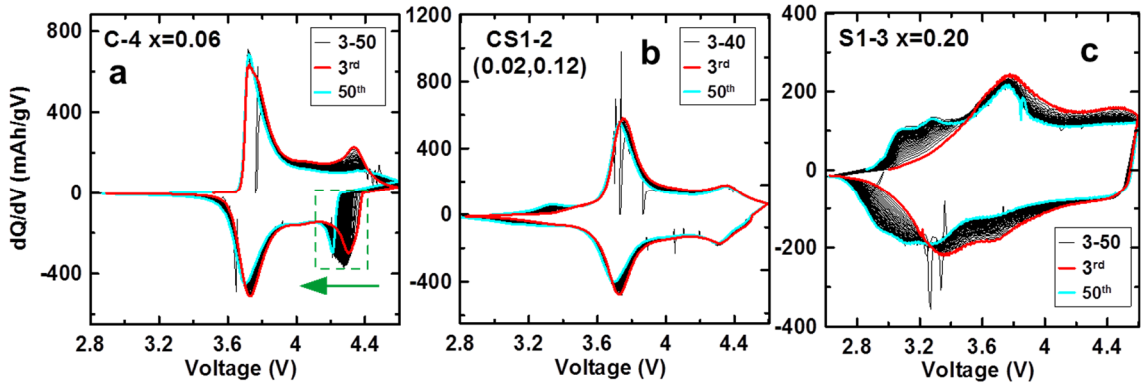

Figure 8.11 dQ/dV vs. V for the C-4 (11a), CS1-2 (11b) and S1-3 (11c) samples between 2.5 – 4.6 V from the 3rd cycle to the 40th cycle shown with black lines. The red lines show the 3rd cycle whereas the cyan lines show the 40th cycle. The green box and arrow in 11a highlight the dramatic potential drop at the start of discharge.

The red lines show the 3rd cycle whereas the cyan lines show the 40th cycle. Figure 8.11a for the core (C-4) sample shows a dramatic potential drop at the start of discharge which is highlighted with the green box and arrow, indicating serious impedance growth within the cell upon cycling. This further suggests that the electrolyte is not stable at the interphase between the Ni-rich surface and electrolyte.

Figure 8.11c for the S1 (S1-3) sample shows a broad new peak at ~ 3 V appears, and the peak area between 3.3 – 4.4 V during discharge decreases whereas the peak area at 2.5 –

3.0 V increases, which are associated with the conversion to a spinel-like phase.[67,68,72,73,88,162,188,189] Figure 8.11c indicates that the lower voltage component contributes increasingly to the total capacity and the average discharge voltage of the cell decreases with cycle number. However, there is no obvious impedance growth in the cell as indicated by the lack of a dramatic voltage drop at the charge-discharge switchpoint, as expected for the Mn-rich materials[20] suggesting a stable electrode-electrolyte interface.

Figure 8.11b shows that dQ/dV vs. V of sample CS1-2 during discharge is very stable compared to the C-4 and S1-3 samples. There is almost no voltage drop at the start of discharge indicating that the Mn-rich shell prohibits the interaction between the Ni-rich core surface and the electrolyte hence providing a stable electrolyte/electrode interphase. Additionally, there is a much smaller increase of peak area at 2.8 – 3.3 V during discharge when compared to that of S1-3, showing a more stable average discharge voltage due to the small percentage of the Mn-rich shell in the CS samples and the diffusion of Ni from the core to the shell.

Figure 8.12 shows the same dQ/dV vs V plots for the C-6 (Figure 8.12a), CS2-3 (Figure 8.12b) and S2-4 (Figure 8.11c) samples. Similarly, Figure 8.12 a for sample C-6 (see the highlighted box) shows a dramatic voltage drop at the switch to discharge, whereas the S2-4 sample shows an increase in capacity in the lower voltage range (2.8 – 3.3 V). Conversely, CS2-3 shows almost no voltage drop at the switch point and very little voltage fade. This work confirms that the CS structure with a Mn-rich shell can effectively protect the Ni-rich core from parasitic reactions with the electrolyte, and help eliminate the voltage fade issues of the Mn-rich shell.

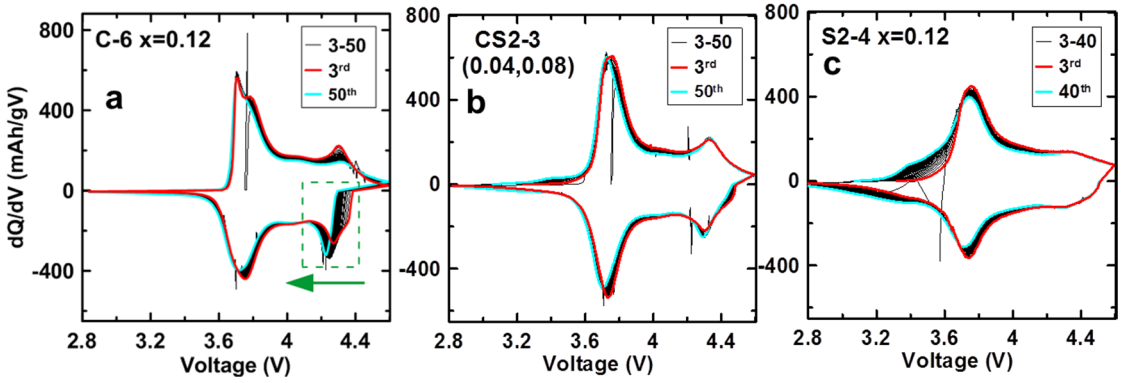

Figure 8.12 dQ/dV for the C-6 (12a), CS2-3 (12b) and S2-4 (12c) samples between 2.5 – 4.6 V from the 3rd cycle to the 40th cycle shown with black lines. The red lines show the 3rd cycle whereas the cyan lines show the 40th cycle. The green box and arrow in 8.11a highlight the dramatic potential drop at the start of discharge.

8.2.6.6 **Average Voltage and ΔV**

Figure 8.13a shows the average discharge voltage of sample C-4 in red triangles, sample CS1-2 in blue diamonds, sample S1-3 in blue triangles, sample CS2-3 in black circles and sample S2-4 in black crosses from the 4th cycle to the 40th cycle. Sample C-4 shows the highest average discharge potential of ~ 3.92 V at the beginning, however it decreases rapidly to be about 3.85 V at the 40th cycle due to impedance increase. The shell-only samples show much lower average discharge potential and also dramatic voltage fade, that is from ~3.62 to 3.51 V in 40 cycles for sample S1-3 and from ~3.80 to 3.74 V in 23 cycles for sample S2-4. Figure 8.13a suggests that the higher the Mn content of the materials (C, S1 and S2), the lower the average discharge potential and the worse the voltage fade. Conversely, the CS2-3 and CS1-2 samples present relatively stable average discharge potentials with only ~ 0.02 V and ~ 0.04 V decrease in 40 cycles respectively. Sample CS1-

2 delivers a relatively lower average discharge potential of ~3.82 V compared to that of ~ 3.88 V for CS2-3 due to the higher concentration of Mn in the shell.

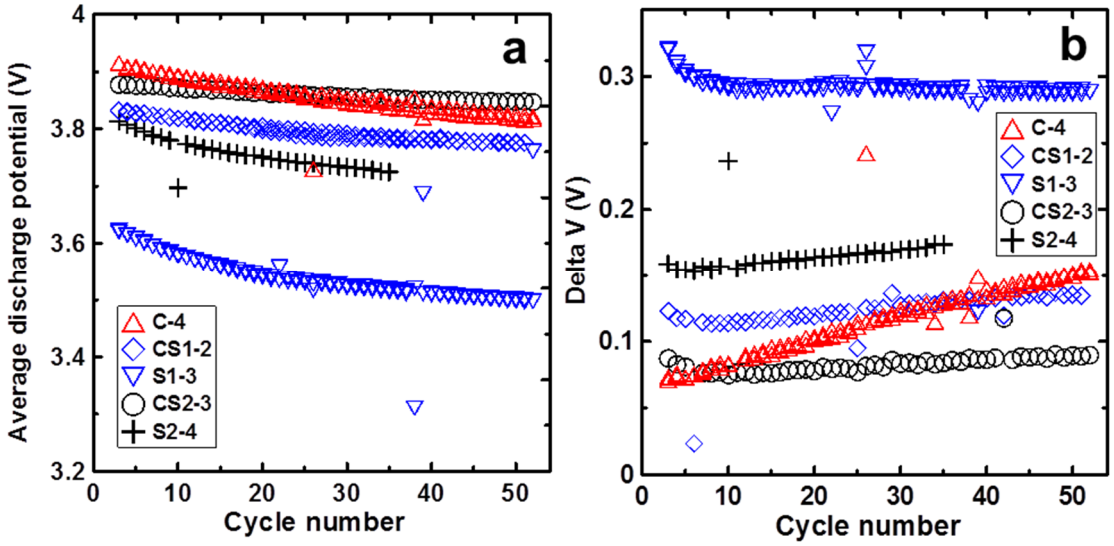

Figure 8.13 The average discharge voltage of sample C-4 in red triangles, sample CS1-2 in blue diamonds, sample S1-3 in blue triangles, sample CS2-3 in black circles and sample S2-4 in black crosses from the 4th cycle to the 40th cycle (a). The difference between the average charge voltage and the average discharge voltage (delta V) as a function of cycle number (b).

Figure 8.13b presents the difference between the average charge voltage and average discharge voltage (delta V) as a function of cycle number for the same cells as discussed in Figure 8.13a. Figure 8.13b tracks the increase in the polarization of the cells with cycle number. Sample C-4 initially shows the smallest delta V of ~ 0.07 V, however, it increases rapidly indicating the impedance growth within the cell. The S1-2 and S2-3 samples show relatively larger delta V of ~0.3 V and ~0.15 V indicating larger cell impedance at the beginning that may be due to the poor rate capability and inherent hysteresis of the Mn-rich materials. In general, the higher the Mn content of the material (C, S1 and S2), the

larger the polarization. Conversely, sample CS2-3 shows much lower delta V of ~ 0.07 V whereas that of CS1-2 is ~ 0.12 V. The CS samples have much smaller polarization compared to the Mn-rich shell materials. Additionally, samples CS2-3 and CS1-2 show more stable delta V versus cycle number when compared to sample C-4, indicating there is no serious impedance growth in the cells and suggests that the Mn-rich shell can effectively protect the Ni-rich core from the reaction with the electrolyte.

8.3 Conclusions

The core-shell strategy that uses a Ni-rich material as the core and a Mn-rich material as the shell was proven to exploit the beneficial properties and minimize the poor properties of the materials in a hybrid system in this work. Core-shell materials with 67 mol% of a core composition of $Li_{1+x}(Ni_{0.67}Mn_{0.33})_{1-x}O_2$ and 33 mol% of a shell composition of $Li_{1+x}(Ni_{0.2}Mn_{0.6}Co_{0.2})_{1-x}O_2$ or $Li_{1+x}(Ni_{0.4}Mn_{0.5}Co_{0.1})_{1-x}O_2$ were synthesized using the co-precipitation method. EDS mapping results showed a clear Mn-rich, Co-rich shell and a Ni-rich core in the CS precursors. The Mn-rich shell was maintained in the lithiated samples after sintering at 900^{o}C whereas the Co content was approximately uniform throughout the particles. The CS samples with optimal lithium content showed extremely low IRC, as well as high capacity and excellent capacity retention. For example, sample CS1-2 had a reversible capacity of ~217 mAh/g with 15.8% IRC and 98.2% capacity retention after 40 cycles at a rate of ~C/20, and sample CS2-3 showed a reversible capacity of ~218 mAh/g with 12.3% IRC and 98% capacity retention. dQ/dV vs. V and delta V versus cycle number analysis showed that the CS samples had no serious impedance increase problems as well as very stable average discharge potentials. Additionally, the

CS samples had small and stable polarization. The Mn-rich shell can apparently protect the Ni-rich core from the reaction with the electrolyte while the Ni-rich core renders a high and stable average voltage. The CS strategy is a promising approach for the future development of high energy density positive electrode materials for use in cells with long lifetime.

CHAPTER 9. INTERDIFFUSION OF TRANSITION METALS IN LAYERED LI-NI-MN-CO OXIDE DURING SINTERING – BINARY SYSTEM

In Chapter 8, it was shown that a Mn-rich shell can effectively protect a Ni-rich core from reactions with the electrolyte, while the Ni-rich core renders a high and stable average voltage. However, it was also found that diffusion of the cations between the core and shell phases occurs during sintering which makes the a-priori design of a particular core-shell structure difficult. Figure 8.3 shows that a Mn-rich shell was still maintained in the oxide whereas the Co, which was only in the shell in the hydroxide precursor, was essentially homogeneously distributed throughout the particles after sintering at 900ºC. The interdiffusion coefficients of the various transition metals in core-shell/gradient materials during sintering have not been measured, to our knowledge, despite the large amount of work on core-shell and gradient positive electrode materials.[27,44,45,159–161,268,269] It is difficult to determine the concentration profiles of the cations in the radial direction in spherical particles, as it is hard to know exactly where the particles were cut during the polishing process. Furthermore the interdiffusion coefficients of Co, Ni and Mn are clearly very different and hard to determine in a single measurement in these small spherical particles.

9.1 Experimental Design

In this work, a series of experiments to measure the interdiffusion coefficients of the transition metal cations in lithium transition metal oxides, with two different transition

metals, were designed and conducted at various temperatures. The diffusion couples of Ni^{3+}/Co^{3+}, Co^{3+}/Mn^{4+} and Ni^{3+}/Mn^{4+} were measured. Pellets of the pure core phase and the pure shell phase were pressed in contact and heated to induce cation diffusion over long, easily measurable distances. Based on the measured composition versus position profiles, interdiffusion constants at 800, 900 and 1000ºC were determined using fits to Fick's law. Using the Arrenhius law, the activation energy barriers were then determined for each diffusion couple. Once the inter diffusion constants were determined, simulations of transition metal diffusion in spherical core-shell particles during sintering were performed to enable the rational design of spherical core-shell particles.

Laminar pellets were introduced in Chapter 3. Stacked $Li_{1.09}(Ni_{0.8}Mn_{0.2})_{0.91}O_2/Li_2MnO_3$ pellets were used to study the Ni^{3+}/Mn^{4+} diffusion couple, stacked $LiNi_{0.8}Co_{0.2}O_2/LiCoO_2$ pellets were used for Ni^{3+}/Co^{3+}, while stacked $Li_{1.05}(Co_{0.9}Mn_{0.1})_{0.95}O_2/Li_2MnO_3$ pellets were used for Co^{3+}/Mn^{4+}. For cases involving Li_2MnO_3, presumably Li^+ and Mn^{4+}, in a 1:2 ratio, must diffuse together in order to maintain charge balance with three Ni^{3+} or three Co^{3+} ions. The reader is reminded that Li_2MnO_3 can be written as $Li(Li_{1/3}Mn_{2/3})O_2$ which has the same basic layered structure as the other materials used in this study. $Li(Li_{1/3}Mn_{2/3})O_2$ forms solid solutions with $LiCoO_2$, and $LiNiO_2$,[7,8] so interdiffusion between the transition metals in the pellets listed above is expected.

SEM/EDS analysis was conducted using a Hitachi S-4700 SEM. The beam size is less than 10 nm. EDS line scans were collected with an accelerating voltage of 15 kV, a beam current of 15 μA, and an acquisition time of 20 seconds for each data point. The penetration depth of the electron beam was ~800 nm, while the X-rays originated primarily from a

radial distance of less than 80 nm from the electron beam. Monte Carlo simulations of electron trajectories in the various materials studied in this work were made using the CASINO software.[270] Figures E.1 – E.6 of Appendix E show the electron trajectories, and a histogram of x-rays emitted, as function of radial distance from the electron beam for $LiCoO_2$ (E.1 and E.2), $LiNiO_2$ (E.3 and E.4) and Li_2MnO_3 (E.5 and E.6). The total number of points measured in the line scans depended on the diffusion couple. Between 20 to 50 points were collected for each diffusion couple, separated by a distance of ~0.5 to ~ 2.0 μm, depending on the sample. Two to four different line scans were measured for each sample. Measured concentration profiles from the same pellets were aligned and an average concentration profile was then calculated for least squares fitting to calculations made with Fick's law. The binary diffusion model and least square fitting method were discussed in Chapter 3.6. The majority of this Chapter was published in Chemistry of Materials.[271] Permission has been granted by the American Chemistry Society for the reuse of the complete article.

9.2 Results and Discussion

9.2.1 SEM Image of the Interface

Figure 9.1 shows SEM images of the cross-sections of the $LiCoO_2$-$LiNi_{0.8}Co_{0.2}O_2$ diffusion couples prepared under various conditions. The $LiCoO_2$ pellet is shown on the left hand side of each of these images. Figures 9.1b, 1c and 1d show SEM images of the cross-sections after sintering at 800°C for 10 h, 900°C for 10 h and 1000°C for 5 h, respectively, while Figure 9.1a shows the cross-section of the pellet heated at 900°C at lower magnification.

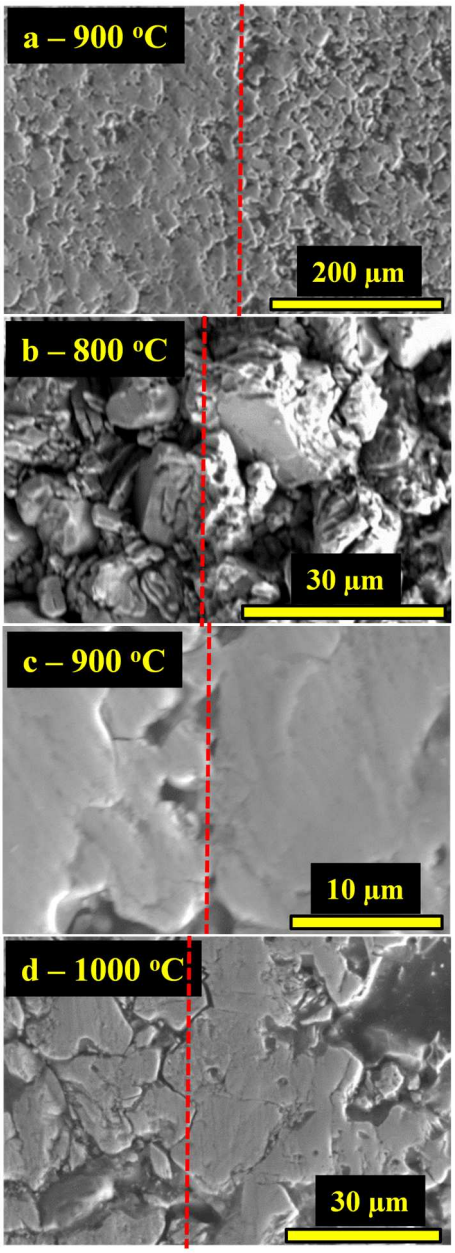

Figure 9.1 SEM images of the cross-section of a composite pellet that had $LiCoO_2$ powder on the left and $LiNi_{0.8}Co_{0.2}O_2$ on the right side after sintering at: (a, c) 900°C for 10 h, (b) 800°C for 10 h, and (d) 1000°C for 5 h, respectively. The red dashed lines are the approximate positions of the interface.

A close contact between the two sides of the composite pellet can be observed. In Figure

9.1b it is apparent that the surface of the composite pellet sintered at 800°C was still quite rough, even after polishing. In comparison, Figures 9.1c and 9.1d show the notably smoother surface of the pellets sintered at 900 and 1000°C, due to rapid grain growth and densification when sintering at the higher temperatures. Some small pores were also observed in the composite pellets due to incomplete densification. SEM line scans were performed on these surfaces, in a direction perpendicular to the interface between the $LiCoO_2$ and $LiNi_{0.8}Co_{0.2}O_2$ pellets.

9.2.2 Concentration Profile from EDS Line Scans

Figures 9.2a1, 2a2, and 2a3 show the Ni and Co atomic concentration profiles plotted versus position, measured using EDS line scans for the $LiNi_{0.8}Co_{0.2}O_2/LiCoO_2$ pellets (Ni^{3+}/Co^{3+} couple) sintered at 800, 900 and 1000°C, respectively. Figures 9.2b1, 2b2, and 2b3 show the Co and Mn profiles for the $Li_{1.05}(Co_{0.9}Mn_{0.1})_{0.95}O_2/Li_2MnO_3$ pellets (Co^{3+}/Mn^{4+}) sintered at 800, 900 and 1000°C, respectively. Figures 9.2c1, 2c2, and 2c3 show the Ni and Mn profiles for the $Li_{1.09}(Ni_{0.8}Mn_{0.2})_{0.91}O_2/Li_2MnO_3$ pellets (Ni^{3+}/Mn^{4+}) sintered at 800, 900 and 1000°C, respectively. The symbols in Figure 9.2 show the original data points, the dashed lines indicate the initial concentration profile before sintering which was calculated from the least square fitting, and the solid lines show the results of fitting Fick's law to the data.

Figure 9.2a1 demonstrates that the initial atomic concentration of Co was ~100% on the left and ~20% on the right, corresponding to the initial individual compositions. The atomic concentration of Co decreased from ~100% to about 20% over approximately 10 μm distance after sintering at 800°C for 20 h, whereas Figures 9.2a2 and 2a3 show this

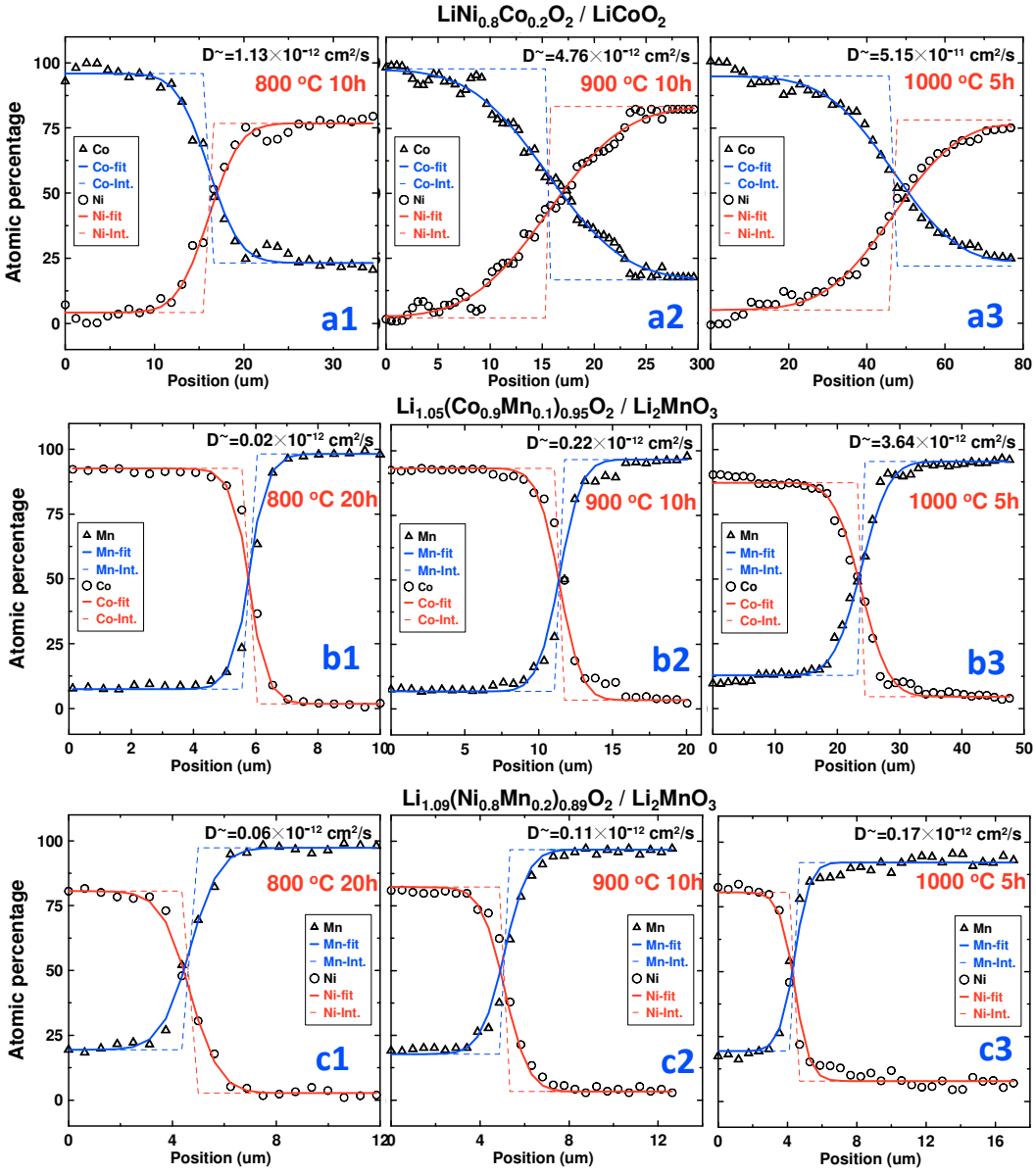

Figure 9.2 The Ni and Co atomic concentration profiles versus position, measured using EDS line scans, for the $LiNi_{0.8}Co_{0.2}O_2/LiCoO_2$ composite pellets (Ni^{3+}/Co^{3+} couple) sintered at: (a1) 800°C, (a2) 900°C and (a3) 1000°C, respectively. The Co and Mn profiles for the $Li_{1.05}(Co_{0.9}Mn_{0.1})_{0.95}O_2/Li_2MnO_3$ composite pellets (Co^{3+}/Mn^{4+} couple) at sintered at: (b1) 800°C, (b2) 900°C and (b3) 1000°C, respectively. The Ni and Mn profiles for the $Li_{1.09}(Ni_{0.8}Mn_{0.2})_{0.91}O_2/Li_2MnO_3$ composite pellets (Ni^{3+}/Mn^{4+} couple) at sintered at: (c1) 800°C, (c2) 900°C and (c3) 1000°C, respectively. The symbols show the original data points. The dashed lines show the initial concentration profile from the fitting and the solid lines show the calculated profiles from Fick's law.

diffusion distance was about 30 μm and 70 μm for the pellets sintered at 900°C for 10 h and 1000°C for 5 h respectively. Figure 9.3 shows the fitted concentration profiles at 800, 900 and 1000°C in the same plot. The calculations using Fick's law match the measured concentration profile very well, and yield interdiffusion coefficients for the Ni^{3+}/Co^{3+} couple at 800, 900 and 1000°C of 1.13×10^{-12}, 4.76×10^{-12} and 5.15×10^{-11} cm^2/s, respectively.

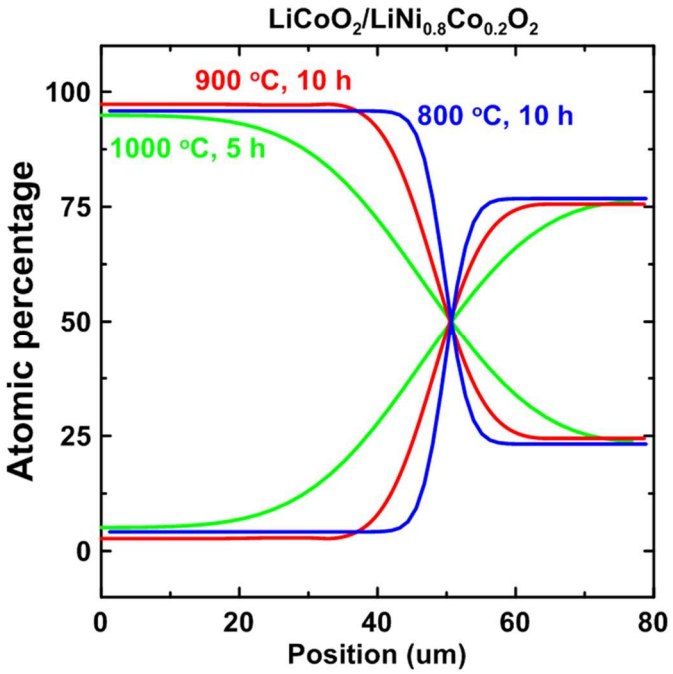

Figure 9.3 The fitted Ni and Co atomic concentration profiles versus position for the $LiCoO_2/LiNi_{0.8}Co_{0.2}O_2$ composite pellets (Ni^{3+}/Co^{3+} couple) sintered at 800, 900 and 1000°C, respectively.

Figures 9.2b1, 2b2 and 2b3 show that the initial atomic concentration of Mn was ~10% on the left and ~100% on the right, while that of Co was ~90% on the left and 0% on the right, again corresponding to the initial compositions. The atomic concentration of Co decreases

from ~90% to about 0% over distances of approximately 3, 5, and 12 μm after sintering for 5 h at 800°C for 20 h, 900°C for 10 h, and 1000°C, respectively. The fits to the measured profiles using Fick's Law yielded interdiffusion coefficients for the Co^{3+}/Mn^{4+} couple of 0.02×10^{-12}, 0.22×10^{-12} and 3.64×10^{-11} cm^2/s at 800, 900 and 1000°C, respectively.

Figures 9.2c1, 2c2 and 2c3 show that the initial atomic concentration of Ni was ~80% on the left and ~0% on the right, while Mn was ~20% on the left and 100% on the right, as with the initial individual pellets. The interdiffusion coefficients for Ni^{3+}/Mn^{4+} couple were 0.06×10^{-12}, 0.11×10^{-12} and 0.17×10^{-11} cm^2/s at 800, 900 and 1000°C, respectively. The interdiffusion coefficient did not increase significantly with increasing temperature for the Ni^{3+}/Mn^{4+} couple. The interdiffusivity between Ni^{3+} and Co^{3+} is much larger than that between Ni^{3+} or Co^{3+} and Mn^{4+} at the same temperature. This result agrees well with the trends observed in the core-shell samples shown in Figure 8.3. Ni^{3+} and Co^{3+} have similar ionic radii and the same oxidation state which favors interdiffusion, whereas exchange between Ni^{3+} or Co^{3+} and Mn^{4+} needs to satisfy charge balance which involves the cooperative motion of several atoms and may hence hinder diffusion.[232,233]

This is the first time the interdiffusion constants of cations in the layered positive electrode materials have **been** reported to our knowledge. These data will help significantly in the understanding and design of core-shell materials. They also help to explain why co-precipitation methods, which generate hydroxide or carbonate precursors with atomically mixed transition metals, are required for the synthesis of Li-Ni-Mn-Co oxide (NMC) compounds. Solid-state reactions between ground mixtures of transition metal oxides and lithium compounds have failed, to this point, to yield NMC materials with acceptable

electrochemical performance, presumably due to the relatively low interdiffusion between Ni and Mn, which makes it impossible to fabricate solid solutions in a reasonable time at acceptable temperatures.

9.2.3 Interdiffusion Constants as a Function of Temperature

Figures 9.4a1, 4b1 and 4c1 show the interdiffusion constants of the Ni^{3+}/Co^{3+}, Co^{3+}/Mn^{4+} and Ni^{3+}/Mn^{4+} couples as a function of temperature, respectively. The red lines show the fits of the Arhennius law to the data. These fits show good agreement with the data, suggesting that the interdiffusion constants follow the Arrhenius equation as a function of temperature.

Figures 9.4a2, 9.4b2 and 9.4c2 shows Arrhenius plots of the interdiffusion constants of the Ni^{3+}/Co^{3+}, Co^{3+}/Mn^{4+} and Ni^{3+}/Mn^{4+} couples with -ln (D) on the vertical axis and 1/T on the horizontal axis. The slopes of the red lines in Figures 9.4a2, 4b2 and 4c2, multiplied by the Boltzmann constant, k_B (units are J/(mol • K)), gives the activation energy barrier for diffusion of each of the diffusion couples.

Table 9.1 provides the activation energies determined from the data presented in Figure 9.3. The Ni^{3+}/Co^{3+} couple shows an activation barrier of ~ 2.2 eV and the highest D_0 of ~$4*10^{-4}$ m^2/s. The Ni^{3+}/Mn^{4+} couple shows the lowest activation barrier of 0.5 eV but also the lowest $\mathbf{D_0}$ which is ~$3*10^{-15}$ m^2/s, and the Co^{3+}/Mn^{4+} couple shows the highest activation energy of ~3.0 eV with D_0 of ~$3*10^{-6}$ m^2/s.

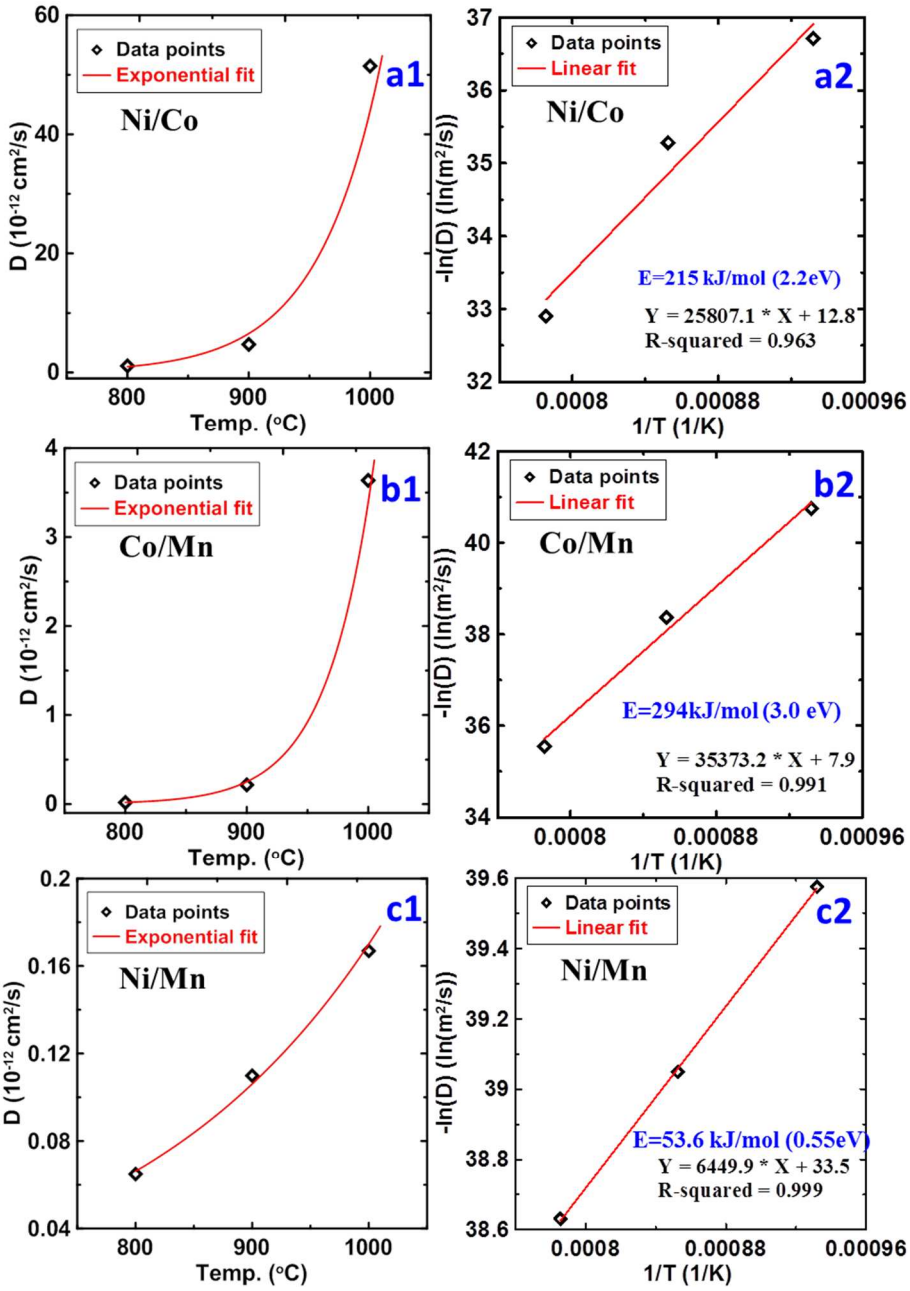

Figure 9.4 The interdiffusion constants of (a1) Ni^{3+}/Co^{3+}, (b1) Co^{3+}/Mn^{4+} and (c1) Ni^{3+}/Mn^{4+} as a function of temperature respectively. Arrhenius plots of the interdiffusion constants of: (a2) Ni^{3+}/Co^{3+}, (b2) Co^{3+}/Mn^{4+} and (c2) Ni^{3+}/Mn^{4+} showing -ln (D^{-}) on the vertical axis and 1/T on the horizontal axis.

Table 9.1 Summary of the Activation Energies and D_0 for Diffusion Measured in This Work

Couple	Activation Energy		
	eV (+/-0.3)	kJ/mol (+/-30)	$D_0(m^2/s)$
Ni/Mn	0.5	54	$3(2)*10^{-15}$
Co/Mn	3.0	290	$4(2)*10^{-4}$
Ni/Co	2.2	210	$3(2)*10^{-6}$

Based on the measured diffusion constants for various diffusion couples, one can simulate interdiffusion in spherical core-shell particles. This will aid in the rational design of core-shell materials after sintering that, in turn, govern the electrochemical properties. These simulations can guide the design of core-shell materials in the selection of core/shell compositions, the shell thickness, the synthesis temperature etc. in order to maintain a Ni-rich core and Mn-rich shell after sintering.

9.2.4 Shell Thickness

Before showing the simulation results, it is necessary to discuss the relationship between the shell thickness and the shell mole percentage during a co-precipitation process for the synthesis of hydroxide core-shell precursors.[26,242] Generally, a core metal sulfate solution (2M concentration) was first pumped into a tank reactor while a sodium hydroxide addition was automatically controlled by a pH controller.

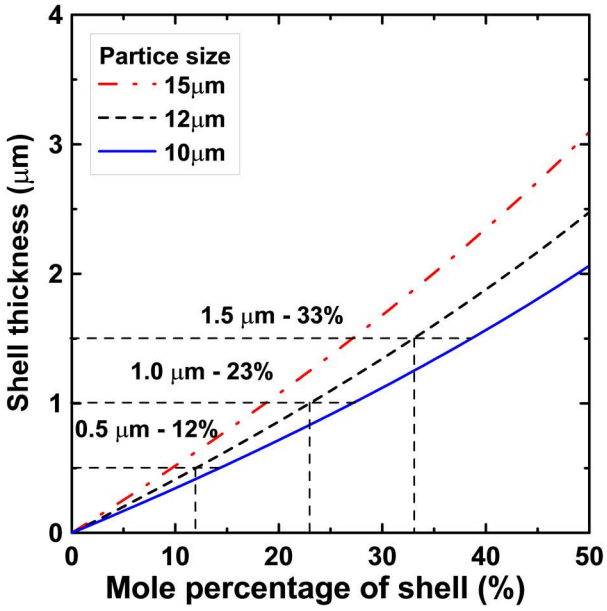

Figure 9.5 Shell thickness, as a function of shell mole fraction, in spherical hydroxide core-shell precursors with the indicated diameters.

The shell metal sulfate solution (2M concentration) will then replace the core metal sulfate solution after a certain amount of time until the reaction is finished. Assuming the solubility of the precipitated metal hydroxide is low, and that the molar volume of the metal hydroxide changes very little with composition, one can show that the shell thickness has the following relationship with the shell mole percentage:

$$R_s = R\left(1-\sqrt[3]{(1-m_s)}\right) \tag{9.1}$$

where R_s is the shell thickness, R is the final radius of the spherical core-shell particle, and m_s is the shell mole fraction (moles of shell metal sulfate compared to the total number of moles of metal sulfate added to the reaction). This model ignores any porosity in the

particles and assumes the particles are spherical. The average particle size of the NMC precursor particles is generally around 10-15 µm.[59,127,129,134,161]

Figure 9.5 shows the shell thickness as a function of shell mole fraction. Final core-shell particle sizes of 10, 12 and 15 µm were used for the calculations, which are shown with the blue solid line, black dashed line and red dashed dot line, respectively. Figure 9.5 shows that the shell thickness is around 1.5 µm for a 33% shell, when the CS particles are around 12 µm, which agrees well with the experimental results shown in Chapter 8. Additionally, 23% and 12% shells correspond to shell thicknesses of about 1 µm and 0.5 µm, respectively.

9.2.5 Simulation Results with Various Diffusion Couples

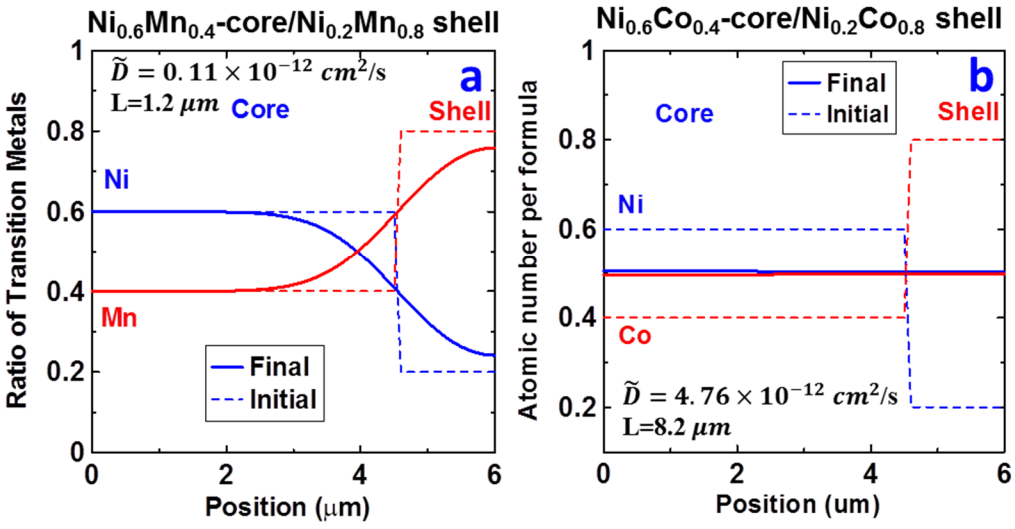

Figure 9.6 Simulation results for the atomic concentrations in spherical core-shell particles sintered at 900°C for 10 h, assuming a particle diameter of 12 µm and a shell thickness of 1.5 µm. Samples have a 33 mole% of shell with and an initial: (a) core of $Ni_{0.6}Mn_{0.4}$ and shell of $Ni_{0.2}Mn_{0.8}$, (b) core of $Ni_{0.6}Co_{0.4}$ and $Ni_{0.2}Co_{0.8}$.

Figure 9.6 shows the modelling results for spherical CS materials sintered at 900°C for 10 h, assuming a particle size of 12 µm and a shell thickness of 1.5 µm for a 33% mole fraction shell. The dashed lines show the initial composition while the solid lines show the final simulation results. The measured interdiffusivity constants of 0.11×10^{-12} and 4.76×10^{-12} cm^2/s were used for Ni/Mn and Ni/Co, respectively. A characteristic diffusion length $L=2\sqrt{Dt}$ was calculated for each case to estimate the order of magnitude of the actual diffusion distance.[232]

Figure 9.6a shows the initial core is 60% Ni and 40 % Mn, while the shell is 20% Ni and 80% Mn. After sintering, a pure core region of $Ni_{0.6}Mn_{0.4}$ with a radius of ~3 µm was maintained, and a gradient region with decreasing Ni content from 0.6 to 0.23 on the surface was observed after sintering at 900°C for 10 h. A Mn-rich shell with a slightly decreased Mn to Ni ratio on the surface can be maintained, which agrees with the EDS results shown in Figure 8.3. Figure 9.6b shows an initial core composition of $Ni_{0.6}Co_{0.4}$ and a shell composition of $Ni_{0.2}Co_{0.8}$. After sintering the Ni and Co are essentially uniform across the whole particle due to the relatively large interdiffusivity of the Ni/Co couple. This result also shows very good agreement with the EDS map presented in Figure 8.3.

9.2.6 Simulation Results with Various Initial Shell Thickness

Figures 9.7a, 7b and 7c show the simulation results for 12 µm diameter core-shell samples, with shell thicknesses of 1.5, 1 and 0.5 µm, respectively. These samples were sintered at 900°C for 10 h, with an initial core composition of $Ni_{0.6}Mn_{0.4}$ and an initial shell composition of $Ni_{0.2}Mn_{0.8}$.

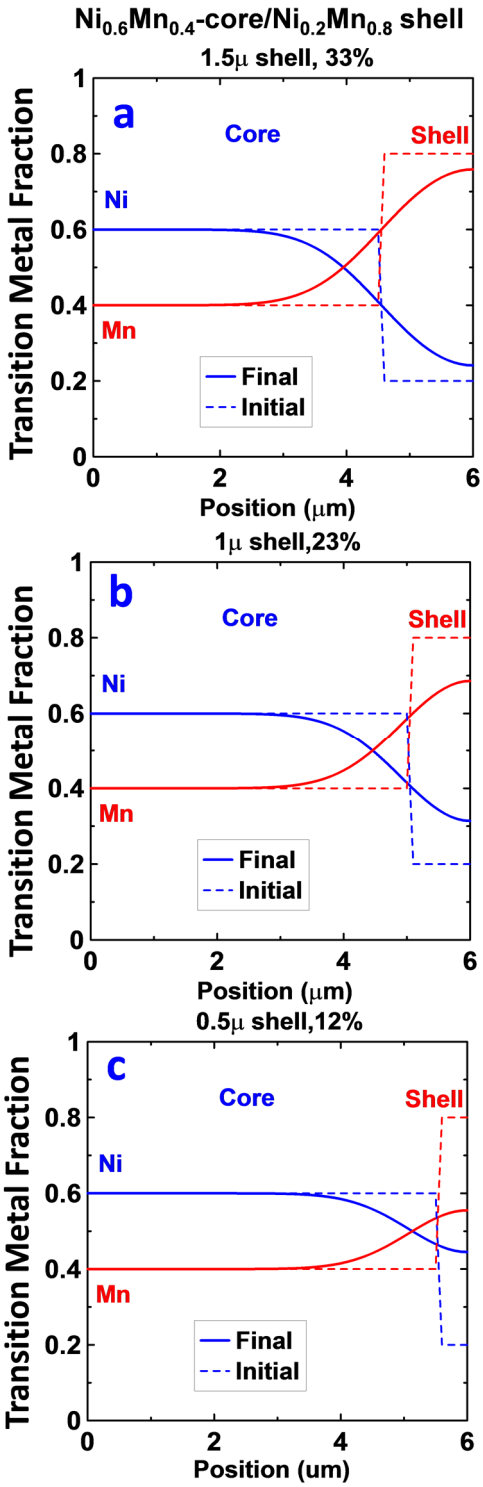

Figure 9.7 Simulation results for the atomic concentrations in 12 μm diameter spherical core-shell particles with shell thicknesses of: (a) 1.5, (b) 1 and (c) 0.5 μm, corresponding to shell mole percentages of 33%, 23% and 12%, respectively, sintered at 900°C for 10 h. The initial core composition was $Ni_{0.6}Mn_{0.4}$ and the initial shell composition was $Ni_{0.2}Mn_{0.8}$.

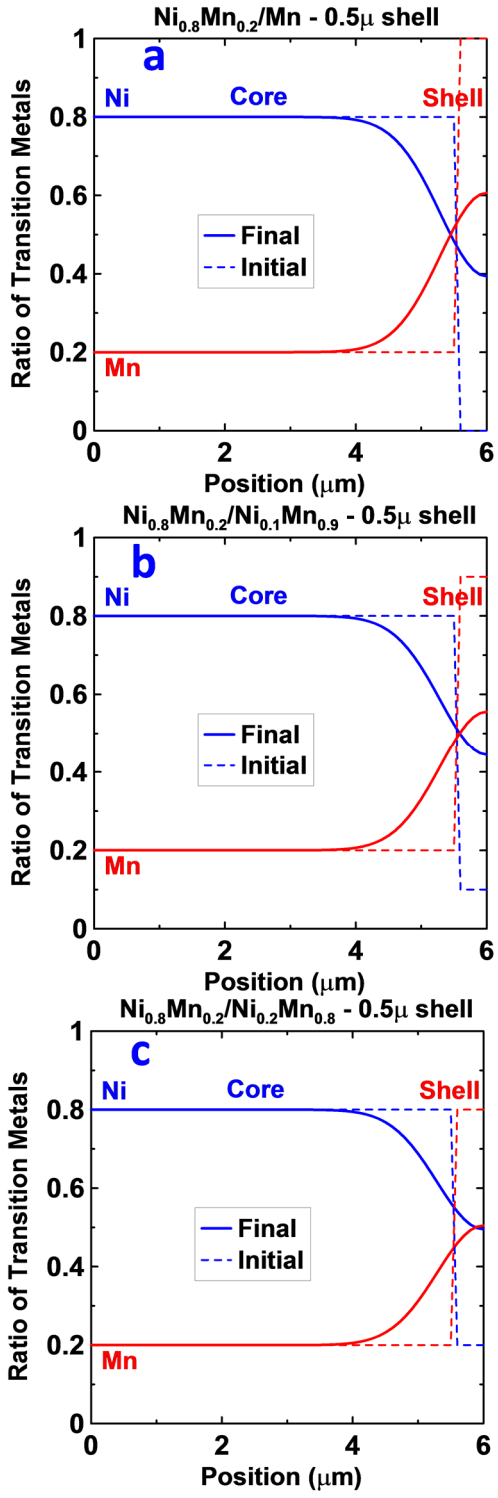

Figure 9.8 Simulation results for the atomic concentrations in 12 μm spherical core-shell samples with initial shell compositions of: (a) 100% Mn, (b) $Ni_{0.1}Mn_{0.9}$ and (c) $Ni_{0.2}Mn_{0.8}$, respectively, after sintering at 900°C for 10 h. The initial core composition was $Ni_{0.8}Mn_{0.2}$ and the initial shell thickness was 0.5 μm.

Figures 9.7a, 9.7b and 9.7c show the radius of the pure core region increases from ~2.5 to 3.5 μm as the initial the shell thickness decreases. Additionally, the Mn to Ni ratio on the surface decreases from ~0.75 to 0.55 when the shell thickness decreases. As a consequence, it is difficult to maintain a Mn-rich shell when the shell thickness is too thin, due to interdiffusion. However, a thin shell is required for materials like NMC811 in order to maximize the capacity.[12,29,242] Ni-rich materials like NMC811 are generally made at lower temperatures of about 800°C.[127,129]

9.2.7 Simulation Results with Various Initial Shell Composition

Figures 9.8a, 9.8b and 9.8c show simulation results for 12 μm diameter core-shell samples, with initial shell compositions of 100% Mn, $Ni_{0.1}Mn_{0.9}$ and $Ni_{0.2}Mn_{0.8}$, respectively. These samples have an initial core composition of $Ni_{0.8}Mn_{0.2}$ and shell thickness of 0.5 μm, after sintering at 800°C for 10 h. Figures 9.8a, 9.8b and 9.8c demonstrate that the final Mn to Ni ratio at the surface decreases from ~0.6 to 0.55, as the Mn content in the shell decreased. A Mn-rich shell cannot be maintained when the initial shell Mn content is lower than 0.8. This result suggests that a high initial shell Mn content is required for an effective thin coating of NMC811 when synthesised at 800°C.

9.3 Conclusions

A series of experiments to measure the interdiffusivity of the cations in binary systems at various temperatures were designed and conducted. The interdiffusion coefficients of Ni^{3+}/Co^{3+}, Co^{3+}/Mn^{4+} and Ni^{3+}/Mn^{4+} were measured using experiments on pressed pellets at 800, 900 and 1000°C, which induced cation diffusion over long, measurable distances.

Based on the analyzed composition profiles from EDS line scans, interdiffusion constants were extracted for the first time, to our knowledge, in layered positive electrode materials. Ni^{3+}/Co^{3+} has the highest interdiffusion coefficient of ~4.7×10^{-12} cm^2/s, while Ni^{3+}/Mn^{4+} has the smallest at ~0.1×10^{-12} cm^2/s, both measured at 900°C. The similarity of the oxidation states and ionic radii of the diffusing ions significantly affects diffusivity. Simulations in spherical core-shell materials with varied initial shell thickness and shell composition were performed to guide core-shell materials design. A relatively thick initial shell with a high Mn content is required in order to maintain a Mn-rich surface after sintering. This work provides a first step in understanding diffusion of transition metal cations in core-shell materials by considering binary systems, and should benefit researchers working on core-shell materials in the future. More complex studies in systems with three diffusing transition metals (i.e. ternary systems) are discussed in Chapter 10.

CHAPTER 10. THE EFFECT OF INTERDIFFUSION ON THE PROPERTIES OF LITHIUM-RICH CORE-SHELL AS POSITIVE ELECTRODE MATERIALS

Chapter 8 and Chapter 9 show diffusion of the cations between the core and shell phases occurs during sintering to prepare the NMC core-shell oxide.[271] Although much research on CS and gradient NMC materials have been reported, there are no detailed studies of how interdiffusion during sintering affects the final composition, structure and electrochemical properties of CS materials containing Li, Ni, Mn and Co. In this Chapter, the effect of interdiffusion of transition metal atoms between the core and shell materials on the electrochemical performance is explored by varying the shell thickness and sintering temperature. In Chapter 9, stacked laminar pellets were designed to study interdiffusion in a binary system (only two of the three elements, Ni, Co and Mn were used)[271]. In this Chapter, both the core and shell contained all of Li, Ni, Mn and Co so that complicated interdiffusion occurred. Concentration profiles were measured on spherical CS particles and also on pre-designed laminar pellets, which were fitted with modeling results, improving the understanding of NMC CS materials and providing guidance for future improvements.

Most reports on electrode material coatings only report tests of materials in half cells with comparisons to uncoated materials using standard electrolytes[39–42,150,198–200,272,273]. However, results can be very different when coated materials are tested in full cells and when electrolyte additives are used. J. Xia *et. al*[274] and K.J Nelson *et.al*[31] have shown that $LaPO_4$-coatings on $Li[Ni_{0.42}Mn_{0.42}Co_{0.16}]O_2$ provided very limited benefit when state-of-

the-art electrolyte additives were used. J. Xia *et. al* also showed that a coating can be very beneficial when combined with appropriate electrolyte additives at voltages above 4.4 V. Here, selected lithium-rich CS materials were tested in full coin cells containing electrolyte additives to evaluate the true benefits of the shell coating.

10.1 Experimental Design

CS precursors with $(Ni_{0.6}Mn_{0.2}Co_{0.2})(OH)_2$ as the core and 10 mol% (CS10), 20 mol% (CS20) or 33 mol% (CS33) $(Ni_{0.2}Mn_{0.6}Co_{0.2})(OH)_2$ shell were first synthesized. Lithiated samples were then prepared by sintering the precursor and LiOH with three different lithium contents (x= 0.02, 0.04 and 0.06 in $Li_{1+x}TM_{1-x}O_2$, where TM stands for transition metal ions) at 850 or 900°C for 10 h. The samples were labeled as CS10 (20, 33) - 850 (900) - 1 (2, 3), which indicates the initial shell content, sintering temperature and lithium content ($1 \rightarrow x = 0.02$; $2 \rightarrow x=0.04$; $3 \rightarrow x = 0.06$), respectively. For example, CS20-900-3 indicates a sample with 20 mol.% shell, sintered at 900°C with x = 0.06.

CS33-900-2 sample for EDS mapping measurements were prepared by first encasing powder in epoxy using the method introduced in Chapter 3 and Chapter 8. The mapping was carried out using a Hitachi S-4700 SEM. Elemental maps of samples were collected in 300 seconds with an accelerating voltage of 20 kV and current of 15 μA. CS33-850-2 sample for EDS mapping measurements were prepared by an ion beam cross-section polisher (JEOL IB-09010CP) at the Canadian Centre for Electron Microscopy (CCEM). The EDS mapping was carried out using a JEOL JSM-7000F SEM at CCEM. Elemental

maps of the samples were collected in 300 seconds with an accelerating voltage of 10 kV and current of 10 μA.

EDS point analysis on CS-850-2 was carried out using an aberration-corrected (image and probe-forming lenses) FEI Titan Cubed 80-300 microscope operated in STEM mode with an acceleration voltage of 200 keV. The TEM sample was prepared using a dual beam focused ion beam/scanning electron microscope (FIB/SEM) (Zeiss NVision 40) to obtain a thin slice from the centre of a particle, which was then mounted onto a FIB lift-out grid (PELCO®) and eventually thinned down to ~ 70 nm prior for the analysis. Laminar pellets were also prepared using the method introduced in Chapter 3 and Chapter 9 and were used for measurements of interdiffusion.

Electrochemical measurements (half cells) were carried out using galvanostatic charge-discharge cycling with standard 2325 coin cells with lithium metal negative electrodes on an E-One Moli Energy Canada battery testing system. The electrolyte was 1.0 M $LiPF_6$ in 1:2 v/v ethylene carbonate:diethyl carbonate (EC:DEC) (BASF, max < 20 ppm water). All the cells were tested with a specific current of 10 mA/g at 30°C. The cells were tested between 2.5-4.4 V for 4 cycles, then 2.5-4.6V for 10 cycles, followed by 2.5-4.8V for 1 cycle, and 2.5-4.6 V for another 10 cycles.

The full coin cells followed the same procedure except a graphite electrode from Magna E-car was used as the counter electrode. The control electrolyte was 1.0 M $LiPF_6$ in 1:2 v/v ethylene carbonate:diethyl carbonate (EC:DEC) (BASF, max < 20 ppm water). Electrolyte additives used in this work were a combinations of 2 wt.% PES + 1 wt.%

MMDS + 1 wt.% TTSPi (PES211). The cells were tested between 2.8 – 4.5 V for 100 cycles.

10.2 Results and Discussion

10.2.1 Properties of Precursors

Figure 10.1 shows the XRD patterns of the as-synthesized hydroxide precursors of the core-only, shell-only, and CS samples with 10%, 20% and 33% shell, respectively.

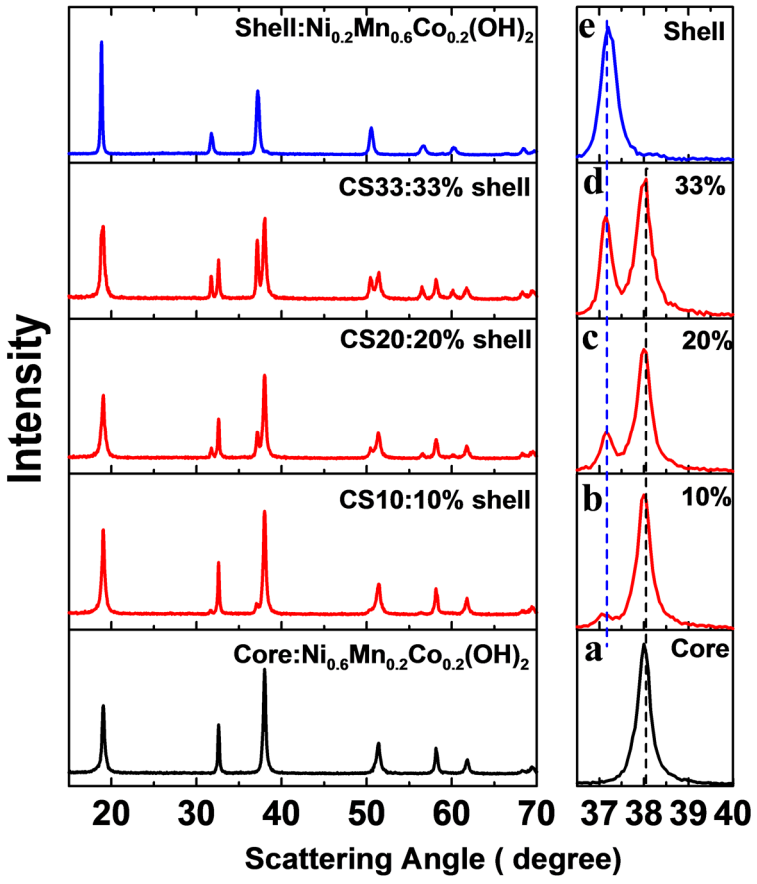

Figure 10.1 XRD patterns of the as synthesized hydroxide precursors of the core-only (a), shell-only (d), and CS samples with 10% (b), 20% (c) and 33% (d) shell respectively.

Figure 10.1 shows that there are two peaks between 37° and 40° in the CS precursors and that these peaks align very well with the core-only (higher angle) and shell-only (lower-angle) peaks, respectively. This indicates that the core and shell phases in the CS samples have the correct composition and structure.

Table 10.1 Composition of the precursors.

Sample	**Composition**	**Target average composition**	**ICP-OES results**
Core (C)	$Ni_{0.60}Mn_{0.20}Co_{0.20}(OH)_2$	$Ni_{0.60}Mn_{0.20}Co_{0.20}(OH)_2$	$Ni_{0.59}Mn_{0.21}Co_{0.2}(OH)_2$
CS10	0.88 $Ni_{0.6}Mn_{0.2}Co_{0.2}(OH)_2$ • 0.12$Ni_{0.2}Mn_{0.6}Co_{0.2}(OH)_2$	$Ni_{0.55}Mn_{0.25}Co_{0.2}(OH)_2$	$Ni_{0.55}Mn_{0.24}Co_{0.21}(OH)_2$
CS20	0.80$Ni_{0.6}Mn_{0.2}Co_{0.2}(OH)_2$ • 0.20$Ni_{0.2}Mn_{0.6}Co_{0.2}(OH)_2$	$Ni_{0.52}Mn_{0.28}Co_{0.2}(OH)_2$	$Ni_{0.52}Mn_{0.28}Co_{0.2}(OH)_2$
CS33	0.67 $Ni_{0.6}Mn_{0.2}Co_{0.2}(OH)_2$ • 0.33$Ni_{0.2}Mn_{0.6}Co_{0.2}(OH)_2$	$Ni_{0.47}Mn_{0.33}Co_{0.2}(OH)_2$	$Ni_{0.46}Mn_{0.34}Co_{0.2}(OH)_2$

Table 10.1 shows the elemental analysis results on the precursors. The ICP-OES results match very well to the average target composition. Figure 10.2 shows scanning electron microscopy (SEM) images and particle size analysis of the CS precursors. The average particle size is around 14 – 16 μm in the CS samples. Figure F.1 in Appendix F shows the SEM images and energy dispersive spectroscopy (EDS) mapping results of the CS precursors. Figure F.1 shows a clear Mn-rich shell in CS10, CS20 and CS33.

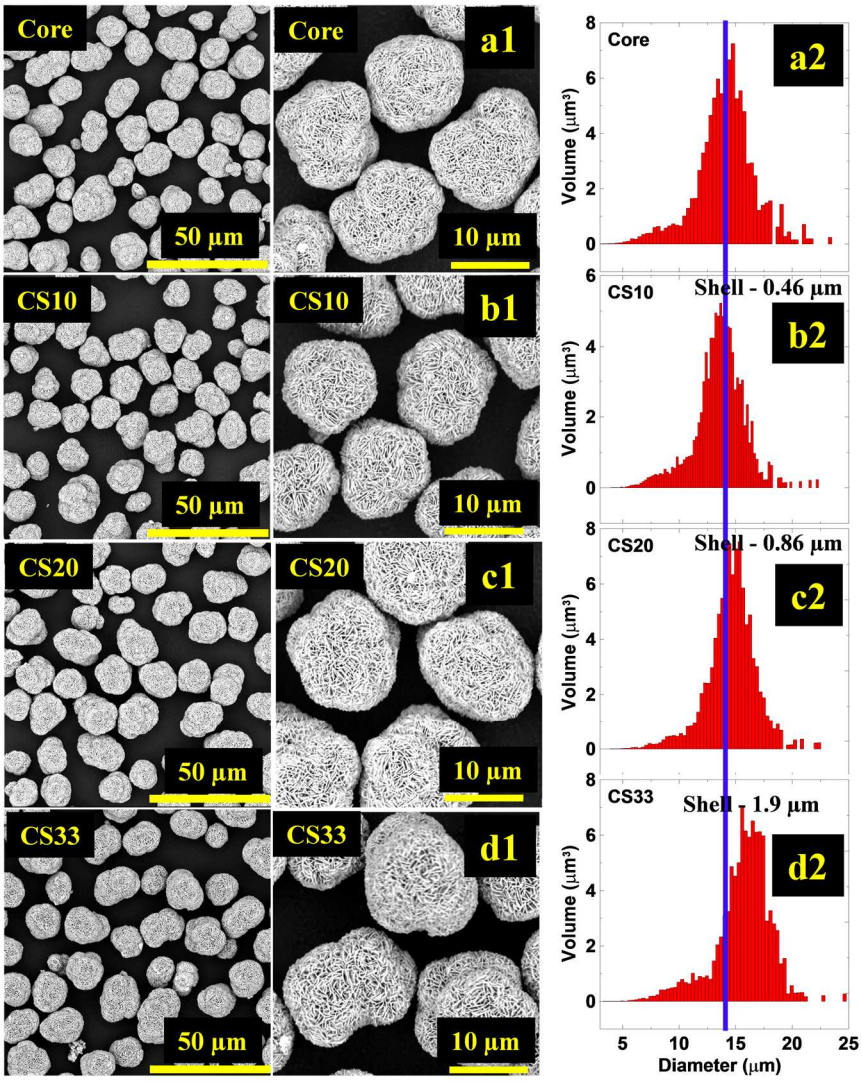

Figure 10.2 **.** SEM images of C (a1), CS10 (b1), CS20 (c1) and CS33 (d1) precursors and particle size analysis of C (a1), CS10 (b1), CS20 (c1) and CS33 (d1). The shell thickness was calculated by assuming spherical particles as introduced in Chapter 9.

10.2.2 EDS of Lithiated CS Samples

Figure 10.3 shows the SEM images and EDS mapping results of lithiated CS samples prepared at 850 and 900°C for 10 h. Figures 10.3a1, 3b1 and 3c1 show the elemental

mapping results for CS10, CS20 and CS33 samples with x = 0.04, respectively, sintered at 850°C.

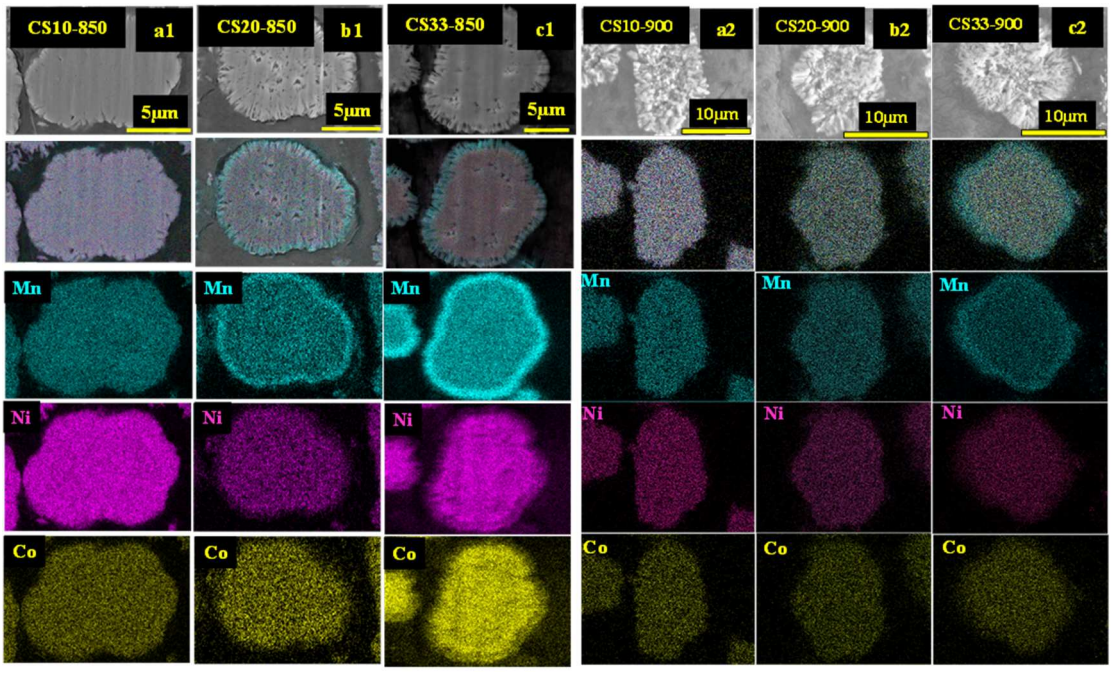

Figure 10.3 Cross-sectional SEM images and EDS maps of CS10-850-2 (1a1), CS20-850-2 (1b1) and CS33-850-2 (1c1), where the SEM samples were prepared using Argon Milling. Cross-sectional SEM images and EDS maps of CS10-900-2 (1a2), CS20-900-2 (1b2) and CS33-900-2 (1c2), where the SEM samples were prepared by hand polishing.

The SEM/EDS samples were prepared by cross-sectional argon ion polishing to achieve a smooth surface. Figures 10.3a1- c1 show a clear Mn-rich shell in CS20-850 and CS33-850 while no obvious Mn-rich shell was observed in CS10-850. Additionally, the Ni and Co content at the surface is lower than that in the core (lower brightness in the EDS maps) in CS33-850. Figures 10.3a2, 3b2 and 3c2 show the mapping results for the corresponding samples prepared 900°C. The SEM/EDS samples for 900°C samples were prepared by

hand polishing. There was no obvious Mn-rich shell maintained in CS20-900 as there was in CS20-850. A clear Mn-rich shell was detected in CS33-900, which indicates that sintering temperature along with shell thickness has a significant effect on the final composition profile of the lithium-rich CS samples due to interdiffusion of TM between the core and shell.

10.2.3 Interdiffusion in Ternary Systems

In order to further examine the interdiffusion phenomena in spherical CS particles with improved spatial resolution, a focused ion-beam (FIB) was used to cut a thin slice (~100 nm) through the center of a randomly selected particle of CS33-850-2 which was then studied with EDS in scanning transmission electron microscopy (STEM). Figure 10.4a shows a STEM image of the prepared slice. The yellow line shows the path where EDS point analyses were performed.

Figure 10.4b shows the measured concentration profiles with symbols, calculated profiles with solid lines and simulated initial concentration profiles with dashed lines respectively. The model based on Fick's law that describes the ternary diffusion phenomena used for the fitting is discussed in Chapter 3. Figure 10.4b shows that Ni moved from the core to the shell following the concentration gradient and that the Ni content on the surface changed from ~21% to ~30% during sintering, while Mn moved from the shell into the bulk, and the Mn content on the surface changed from ~57% to ~55%.

Surprisingly, the Co content near the interface on the core side is higher than its initial concentration while it is lower on the shell side. This indicates that Co moved into the core

from the shell, even though the initial Co contents in the core and shell were the same, in order to compensate for the increase of Ni content at the surface.

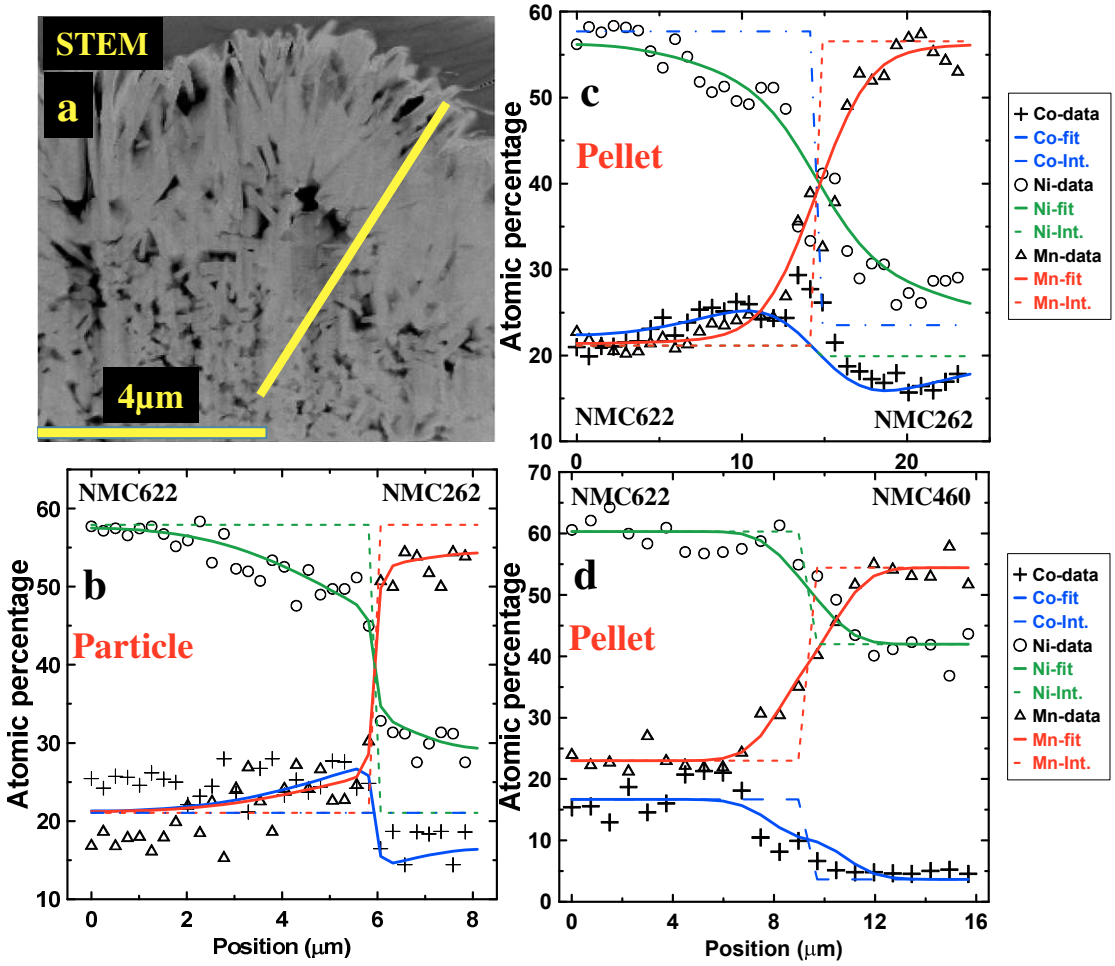

Figure 10.4 STEM image of the central slice of a CS33-850-2 particle prepared using FIB (a). The yellow line shows the path where EDS point analysis was performed. The concentration profile from the surface to the bulk detected with EDS is shown with symbols, and the simulation results are shown with lines (b). The measured concentration profiles of the NMC622 and NMC262 couple (c), and the measured concentration profile of the NMC622 and NMC460 couple (d) from laminar pellets. The symbols show the measured concentration profiles, solid lines show the calculated (-fit) profiles and dashed lines show the simulated initial concentration profiles (-Int.).

This is because the interdiffusion between Ni/Co is much faster than Ni/Mn and Co/Mn as discussed in Chapter 9. This suggests that the presence of Co in the shell can accelerate the diffusion of Ni from the core to the shell.

To further verify this phenomenon, laminar pellets as introduced in Chapter 9 with lithiated samples of a Ni:Mn:Co ratio of 6:2:2 (NMC622) and 2:6:2 (NMC262) or 4:6:0 (NMC460) on each side were designed and studied with EDS. Briefly, a pellet of NMC622 and a pellet of NMC262 or NMC460 were compressed together with high pressure, and then heated at 900^{o}C for 10 h. A concentration profile across the interface can then be measured on the polished cross-section of the pellet surface using SEM/EDS point scans. Figure 10.4c shows the measured concentration profile of the NMC622 and NMC262 couple, while Figure F.2 shows the SEM image and EDS mapping results near the interface. Figure 10.4c shows the same trend as discussed in the spherical case: Co moved from the shell to the core even there is almost no initial Co concentration gradient. Additionally, Figure 10.4d shows the measured concentration profile of the NMC622 and NMC460 couple, while Figure F.3 shows the SEM image and EDS mapping results near the interface. Figure 10.4d shows that the direction of the diffusion path of each element follows its initial concentration gradient.

Table 10.2 summarizes the calculated diffusion constants for each diffusion couple discussed in Figure 10.4. The average effective diffusion coefficients, which can be understood as the flux per unit concentration gradient as described in Chapter 3, of Mn, Ni and Co in the spherical CS particle (NMC622/NMC262) sintered at 850^{o}C (Figure 10.4b) are about $0.2*10^{-16}$, $0.49*10^{-16}$ and $-1.6*10^{-16}$ m^2/s, respectively and are about $1.6*10^{-16}$,

$5.5*10^{-16}$ and $-37.*10^{-16}$, respectively, for the pellet case heated at 900ºC (Figure 10.4c). The average effective diffusion coefficient of Ni is about three times of Mn in both cases.

Table 10.2 Calculated diffusion constants for the indicated diffusion couple, where the numbers 1, 2 and 3 in the interdiffusion coefficient correspond to Mn, Ni and Co, respectively.

Figure	Temp (°C)	Type	Material (a)	Material (b)	$*D_{12}^3$ (±0.05)	D_{12}^3 (±0.05)	D_{21}^3 (±0.05)	D_{22}^3 (±0.05)	D_{Mn}^{eff} (±0.05)	D_{Ni}^{eff} (±0.05)	D_{Co}^{eff} (±0.05)
4b	850	Sphere	NMC622	NMC262	-0.23	-0.49	0.54	1.12	0.20	0.49	#-1.57
4c	900	Pellet	NMC622	NMC262	0.16	-1.60	4.35	10.24	1.61	5.46	#-36.89^
4d	900	Pellet	NMC622	NMC460	0.02	-0.56	0.09	0.40	0.35	0.24	0.50

***** The unit for all the diffusion constant is 10^{-16} m^2/s. **#**The value is less meaningful since the denominator is close to 0.

The effective diffusion co-efficient for Co is negative because it moves opposite to the Ni motion. The absolute values of the diffusion coefficents in the spherical particles (10.4b) are much smaller than those in the pellet (10.4c), which can be attributed to higher temperature and different contacts between the core and shell materials in the pellet case (10.4c). The value of the average effective diffusion coefficient of Co is less meaningful in both cases (10.4b and 10.4c) since denominator is close to 0 (difference in the concentration of Co at the far end of core and shell structures) as shown in Equation (3.19). The average effective diffusion coefficients of Mn, Ni and Co in the NMC622/NMC460 pellet case (refer to Figure 10.4d) are about $0.4*10^{-16}$, $0.35*10^{-16}$ and $0.5*10^{-16}$ m^2/s respectively, where the average effective diffusion coefficient of Mn is slightly higher than Ni. This is because of the interdiffusion between Mn and both Ni and Co due to a relatively high Mn concentration gradient. These results show that ternary diffusion is a very

complex problem and has a strong dependence on the relative concentration of each element.

10.2.4 Voltage vs Capacity and Capacity vs Cycle Number

Figures 10.5a and 5b show the cell voltage as a function of specific capacity for CS10-1, CS10-2 and CS10-3 prepared at 850ºC and 900ºC respectively. The cells were tested between 2.5 - 4.4 V for 4 cycles, then 2.5 - 4.6V for 10 cycles, followed by 2.5 - 4.8V for 1 cycle, and 2.5 - 4.6 V for another 10 cycles with a current of 10 mA/g at 30ºC. Figures 5a1, a2 and a3 show a clear oxygen release plateau at ~4.5 V for the CS20 series heated at 850ºC regardless of the lithium content, which is attributed to the Li-rich and Mn-rich shell. Conversely, Figures 10.5b1, 10.5b2 and 10.5b3 show this plateau is barely noticeable in the CS20 series prepared at 900ºC, further confirming that there is virtually no Li-rich and Mn-rich shell remaining in the CS20-900 series as discussed in Figure 10.3.

Figures 10.5c and 10.5d show the specific capacity as a function of cycle number for CS20-1, CS20-2 and CS20-3 prepared at 850ºC and 900ºC respectively. The reversible capacities of CS20-850-1, CS20-850-2 and CS20-850-3 at 4.4 V are 190(2), 182(1) and 184(2) mAh/g respectively, while they are 196(2), 193(1) and 192(1) mAh/g for CS20-900-1, CS20-900-2 and CS20-900-3 respectively. The Li-rich and Mn-rich shell materials have low specific capacity at voltages below 4.4 V compared to the Ni-rich materials, hence, it is reasonable that the CS20-850 series show relatively lower capacities compared to the CS20-900 series, due to the presence of the Li-rich and Mn-rich shell. A reversible capacity of ~215(5) mAh/g for cells charged to 4.6 V was observed in both the 850 and 900ºC series. After the one charge to 4.8 V, a relatively rapid capacity fade rate was

observed for all the cells compared to the 3.0 – 4.6 V cycling before the 4.8 V charge, indicating there is little benefit to activating these lithium rich CS materials to 4.8 V.[29]

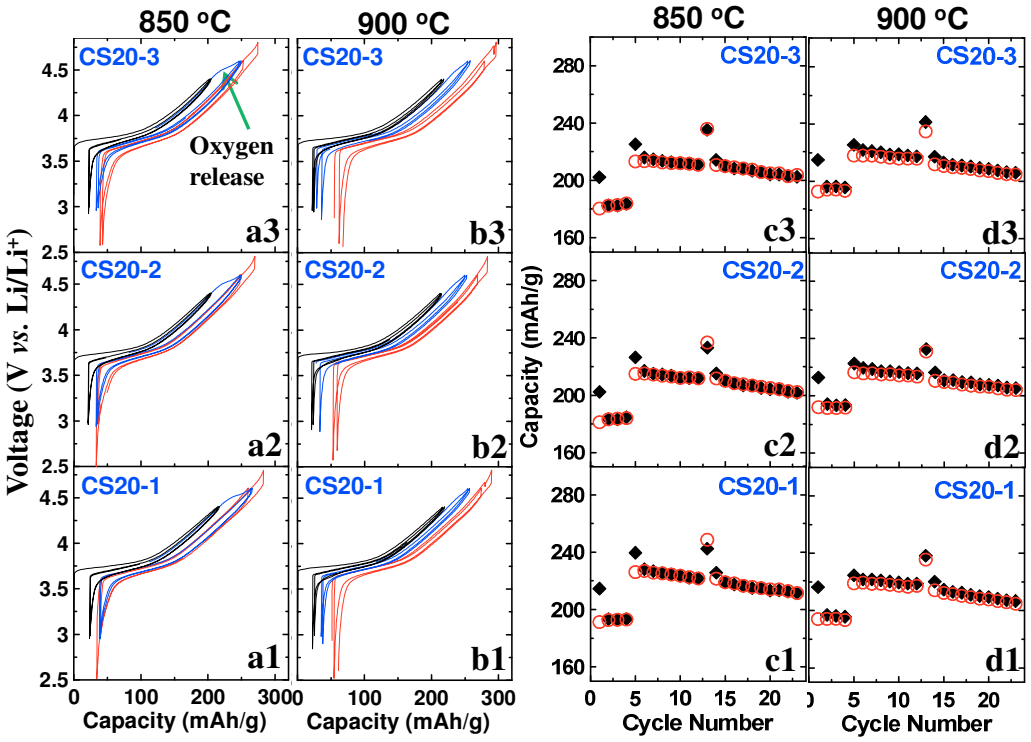

Figure 10.5 Cell voltage as a function of specific capacity for CS20-1 (a1), CS20-2 (a2) and CS20-3 (a3) prepared at 850°C respectively. Cell voltage as a function of specific capacity for CS20-1 (b1), CS20-2 (b2) and CS20-3 (b3) prepared at 900°C, respectively. Specific capacity as a function of cycle number for CS20-1 (c1), CS20-2 (c2) and CS20-3 (c3) prepared at 850°C respectively. Specific capacity as a function of cycle number for CS20-1 (d1), CS20-2 (d2) and CS20-3 (d3) prepared at 900°C respectively.

10.2.5 Summary of Reversible, Irreversible Capacity and Capacity Fade

Figures 10.6a and 10.6b show a summary of the reversible capacity as a function of target lithium content for cells made of the core (C), CS10, CS20 and CS33 series synthesized at

850 and 900ºC, respectively, when cycled between 2.5 – 4.4 V. Figure 10.6a shows that C-850-3 (x = 0.06), CS10-850-3, CS20-850-3, and CS30-850-3 have reversible capacities of ~200(3), 198(1), 185(2) and 167(3) mAh/g, respectively, whereas Figure 10.6b shows that C-900-3, CS10-900-3, CS20-900-3 and CS30-850-3 have reversible capacities of ~200(5), 196(1), 192(2) and 182(3) mAh/g respectively. In general, the reversible capacity decreases with increases of the initial shell thickness at both temperatures, due to the lower capacity of the Mn-rich shell. However, CS20 and CS33 sintered at 900ºC show higher capacity than the same materials sintered at 850 ºC because of a thinner Mn-rich shell created at higher temperature due to interdiffusion.

Figures 10.6c and 10.6d show a summary of the reversible capacity as a function of target lithium content for cells made of the core (C), CS10, CS20 and CS33 series synthesized at 850 and 900ºC, respectively, when cycled between 2.5 – 4.6 V. Figure 10.6c demonstrates that C-850-3, CS10-850-3, CS20-850-3 and CS33-850-3 have reversible capacities of 219(3), 220(3), 215(2) and 208(1) mAh/g respectively, where CS33-850-3 shows a relatively lower capacity, indicating that the shell thickness needs to be optimized. Figure 10.6d shows that the C-900-5, CS10-900-5, CS20-900-5 and CS33-900-5 have similar reversible capacities of ~218(3) mAh/g. Figures 10.6e and 10.6f show the capacity fade from the second cycle of the first 3 – 4.6 V charge to the last cycle (22^{nd} cycle) as a function of the target lithium content for cells made of the C, CS10, CS20 and CS33 series sintered at 850 and 900ºC respectively. Figures 10.6e and 10.6f show that the percentage of capacity fade decreases with increasing lithium content. Additionally, Figure 10.6e shows that the CS20-850 series has the least capacity fade compared to the others with the same target lithium content.

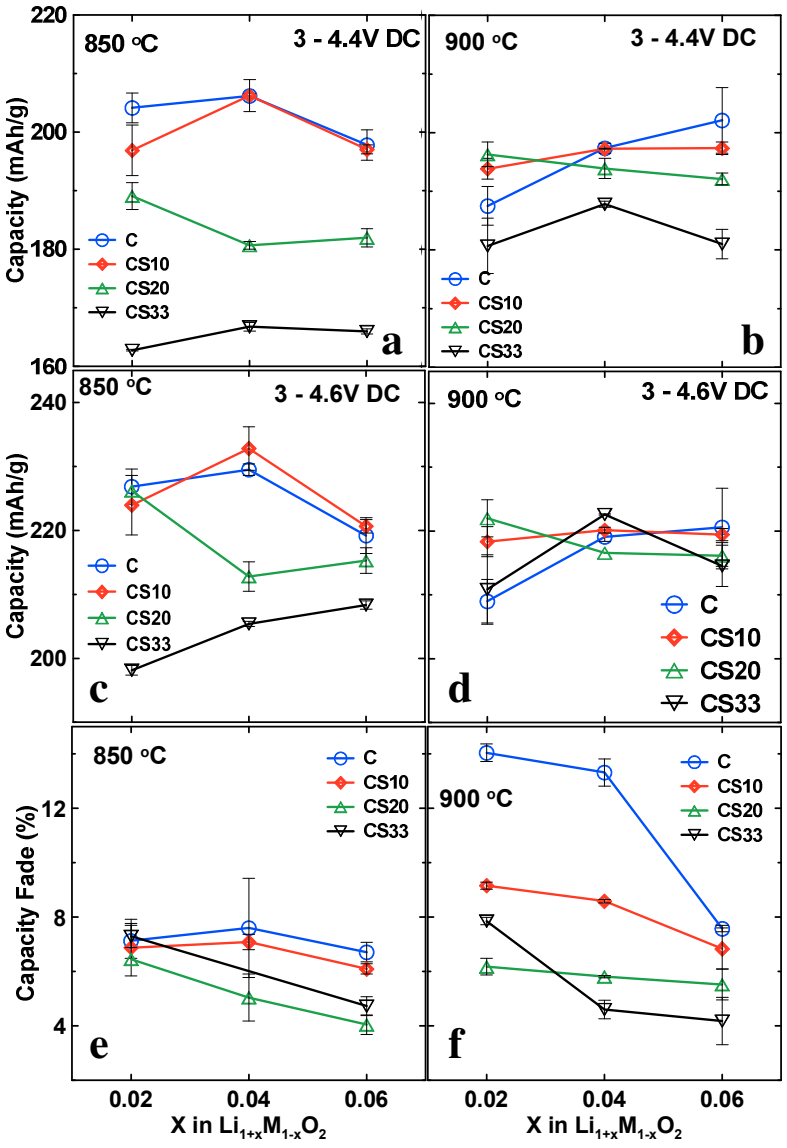

Figure 10.6 Summary of the reversible capacity as a function of target lithium content for cells made of the core (C), CS10, CS20 and CS33 series synthesized at 850°C (a) and 900°C (b), respectively, when cycled between 2.5 – 4.4 V. Summary of the reversible capacity as a function of target lithium content for cells made of the core (C), CS10, CS20 and CS33 series synthesized at 850°C (c) and 900°C (d), respectively, when cycled between 2.5 – 4.6 V. Capacity fade from the second cycle of the first 3 – 4.6 V charge to the last cycle (22nd cycle) as a function of the target lithium content for cells made of the C, CS10, CS20 and CS33 series sintered at 850°C (e) and 900°C (f) respectively.

The capacity fade of C-850-3, CS10-850-3, CS20-850-3 and S33-850-3 is about 6.7(3), 6.09(2), 4.04(1) and 4.7(3) % respectively, where CS33-850-3 shows more capacity fade compared to CS20-850-3. This result suggests that an optimized final shell thickness is required for the best performance. Figure 10.6f shows there is more capacity fade for the C, CS10 and CS20 series sintered at 900ºC compared to the same series made at 850ºC. This is possibly due to a higher Ni content on the surface of CS10-900 and CS20-900 because of interdiffusion. Moreover, the capacity fade of C-900-3, CS10-900-3, CS20-900-3 and CS33-900-3 is about 7.5(1), 6.8(1), 5.5(1) and 4.2(1) respectively, which decreases with increasing shell thickness. CS33-900-3 shows similar capacity fade compared to CS20-850-3. These results suggest that changing the sintering temperature will significantly affect the final shell thickness and the CS surface composition due to interdiffusion, which must be controlled for the best cell performance.

10.2.6 Full Cell Coin Cell Results

Samples CS20-850-3 and CS33-900-3 were selected from the 24 synthesized samples for testing in full cell Li-ion coin cells with graphite as the counter electrode using two different electrolytes. The control electrolyte was 1M $LiPF_6$ in 3:7 v:v ethylene carbonate (EC): diethylcarbonate (DEC). PES211 electrolyte is the control electrolyte plus 2% prop-1-ene-1,3-sultone (PES) + 1% methylene methane disulfonate + 1% tri(trimethylsilyl) phosphite (TTSPi) [133]. The cells were tested between 2.8 and 4.5 V using a rate of C/5 followed by one cycle of C/20 every 20 cycles. Figure 10.7 shows the capacity of the cells as a function of cycle number. Figure 10.7a shows that the cells made with CS33-900-3

and CS20-850-3 using control electrolyte have capacity retentions of ~75% and 80%, respectively, after 100 cycles.

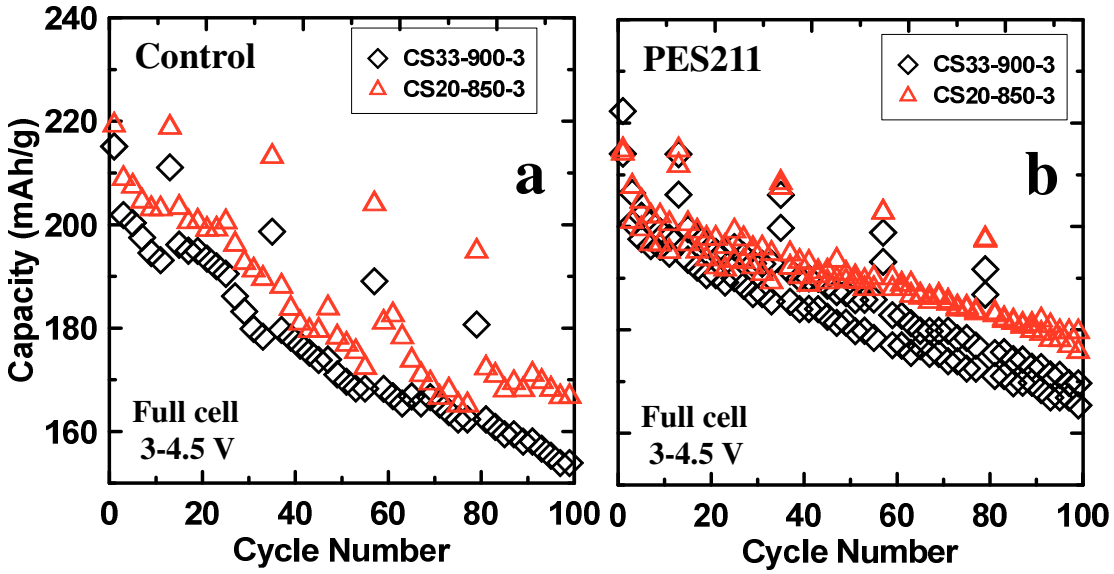

Figure 10.7 Capacity versus cycle number for coin-type full cells of CS positive materials with 20% shell prepared at 850ºC (CS20-850-3), 33% shell prepared at 900ºC (CS33-900-3) with control electrolyte (control) (a), and control electrolyte plus PES211 additive (PES211) (b). The cells were cycled between 2.8 – 4.5 V. The cycling was at C/5 with one C/20 cycle every 20 cycles.

The rate capability of the cells become worse with increasing cycling by comparing the capacity of the C/20 and C/5 cycles every 20 cycles, which suggests an impedance increase due to parasitic reactions with the electrolyte. Conversely, Figure 10.7b shows CS33-900-3 and CS20-850 have better capacity retention with PES211 electrolyte, which are ~85% and 90% respectively after 100 cycles. Additionally, there is no significant increase in the capacity difference between the C/20 and C/5 cycles every 10 cycles, indicating that the cell impedance is under control. This result suggests that it is necessary to combine both

surface modifications and electrolyte modification for cells operating at high voltages in order to achieve both high energy density and long life-time.

10.3 Conclusions

In summary, the effect of interdiffusion of transition metal atoms between the core and shell materials on the electrochemical performance was systematically studied by varying the shell thickness and sintering temperature. It was observed in SEM/EDS mapping that there is almost no Mn-rich shell maintained for CS samples with an initial shell content less than 10% when sintered at 850 ^{o}C and less than 20% when sintered at 900 ^{o}C. The concentration profile across the centre slice of a spherical CS particle was measured using STEM and the results were modeled based on Fick's law. The ternary interdiffusion constants were then determined and it was found that Co moved from the shell into the core even when there was no initial Co concentration gradient. This phenomenon was confirmed with the laminar pellet experiments, which also showed that the ternary diffusion coefficients have a strong dependence on the initial concentration of each element. Electrochemical testing showed that the CS20-850 series has an prolonged oxygen release plateau at ~4.5 V whereas it is not observed in the CS20-900 series which further confirms that the disappearance of the Mn-rich shell when heated at high temperatures due to significant interdiffusion. Analysis of the electrochemical testing results of cells made from the 24 synthesized samples strongly suggests that optimizing the sintering temperature and the initial shell thickness is essential for the best cell performance due to interdiffusion. Combining CS samples with electrolyte additives allowed a full cell charged to 4.5 V to deliver both high energy density and long-life time. Full cell coin cells

made of CS20-850-3 showed ~90% capacity retention after cycling to 4.5 V for 100 cycles. This study of interdiffusion in a ternary system of NMC materials may help design new generation positive electrode materials using CS and coating strategies.

CHAPTER 11. CONCLUSIONS AND FUTURE WORK

11.1 Structural and Electrochemical Studies of the Layered Li-Ni-Mn oxides

Through a systematic study of bulk samples near the layered region of the Li-Mn-Ni oxide system in Chapter 4, it was demonstrated that phase separation should be avoided and single phase samples should be prepared in order to obtain materials with the highest capacity. When samples were tested between 2.8 – 4.4 V (vs. Li), the maximum discharge capacity in each series was found in the sample that was close to the top of the single phase boundary (lowest Li/TM ratio) when the Mn/Ni ratio was equal or higher than 0.5, or in samples with a Li/TM ratio close to 1 when the Mn/Ni ratio was lower than 0.5. An increase in the Ni/Mn ratio leads to an increase of the specific discharge capacity when cycled to 4.4 V.

When samples were tested between 2.8 – 4.6 V (vs. Li), the maximum reversible capacity was found near the middle of the single phase region when the Mn/Ni ratio was lower than 0.5, while it was at the top (smallest lithium content) of the single phase region when Mn/Ni ratio was equal or higher than 0.5. This work was a baseline study for rational selection of core and shell compositions for core-shell materials.

11.2 Effect of Particle Size on Li-rich NMC

It was demonstrated in Chapter 5 that the particle size (secondary) of Li and Mn-rich materials can significantly affect the structural evolution during electrochemical testing

and the corresponding electrochemical performance. Lithium rich samples of $Li[Li_{0.23}(Ni_{0.2}Mn_{0.8})_{0.77}]O_2$ with different particle sizes were synthesized for *in-situ* XRD experiments. Two-phase (surface and bulk phases) behavior for a sample with big particles, and one-phase behaviour for a sample with small particles were observed at high potential. The surface phase of the sample with big particles had a similar structure to the sample with small particles at the end of the first charge. This suggests that oxygen loss occurred throughout the bulk of the sample with small particles while only at the surface of the large particle sample. This suggests that Li and Mn-rich layered oxides with large particle size should have smaller irreversible capacity and better cycle life. These should be prepared for the best electrochemical performance at the possible sacrifice of high rate performance. This work also clarified the confusion in the literature about whether these materials show a two-phase reaction or single-phase reaction at the top of charge during the oxygen release plateau.

11.3 Failure Mechanism of $LiNi_{0.8}Mn_{0.1}Co_{0.1}O_2$ (NMC811)

Electrochemical tests of NMC811/Li coin cells and NMC811/graphite pouch cells showed poor cycling performance for cells that were cycled to potentials greater than 4.2 V. Pouch cells containing control electrolyte with 2% VC showed much better capacity retention and lower ΔV than cells with PES211 when cycled to the same upper cut-off potential. Isothermal micro-calorimetry results showed that the parasitic heat flow increased as a function of potential, dramatically to above 4.2 V, for both 2% VC and PES211 cells. *In-situ* XRD measurement revealed a significant c-axis contraction from ~14.47 Å to ~13.96 Å during charging between 4.0 – 4.4 V. However, no significant changes of the

morphology of the electrodes or the atomic structure of the recovered active materials after 200 cycles were observed from SEM or *ex-situ* XRD results. The dramatic structural change of the active material during charge and discharge may not be the major contributor to the poor cycling performance of the cells cycled to higher potentials.

In order to further explore the failure mechanism of NMC811/graphite cells, the impact of electrolyte additives and cell upper cut-off voltage on the formation of a rocksalt surface layer in NMC811 cells was studied. For NMC811 cells tested to 4.3 V with control electrolyte, the rocksalt surface layer on the NMC811 particles doubled compared to the pristine material. However, when 2% PES or 2% VC were used in the cells the rocksalt surface layer did not increase in thickness compared to the pristine sample, even though dramatic capacity fade, worse than control cells, was observed in the case of cells with 2% PES. At least for NMC811/graphite cells with PES or VC additives, failure cannot only be ascribed to a growing rocksalt surface layer on the NMC811 particles. Instead, the parasitic reactions that arise from the interactions between the electrolytes and the highly reactive delithiated positive electrode surface at high potentials are suggested to be responsible for the failure of cells cycled above 4.2 V.

11.4 Synthesis and Understanding of Li-Rich Core-Shell Materials

Based on the studies from Chapters 4 – 7, lithium-rich core-shell materials that used Ni-rich material as the core and Mn-rich materials as the shell were proven to exploit the beneficial properties and minimize the poor properties of the materials in a hybrid system. The CS samples with optimal lithium content showed extremely low IRC, as well as high

capacity and excellent capacity retention. dQ/dV vs. V and delta V versus cycle number analysis showed that the CS samples had no serious impedance increase problems as well as very stable average discharge potentials. The Mn-rich shell can effectively protect the Ni-rich core from the reaction with the electrolyte while the Ni-rich core renders a high and stable average voltage. *In-situ* XRD measurements for layered Li-Ni-Mn-Co oxides with varied nickel content in Chapter 5 revealed that samples with higher nickel content showed much faster contraction of unit cell volume as a function of increasing cell potential. This suggests that the core-shell structure in particles with a nickel rich core and a Mn-rich shell should be stable during extended charge-discharge cycling.

EDS mapping results in Chapter 8 showed a clear Mn-rich, Co-rich shell and a Ni-rich core in the CS precursors. The Mn-rich shell was maintained in the lithiated samples after sintering at 900°C whereas the Co content was approximately uniform throughout the particles, which shows interdiffusion of transition metals between the core and shell phase during sintering. A series of experiments and simulations to measure the interdiffusivity of the cations in binary systems at various temperatures were designed and conducted. It was found that Ni^{3+}/Co^{3+} has the highest interdiffusion coefficient of ~4.7×10^{-12} cm^2/s, while Ni^{3+}/Mn^{4+} has the smallest at ~0.1×10^{-12} cm^2/s, both measured at 900°C. The similarity of the oxidation states and ionic radii of the diffusing ions significantly affects the activation energy and diffusivity. Simulations in spherical core-shell materials with varied initial shell thickness and shell composition were performed to guide core-shell materials design.

The effect of interdiffusion of transition metal atoms between the core and shell on the electrochemical performance was further studied by varying the shell thickness and sintering temperature. Ternary interdiffusion constants were then determined and it was found that Co moved from the shell into the core even when there was no initial Co concentration gradient. This phenomenon was confirmed with laminar pellet experiments, which also showed that the ternary diffusion coefficients have a strong dependence on the initial concentration of each element. Analysis of the electrochemical testing results of cells made from the 24 synthesized samples strongly suggests that optimizing the sintering temperature and the initial shell thickness is essential for the best cell performance due to interdiffusion. Combining CS samples with electrolyte additives allowed a full cell charged to 4.5 V to deliver both high energy density and long-life time.

11.5 Future Work

11.5.1 Systematic Structural and Electrochemical Studies of Li-Ni-Mn-Co Oxides with Low Cobalt Content within the Layered Region

Manthiriam's group reported studies of the effect of substitution of Co^{3+} for equal amounts of Mn^{4+} and Ni^{2+} in the lithium-rich layered oxide $Li[Li_{0.2}Ni_{0.2-x/2}Mn_{0.6-x/2}Co_x]O_2$ ($0 \leq x \leq 0.24$), and the effect of Mn content in the Ni-rich layered oxide $LiNi_{0.8-x}Co_{0.1}Mn_{0.1+x}O_2$ ($0.0 \leq x \leq 0.08$) on the electrochemical performance.[60,72] Additionally, Y.K. Sun's group reported studies of some regular NMC materials $Li[Ni_xCo_yMn_z]O_2$ (x= 1/3, 0.5, 0.6, 0.7, 0.8 and 0.85).[127] Chapter 2 of this thesis provided a systematic study about the structural and electrochemical properties of layered Li-Ni-Mn oxides. However, **systematic** studies

of the layered Li-Ni-Mn-Co oxides with varied lithium and transition metal composition have not been reported.

Recently, E. McCalla *et. al* and C. Brown *et. al* have established the composition – structure diagram of the Li-Ni-Mn-Co oxide system with 0, 10, 20 and 30% cobalt using combinatorial methods.[5,10] As a future work, it is necessary to map out the structural and electrochemical properties of bulk samples in the layered region of the Li-Ni-Mn-Co oxides, predicted by the structure – composition diagram. This allows a deep understanding of the effect of Ni, Mn and Co content as well as lithium content on electrochemical performance. This can be used to establish a database of layered NMC materials with low cobalt content, which provides both structural and electrochemical information, for the selection of possible commercial materials and for the rational selection of possible core and shell compositions in core-shell materials.

11.5.2 *In-situ* XRD and Neutron Diffraction Studies of the Structural Stability of Single Phase Layered $Li[Ni_xCo_yMn_z]O_2$

Chapter 5 and Chapter 6 provided structural stability studies of some NMC compositions using *in-situ* XRD and *ex-situ* XRD. Additionally, J. Li *et. al* reported an *in-situ* neutron powder diffraction (NPD) study of high voltage NMC442/graphite cells, which demonstrated that the structure of NMC442 was stable during high voltage hold at 4.7 V.[145] Such experiments using *in-situ* XRD or NPD should also be conducted on other NMC grades at voltages above 4.6 V (*vs.* Li) such as NMC111, NMC442, NMC532, NMC622 and NMC811 *etc*. The *in-situ* XRD results reported in Chapter 5 and Chapter 6 did not directly extract the percentage of Ni in the lithium layer as a function of lithium content or

voltage, which should be the focus of the future experiments. Futuremore, *in-situ* NPD may be able to provide more information about oxygen site occupancies (large difference in the neutron-scattering cross section between Ni^{28} and O^{16}), which is important for the evaluation of the structural stability of NMC during high voltage hold. The cells for *in-situ* XRD or NPD experiments should also be tested at a very low rate to avoid large lithium concentration gradients in the particles.

11.5.3 Anomalous X-ray Diffraction for the Studies of Cation Ordering in Li-rich NMC Materials

In normal powder X-ray diffraction, the scattering factor *f* for an atom is proportional to the number of electrons that it possesses at $2\theta = 0^{o}$. When the energy of the incident radiation is close to the absorption energies of the atom, the scattering factor undergoes a change due to the anomalous dispersion. This modification to the scattering factor is referred to as "anomalous scattering". Differences between scattering factors of Ni, Mn and Co can be magnified by tuning the wavelength before the K absorption edges of the transition metals using a synchrotron source.[275] In Chapter 2, Chapter 4 and Chapter 5, it was discussed that the lithium-rich NMC materials are single phase with cation ordering in the transition metal layer, since low charge and high charge cations ordered (long range) on a $\sqrt{3}a_{hex} \times \sqrt{3}a_{hex}$ superstructure. Experiments using anomalous scattering are useful to confirm this type of ordering in Li-rich NMC materials by tuning the wavelength before Ni, Mn and Co K-edge respectively.

11.5.4 Symmetric Cells and dV/dQ Analysis of the Aged NMC811/Graphite Cells

It was demonstrated in Chapter 7 that the polarization of the cells with 2% PES cycled to 4.3 V increased dramatically with cycle number. However, the diameter of the impedance semi-circle and the thickness of the rocksalt surface layer did not increase. In cells with 2% VC tested to 4.3 V, there was significant polarization growth and a dramatic increase in the diameter of the impedance semicircle, but no increase in the thickness of the rocksalt surface layer. In order to further confirm if polarization growth of the 2% PES and 2% VC cells is due to the R_{ct} growth of the positive electrodes, impedance of symmetric cells (coin type) that are constructed of two positive electrodes from the same cell after cycling should be measured. This will allow exclusion of the R_{ct} contribution from the negative electrode. Additionally, dV/dQ analysis of the cycled cells should also be studied to evaluate the active mass loss and the slippage of the positive and negative electrodes,[276] helping to further clarify the failure mechanism of NMC811/graphite cells. Moreover, the aged electrodes should be recovered and tested in half cells to make sure that there was no significant capacity loss due to structural degradation of the positive materials after long term cycling.

11.5.5 Minimizing Porosity of the Shell Layer in Li-rich Core-Shell Materials

The Li-rich core-shell materials demonstrated in Chapter 8 and 9 usually have a relatively porous surface compared to regular NMC materials, due to the properties of the Li and Mn-rich shell materials. Y. K. Sun's group showed numerous studies of full concentration gradient (FCG) NMC materials, which have a high Ni content in the core with increasing Mn content and decreasing Ni content from the core to the surface.[44,45,159–161] A

concentration gradient shell layer with gradually decreasing Ni content and increasing Mn content while maintaining the core content in the precursor may help improve the sintering properties of the shell. This is because the shell layer can have a relatively higher Ni content while maintaining a relatively high Mn content at the surface, which may have a higher degree of sintering at the same temperature.

11.5.6 Developing Effective Methods for Evaluation of Core-Shell Materials and other Surface Modification Techniques in Minimizing Electrolyte Oxidation

It was discussed in Chapter 9 that most reports on electrode material coatings and core-shell materials only report tests of materials in half cells with comparisons to uncoated materials using standard electrolytes.[39–42,150,198–200,272,273] However, results can be very different when coated/core-shell materials are tested in full cells and when electrolyte additives are used. J.R. Dahn's group has developed methods including ultra high precision coulometry (HPC)[16–19], *in-situ* gas analysis (AISGA)[230,231] and isothermal battery microcalorimetry *etc.*[94,246] to study electrolyte additives. These unique techniques can also allow one to study if a surface modification technique, including the core-shell strategy, can make a positive impact to the cell lifetime (full cells) in a short period. However, these techniques require the use of machine-made pouch cells, which have very good reproducibility. To make machine-made pouch cells, a minimum of ten kilograms of active material is required, which is not practical for laboratory studies. It is thus important to develop effective methods to evaluate if a core-shell material or coating, together with electrolyte additives, could make an improvement in the lifetime of a full cell using powders produced in lab scale.

R. Petibon[111], C. Burns *et. al*[277] and P. Ping *et. al*[278] studied additives in lithium ion batteries using electrochemical impedance spectroscopy (EIS) on symmetric cells. Electrolyte oxidation is more severe in the positive – positive symmetric cells compared to full cells with graphite negative electrodes, which allows one to obtain results in a short period of testing. This method can be used to study the interaction between the charged positive electrode materials and the electrolyte. By cycling a positive – positive symmetric cell, or observing the impedance growth of a symmetric cell stored at high temperatures (60 – 80^{o}C) as a function of time and voltage, it is possible to evaluate if the core-shell materials or a type of coating can mitigate electrolyte oxidation at high voltages.

Additionally, D. J. Xiong *et. al*[114] used pouch bag experiments to study the interaction between positive electrode materials and the electrolyte. The charged positive electrode with added electrolyte was stored in a pouch bag at high temperatures (60 – 80^{o}C). Gas chromatography mass spectroscopy (GCMS), EIS *etc.* were used to obtain an understanding of the positive electrode and electrolyte interactions. For laboratory powder materials, it is also possible to conduct pouch bag experiments by storing the pellets of charged powder materials or a charged electrode (coin cell size) in a pouch bag with electrolyte at high temperatures. GCMS can be used to study the gas products and other byproducts from electrolyte oxidation. Symmetric cells can also be used to study impedance growth of the electrodes taken from the pouch bags. Moreover, storage experiments of charged full coin cells which measure the open circuit voltage as a function of time can also allow one to study the effectiveness of a type of surface modification.[274] These studies allow the preliminary selection of new materials with varied surface

modification techniques, including core-shell materials presented in this thesis, before moving to larger scale studies.

REFERENCES

(1) Andre, D.; Kim, S.-J.; Lamp, P.; Lux, S. F.; Maglia, F.; Paschos, O.; Stiaszny, B. Future Generations of Cathode Materials: An Automotive Industry Perspective. *J. Mater. Chem. A* **2015**, *3*, 6709–6732.

(2) Dahn, J. R.; Ehrlich, G. M. Lithium-Ion Batteries. In *Linden's Handbook of Batteries*; New York : McGraw-Hill, 2011.

(3) Diouf, B.; Pode, R. Potential of Lithium-Ion Batteries: In Renewable Energy. *Renew. Energy* **2015**, *76*, 375–380.

(4) London Metal Exchange: Cobalt. Last accesed April 20, 2016 http://wwaw.lme.com/metals/minor-metals/cobalt/.

(5) Brown, C. R.; McCalla, E.; Watson, C.; Dahn, J. R. Combinatorial Study of the Li–Ni–Mn–Co Oxide Pseudoquaternary System for Use in Li–Ion Battery Materials Research. *ACS Comb. Sci.* **2015**, *17*, 381–391.

(6) Mccalla, E.; Rowe, A. W.; Camardese, J.; Dahn, J. R. The Role of Metal Site Vacancies in Promoting Li−Mn−Ni−O Layered Solid Solutions. *Chem. Mater.* **2013**, *25*, 2716–2721.

(7) McCalla, E.; Rowe, A. W.; Brown, C. R.; Hacquebard, L. R. P.; Dahn, J. R. How Phase Transformations during Cooling Affect Li-Mn-Ni-O Positive Electrodes in Lithium Ion Batteries. *J. Electrochem. Soc.* **2013**, *160*, A1134–A1138.

(8) Mccalla, E.; Lowartz, C. M.; Brown, C. R.; Dahn, J. R. Formation of Layered − Layered Composites in the Li−Co−Mn Oxide Pseudoternary System during Slow Cooling. *Chem. Mater.* **2013**, *25* , 912-918.

(9) McCalla, E.; Carey, G. H.; Dahn, J. R. Lithium Loss Mechanisms during Synthesis of Layered $Li_xNi_{2-x}O_2$ for Lithium Ion Batteries. *Solid State Ionics* **2012**, *219*, 11–19.

(10) McCalla, E.; Rowe, A. W.; Shunmugasundaram, R.; Dahn, J. R. Structural Study of the Li–Mn–Ni Oxide Pseudoternary System of Interest for Positive Electrodes of Li-Ion Batteries. *Chem. Mater.* **2013**, *25*, 989–999.

(11) Pillot, C. The Rechargeable Battery Market and Main Trends 2014-2025, Avicenne Energy. Last accesed Mar 9, 2015 http://www.avicenne.com/pdf/Fort_Lauderdale_Tutorial_C_Pillot_March2015.pdf.

(12) Li, J.; Downie, L. E.; Ma, L.; Qiu, W.; Dahn, J. R. Study of the Failure Mechanisms of $LiNi_{0.8}Mn_{0.1}Co_{0.1}O_2$ Cathode Material for Lithium Ion Batteries. *J. Electrochem. Soc.* **2015**, *162*, A1401–A1408.

(13) Whittingham, M. S. Lithium Batteries and Cathode Materials. *Chem. Rev.* **2004**, *104*, 4271–4301.

(14) Manthiram, A.; Knight, J. C.; Myung, S.-T.; Oh, S.-M.; Sun, Y.-K. Nickel-Rich and Lithium-Rich Layered Oxide Cathodes: Progress and Perspectives. *Adv. Energy Mater.* **2016**, *6*, 1501010.

(15) Chen, Z.; Lu, Z.; Dahn, J. R. Staging Phase Transitions in Li_xCoO_2. *J. Electrochem. Soc.* **2002**, *149*, A1604–A1609.

(16) Smith, A. J.; Burns, J. C.; Trussler, S.; Dahn, J. R. Precision Measurements of the Coulombic Efficiency of Lithium-Ion Batteries and of Electrode Materials for Lithium-Ion Batteries. *J. Electrochem. Soc.* **2010**, *157*, A196–A202.

(17) Smith, A. J.; Burns, J. C.; Dahn, J. R. A High Precision Study of the Coulombic Efficiency of Li-Ion Batteries. *Electrochem. Solid-State Lett.* **2010**, *13*, A177–A179.

(18) Smith, A. J.; Burns, J. C.; Zhao, X.; Xiong, D.; Dahn, J. R. A High Precision Coulometry Study of the SEI Growth in Li/Graphite Cells. *J. Electrochem. Soc.* **2011**, *158*, A447–A452.

(19) Smith, A. J.; Burns, J. C.; Xiong, D.; Dahn, J. R. Interpreting High Precision Coulometry Results on Li-Ion Cells. *J. Electrochem. Soc.* **2011**, *158*, A1136–A1142.

(20) Rowe, A. W.; Camardese, J.; McCalla, E.; Dahn, J. R. High Precision Coulometry Studies of Single-Phase Layered Compositions in the Li-Mn-Ni-O System. *J. Electrochem. Soc.* **2014**, *161*, A1189–A1193.

(21) Wang, D. Y.; Xia, J.; Ma, L.; Nelson, K. J.; Harlow, J. E.; Xiong, D.; Downie, L. E.; Petibon, R.; Burns, J. C.; Xiao, A.; Lamanna, W. M.; Dahn, J. R. A Systematic Study of Electrolyte Additives in $Li[Ni_{1/3}Mn_{1/3}Co_{1/3}]O_2$ (NMC)/Graphite Pouch Cells. *J. Electrochem. Soc.* **2014**, *161*, A1818–A1827.

(22) Wang, D. Y.; Sinha, N. N.; Burns, J. C.; Petibon, R.; Dahn, J. R. A High Precision Study of the Electrolyte Additives Vinylene Carbonate, Vinyl Ethylene Carbonate and Lithium Bis(oxalate)borate in $LiCoO_2$/graphite Pouch Cells. *J. Power Sources* **2014**, *270*, 68–78.

(23) Wang, D. Y.; Xiao, A.; Wells, L.; Dahn, J. R. Effect of Mixtures of Lithium Hexafluorophosphate ($LiPF_6$) and Lithium Bis(fluorosulfonyl)imide (LiFSI) as Salts in $Li[Ni_{1/3}Mn_{1/3}Co_{1/3}]O_2$/Graphite Pouch Cells. *J. Electrochem. Soc.* **2014**, *162*, A169–A175.

(24) Xu, K. Electrolytes and Interphases in Li-Ion Batteries and Beyond. *Chem. Rev.* **2014**, *114*, 11503–11618.

(25) Burns, J. C.; Kassam, A.; Sinha, N. N.; Downie, L. E.; Solnickova, L.; Way, B. M.; Dahn, J. R. Predicting and Extending the Lifetime of Li-Ion Batteries. *J. Electrochem. Soc.* **2013**, *160*, A1451–A1456.

(26) Camardese, J.; Li, J.; Abarbanel, D. W.; Wright, A. T. B.; Dahn, J. R. The Effect of Lithium Content and Core to Shell Ratio on Structure and Electrochemical Performance of Core-Shell $Li_{(1+x)}[Ni_{0.6}Mn_{0.4}]_{(1-x)}O_2 \cdot Li_{(1+y)}[Ni_{0.2}Mn_{0.8}]_{(1-y)}O_2$ Positive Electrode Materials. *J. Electrochem. Soc.* **2014**, *162*, A269–A277.

(27) Myung, S.-T.; Noh, H.-J.; Yoon, S.-J.; Lee, E.-J.; Sun, Y.-K. Progress in High-Capacity Core–Shell Cathode Materials for Rechargeable Lithium Batteries. *J. Phys. Chem. Lett.* **2014**, *5*, 671–679.

(28) Ju, J.; Lee, E.; Yoon, C. S.; Myung, S.; Sun, Y. Optimization of Layered Cathode Material with Full Concentration Gradient for Lithium-Ion Batteries. *J. Phys. Chem. C* **2013**, *118*, 175–182.

(29) Li, J.; Camardese, J.; Glazier, S.; Dahn, J. R. Structural and Electrochemical Study of the Li − Mn − Ni Oxide System within the Layered Single Phase Region. *Chem. Mater.* **2014**, *26*, 7059–7066.

(30) Lu, Z.; MacNeil, D. D.; Dahn, J. R. Layered $Li[Ni_xCo_{1-2x}Mn_x]O_2$ Cathode Materials for Lithium-Ion Batteries. *Electrochem. Solid-State Lett.* **2001**, *4*, A200–A203.

(31) Nelson, K. J.; Abarbanel, D. W.; Xia, J.; Lu, Z.; Dahn, J. R. Effects of Upper Cutoff Potential on $LaPO_4$-Coated and Uncoated $Li[Ni_{0.42}Mn_{0.42}Co_{0.16}]O_2$ /Graphite Pouch Cells. *J. Electrochem. Soc.* **2015**, *163*, A272–A280.

(32) Xia, J.; Sinha, N. N.; Chen, L. P.; Kim, G. Y.; Xiong, D. J.; Dahn, J. R. Study of Methylene Methanedisulfonate as an Additive for Li-Ion Cells. *J. Electrochem. Soc.* **2013**, *161*, A84–A88.

(33) Xia, J.; Ma, L.; Aiken, C. P.; Nelson, K. J.; Chen, L. P.; Dahn, J. R. Comparative Study on Prop-1-Ene-1,3-Sultone and Vinylene Carbonate as Electrolyte Additives for $Li(Ni_{1/3}Mn_{1/3}Co_{1/3})O_2$/Graphite Pouch Cells. *J. Electrochem. Soc.* **2014**, *161*, A1634–A1641.

(34) Ma, L.; Xia, J.; Dahn, J. R. Improving the High Voltage Cycling of $Li[Ni_{0.42}Mn_{0.42}Co_{0.16}]O_2$ (NMC442)/Graphite Pouch Cells Using Electrolyte Additives. *J. Electrochem. Soc.* **2014**, *161*, A2250–A2254.

(35) Xia, J.; Sinha, N. N.; Chen, L. P.; Dahn, J. R. A Comparative Study of a Family of Sulfate Electrolyte Additives. *J. Electrochem. Soc.* **2013**, *161*, A264–A274.

(36) Xia, J.; Nelson, K. J.; Sun, J.; Hill, I. G.; Dahn, J. R. Effect of Sulfate Electrolyte Additives on $LiNi_{1/3}Mn_{1/3}Co_{1/3}O_2$/Graphite Pouch Cell Lifetime : Correlation between XPS Surface Studies and Electrochemical Test Results. *J. Phys. Chem. C* **2014**, *118*, 29608–29622.

(37) Nelson, K. J.; Xia, J.; Dahn, J. R. Studies of the Effect of Varying Prop-1-Ene-1,3-Sultone Content in Lithium Ion Pouch Cells. *J. Electrochem. Soc.* **2014**, *161*, A1884–A1889.

(38) Burns, J. C.; Petibon, R.; Nelson, K. J.; Sinha, N. N.; Kassam, A.; Way, B. M.; Dahn, J. R. Studies of the Effect of Varying Vinylene Carbonate (VC) Content in Lithium Ion Cells on Cycling Performance and Cell Impedance. *J. Electrochem. Soc.* **2013**, *160*, A1668–A1674.

(39) Kim, H.-S.; Kim, Y.; Kim, S.-I.; Martin, S. W. Enhanced Electrochemical Properties of $LiNi_{1/3}Co_{1/3}Mn_{1/3}O_2$ Cathode Material by Coating with $LiAlO_2$ Nanoparticles. *J. Power Sources* **2006**, *161*, 623–627.

(40) Kim, Y.; Kim, H. S.; Martin, S. W. Synthesis and Electrochemical Characteristics of Al_2O_3-Coated $LiNi_{1/3}Co_{1/3}Mn_{1/3}O_2$ Cathode Materials for Lithium Ion Batteries. *Electrochim. Acta* **2006**, *52*, 1316–1322.

(41) Sun, Y.-K.; Lee, M.-J.; Yoon, C. S.; Hassoun, J.; Amine, K.; Scrosati, B. The Role of AlF_3 Coatings in Improving Electrochemical Cycling of Li-Enriched Nickel-Manganese Oxide Electrodes for Li-Ion Batteries. *Adv. Mater.* **2012**, *24*, 1192–1196.

(42) Liu, H.; Qian, D.; Verde, M. G.; Zhang, M.; Baggetto, L.; An, K.; Chen, Y.; Carroll, K. J.; Lau, D.; Chi, M.; Veith, G. M.; Meng, Y. S. Understanding the Role of NH_4F and Al_2O_3 Surface Co-Modification on Lithium-Excess Layered Oxide $Li_{1.2}Ni_{0.2}Mn_{0.6}O_2$. *ACS Appl. Mater. Interfaces* **2015**, *7*, 19189–19200.

(43) Wu, F.; Zhang, X.; Zhao, T.; Li, L.; Xie, M.; Chen, R. Multifunctional $AlPO_4$ Coating for Improving Electrochemical Properties of Low-Cost $Li[Li_{0.2}Fe_{0.1}Ni_{0.15}Mn_{0.55}]O_2$ Cathode Materials for Lithium-Ion Batteries. *ACS Appl. Mater. Interfaces* **2015**, *7*, 3773–3781.

(44) Noh, H.-J.; Myung, S.-T.; Jung, H.-G.; Yashiro, H.; Amine, K.; Sun, Y.-K. Formation of a Continuous Solid-Solution Particle and Its Application to Rechargeable Lithium Batteries. *Adv. Funct. Mater.* **2013**, *23*, 1028–1036.

(45) Sun, Y.-K.; Chen, Z.; Noh, H.-J.; Lee, D.-J.; Jung, H.-G.; Ren, Y.; Wang, S.; Yoon, C. S.; Myung, S.-T.; Amine, K. Nanostructured High-Energy Cathode Materials for Advanced Lithium Batteries. *Nat. Mater.* **2012**, *11*, 942–947.

(46) Qian, D.; Hagh, N. M.; Meng, Y. S. Insight into Designing High-Energy, High-Power Cathode Material for Lithium Ion Batteries. *ECS Electrochem. Lett.* **2014**, *3*, A72–A75.

(47) McKinnon, W. R. Insertion Elecrodes I: Atomic and Electronic Structure of the Hosts and Their Insertion Compounds. In *Solid State Electrochemistry*; Bruce, P. G., Ed.; Cambridage University Press, 1997.

(48) Goodenough, J. B.; Park, K.-S. S. The Li-Ion Rechargeable Battery: A Perspective. *J. Am. Chem. Soc.* **2013**, *135*, 1167–1176.

(49) Ohzuku, T.; Brodd, R. J. An Overview of Positive-Electrode Materials for Advanced Lithium-Ion Batteries. *J. Power Sources* **2007**, *174*, 449–456.

(50) Goodenough, J. B.; Kim, Y. Challenges for Rechargeable Batteries. *J. Power Sources* **2011**, *196*, 6688–6694.

(51) Dahn, J.; Fong, R.; Spoon, M. Suppression of Staging in Lithium-Intercalated Carbon by Disorder in the Host. *Phyical Rev. B* **1990**, *42*, 6424.

(52) Chen, Z.; Lu, Z.; Dahn, J. R. Staging Phase Transitions in Li_xCoO_2. *J. Electrochem. Soc.* **2002**, *149*, A1604–A1609.

(53) Brandt, K. Historical Development of Secondary Lithium Batteries. *Solid State Ionics* **1994**, *69*, 173–183.

(54) Sun, Y.-K.; Lee, D.-J.; Lee, Y. J.; Chen, Z.; Myung, S.-T. Cobalt-Free Nickel Rich Layered Oxide Cathodes for Lithium-Ion Batteries. *ACS Appl. Mater. Interfaces* **2013**, *5*, 11434–11440.

(55) Jo, C.-H.; Cho, D.-H.; Noh, H.-J.; Yashiro, H.; Sun, Y.-K.; Myung, S. T. An Effective Method to Reduce Residual Lithium Compounds on Ni-Rich $Li[Ni_{0.6}Co_{0.2}Mn_{0.2}]O_2$ Active Material Using a Phosphoric Acid Derived Li_3PO_4 Nanolayer. *Nano Res.* **2014**, *8*, 1464-1479.

(56) Lee, S.-H.; Yoon, C. S.; Amine, K.; Sun, Y.-K. Improvement of Long-Term Cycling Performance of $Li[Ni_{0.8}Co_{0.15}Al_{0.05}]O_2$ by AlF_3 Coating. *J. Power Sources* **2013**, *234*, 201–207.

(57) Hwang, I.; Lee, C. W.; Kim, J. C.; Yoon, S. Particle Size Effect of Ni-Rich Cathode Materials on Lithium Ion Battery Performance. *Mater. Res. Bull.* **2012**, *47*, 73–78.

(58) Hwang, S.; Kim, D. H.; Chung, K. Y.; Chang, W. Understanding Local Degradation of Cycled Ni-Rich Cathode Materials at High Operating Temperature for Li-Ion Batteries. *Appl. Phys. Lett.* **2014**, *105*, 103901.

(59) Cho, D.-H.; Jo, C.-H.; Cho, W.; Kim, Y.-J.; Yashiro, H.; Sun, Y.-K.; Myung, S.-T. Effect of Residual Lithium Compounds on Layered Ni-Rich $Li[Ni_{0.7}Mn_{0.3}]O_2$. *J. Electrochem. Soc.* **2014**, *161*, A920–A926.

(60) Zheng, J.; Kan, W. H.; Manthiram, A. Role of Mn Content on the Electrochemical Properties of Nickel-Rich Layered $LiNi_{(0.8-x)}Co_{0.1}Mn_{(0.1+x)}O_2$ ($0.0 \leq x \leq 0.08$) Cathodes for Lithium-Ion Batteries. *ACS Appl. Mater. Interfaces* **2015**, *7*, 6926–6934.

(61) Kang, K. S.; Choi, S.; Song, J.; Woo, S.-G.; Jo, Y. N.; Choi, J.; Yim, T.; Yu, J.-S.; Kim, Y.-J. Effect of Additives on Electrochemical Performance of Lithium Nickel Cobalt Manganese Oxide at High Temperature. *J. Power Sources* **2014**, *253*, 48–54.

(62) Lee, W. J.; Prasanna, K.; Jo, Y. N.; Kim, K. J.; Kim, H. S.; Lee, C. W. Depth Profile Studies on Nickel Rich Cathode Material Surfaces after Cycling with an Electrolyte Containing Vinylene Carbonate at Elevated Temperature. *Phys. Chem. Chem. Phys.* **2014**, *16*, 17062–17071.

(63) Nurpeissova, A.; Park, D.-I.; Kim, S.-S.; Sun, Y.-K. Epicyanohydrin as an Interface Stabilizer Agent for Cathodes of Li-Ion Batteries. *J. Electrochem. Soc.* **2015**, *163*, A171–A177.

(64) Yim, T.; Kang, K. S.; Mun, J.; Lim, S. H.; Woo, S. G.; Kim, K. J.; Park, M. S.; Cho, W.; Song, J. H.; Han, Y. K.; Yu, J. S.; Kim, Y. J. Understanding the Effects of a Multi-Functionalized Additive on the Cathode-Electrolyte Interfacial Stability of Ni-Rich Materials. *J. Power Sources* **2016**, *302*, 431–438.

(65) Martha, S. K.; Nanda, J.; Veith, G. M.; Dudney, N. J. Electrochemical and Rate Performance Study of High-Voltage Lithium-Rich Composition: $Li_{1.2}Mn_{0.525}Ni_{0.175}Co_{0.1}O_2$. *J. Power Sources* **2012**, *199*, 220–226.

(66) Jarvis, K. A.; Deng, Z.; Allard, L. F.; Manthiram, A.; Ferreira, P. J. Atomic Structure of a Lithium-Rich Layered Oxide Material for Lithium-Ion Batteries: Evidence of a Solid Solution. *Chem. Mater.* **2011**, *23*, 3614–3621.

(67) Lee, E.-S.; Manthiram, A. Smart Design of Lithium-Rich Layered Oxide Cathode Compositions with Suppressed Voltage Decay. *J. Mater. Chem. A* **2014**, *2*, 3932–3939.

(68) Gu, M.; Belharouak, I.; Zheng, J.; Wu, H.; Xiao, J.; Genc, A.; Amine, K.; Thevuthasan, S.; Baer, D. R.; Zhang, J.; Browning, N. D.; Liu, J.; Wang, C. Formation of the Spinel Phase in the Layered Composite Cathode Used in Li-Ion Batteries. *ACS Nano* **2013**, *7*, 760–767.

(69) Jarvis, K. A.; Deng, Z.; Allard, L. F.; Manthiram, A.; Ferreira, P. J. Understanding Structural Defects in Lithium-Rich Layered Oxide Cathodes. *J. Mater. Chem.* **2012**, *22*, 11550–11555.

(70) Cheng, F.; Chen, J.; Zhou, H.; Manthiram, A. Structural and Electrochemical Characterization of $(NH4)_2HPO_4$-Treated Lithium-Rich Layered $Li_{1.2}Ni_{0.2}Mn_{0.6}O_2$ Cathodes for Lithium-Ion Batteries. *J. Electrochem. Soc.* **2013**, *160*, A1661–A1667.

(71) Deng, Z. Q.; Manthiram, A. Influence of Cationic Substitutions on the Oxygen Loss and Reversible Capacity of Lithium-Rich Layered Oxide Cathodes. *J. Phys. Chem. C* **2011**, *115*, 7097–7103.

(72) Xiang, X.; Knight, J. C.; Li, W.; Manthiram, A. Understanding the Effect of Co^{3+} Substitution on the Electrochemical Properties of Lithium-Rich Layered Oxide Cathodes for Lithium-Ion Batteries. *J. Phys. Chem. C* **2014**, 118, 21826–21833.

(73) Fell, C. R.; Chi, M.; Meng, Y. S.; Jones, J. L. In Situ X-Ray Diffraction Study of the Lithium Excess Layered Oxide Compound $Li[Li_{0.2}Ni_{0.2}Mn_{0.6}]O_2$ during Electrochemical Cycling. *Solid State Ionics* **2012**, *207*, 44–49.

(74) Fell, C. R.; Qian, D.; Carroll, K. J.; Chi, M.; Jones, J. L.; Meng, Y. S. Correlation Between Oxygen Vacancy, Microstrain, and Cation Distribution in Lithium-Excess Layered Oxides During the First Electrochemical Cycle. *Chem. Mater.* **2013**, *25*, 1621–1629.

(75) Qian, D.; Xu, B.; Chi, M.; Meng, Y. S. Uncovering the Roles of Oxygen Vacancies in Cation Migration in Lithium Excess Layered Oxides. *Phys. Chem. Chem. Phys.* **2014**, *16*, 14665–14668.

(76) Xu, B.; Qian, D.; Wang, Z.; Meng, Y. S. Recent Progress in Cathode Materials Research for Advanced Lithium Ion Batteries. *Mater. Sci. Eng. R Reports* **2012**, *73*, 51–65.

(77) Lu, Z.; Beaulieu, L. Y.; Donaberger, R. A.; Thomas, C. L.; Dahn, J. R. Synthesis, Structure, and Electrochemical Behavior of $Li[Ni_xLi_{1/3-2x/3}Mn_{2/3-x/3}]O_2$. *J. Electrochem. Soc.* **2002**, *149*, A778–A791.

(78) Lu, Z.; Dahn, J. R. Understanding the Anomalous Capacity of $Li/Li[Ni_xLi_{1/3-2x/3}Mn_{2/3-x/3}]O_2$ Cells Using In Situ X-Ray Diffraction and Electrochemical Studies. *J. Electrochem. Soc.* **2002**, *149*, A815–A822.

(79) Lu, Z.; MacNeil, D. D.; Dahn, J. R. Layered Cathode Materials $Li[Ni_xLi_{1/3-2x/3}Mn_{2/3-x/3}]O_2$ for Lithium-Ion Batteries. *Electrochem. Solid-State Lett.* **2001**, *4*, A191–A194.

(80) Reimers, J. N.; Dahn, J. R. Electrochemical In Situ X-Ray Diffraction Studies of Lithium Intercalation in $LixCoO_2$. *J. Electrochem. Soc.* **1992**, *139*, 2091–2096.

(81) McCalla, E.; Li, J.; Rowe, A. W.; Dahn, J. R. The Negative Impact of Layered-Layered Composites on the Electrochemistry of Li-Mn-Ni-O Positive Electrodes for Lithium-Ion Batteries. *J. Electrochem. Soc.* **2014**, *161*, A606–A613.

(82) Mukai, K.; Kishida, Y.; Nozaki, H.; Dohmae, K. Structural Phase Transition from Rhombohedral ($R\bar{3}m$) to Monoclinic (C_2/m) Symmetry in Lithium Overstoichiometric $Li_{1+\delta}Co_{1-\delta}O_{2-\delta}$. *Chem. Mater.* **2013**, *25*, 2828–2837.

(83) Boulineau, A.; Croguennec, L.; Delmas, C.; Weill, F. Structure of Li_2MnO_3 with Different Degrees of Defects. *Solid State Ionics* **2010**, *180*, 1652–1659.

(84) Boulineau, A.; Croguennec, L.; Delmas, C.; Weill, F. Reinvestigation of Li_2MnO_3 Structure: Electron Diffraction and High Resolution TEM. *Chem. Mater.* **2009**, *21*, 4216–4222.

(85) Genevois, C.; Koga, H.; Croguennec, L.; Ménétrier, M.; Delmas, C.; Weill, F. Insight into the Atomic Structure of Cycled Lithium-Rich Layered Oxide $Li_{1.20}Mn_{0.54}Co_{0.13}Ni_{0.13}O_2$ Using HAADF STEM and Electron Nanodiffraction. *J. Phys. Chem. C* **2015**, *119*, 75–83.

(86) Koga, H.; Croguennec, L.; Menetrier, M.; Douhil, K.; Belin, S.; Bourgeois, L.; Suard, E.; Weill, F.; Delmas, C. Reversible Oxygen Participation to the Redox Processes Revealed for $Li_{1.20}Mn_{0.54}Co_{0.13}Ni_{0.13}O_2$. *J. Electrochem. Soc.* **2013**, *160*, A786–A792.

(87) Koga, H.; Croguennec, L.; Mannessiez, P.; Bourgeois, L.; Duttine, M.; Suard, E.; Delmas, C. $Li_{1.20}Mn_{0.54}Co_{0.13}Ni_{0.13}O_2$ with Different Particle Sizes as Attractive Positive Electrode Materials for Lithium‐Ion Batteries: Insights into Their Structure. *J. Phys. Chem. C* **2012**, *116*, 13497–13506.

(88) Koga, H.; Croguennec, L.; Ménétrier, M.; Mannessiez, P.; Weill, F.; Delmas, C. Different Oxygen Redox Participation for Bulk and Surface: A Possible Global Explanation for the Cycling Mechanism of $Li_{1.20}Mn_{0.54}Co_{0.13}Ni_{0.13}O_2$. *J. Power Sources* **2013**, *236*, 250–258.

(89) Weill, F.; Tran, N.; Croguennec, L.; Delmas, C. Cation Ordering in the Layered $Li_{1+x}(Ni_{0.425}Mn_{0.425}Co_{0.15})_{1-x}O_2$ Materials (x=0 and 0.12). *J. Power Sources* **2007**, *172*, 893–900.

(90) Atlung, S.; West, K.; Jacobsen, T. Dynamic Aspects of Solid Solution Cathodes for Electrochemical Power Sources. *J. Electrochem. Soc.* **1979**, *126*,1311–1321.

(91) Wang, Y.; Jiang, J.; Dahn, J. R. The Reactivity of Delithiated $Li(Ni_{1/3}Co_{1/3}Mn_{1/3})O_2$, $Li(Ni_{0.8}Co_{0.15}Al_{0.05})O_2$ or $LiCoO_2$ with Non-Aqueous Electrolyte. *Electrochem. commun.* **2007**, *9*, 2534–2540.

(92) Jiang, J.; Eberman, K. W.; Krause, L. J.; Dahn, J. R. Structure, Electrochemical Properties, and Thermal Stability Studies of Cathode Materials in the $xLiMn_{1/2}Ni_{1/2}O_2 \cdot yLiCoO_2 \cdot zLi[Li_{1/3}Mn_{2/3}]O_2$ Pseudoternary System (x+y+z = 1). *J. Electrochem. Soc.* **2005**, *152*, A1879–A1889.

(93) Ma, L.; Xia, J.; Xia, X.; Dahn, J. R. The Impact of Vinylene Carbonate, Fluoroethylene Carbonate and Vinyl Ethylene Carbonate Electrolyte Additives on Electrode/Electrolyte Reactivity Studied Using Accelerating Rate Calorimetry. *J. Electrochem. Soc.* **2014**, *161*, A1495–A1498.

(94) Downie, L. E.; Hyatt, S. R.; Wright, A. T. B.; Dahn, J. R. Determination of the Time Dependent Parasitic Heat Flow in Lithium Ion Cells Using Isothermal Microcalorimetry. *J. Phys. Chem. C* **2014**, *118*, 29533–29541.

(95) Chiang, Y.-M.; Jang, Y.-I.; Wang, H.; Huang, B.; Sadoway, D. R.; and Ye, P. Synthesis of $LiCoO_2$ by Decomposition and Intercalation of Hydroxides. *J. Electrochem. Soc.* **1998**, *145*, 887–891.

(96) Huang, B.; Jang, Y.; Chiang, Y.; Sadoway, D. R. Electrochemical Evaluation of $LiCoO_2$ Synthesized by Decomposition and Intercalation of Hydroxides for Lithium-Ion Battery Applications. *J. Appl. Electrochem.* **1998**, *28*, 1365–1369.

(97) Ariyoshi, K.; Iwata, E.; Kuniyoshi, M.; Wakabayashi, H.; Ohzuku, T. Lithium Aluminum Manganese Oxide Having Spinel-Framework Structure for Long-Life Lithium-Ion Batteries. *Electrochem. Solid-State Lett.* **2006**, *9*, A557–A560.

(98) Bommel, A. Van; Dahn, J. R. Analysis of the Growth Mechanism of Coprecipitated Spherical and Dense Nickel , Manganese , and Cobalt-Containing Hydroxides in the Presence of Aqueous Ammonia. *Chem. Mater.* **2009**, *21*, 1500–1503.

(99) Bommel, A. Van; Dahn, J. R. Synthesis of Spherical and Dense Particles of the Pure Hydroxide Phase $Ni_{1/3}Mn_{1/3}Co_{1/3}(OH)_2$. *J. Electrochem. Soc.* **2009**, *156*, A362–A365.

(100) Zeinalipour-Yazdi, C. D. *Structure and Symmetry of Graphite*; Taylor & Francis Group, LLC, 2008.

(101) Dahn, J. R. Phase Diagram of Li_xC_6 J. *Physical Rev. B* **1991**, *44*,9170–9177.

(102) Zheng, T.; Reimers, J. N.; Dahn, J. R. Effect of Turbostratic Disorder in Graphitic Carbon Hosts on the Intercalation of Lithium. *Physical Rev. B* **1995**, *51*, 734–742.

(103) Zheng, T.; Dahn, J. R. The Effect of Turbostratic Disorder on the Staging Transitions in Lithium Intercalated Graphite. *Synth. Matals* **1995**, *73*, 1–7.

(104) Zheng, T.; Dahn, J. R. Effect of Turbostratic Disorder on the Staging Phase Diagram of Lithium-Intercalated Graphitic Carbon Hosts. *Physical Rev. B* **1996**, *53*, 3061–3071.

(105) Fong, R.; Sacken, U. V.; and Dahn, J. R. Studies of Lithium Intercalation into Carbons Using Nonaqueous Electrochemical Cells. *J. Electrochem. Soc.* **2009**, *137*, 3–7.

(106) MacNeil, D. D. Comparison of the Reactivity of Various Carbon Electrode Materials with Electrolyte at Elevated Temperature. *J. Electrochem. Soc.* **1999**, *146*, 3596–3602.

(107) Xu, K. Nonaqueous Liquid Electrolytes for Lithium-Based Rechargeable Batteries. *Chem. Rev.* **2004**, *104*, 4303–4417.

(108) Ding, M. S.; Xu, K.; Zhang, S. S.; Amine, K.; Henriksen, G. L.; Jow, T. R. Change of Conductivity with Salt Content, Solvent Composition, and Temperature for Electrolytes of $LiPF_6$ in Ethylene Carbonate-Ethyl Methyl Carbonate. *J. Electrochem. Soc.* **2001**, *148*, A1196–A1204.

(109) Takata, K.; Morita, M.; Matsuda, Y.; Matsui, K. Cycling Characteristics of Secondary Li Electrode in $LiBF_4$/Mixed Ether Electrolytes. *J. Electrochem. Soc.* **1985**, *132*, 126–128.

(110) Xu, K.; Zhang, S.; Jow, T. R.; Xu, W.; Angell, C. A. LiBOB as Salt for Lithium-Ion Batteries:A Possible Solution for High Temperature Operation. *Electrochem. Solid-State Lett.* **2002**, *5*, A26–A29.

(111) Petibon, R. Study of Electrolyte Additives Using Electrochemical Impedance Spectroscopy on Symmetric Cells, MSc. Thesis, Dalhousie University, 2013.

(112) Peled, E. The Electrochemical-Behavior of Alkali and Alkaline-Earth Metals in Non-Aqueous Battery Systems - the Solid Electrolyte Interphase Model. *J. Electrochem. Soc.* **1979**, *126*, 2047–2051.

(113) Broussely, M.; Biensan, P.; Bonhomme, F.; Blanchard, P.; Herreyre, S.; Nechev, K.; Staniewicz, R. J. Main Aging Mechanisms in Li Ion Batteries. *J. Power Sources* **2005**, *146*, 90–96.

(114) Xiong, D. J.; Petibon, R.; Nie, M.; Ma, L.; Xia, J.; Dahn, J. R. Interactions between Positive and Negative Electrodes in Li-Ion Cells Operated at High Temperature and High Voltage. *J. Electrochem. Soc.* **2016**, *163*, 546–551.

(115) Aurbach, D.; Gamolsky, K.; Markovsky, B.; Gofer, Y.; Schmidt, M.; Heider, U. On the Use of Vinylene Carbonate (VC) as an Additive to Electrolyte Solutions for Li-Ion Batteries. *Electrochim. Acta* **2002**, *47*, 1423–1439.

(116) Li, Y.; Zhang, R.; Liu, J.; Yang, C. Effect of Heptamethyldisilazane as an Additive on the Stability Performance of $LiMn_2O_4$ Cathode for Lithium-Ion Battery. *J. Power Sources* **2009**, *189*, 685–688.

(117) Rowe, A. W. Structural and Electrochemical Studies of Positive Electrode Materials in the Li-Mn-Ni-O System for Lithium-Ion Batteries, Ph.D Thesis, Dalhousie University, 2014.

(118) Myung, S.-T.; Komaba, S.; Kurihara, K.; Hosoya, K.; Kumagai, N.; Sun, Y.; Nakai, I.; Yonemura, M.; Kamiyama, T. Synthesis of $Li[(Ni_{0.5}Mn_{0.5})_{1-X}Li_X]O_2$ by Emulsion Drying Method and Impact of Excess Li on Structural and Electrochemical Properties. *Chem. Mater.* **2006**, *18*, 1658–1666.

(119) Lu, Z.; MacNeil, D. D.; Dahn, J. R. Layered $Li[Ni_xCo_{1-2x}Mn_x]O_2$ Cathode Materials for Lithium-Ion Batteries. *Electrochem. Solid-State Lett.* **2001**, *4*, A200–A203.

(120) MacNeil, D. D.; Lu, Z.; Dahn, J. R. Structure and Electrochemistry of $LiNi_xCo_{1-2x}Mn_xO2$ ($0 \leq x \leq 1/2$). *J. Electrochem. Soc.* **2002**, *149*, A1332–1336.

(121) Lee, K.-S.; Myung, S.-T.; Moon, J.-S.; Sun, Y.-K. Particle Size Effect of $Li[Ni_{0.5}Mn_{0.5}]O_2$ Prepared by Co-Precipitation. *Electrochim. Acta* **2008**, *53*, 6033–6037.

(122) Cherkashinin, G.; Motzko, M.; Schulz, N.; Spath, T.; Jaegermann, W. Electron Spectroscopy Study of $Li[Ni,Co,Mn]O_2$/Electrolyte Interface: Electronic Structure, Interface Composition, and Device Implications. *Chem. Mater.* **2015**, *27*, 2875–2887.

(123) Wang, C.-C.; Manthiram, A. Influence of Cationic Substitutions on the First Charge and Reversible Capacities of Lithium-Rich Layered Oxide Cathodes. *J. Mater. Chem. A* **2013**, *1*, 10209.

(124) Julien, C. M.; Mauger, A.; Zaghib, K.; Groult, H. Comparative Issues of Cathode Materials for Li-Ion Batteries. *Inorganics* **2014**, *2*, 132–154.

(125) Lin, F.; Nordlund, D.; Li, Y.; Quan, M. K.; Cheng, L.; Weng, T.; Liu, Y.; Xin, H. L.; Doe, M. M. Metal Segregation in Hierarchically Structured Cathode Materials for High-Energy Lithium Batteries. *Nat. Energy* **2016**, *1*, 15004.

(126) Lee, K.-S.; Myung, S.-T.; Amine, K.; Yashiro, H.; Sun, Y.-K. Structural and Electrochemical Properties of Layered $Li[Ni_{1-2x}Co_xMn_x]O_2$ ($x = 0.1 – 0.3$) Positive Electrode Materials for Li-Ion Batteries. *J. Electrochem. Soc.* **2007**, *154*, A971–A977.

(127) Noh, H.-J.; Youn, S.; Yoon, C. S.; Sun, Y.-K. Comparison of the Structural and Electrochemical Properties of Layered $Li[Ni_xCo_yMn_z]O_2$ ($x = 1/3$, 0.5, 0.6, 0.7, 0.8 and 0.85) Cathode Material for Lithium-Ion Batteries. *J. Power Sources* **2013**, *233*, 121–130.

(128) Sun, Y.-K.; Myung, S.-T.; Bang, H. J.; Park, B.-C.; Park, S.-J.; Sung, N.-Y. Physical and Electrochemical Properties of $Li[Ni_{0.4}Co_xMn_{0.6-x}]O_2$ ($x = 0.1–0.4$) Electrode Materials Synthesized via Coprecipitation. *J. Electrochem. Soc.* **2007**, *154*, A937–A942.

(129) Yoon, S.-J.; Myung, S.-T.; Sun, Y.-K. Low Temperature Electrochemical Properties of $Li[Ni_xCo_yMn_{1-x-y}]O_2$ Cathode Materials for Lithium-Ion Batteries. *J. Electrochem. Soc.* **2014**, *161*, A1514–A1520.

(130) Palacin, M. R.; Larcher, D.; Audemer, A.; Sac-Epee, N.; Amatucci, G. G.; Tarascon, J-M. Low-Temperature Synthesis of $LiNiO_2$. *J. Electrochem. Soc.* **1997**, *144*, 4226–4236.

(131) Lee, K. K.; Yoon, W. S.; Kim, K. B.; Lee, K. Y.; Hong, S. T. Thermal Behavior and the Decomposition Mechanism of Electrochemically Delithiated $Li_{1-x}NiO_2$. *J. Power Sources* **2001**, *97*, 321–325.

(132) Jo, J. H.; Jo, C.-H.; Yashiro, H.; Kim, S.-J.; Myung, S.-T. Re-Heating Effect of Ni-Rich Cathode Material on Structure and Electrochemical Properties. *J. Power Sources* **2016**, *313*, 1–8.

(133) Ma, L.; Xia, J.; Dahn, J. R. Improving the High Voltage Cycling of $Li[Ni_{0.42}Mn_{0.42}Co_{0.16}]O_2$ (NMC442)/Graphite Pouch Cells Using Electrolyte Additives. *J. Electrochem. Soc.* **2014**, *161*, A2250–A2254.

(134) Bak, S.; Hu, E.; Zhou, Y.; Yu, X.; Senanayake, S. D.; Cho, S.; Kim, K.; Chung, K. Y.; Yang, X.; Nam, K. Structural Changes and Thermal Stability of Charged NMC. *ACS Appl. Mater. Interfaces* **2014**, *6*, 22594–22601.

(135) Kim, M.-H.; Shin, H.-S.; Shin, D.; Sun, Y.-K. Synthesis and Electrochemical Properties of $Li[Ni_{0.8}Co_{0.1}Mn_{0.1}]O_2$ and $Li[Ni_{0.8}Co_{0.2}]O_2$ via Co-Precipitation. *J. Power Sources* **2006**, *159*, 1328–1333.

(136) Cho, Y.; Oh, P.; Cho, J. A New Type of Protective Surface Layer for High-Capacity Ni-Based Cathode Materials: Nanoscaled Surface Pillaring Layer. *Nano Lett.* **2013**, *13*, 1145–1152.

(137) Amine, K.; Sun, Y. Development of Microstrain in Aged Lithium Transition Metal Oxides. *Nano Lett.* **2014**, *14*, 4873–4880.

(138) Huang, R.; Ikuhara, Y. STEM Characterization for Lithium-Ion Battery Cathode Materials. *Curr. Opin. Solid State Mater. Sci.* **2012**, *16*, 31–38.

(139) Kim, N. Y.; Yim, T.; Song, J. H.; Yu, J.-S.; Lee, Z. Microstructural Study on Degradation Mechanism of Layered $LiNi_{0.6}Co_{0.2}Mn_{0.2}O_2$ Cathode Materials by Analytical Transmission Electron Microscopy. *J. Power Sources* **2016**, *307*, 641–648.

(140) Hayashi, T.; Okada, J.; Toda, E.; Kuzuo, R.; Oshimura, N.; Kuwata, N.; Kawamura, J. Degradation Mechanism of $LiNi_{0.82}Co_{0.15}Al_{0.03}O_2$ Positive Electrodes of a Lithium-Ion Battery by a Long-Term Cycling Test. *J. Electrochem. Soc.* **2014**, *161*, A1007–A1011.

(141) Lin, F.; Markus, I. M.; Nordlund, D.; Wend, T.-C.; Asta, M. D.; Xin, H. L.; Doeff, M. M. Surface Reconstruction and Chemical Evolution of Stoichiometric Layered Cathode Materials for Lithium-Ion Batteries. *Nat. Commun.* **2014**, *5*, 3529–3538.

(142) Lin, F.; Nordlund, D.; Pan, T.; Markus, I. M.; Weng, T.-C.; Xin, H. L.; Doeff, M. M. Influence of Synthesis Conditions on the Surface Passivation and Electrochemical Behavior of Layered Cathode Materials. *J. Mater. Chem. A* **2014**, *2*, 19833–19840.

(143) Makimura, Y.; Zheng, S.; Ikuhara, Y.; Ukyo, Y. Microstructural Observation of $LiNi_{0.8}Co_{0.15}Al_{0.05}O_2$ after Charge and Discharge by Scanning Transmission Electron Microscopy. *J. Electrochem. Soc.* **2012**, *159*, A1070–A1073.

(144) Labrini, M.; Scheiba, F.; Almaggoussi, A.; Larzek, M.; Braga, M. H.; Ehrenberg, H.; Saadoune, I. Delithiated $Li_yCo_{0.8}Ni_{0.1}Mn_{0.1}O_2$ Cathode Materials for Lithium-Ion Batteries: Structural, Magnetic and Electrochemical Studies. *Solid State Ionics* **2016**, *289*, 207–213.

(145) Li, J.; Petibon, R.; Glazier, S.; Sharma, N.; Pang, W. K.; Peterson, V. K.; Dahn, J. R. In-Situ Neutron Diffraction Study of a High Voltage $Li(Ni_{0.42}Mn_{0.42}Co_{0.16})O_2$/Graphite Pouch Cell. *Electrochim. Acta* **2015**, *180*, 234–240.

(146) Li, J.; Shunmugasundaram, R.; Doig, R.; Dahn, J. R. In Situ X-Ray Diffraction Study of Layered Li–Ni–Mn–Co Oxides: Effect of Particle Size and Structural Stability of Core–Shell Materials. *Chem. Mater.* **2016**, *28*, 162–171.

(147) Obrovac, M. N.; Christensen, L.; Le, D. B.; Dahn, J. R. Alloy Design for Lithium-Ion Battery Anodes. *J. Electrochem. Soc.* **2007**, *154*, A849–A855.

(148) Sasaki, T.; Nonaka, T.; Oka, H.; Okuda, C.; Itou, Y.; Kondo, Y.; Takeuchi, Y.; Ukyo, Y.; Tatsumi, K.; Muto, S. Capacity-Fading Mechanisms of LiNiO2-Based Lithium-Ion Batteries - I. Analysis by Electrochemical and Spectroscopic Examination. *J. Electrochem. Soc.* **2009**, *156*, A289–A293.

(149) Muto, S.; Sasano, Y.; Tatsumi, K.; Sasaki, T.; Horibuchi, K.; Takeuchi, Y.; and Ukyo, Y. Capacity-Fading Mechanisms of $LiNiO_2$-Based Lithium-Ion Batteries - II. Diagnostic Analysis by Electron Microscopy and Spectroscopy. *J. Electrochem. Soc.* **2009**, *156*, A371–A377.

(150) Wang, J.; Du, C.; Xu, X.; He, X.; Yin, G.; Ma, Y.; Zuo, P.; Cheng, X.; Gao, Y. Lithium Phosphorus Oxynitride Coated Concentration Gradient $Li[Ni_{0.73}Co_{0.12}Mn_{0.15}]O_2$ Cathode Material with Enhanced Electrochemical Properties. *Electrochim. Acta* **2016**, *192*, 340–345.

(151) Wang, D.; Wang, Z.; Li, X.; Guo, H.; Xu, Y.; Fan, Y.; Pan, W. Effect of Surface Fluorine Substitution on High Voltage Electrochemical Performances of Layered $LiNi_{0.5}Co_{0.2}Mn_{0.3}O_2$ Cathode Materials. *Appl. Surf. Sci.* **2016**, *371*, 172–179.

(152) Wang, D.; Li, X.; Wang, Z.; Guo, H.; Xu, Y.; Fan, Y. Co-Modification of $LiNi_{0.5}Co_{0.2}Mn_{0.3}O_2$ Cathode Materials with Zirconium Substitution and Surface Polypyrrole Coating: Towards Superior High Voltage Electrochemical Performances for Lithium Ion Batteries. *Electrochim. Acta* **2016**, *196*, 101–109.

(153) Cho, W.; Kim, S.-M.; Lee, K.-W.; Song, J. H.; Jo, Y. N.; Yim, T.; Kim, H.; Kim, J.-S.; Kim, Y.-J. Investigation of New Manganese Orthophosphate $Mn_3(PO4)_2$ Coating for Nickel-Rich $LiNi_{0.6}Co_{0.2}Mn_{0.2}O_2$ Cathode and Improvement of Its Thermal Properties. *Electrochim. Acta* **2016**, *198*, 77–83.

(154) Lee, Y.; Lee, J.; Lee, K. Y.; Mun, J.; Lee, J. K.; Choi, W. Facile Formation of a Li_3PO_4 Coating Layer during the Synthesis of a Lithium-Rich Layered Oxide for High-Capacity Lithium-Ion Batteries. *J. Power Sources* **2016**, *315*, 284–293.

(155) Liu, S.; Wu, H.; Huang, L.; Xiang, M.; Liu, H.; Zhang, Y. Synthesis of $Li_2Si_2O_5$-Coated $LiNi_{0.6}Co_{0.2}Mn_{0.2}O_2$ Cathode Materials with Enhanced High-Voltage Electrochemical Properties for Lithium-Ion Batteries. *J. Alloys Compd.* **2016**, *674*, 447–454.

(156) Hu, G.; Zhang, M.; Liang, L.; Peng, Z.; Du, K.; Cao, Y. Mg–Al–B Co-Substitution $LiNi_{0.5}Co_{0.2}Mn_{0.3}O_2$ Cathode Materials with Improved Cycling Performance for Lithium-Ion Battery under High Cutoff Voltage. *Electrochim. Acta* **2016**, *190*, 264–275.

(157) Wang, J.; Du, C.; Yan, C.; Xu, X.; He, X.; Yin, G.; Zuo, P.; Cheng, X.; Ma, Y.; Gao, Y. Role of Fluorine Surface Modification in Improving Electrochemical Cyclability of Concentration Gradient $Li[Ni_{0.73}Co_{0.12}Mn_{0.15}]O_2$ Cathode Material for Li-Ion Batteries. *RSC Adv.* **2016**, *6*, 26307–26316.

(158) Wang, D.; Wang, Z.; Li, X.; Guo, H.; Xu, Y.; Fan, Y.; Pan, W. Effect of Surface Fluorine Substitution on High Voltage Electrochemical Performances of Layered $LiNi_{0.5}Co_{0.2}Mn_{0.3}O_2$ Cathode Materials. *Appl. Surf. Sci.* **2016**, *371*, 172–179.

(159) Ju, J.; Lee, E.; Yoon, C. S.; Myung, S.; Sun, Y. Optimization of Layered Cathode Material with Full Concentration Gradient for Lithium-Ion Batteries. *J. Phys. Chem. C* **2014**, *118*, 175–182.

(160) Noh, H.; Myung, S.; Lee, Y. J.; Sun, Y. High-Energy Layered Oxide Cathodes with Thin Shells for Improved Surface Stability. *Chem. Mater.* **2014**, *26*, 5973–5979.

(161) Lee, E.-J.; Noh, H.-J.; Yoon, C. S.; Sun, Y.-K. Effect of Outer Layer Thickness on Full Concentration Gradient Layered Cathode Material for Lithium-Ion Batteries. *J. Power Sources* **2015**, *273*, 663–669.

(162) Boulineau, A.; Simonin, L.; Colin, J.-F.; Bourbon, C.; Patoux, S. First Evidence of Manganese – Nickel Segregation and Densification upon Cycling in Li-Rich Layered Oxides for Lithium Batteries. *Nano Lett.* **2013**, *13*, 3857–3863.

(163) Dou, S. Review and Prospect of Layered Lithium Nickel Manganese Oxide as Cathode Materials for Li-Ion Batteries. *J. Solid State Electrochem.* **2013**, *17*, 911–926.

(164) Xiao, P.; Deng, Z. Q.; Manthiram, A.; Henkelman, G. Calculations of Oxygen Stability in Lithium-Rich Layered Cathodes. *J. Phys. Chem. C* **2012**, *116*, 23201–23204.

(165) Mohanty, D.; Kalnaus, S.; Meisner, R. A.; Rhodes, K. J.; Li, J.; Payzant, E. A.; Wood, D. L.; Daniel, C. Structural Transformation of a Lithium-Rich $Li_{1.2}Co_{0.1}Mn_{0.55}Ni_{0.15}O_2$ Cathode during High Voltage Cycling Resolved by in Situ X-Ray Diffraction. *J. Power Sources* **2013**, *229*, 239–248.

(166) Gummow, R. J.; Sharma, N.; Feng, R.; Han, G.; He, Y. High Performance Composite Lithium-Rich Nickel Manganese Oxide Cathodes for Lithium-Ion Batteries. *J. Electrochem. Soc.* **2013**, *160*, A1856–A1862.

(167) Liu, J.; Wang, R.; Xia, Y. Degradation and Structural Evolution of $xLi_2MnO_3\cdot(1-x)LiMn_{1/3}Ni_{1/3}Co_{1/3}O_2$ during Cycling. *J. Electrochem. Soc.* **2013**, *161*, A160–A167.

(168) Lee. J, Urban. A, Li. A, Su. D, Hautier. G, C. G. Unlocking the Potential of Cation-Disordered Oxides for Rechargeable Lithium Batteries. *Science* **2014**, *343*, 519–522.

(169) Koga, H.; Croguennec, L.; Menetrier, M.; Mannessiez, P.; Weill, F.; Delmas, C.; and Belin, S. Operando X-Ray Absorption Study of the Redox Processes Involved upon Cycling of the Li-Rich Layered Oxide $Li_{1.20}Mn_{0.54}Co_{0.13}Ni_{0.13}O_2$ in Li Ion Batteries. *J. Phys. Chem. C* **2014**, *118*, 5700–5709.

(170) Wen, J. G.; Bareño, J.; Lei, C. H.; Kang, S. H.; Balasubramanian, M.; Petrov, I.; Abraham, D. P. Analytical Electron Microscopy of $Li_{1.2}Co_{0.4}Mn_{0.4}O_2$ for Lithium-Ion Batteries. *Solid State Ionics* **2011**, *182*, 98–107.

(171) Long, B. R.; Croy, J. R.; Dogan, F.; Suchomel, M. R.; Key, B.; Wen, J.; Miller, D. J.; Thackeray, M. M.; Balasubramanian, M. Effect of Cooling Rates on Phase Separation in $0.5Li_2MnO_3 \cdot 0.5LiCoO_2$ Electrode Materials for Li-Ion Batteries. *Chem. Mater.* **2014**, *26*, 3565–3572.

(172) Kim, D.; Sandi, G.; Croy, J. R.; Gallagher, K. G.; Kang, S.-H.; Lee, E.; Slater, M. D.; Johnson, C. S.; Thackeray, M. M. Composite "Layered-Layered-Spinel" Cathode Structures for Lithium-Ion Batteries. *J. Electrochem. Soc.* **2012**, *160*, A31–A38.

(173) Croy, J. R.; Kim, D.; Balasubramanian, M.; Gallagher, K.; Kang, S.-H.; Thackeray, M. M. Countering the Voltage Decay in High Capacity $xLi_2MnO_3 \cdot (1–x)LiMO_2$ Electrodes (M=Mn, Ni, Co) for Li-Ion Batteries. *J. Electrochem. Soc.* **2012**, *159*, A781–A790.

(174) Croy, J. R.; Gallagher, K. G.; Balasubramanian, M.; Chen, Z.; Ren, Y.; Kim, D.; Kang, S.-H.; Dees, D. W.; Thackeray, M. M. Examining Hysteresis in Composite $xLi_2MnO_3 \cdot (1–x)LiMO_2$ Cathode Structures. *J. Phys. Chem. C* **2013**, *117*, 6525–6536.

(175) Croy, J. R.; Iddir, H.; Gallagher, K.; Johnson, C. S.; Benedek, R.; Balasubramanian, M. First-Charge Instabilities of Layered-Layered Lithium-Ion-Battery Materials. *Phys. Chem. Chem. Phys.* **2015**, *17*, 24382–24391.

(176) Bareno, J.; Balasubramanian, M.; Kang, S. H.; Wen, J. G.; Lei, C. H.; Pol, S. V; Petrov, I.; Abraham, D. P. Long-Range and Local Structure in the Layered Oxide. *Chem. Mater.* **2011**, *23*, 2039–2050.

(177) Rinaldo, S. G.; Gallagher, K. G.; Long, B. R.; Croy, J. R.; Bettge, M.; Abraham, D. P.; Bareno, J.; Dees, D. W. Physical Theory of Voltage Fade in Lithium- and Manganese-Rich Transition Metal Oxides. *J. Electrochem. Soc.* **2015**, *162*, A897–A904.

(178) Iddir, H.; Key, B.; Dogan, F.; Russell, J. T.; Long, B. R.; Bareño, J.; Croy, J. R.; Benedek, R. Pristine-State Structure of Lithium-Ion-Battery Cathode Material $Li_{1.2}Mn_{0.4}Co_{0.4}O_2$ Derived from NMR Bond Pathway Analysis. *J. Mater. Chem. A* **2015**, *3*, 11471–11477.

(179) Croy, J. R.; Gallagher, K. G.; Balasubramanian, M.; Long, B. R.; Thackeray, M. M. Quantifying Hysteresis and Voltage Fade in $xLi_2MnO_3 \cdot (1\text{-}x)LiMn_{0.5}Ni_{0.5}O_2$ Electrodes as a Function of Li_2MnO_3 Content. *J. Electrochem. Soc.* **2014**, *161*, A318–A325.

(180) Dogan, F.; Long, B. R.; Croy, J. R.; Gallagher, K. G.; Iddir, H.; Russell, J. T.; Balasubramanian, M.; Key, B. Re-Entrant Lithium Local Environments and Defect Driven Electrochemistry of Li- and Mn-Rich Li-Ion Battery Cathodes. *J. Am. Chem. Soc.* **2015**, *137*, 2328–2335.

(181) Dogan, F.; Croy, J. R.; Balasubramanian, M.; Slater, M. D.; Iddir, H.; Johnson, C. S.; Vaughey, J. T.; Key, B. Solid State NMR Studies of Li_2MnO_3 and Li-Rich Cathode Materials: Proton Insertion, Local Structure, and Voltage Fade. *J. Electrochem. Soc.* **2015**, *162*, A235–A243.

(182) Johnson, C. S.; Kim, J.; Kropf, A. J.; Kahaian, A. J.; Vaughey, J. T.; Fransson, L. M. L.; Edstro, K.; Thackeray, M. M. Structural Characterization of Layered $Li_xNi_{0.5}Mn_{0.5}O_2$ ($0 < x < 2$) Oxide Electrodes for Li Batteries. *Chem. Mater.* **2003**, *2*, 2313–2322.

(183) Li, Y.; Bareño, J.; Bettge, M.; Abraham, D. P.; Bareno, J.; Bettge, M.; Abraham, D. P. Unexpected Voltage Fade in LMR-NMC Oxides Cycled below the "Activation" Plateau. *J. Electrochem. Soc.* **2014**, *162*, A155–A161.

(184) Mohanty, D.; Li, J.; Abraham, D. P.; Payzant, E. A.; Wood, D. L.; Daniel, C. Unraveling the Voltage-Fade Mechanism in High-Energy-Density Lithium-Ion Batteries: Origin of the Tetrahedral Cations for Spinel Conversion. *Chem. Mater.* **2014**, *26*, 6272–6280.

(185) Thackeray, M. M.; Johnson, C. S.; Vaughey, J. T.; Li, N.; Hackney, S. A. Advances in Manganese-Oxide "Composite" Electrodes for Lithium-Ion Batteries. *J. Mater. Chem.* **2005**, *15*, 2257–2267.

(186) Shukla, A. K.; Ramasse, Q. M.; Ophus, C.; Duncan, H.; Hage, F.; Chen, G. Unravelling Structural Ambiguities in Lithium- and Manganese-Rich Transition Metal Oxides. *Nat. Commun.* **2015**, *6*, 8711–8720.

(187) Koga, H.; Croguennec, L.; Mannessiez, P.; Bourgeois, L.; Duttine, M.; Suard, E.; Delmas, C. $Li_{1.20}Mn_{0.54}Co_{0.13}Ni_{0.13}O_2$ with Different Particle Sizes as Attractive Positive Electrode Materials for Lithium ‐ Ion Batteries: Insights into Their Structure. *J. Phys. Chem* **2012**, *116*, 13497–13506.

(188) Song, B.; Liu, Z.; Lai, M. O; Lu, L. Structural Evolution and the Capacity Fade Mechanism upon Long-Term Cycling in Li-Rich Cathode Material. *Phys. Chem. Chem. Phys.* **2012**, *14*, 12875–12883.

(189) Ates, M. N.; Jia, Q.; Shah, A.; Busnaina, A.; Mukerjee, S.; Abraham, K. M. Mitigation of Layered to Spinel Conversion of a Li-Rich Layered Metal Oxide Cathode Material for Li-Ion Batteries. *J. Electrochem. Soc.* **2013**, *161*, A290–A301.

(190) Sathiya, M.; Ramesha, K.; Rousse, G.; Foix, D.; Gonbeau, D.; Prakash, A. S.; Doublet, M. L.; Hemalatha, K. High Performance $Li_2Ru_{1-y}Mn_yO_3$ ($0.2 \leq y \leq 0.8$) Cathode Materials for Rechargeable Lithium-Ion Batteries: Their Understanding. *Chem. Mater.* **2013**, *3*, 1121–1131.

(191) Luo, K.; Roberts, M. R.; Hao, R.; Guerrini, N.; Pickup, D. M.; Liu, Y.-S.; Edström, K.; Guo, J.; Chadwick, A. V.; Duda, L. C.; Bruce, P. G. Charge-Compensation in 3d-Transition-Metal-Oxide Intercalation Cathodes Through the Generation of Localized Electron Holes on Oxygen. *Nat. Chem.* **2016**, published online.

(192) Kim, J. H.; Park, C. W.; Sun, Y. K. Synthesis and Electrochemical Behavior of $Li[Li_{0.1}Ni_{0.35-x/2}Co_xMn_{0.55-x/2}]O_2$ Cathode Materials. *Solid State Ionics* **2003**, *164*, 43–49.

(193) Jin, X.; Xu, Q.; Liu, H.; Yuan, X.; Xia, Y. Excellent Rate Capability of Mg Doped $Li[Li_{0.2}Ni_{0.13}Co_{0.13}Mn_{0.54}]O_2$ Cathode Material for Lithium-Ion Battery. *Electrochim. Acta* **2014**, *136*, 19–26.

(194) Iftekhar, M.; Drewett, N. E.; Armstrong, A. R.; Hesp, D.; Braga, F.; Ahmed, S.; Hardwick, L. J. Characterization of Aluminum Doped Lithium-Manganese Rich Composites for Higher Rate Lithium-Ion Cathodes. *J. Electrochem. Soc.* **2014**, *161*, A2109–A2116.

(195) Kang, S. H.; Amine, K. Layered $Li(Li_{0.2}Ni_{0.15+0.5z}Co_{0.10}Mn_{0.55-0.5z})O_{2-z}F_z$ Cathode Materials for Li-Ion Secondary Batteries. *J. Power Sources* **2005**, *146*, 654–657.

(196) Croguennec, L.; Bains, J.; Ménétrier, M.; Flambard, A.; Bekaert, E.; Jordy, C.; Biensan, P.; Delmas, C. Synthesis of $Li_{1.1}(Ni_{0.425}Mn_{0.425}Co_{0.15})_{0.9}O_{1.8}F_{0.2}$ Materials by Different Routes: Is There Fluorine Substitution for Oxygen? *J. Electrochem. Soc.* **2009**, *156*, A349–A355.

(197) Song, B.; Lai, M. O.; Lu, L. Influence of Ru Substitution on Li-Rich $0.55Li_2MnO_3 \cdot 0.45LiNi_{1/3}Co_{1/3}Mn_{1/3}O_2$ Cathode for Li-Ion Batteries. *Electrochim. Acta* **2012**, *80*, 187–195.

(198) Chen, D.; Tu, W.; Chen, M.; Hong, P.; Zhong, X.; Zhu, Y.; Yu, Q.; Li, W. Synthesis and Performances of Li-Rich@AlF_3@Graphene as Cathode of Lithium Ion Battery. *Electrochim. Acta* **2016**, *193*, 45–53.

(199) Pang, S.; Wang, Y.; Chen, T.; Shen, X.; Xi, X.; Liao, D. The Effect of AlF3 Modification on the Physicochemical and Electrochemical Properties of Li-Rich Layered Oxide. *Ceram. Int.* **2016**, *42*, 5397–5402.

(200) Zhu, Z.; Cai, F.; Yu, J. Improvement of Electrochemical Performance for AlF_3-Coated $Li_{1.3}[Mn_{4/6}Ni_{1/6}Co_{1/6}]_{0.7}O_2$ Cathode Materials for Li-Ion Batteries. *Ionics.* **2016**, published online.

(201) Zheng, J.; Deng, S.; Shi, Z.; Xu, H.; Xu, H.; Deng, Y.; Zhang, Z.; Chen, G. The Effects of Persulfate Treatment on the Electrochemical Properties of $Li[Li_{0.2}Ni_{0.13}Co_{0.13}Mn_{0.54}]O_2$ Cathode Material. *J. Power Sources* **2013**, *221*, 108–113.

(202) Kang, S.-H.; Johnson, C. S.; Vaughey, J. T.; Amine, K.; Thackeray, M. M. The Effects of Acid Treatment on the Electrochemical Properties of $0.5Li_2MnO_3 \cdot 0.5LiNi_{0.44}Co_{0.25}Mn_{0.31}O_2$ Electrodes in Lithium Cells. *J. Electrochem. Soc.* **2006**, *153*, A1186–A1192.

(203) Gao, J.; Kim, J.; Manthiram, A. High Capacity $Li[Li_{0.2}Mn_{0.54}Ni_{0.13}Co_{0.13}]O_2$-$V_2O_5$ Composite Cathodes with Low Irreversible Capacity Loss for Lithium Ion Batteries. *Electrochem. commun.* **2009**, *11*, 84–86.

(204) Gao, J.; Manthiram, A. Eliminating the Irreversible Capacity Loss of High Capacity Layered $Li[Li_{0.2}Mn_{0.54}Ni_{0.13}Co_{0.13}]O_2$ Cathode by Blending with Other Lithium Insertion Hosts. *J. Power Sources* **2009**, *191*, 644–647.

(205) Lee, E. S.; Manthiram, A. High Capacity $Li[Li_{0.2}Mn_{0.54}Ni_{0.13}Co_{0.13}]O_2$–$VO_2$(B) Composite Cathodes with Controlled Irreversible Capacity Loss for Lithium-Ion Batteries. *J. Electrochem. Soc.* **2011**, *158*, A47–A50.

(206) Zhu, Y.; Li, Y.; Abraham, D. P. Mitigating Performance Degradation of High-Capacity Lithium-Ion Cells with Boronate-Based Electrolyte Additives. *J. Electrochem. Soc.* **2014**, *161*, A1580–A1585.

(207) Lee, S. J.; Han, J.-G.; Park, I.; Song, J.; Cho, J.; Kim, J.-S.; Choi, N.-S. Effect of Lithium Bis(oxalato)borate Additive on Electrochemical Performance of $Li_{1.17}Ni_{0.17}Mn_{0.5}Co_{0.17}O_2$ Cathodes for Lithium-Ion Batteries. *J. Electrochem. Soc.* **2014**, *161*, A2012–A2019.

(208) Zhang, J.; Wang, J.; Yang, J.; Nuli, Y. Artificial Interface Deriving from Sacrificial Tris(trimethylsilyl) Phosphate Additive for Lithium Rich Cathode Materials. *Electrochim. Acta* **2014**, *117*, 99–104.

(209) Chernyshov, D. V.; Krachkovskiy, S. A.; Kapylou, A. V.; Bolshakov, I. A.; Shin, W. C.; Ue, M. Substituted Dioxaphosphinane as an Electrolyte Additive for High Voltage Lithium-Ion Cells with Overlithiated Layered Oxide. *J. Electrochem. Soc.* **2014**, *161*, A633–A642.

(210) Noh, J.-K.; Kim, S.; Kim, H.; Choi, W.; Chang, W.; Byun, D.; Cho, B.-W.; Chung, K. Y. Mechanochemical Synthesis of Li_2MnO_3 shell/$LiMO_2$ (M = Ni, Co, Mn) Core-Structured Nanocomposites for Lithium-Ion Batteries. *Sci. Rep.* **2014**, *4*, 4847–4856.

(211) Shunmugasundaram, R.; Senthil Arumugam, R.; Dahn, J. R. High Capacity Li-Rich Positive Electrode Materials with Reduced First-Cycle Irreversible Capacity Loss. *Chem. Mater.* **2015**, *27*, 757–767.

(212) Chen, L.; Su, Y.; Chen, S.; Li, N.; Bao, L.; Li, W.; Wang, Z.; Wang, M.; Wu, F. Hierarchical $Li_{1.2}Ni_{0.2}Mn_{0.6}O_2$ Nanoplates with Exposed {010} Planes as High-Performance Cathode Material for Lithium-Ion Batteries. *Adv. Mater.* **2014**, *26*, 6756–6760.

(213) Zheng, J. M.; Wu, X. B.; Yang, Y. A Comparison of Preparation Method on the Electrochemical Performance of Cathode Material $Li[Li_{0.2}Mn_{0.54}Ni_{0.13}Co_{0.13}]O_2$ for Lithium Ion Battery. *Electrochim. Acta* **2011**, *56*, 3071–3078.

(214) Zheng, J.; Wu, X.; Yang, Y. Improved Electrochemical Performance of $Li[Li_{0.2}Mn_{0.54}Ni_{0.13}Co_{0.13}]O_2$ Cathode Material by Fluorine Incorporation. *Electrochim. Acta* **2013**, *105*, 200–208.

(215) Martha, S. K.; Nanda, J.; Kim, Y.; Unocic, R. R.; Pannala, S.; Dudney, N. J. Solid Electrolyte Coated High Voltage Layered–layered Lithium-Rich Composite Cathode: $Li_{1.2}Mn_{0.525}Ni_{0.175}Co_{0.1}O_2$. *J. Mater. Chem. A* **2013**, *1*, 5587–5595.

(216) Park, S. H.; Kang, S. H.; Belharouak, I.; Sun, Y. K.; Amine, K. Physical and Electrochemical Properties of Spherical $Li_{1+x}(Ni_{1/3}Co_{1/3}Mn_{1/3})_{1-x}O_2$ Cathode Materials. *J. Power Sources* **2008**, *177*, 177–183.

(217) Wang, Z.; Liu, E.; Guo, L.; Shi, C.; He, C.; Li, J.; Zhao, N. Cycle Performance Improvement of Li-Rich Layered Cathode Material $Li[Li_{0.2}Mn_{0.54}Ni_{0.13}Co_{0.13}]O_2$ by ZrO_2 Coating. *Surf. Coatings Technol.* **2013**, *235*, 570–576.

(218) Chen, Z.; Dahn, J. R. Methods to Obtain Excellent Capacity Retention in $LiCoO_2$ Cycled to 4.5 V. *Electrochim. Acta* **2004**, *49*, 1079–1090.

(219) Cullity, B. D.; and Stock, S. R. *Elements of X-Ray Diffraction*, Third Edition.; Prentice Hall, Inc., New Jersey, 2001.

(220) Warren, B. E. *X-Ray Diffraction*; Dover Publications. Inc., New York, 1990.

(221) Hunter, B. A.; and Howard, C. J. *A Computer Program For Rietveld Analysis of X-Ray and Neutron Powder Diffraction Patterns*; Australian Nuclear Science and Technology Organization, 2000.

(222) McCalla, E. Structural and Electrochemical Studies of the Li-Mn-Ni-O and Li-Co-Mn-O Pseudo-Ternary Systems, Ph. D Thesis, Dalhousie University, 2013.

(223) Camardese, J. Core-Shell Materials as Positive Electrodes in Lithium-Ion Batteries, Ph. D Thesis, Dalhousie University, 2015.

(224) Toby, B. H. EXPGUI , A Graphical User Interface for GSAS. *J. Appl. Crystallogr.* **2001**, *34*, 210–213.

(225) Zhou, W.; Wang, Z. L. *Scanning Microscopy for Nanotechnology*; Springer Science + Business Media, New York, 2006.

(226) Echlin, P. *Handbook of Sample Preparation for Scanning Electron Microscopy and X-Ray Microanalysis*; Springer Science + Business Media, New York, 2009.

(227) Egerton, R. F. *Physical Principles of Electron Microscopy*; Springer Science + Business Media, New York, 2005.

(228) Jesson, D. E.; and Pennycook, S. J. Incoherent Imaging of Crystal Using Thermally Scattered Electrons. *Proc. R. Soc. Lond. A* **1995**, *449*, 273–293.

(229) Egerton, R. F. Electron Energy-Loss Spectroscopy in the TEM. *Reports Prog. Phys.* **2009**, *72*, 16502–16527.

(230) Aiken, C. P.; Xia, J.; Wang, D. Y.; Stevens, D. A.; Trussler, S.; Dahn, J. R. An Apparatus for the Study of In Situ Gas Evolution in Li-Ion Pouch Cells. *J. Electrochem. Soc.* **2014**, *161*, A1548–A1554.

(231) Self, J.; Aiken, C. P.; Petibon, R.; Dahn, J. R. Survey of Gas Expansion in Li-Ion NMC Pouch Cells. *J. Electrochem. Soc.* **2015**, *162*, A796–A802.

(232) Methre, H. *Diffusion in Solids: Fundamentals, Methods, Materials,Diffusion-Controlled Processes*; Springer (Berlin, Heidelberg, New York) 2007.

(233) Kozeschnik, E. Modeling Solid-State Diffusion. In *Computational Materials Engineering: An Introduction to Microstructure Evolution*; Elsevier Academic Press, London, 2007.

(234) Day, K. M. Analysis of Interdiffusion and Diffusion Paths in Multicomponent Systmes, Ph. D Thesis, Purdue University, 2007.

(235) Toshiyuki; Sata. High-Temperature Vaporization of Li_2O Component from Solid Solution $Li_xNi_{1-x}O_2$ in Air. *Ceremics Int.* **1998**, *8842*, 53–59.

(236) Antolini, E. Lithium Loss Kinetics from Polycrystalline $LiNiO_2$ at High Temperatures. *J. Mater. Chem,* **1998**, *2*, 2783–2786.

(237) Shunmugasundaram, R.; Arumugam, R. S.; Dahn, J. R. A Study of Stacking Faults and Superlattice Ordering in Some Li-Rich Layered Transition Metal Oxide Positive Electrode Materials. *J. Electrochem. Soc.* **2016**, *163*, A1394–A1400.

(238) Bréger, J.; Jiang, M.; Dupré, N.; Meng, Y. S.; Shao-Horn, Y.; Ceder, G.; Grey, C. P. High-Resolution X-Ray Diffraction, DIFFaX, NMR and First Principles Study of Disorder in the Li_2MnO_3–$Li[Ni_{1/2}Mn_{1/2}]O_2$ Solid Solution. *J. Solid State Chem.* **2005**, *178*, 2575–2585.

(239) Boulineau, A.; Croguennec, L.; Delmas, C.; Weill, F. Reinvestigation of Li_2MnO_3 Structure: Electron Diffraction and High Resolution TEM. *Chem. Mater.* **2009**, *21*, 4216–4222.

(240) Ariyoshi, K.; Ichikawa, T.; Ohzuku, T. Structural Change of $LiNi_{1/2}Mn_{1/2}O_2$ during Charge and Discharge in Nonaqueous Lithium Cells. *J. Phys. Chem. Solids* **2008**, *69*, 1238–1241.

(241) Li, W.; Reimers, J. N.; Dahn, J. R. In Situ X-Ray Diffraction and Electrochemical Studies of $Li_{1-x}NiO_2$. *Solid State Ionics* **1993**, *67*, 123–130.

(242) Li, J.; Camardese, J.; Shunmugasundaram, R.; Glazier, S.; Lu, Z.; Dahn, J. R. Synthesis and Characterization of the Lithium-Rich Core–Shell Cathodes with Low Irreversible Capacity and Mitigated Voltage Fade. *Chem. Mater.* **2015**, *27*, 3366–3377.

(243) Li, J.; Petibon, R.; Glazier, S.; Sharma, N.; Pange, W. K.; Petersone, V. K.; Dahn, J. R. In-Situ Neutron Diffraction Study of a High Voltage $Li(Ni_{0.42}Mn_{0.42}Co_{0.16})O_2$/Graphite Pouch Cell. *Electrochim. Acta* **2015**, *180*, 234–240.

(244) Zheng, T.; Reimers, J.; Dahn, J. R. Effect of Trubostratic Disorder in Grahitic Carbon Hosts on the Intercalation of Lithium. *Phyical Rev. B* **1995**, *51*, 734–741.

(245) Li, W.; Reimers, J. N.; Dahn, J. R. Rechargeable $LiNiO_2$/Carbon Cells. *J. Electrochem. Soc.* **1991**, *138*, 2207-2211.

(246) Downie, L. E.; Dahn, J. R. Determination of the Voltage Dependence of Parasitic Heat Flow in Lithium Ion Cells Using Isothermal Microcalorimetry. *J. Electrochem. Soc.* **2014**, *161*, A1782–A1787.

(247) Kalikmanov, V. I.; Leeuw, S. W. De. Phase Diagram of an Intercalation Compound in the Presence of Elastic Interactions : A Mean-Field Approach. *Solid State Ionics* **2002**, *155*, 195–201.

(248) Kalikmanov, V. I.; Koudriachova, M. V; Leeuw, S. W. De. Lattice – Gas Model for Intercalation Compounds. *Solid State Ionics* **2000**, *137*, 1373–1378.

(249) McKinnon, W. R. Lattice Gas Models of Intercalation: Comparison of Monte Carlo, Cluster Variation Method and Renormalization Group Calculations. *Solid State Commun.* **1981**, *40*, 343–345.

(250) McKinnon, W. R. Physical Mechanisms of Intercalation Batteries, Ph. D Thesis, Univ. Brit. Col., 1980.

(251) Xu, B.; Fell, C. R.; Chi, M.; Meng, Y. S. Identifying Surface Structural Changes in Layered Li-Excess Nickel Manganese Oxides in High Voltage Lithium Ion Batteries: A Joint Experimental and Theoretical Study. *Energy Environ. Sci.* **2011**, *4*, 2223–2234.

(252) Zheng, J.; Xu, P.; Gu, M.; Xiao, J.; Browning, N. D.; Yan, P.; Wang, C.; Zhang, J.-G. Structural and Chemical Evolution of Li- and Mn-Rich Layered Cathode Material. *Chem. Mater.* **2015**, *27*, 1381–1390.

(253) Yan, P.; Nie, A.; Zheng, J.; Zhou, Y.; Lu, D.; Zhang, X.; Xu, R.; Zhang, J.; Wang, C. Evolution of Lattice Structure and Chemical Composition of the Surface Reconstruction Layer in $Li_{1.2}Ni_{0.2}Mn_{0.6}O_2$ Cathode Material for Lithium Ion Batteries. *Nano Lett.* **2015**, *15*, 514–522.

(254) Dixit, H.; Zhou, W.; Idrobo, J.; Nanda, J.; Cooper, V. R. Facet-Dependent Disorder in Pristine High-Voltage Lithium À Manganese-Rich Cathode Material. *ACS Nano* **2014**, *12*, 12710–12716.

(255) Yan, P.; Zheng, J.; Xiao, J.; Wang, C.-M.; Zhang, J.-G. Recent Advances on the Understanding of Structural and Composition Evolution of LMR Cathodes for Li-Ion Batteries. *Front. Energy Res.* **2015**, *3*, 1–10.

(256) Tavakoli, A. H.; Kondo, H.; Ukyo, Y.; Navrotsky, A. Cathode Material for Lithium Ion Batteries Li(Ni,Co,Al)O_2 Stabilizing Effect of Mg on the Energetics of the Service Email Alerting Stabilizing Effect of Mg on the Energetics of the Li(Ni,Co,Al)O_2 Cathode Material for Lithium Ion Batteries. *J. Electrochem. Soc.* **2013**, *160*, 302–305.

(257) Wolff-Goodrich, S.; Lin, F.; Markus, I. M.; Nordlund, D.; Xin, H. L.; Asta, M.; Doeff, M. M. Tailoring the Surface Properties of $LiNi_{0.4}Mn_{0.4}Co_{0.2}O_2$ by Titanium Substitution for Improved High Voltage Cycling Performance. *Phys. Chem. Chem. Phys.* **2015**, *17*, 21778–21781.

(258) Makimura, Y.; Rougier, A.; Tarascon, J. M. Pulsed Laser Deposited Iron Fluoride Thin Films for Lithium-Ion Batteries. *Appl. Surf. Sci.* **2006**, *252*, 4587–4592.

(259) Pralong, V.; Leriche, J. B.; Beaudoin, B.; Naudin, E.; Morcrette, M.; Tarascon, J. M. Electrochemical Study of Nanometer Co_3O_4, Co, $CoSb_3$ and Sb Thin Films toward Lithium. *Solid State Ionics* **2004**, *166*, 295–305.

(260) Urban, A.; Lee, J.; Ceder, G. The Configurational Space of Rocksalt-Type Oxides for High-Capacity Lithium Battery Electrodes. *Adv. Energy Mater.* **2014**, *4*, 1400478.

(261) Glazier, S. L.; Li, J.; Zhou, J.; Bond, T.; Dahn, J. R. Characterization of Disordered $Li_{(1+x)}Ti_{2x}Fe_{(1-3x)}O_2$ as Positive Electrode Materials in Li-Ion Batteries Using Percolation Theory. *Chem. Mater.* **2015**, *27*, 7751–7756.

(262) Yabuuchi, N.; Takeuchi, M.; Nakayama, M.; Shiiba, H.; Ogawa, M.; Nakayama, K.; Ohta, T.; Endo, D.; Ozaki, T.; Inamasu, T.; Sato, K.; Komaba, S. High-Capacity Electrode Materials for Rechargeable Lithium Batteries: Li_3NbO_4-Based System with Cation-Disordered Rocksalt Structure. *Proc. Natl. Acad. Sci. U. S. A.* **2015**, *112*, 7650–7655.

(263) Takamatsu, D.; Orikasa, Y.; Mori, S.; Nakatsutsumi, T.; Yamamoto, K.; Koyama, Y.; Minato, T.; Hirano, T.; Tanida, H.; Arai, H.; Uchimoto, Y.; Ogumi, Z. Effect of an Electrolyte Additive of Vinylene Carbonate on the Electronic Structure at the Surface of a Lithium Cobalt Oxide Electrode under Battery Operating Conditions. *J. Phys. Chem. C* **2015**, *119*, 9791–9797.

(264) Ferreira, T.; and Rasband, W. *ImageJ User Guide*; IJ 1.46r, Revised Edition, 2012.

(265) Abràmoff, M. D.; Magalhães, P. J.; Ram, S. J. Image Processing with ImageJ. *Biophotonics Int.* **2004**, *11*, 36–41.

(266) Zheng, J.; Gu, M.; Xiao, J.; Zuo, P.; Wang, C.; Zhang, J. Corrosion/Fragmentation of Layered Composite Cathode and Related Capacity/Voltage Fading during Cycling Process. *Nano Lett.* **2013**, *13*, 3824-3830.

(267) Lin, F.; Nordlund, D.; Markus, I. M.; Weng, T.-C.; Xin, H. L.; Doeff, M. M. Profiling the Nanoscale Gradient in Stoichiometric Layered Cathode Particles for Lithium-Ion Batteries. *Energy Environ. Sci.* **2014**, *7*, 3077–3085.

(268) Hou, P.; Guo, J.; Song, D.; Zhang, J.; Zhou, E.; Zhang, L. A Novel Double-Shelled $LiNi_{0.5}Co_{0.2}Mn_{0.3}O_2$ Cathode Material for Li-Ion Batteries. *Chem. Lett.* **2012**, *41*, 1712–1714.

(269) Liang, L.; Du, K.; Peng, Z.; Cao, Y.; Hu, G. Synthesis and Electrochemical Performance of $LiNi_{0.6}Co_{0.2}Mn_{0.2}O_2$ as a Concentration-Gradient Cathode Material for Lithium Batteries. *Chinese Chem. Lett.* **2014**, *25*, 883–886.

(270) Drouin, D.; Couture, A. R.; Joly, D.; Tastet, X.; Aimez, V.; Gauvin, R. CASINO V2.42 - A Fast and Easy-to-Use Modeling Tool for Scanning Electron Microscopy and Microanalysis Users. *Scanning* **2007**, *29*, 92–101.

(271) Li, J.; Doig, R.; Camardese, J.; Plucknett, K.; Dahn, J. R.; Measurements of Interdiffusion Coefficients of Transition Metals in Layered Li-Ni-Mn-Co Oxide Core-Shell Materials during Sintering. **2015**, *17*, 7765-7773.

(272) Wang, C.; Zhang, J. Functioning Mechanism of AlF_3 Coating on the Li- and Mn-Rich Cathode Materials. *Chem. Mater.* **2014**, *26*, 6320–6327.

(273) Yan, P.; Zheng, J.; Zhang, X.; Xu, R.; Amine, K.; Xiao, J.; Zhang, J.-G.; Wang, C.-M. Atomic to Nanoscale Investigation of Functionalities of an Al_2O_3 Coating Layer on a Cathode for Enhanced Battery Performance. *Chem. Mater.* **2016**, *28*, 857–863.

(274) Xia, J.; Lu, Z.; Camardese, J.; Dahn, J. R. The Effect of Electrolyte Additives on Both $LaPO_4$-Coated $Li(Ni_{0.4}Mn_{0.4}Co_{0.2})O_2$ and Uncoated $Li(Ni_{0.4}Mn_{0.4}Co_{0.2})O_2$ in Li-Ion Pouch Cells. *J. Power Sources* **2016**, *306*, 516–525.

(275) Hodeau, J. L.; Favre-Nicolin, V.; Bos, S.; Renevier, H.; Lorenzo, E.; Berar, J. F. Resonant Diffraction. *Chem. Rev.* **2001**, *101*, 1843–1867.

(276) Dahn, H. M.; Smith, A. J.; Burns, J. C.; Stevens, D. A.; Dahn, J. R. User-Friendly Differential Voltage Analysis Freeware for the Analysis of Degradation Mechanisms in Li-Ion Batteries. *J. Electrochem. Soc.* **2012**, *159*, A1405–A1409.

(277) Burns, J. C.; Krause, L. J.; Le, D.-B.; Jensen, L. D.; Smith, A. J.; Xiong, D.; Dahn, J. R. Introducing Symmetric Li-Ion Cells as a Tool to Study Cell Degradation Mechanisms. *J. Electrochem. Soc.* **2011**, *158*, A1417–A1422.

(278) Ping, P.; Wang, Q. S.; Sun, J. H.; Xia, X.; and Dahn, J. R. Studies of the Effect of Triphenyl Phosphate on the Negative Electrode of Li-Ion Cells. *J. Electrochem. Soc.* **2012**, *159*, A1460–A1466.

(279) Obrovac, M. N. A Model of the Electrochemistry of Chromium Substituted Lithium Manganese Oxides Based on Photoelectron Spectroscopy Valence Band Measurements, MSc. Thesis, Dalhousie University, 1997.

A- APPENDIX A

Table A.1 The target chemical composition and the elemental analysis results

$Li_{1+x}(Ni_{0.5}Mn_{0.5})_{1-x}O_2$			
ID	Sample	x	EA
2A	$LiNi_{0.5}Mn_{0.5}O_2$	0.00	$Li_{1.013}Ni_{0.489}Mn_{0.497}O_2$
2B	$Li_{1.04}Ni_{0.48}Mn_{0.48}O_2$	0.04	$Li_{1.059}Ni_{0.466}Mn_{0.474}O_2$
2C	$Li_{1.08}Ni_{0.46}Mn_{0.46}O_2$	0.08	$Li_{1.092}Ni_{0.448}Mn_{0.458}O_2$
2D	$Li_{1.12}Ni_{0.44}Mn_{0.44}O_2$	0.12	$Li_{1.127}Ni_{0.432}Mn_{0.439}O_2$
2E	$Li_{1.16}Ni_{0.42}Mn_{0.42}O_2$	0.16	$Li_{1.161}Ni_{0.415}Mn_{0.423}O_2$
2F	$Li_{1.20}Ni_{0.4}Mn_{0.4}O_2$	0.20	$Li_{1.194}Ni_{0.404}Mn_{0.402}O_2$
2G	$Li_{1.24}Ni_{0.38}Mn_{0.38}O_2$	0.24	$Li_{1.230}Ni_{0.381}Mn_{0.389}O_2$

$Li_{1+x}(Ni_{0.2}Mn_{0.8})_{1-x}O_2$			
ID	Sample	x	EA
3A	$Li_{1.20}Ni_{0.16}Mn_{0.64}O_2$	0.20	$Li_{1.166}Ni_{0.139}Mn_{0.694}O_2$
3B	$Li_{1.22}Ni_{0.156}Mn_{0.624}O_2$	0.22	$Li_{1.214}Ni_{0.134}Mn_{0.652}O_2$
3C	$Li_{1.24}Ni_{0.152}Mn_{0.608}O_2$	0.24	$Li_{1.215}Ni_{0.131}Mn_{0.654}O_2$
3D	$Li_{1.26}Ni_{0.148}Mn_{0.592}O_2$	0.26	$Li_{1.232}Ni_{0.128}Mn_{0.640}O_2$
3E	$Li_{1.28}Ni_{0.144}Mn_{0.576}O_2$	0.28	$Li_{1.247}Ni_{0.133}Mn_{0.620}O_2$
3F	$Li_{1.30}Ni_{0.14}Mn_{0.56}O_2$	0.30	$Li_{1.252}Ni_{0.126}Mn_{0.622}O_2$
3G	$Li_{1.32}Ni_{0.136}Mn_{0.544}O_2$	0.32	$Li_{1.271}Ni_{0.123}Mn_{0.606}O_2$

$Li_{1+x}(Ni_{0.6}Mn_{0.4})_{1-x}O_2$			
ID	Sample	x	EA
4A	$Li_{0.8}Ni_{0.72}Mn_{0.48}O_2$	-0.20	$Li_{0.785}Ni_{0.728}Mn_{0.487}O_2$
4B	$LiNi_{0.6}Mn_{0.4}O_2$	0.00	$Li_{0.985}Ni_{0.612}Mn_{0.403}O_2$
4C	$Li_{1.04}Ni_{0.576}Mn_{0.384}O_2$	0.04	$Li_{1.014}Ni_{0.593}Mn_{0.393}O_2$
4D	$Li_{1.08}Ni_{0.552}Mn_{0.368}O_2$	0.08	$Li_{1.061}Ni_{0.564}Mn_{0.375}O_2$
4E	$Li_{1.12}Ni_{0.528}Mn_{0.352}O_2$	0.12	$Li_{1.084}Ni_{0.551}Mn_{0.365}O_2$
4F	$Li_{1.16}Ni_{0.504}Mn_{0.336}O_2$	0.16	$Li_{1.133}Ni_{0.521}Mn_{0.345}O_2$

$Li_{1+x}(Ni_{0.7}Mn_{0.3})_{1-x}O_2$			
ID	Sample	x	EA
5A	$Li_{0.8}Ni_{0.84}Mn_{0.36}O_2$	-0.20	$Li_{0.779}Ni_{0.854}Mn_{0.0.36}O_2$
5B	$LiNi_{0.7}Mn_{0.3}O_2$	0.00	$Li_{0.934}Ni_{0.747}Mn_{0.315}O_2$
5C	$Li_{1.02}Ni_{0.686}Mn_{0.294}O_2$	0.02	$Li_{0.968}Ni_{0.724}Mn_{0.308}O_2$
5D	$Li_{1.04}Ni_{0.672}Mn_{0.288}O_2$	0.04	$Li_{0.972}Ni_{0.722}Mn_{0.305}O_2$
5E	$Li_{1.06}Ni_{0.658}Mn_{0.282}O_2$	0.06	$Li_{0.999}Ni_{0.701}Mn_{0.299}O_2$
5F	$Li_{1.08}Ni_{0.644}Mn_{0.276}O_2$	0.08	$Li_{1.018}Ni_{0.691}Mn_{0.291}O_2$

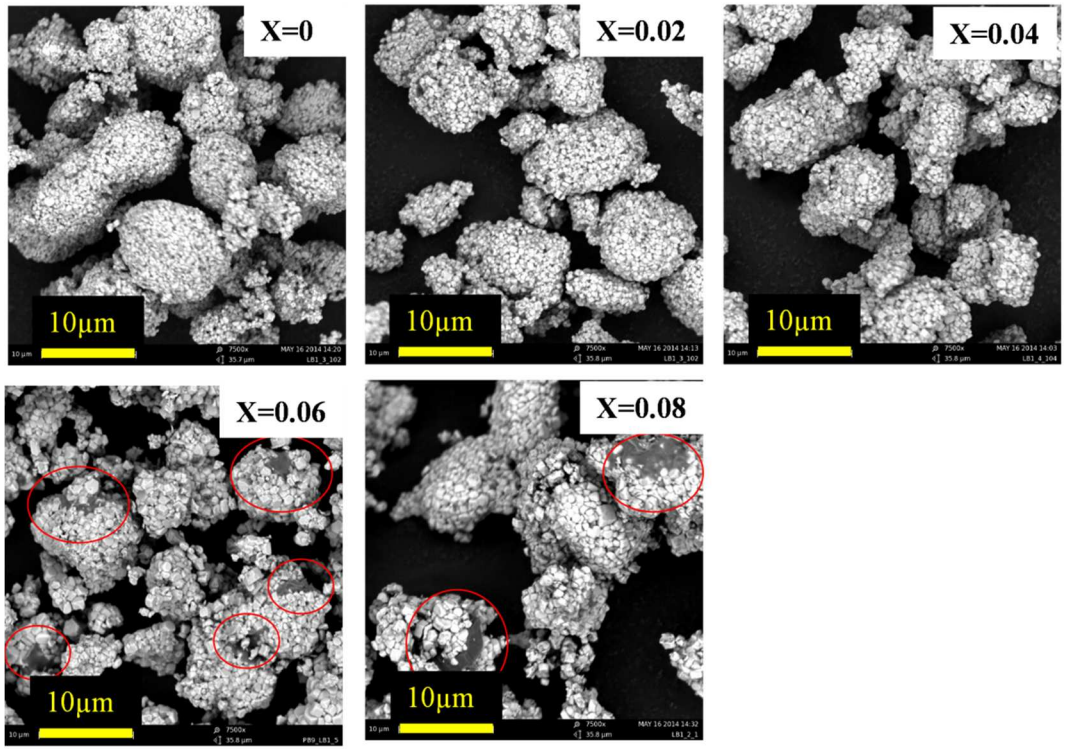

Figure A.1 SEM images of $Li_{1+x}(Ni_{0.7}Mn_{0.3})_{1-x}O_2$ ($0 \leq x \leq 0.08$). The red circles highlight the Li_2CO_3 residuals

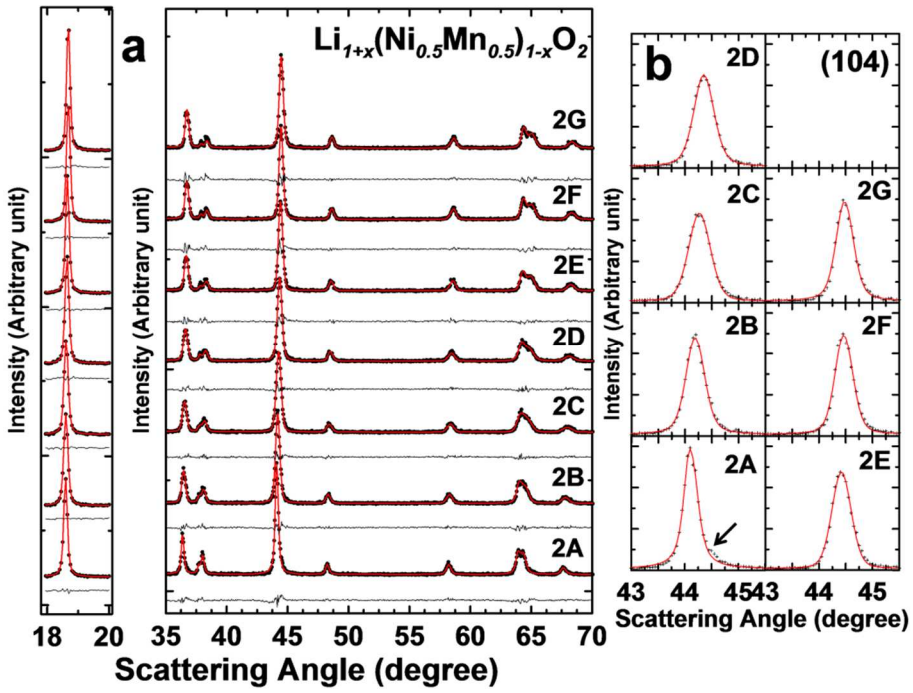

Figure A.2 (a) XRD patterns for samples of the composition series $Li_{1+x}(Ni_{0.5}Mn_{0.5})_{1-x}O_2$ ($0 \leq x \leq 0.24$). (b) An expanded view of the (104) reflection indexed in the R-3m space group. The arrow indicates the presence of a 2nd peak in sample 2A. The red lines are single-phase layered fits to the data. The cross symbols are the original data points.

Table A.2 XRD Rietveld refinement results for samples along the composition line $Li_{1+x}[Ni_{0.5}Mn_{0.5}]_{1-x}O_2$ with $0 \leq x \leq 0.24$.

$Li_{1+x}(Ni_{0.5}Mn_{0.5})_{1-x}O_2$							
ID	Sample	x	a(Å) (± 0.0004 Å)	c (Å) (± 0.002 Å)	Ni_{Li} (%)	Single phase	R-factor
2A	$LiNi_{0.5}Mn_{0.5}O_2$	0.00	2.8944	14.308	10.9	No	2.51
2B	$Li_{1.04}Ni_{0.48}Mn_{0.48}O_2$	0.04	2.8870	14.301	8.7	Yes	1.87
2C	$Li_{1.08}Ni_{0.46}Mn_{0.46}O_2$	0.08	2.8817	14.288	8.2	Yes	2.80
2D	$Li_{1.12}Ni_{0.44}Mn_{0.44}O_2$	0.12	2.8765	14.274	5.2	Yes	2.26
2E	$Li_{1.16}Ni_{0.42}Mn_{0.42}O_2$	0.16	2.8704	14.255	3.7	No*	2.29
2F	$Li_{1.20}Ni_{0.4}Mn_{0.4}O_2$	0.20	2.8678	14.250	2.2	No*	1.93
2G	$Li_{1.24}Ni_{0.38}Mn_{0.38}O_2$	0.24	2.8679	14.242	0.6	No*	2.72

* This co-existence is between the layered material and un-reacted Li_2CO_3.

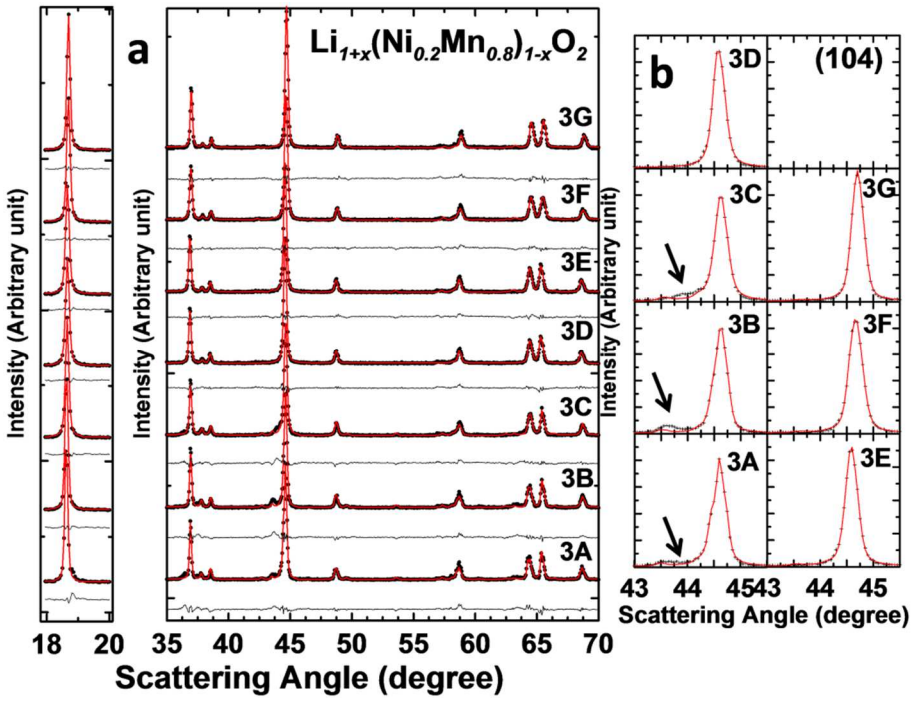

Figure A.3 (a) XRD patterns for samples of the composition series $Li_{1+x}(Ni_{0.2}Mn_{0.8})_{1-x}O_2$ ($0.20 \leq x \leq 0.32$). (b) An expanded view of the (104) reflection indexed in the R-3m space group. The arrow indicates the presence of a 2nd peak in sample 3A, 3B and 3C. The red lines are single-phase layered fits to the data. The cross symbols are the original data points.

Table A.3 XRD Rietveld refinement results for samples along the composition line $Li_{1+x}[Ni_{0.2}Mn_{0.8}]_{1-x}O_2$ with $0.20 \leq x \leq 0.32$.

$Li_{1+x}(Ni_{0.2}Mn_{0.8})_{1-x}O_2$							
ID	Sample	x	a(Å) (± 0.0004 Å)	c (Å) (± 0.002 Å)	Ni_{Li} (%)	Single phase	R-factor
3A	$Li_{0.20}Ni_{0.16}Mn_{0.64}O_2$	0.20	2.8521	14.278	2.228	No	6.04
3B	$Li_{1.22}Ni_{0.156}Mn_{0.624}O_2$	0.22	2.8512	14.275	1.29	No	4.94
3C	$Li_{1.24}Ni_{0.152}Mn_{0.608}O_2$	0.24	2.852	14.263	1.313	No	4.68
3D	$Li_{1.26}Ni_{0.148}Mn_{0.592}O_2$	0.26	2.8557	14.251	1.819	yes	2.94
3E	$Li_{1.28}Ni_{0.144}Mn_{0.576}O_2$	0.28	2.8533	14.242	1.635	yes	3.15
3F	$Li_{1.30}Ni_{0.14}Mn_{0.56}O_2$	0.30	2.8511	14.240	1.421	yes	3.22
3G	$Li_{1.32}Ni_{0.136}Mn_{0.544}O_2$	0.32	2.8478	14.231	1.022	yes	3.52

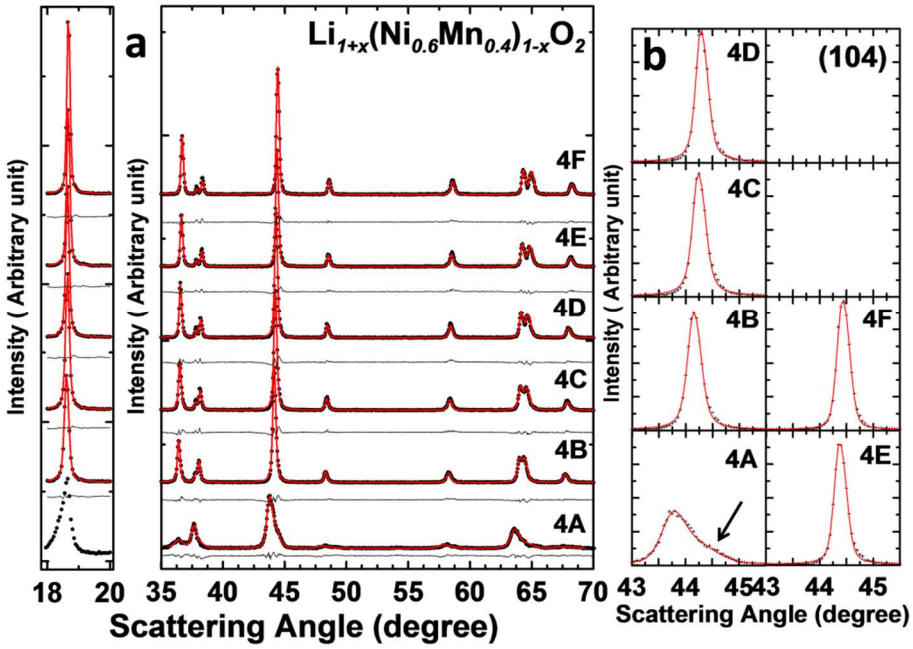

Figure A.4 (a) XRD patterns for samples of the composition series $Li_{1+x}(Ni_{0.6}Mn_{0.4})_{1-x}O_2$ ($-0.20 \leq x \leq 0.16$). (b) An expanded view of the (104) reflection indexed in the R-3m space group. The arrow indicates the presence of a 2nd peak in sample 4A. The red lines are single-phase layered fits to the data. The cross symbols are the original data points.

Table A.4 XRD Rietveld refinement results for samples along the composition line $Li_{1+x}[Ni_{0.6}Mn_{0.4}]_{1-x}O_2$ with $-0.20 \leq x \leq 0.16$.

$Li_{1+x}(Ni_{0.6}Mn_{0.4})_{1-x}O_2$							
ID	Sample	x	a(Å) (± 0.0004 Å)	c (Å) (± 0.002 Å)	Ni_{Li} (%)	Single phase	R-factor
4A	$Li_{0.8}Ni_{0.72}Mn_{0.48}O_2$	-0.20	2.8908	14.3629	17.49	No	1.87
4B	$LiNi_{0.6}Mn_{0.4}O_2$	0.00	2.8915	14.2907	11.287	yes	2.69
4C	$Li_{1.04}Ni_{0.576}Mn_{0.384}O_2$	0.04	2.8856	14.2822	8.572	yes	3.06
4D	$Li_{1.08}Ni_{0.552}Mn_{0.368}O_2$	0.08	2.8808	14.2721	6.594	yes	3.41
4E	$Li_{1.12}Ni_{0.528}Mn_{0.352}O_2$	0.12	2.8748	14.2604	4.594	No*	3.06
4F	$Li_{1.16}Ni_{0.504}Mn_{0.336}O_2$	0.16	2.8701	14.2487	2.553	No*	2.65

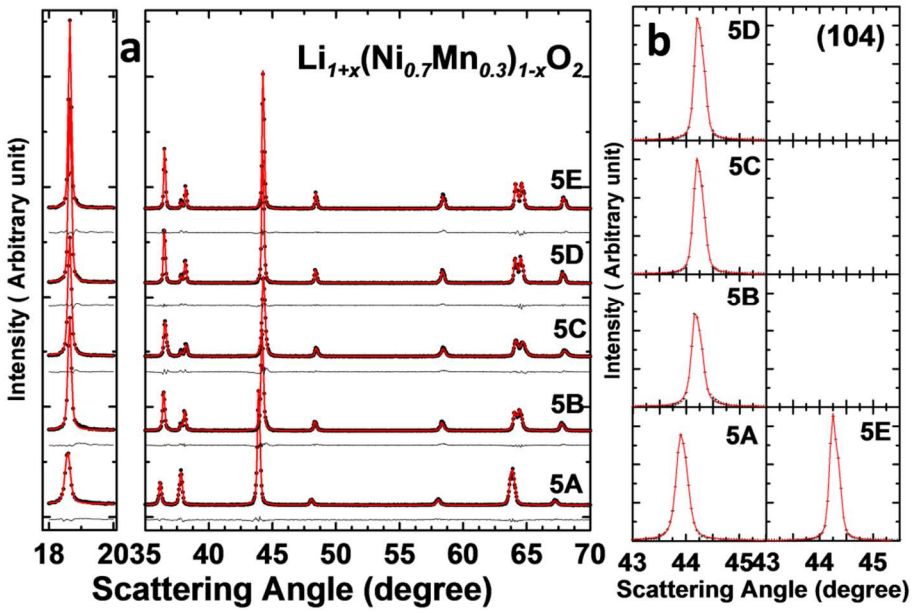

Figure A.5 (a) XRD patterns for samples of the composition series $Li_{1+x}(Ni_{0.7}Mn_{0.3})_{1-x}O_2$ ($-0.20 \leq x \leq 0.06$). (b) An expanded view of the (104) reflection indexed in the R-3m space group. The red lines are single-phase layered fits to the data. The cross symbols are the original data points.

Table A.5 XRD Rietveld refinement results for samples along the composition line $Li_{1+x}[Ni_{0.7}Mn_{0.3}]_{1-x}O_2$ with $-0.20 \leq x \leq 0.06$.

$Li_{1+x}(Ni_{0.7}Mn_{0.3})_{1-x}O_2$							
ID	Sample	x	a(Å) (± 0.0004 Å)	c (Å) (± 0.002 Å)	Ni_{Li} (%)	Single phase	R-factor
5A	$Li_{0.8}Ni_{0.84}Mn_{0.36}O_2$	-0.20	2.9115	14.3208	29.953	yes	2.85
5B	$LiNi_{0.7}Mn_{0.3}O_2$	0.00	2.8905	14.2807	11.223	yes	3.42
5C	$Li_{1.02}Ni_{0.686}Mn_{0.294}O_2$	0.02	2.883	14.2768	9.122	yes	2.39
5D	$Li_{1.04}Ni_{0.672}Mn_{0.288}O_2$	0.04	2.8869	14.2751	7.894	yes	2.53
5E	$Li_{1.06}Ni_{0.658}Mn_{0.282}O_2$	0.06	2.8837	14.2671	6.396	No*	2.73
5E+	$Li_{1.06}Ni_{0.658}Mn_{0.282}O_2$	0.06	2.8982	14.2886	12.7	yes	2.65

+ Samples were reheated to 900 °C for 10 hours to remove the un-reacted Li_2CO_3

Table A.6 XRD Rietveld refinement results for samples along the composition line $Li_{1+x}[Ni_{0.33}Mn_{0.67}]_{1-x}O_2$ with $0.20 \leq x \leq 0.32$.

$Li_{1+x}(Ni_{0.33}Mn_{0.67})_{1-x}O_2$							
ID	Sample	x	a(Å) (± 0.0004 Å)	c (Å) (± 0.002 Å)	Ni_{Li} (%)	Single phase	R-factor
6A	$Li_{1.2}Ni_{0.264}Mn_{0.536}O_2$	0.20	2.8633	14.2637	3.1	yes	4.13
6B	$Li_{1.24}Ni_{0.251}Mn_{0.509}O_2$	0.24	2.86	14.2488	2.29	yes	3.70
6C	$Li_{1.28}Ni_{0.238}Mn_{0.482}O_2$	0.28	2.8552	14.23510	1.32	yes	2.94
6D	$Li_{1.32}Ni_{0.224}Mn_{0.456}O_2$	0.32	2.8556	14.24250	1.7	No*	2.53

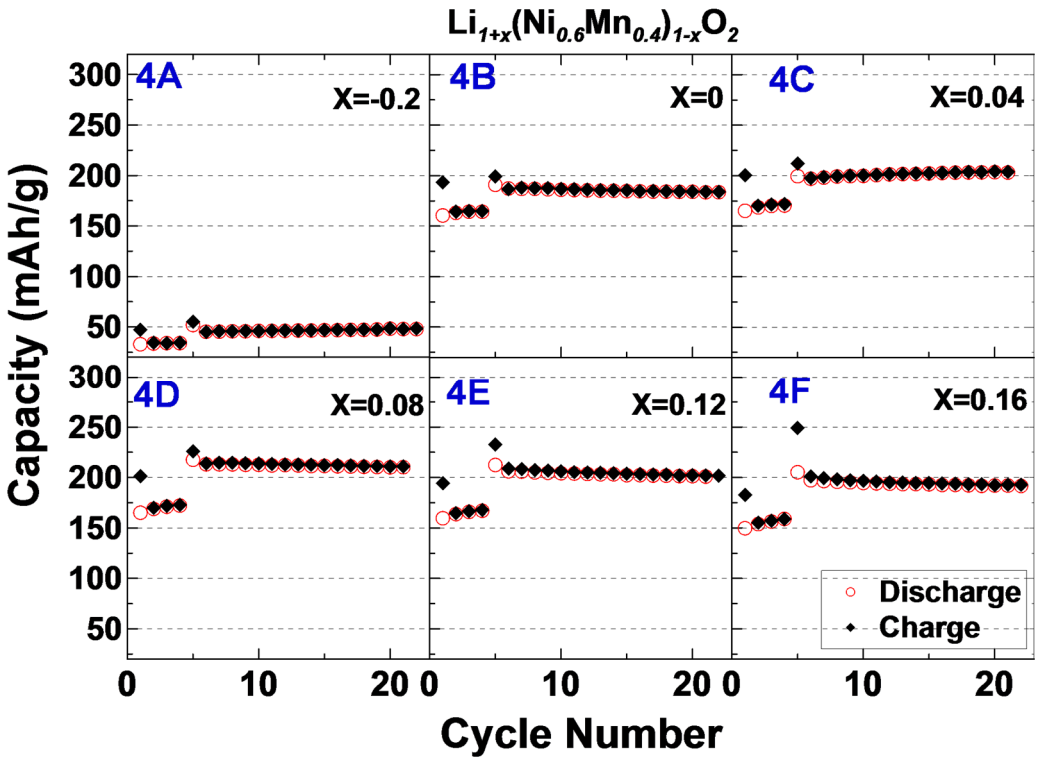

Figure A.6 Cycling performance of samples along the composition series $Li_{1+x}(Ni_{0.6}Mn_{0.4})_{1-x}O_2$ ($-0.20 \leq x \leq 0.16$). The cells were first tested between 2.5 – 4.4 V for four cycles, then charged to 4.8 V for one cycle and followed by cycling between 2.5–4.6 V.

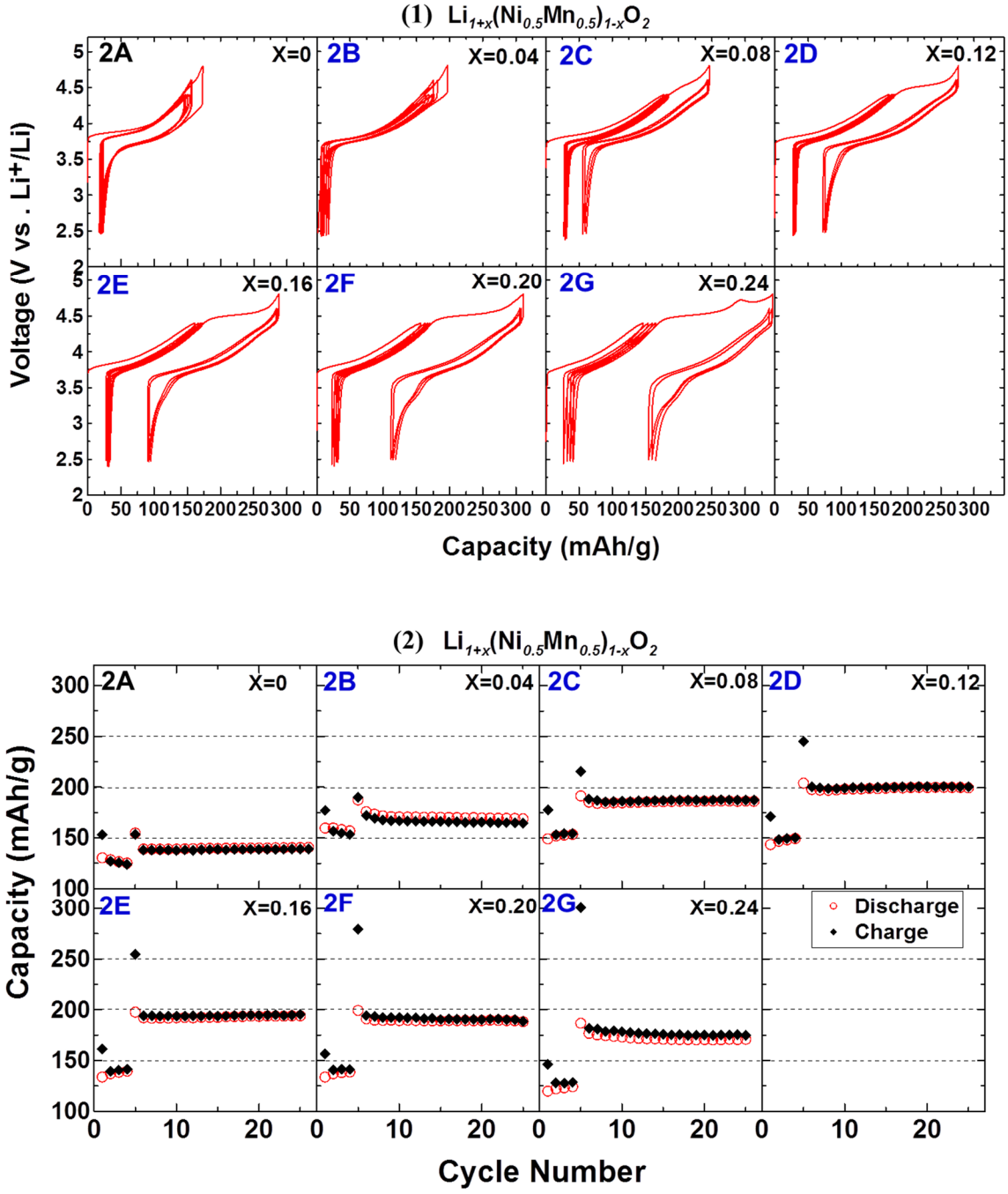

Figure A.7 The voltage-capacity curves (1) and capacity as a function of cycle number (2) for samples along the composition series $Li_{1+x}(Ni_{0.5}Mn_{0.5})_{1-x}O_2$ ($0 \leq x \leq 0.24$). The cells were first tested between 2.5 – 4.4 V for four cycles, then charged to 4.8 V for one cycle and followed by cycling between 2.5–4.6V. The blue labels indiacte the single phase materials.

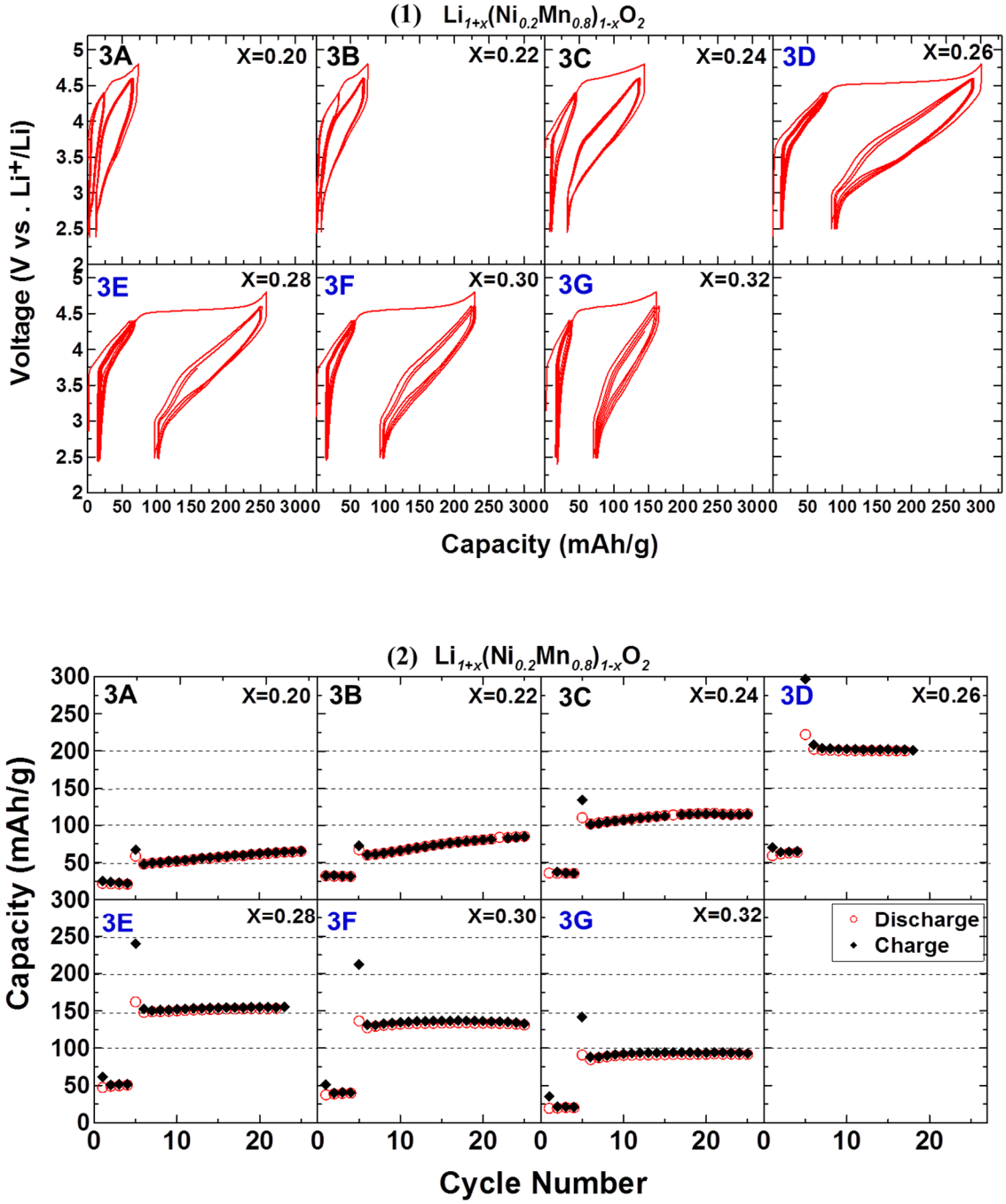

Figure A.8 The voltage-capacity curves and capacity as a function of cycle number for samples along the composition series $Li_{1+x}(Ni_{0.2}Mn_{0.8})_{1-x}O_2$ ($0.2 \leq x \leq 0.32$). The cells were first tested between 2.5 – 4.4 V for four cycles, then charged to 4.8 V for one cycle and followed by cycling between 2.5–4.6 V.

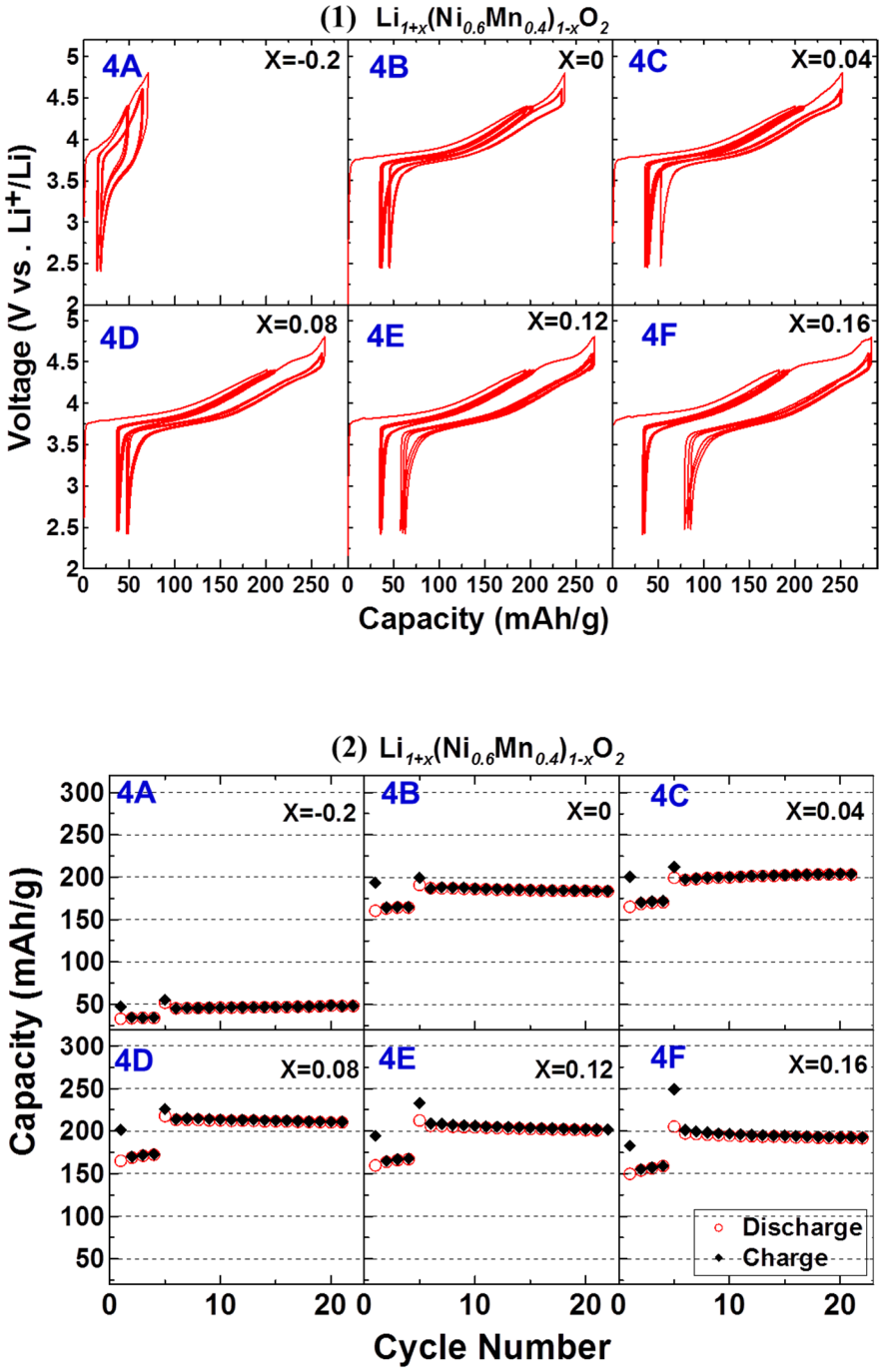

Figure A.9 The voltage curves of samples along the composition series $Li_{1+x}(Ni_{0.6}Mn_{0.4})_{1-x}O_2$ ($0 \leq x \leq 0.16$). The cells were first tested between 2.5 – 4.4 V for four cycles, then charged to 4.8 V for one cycle and followed by cycling between 2.5–4.6 V.

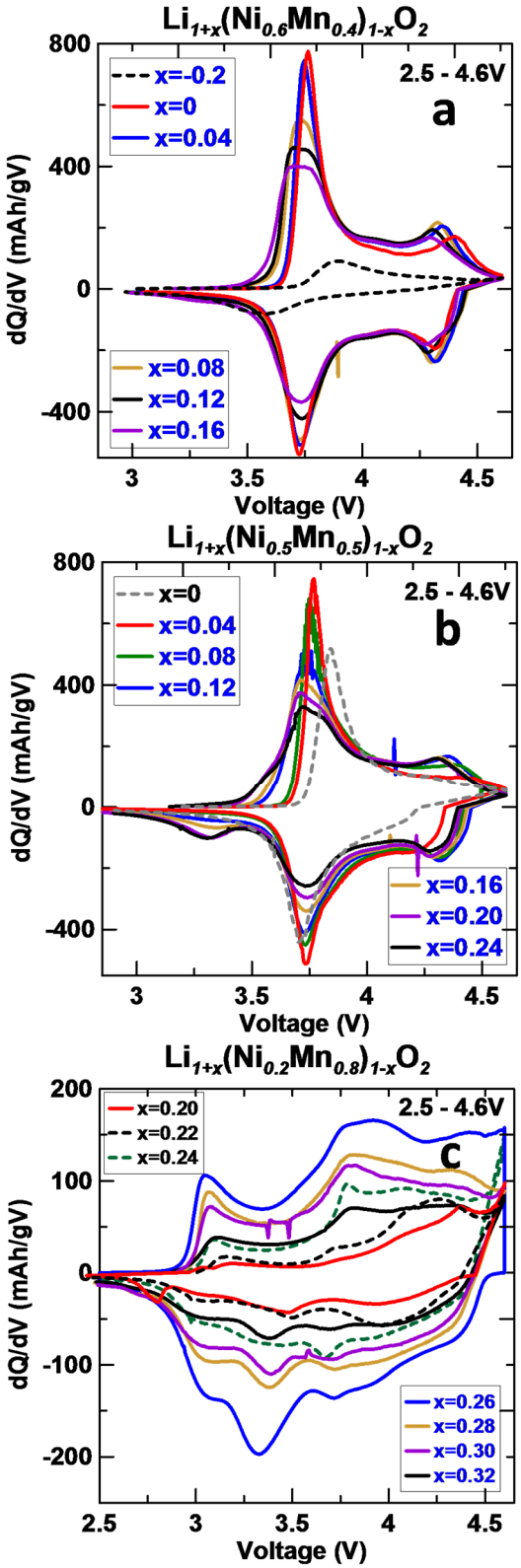

Figure A.10 Differential capacity (dQ/dV) vs potential (the 5th cycle after charging to 4.8 V) for the series (a) $Li_{1+x}(Ni_{0.6}Mn_{0.4})_{1-x}O_2$ ($-0.20 \leq x \leq 0.16$) and (b) $Li_{1+x}(Ni_{0.5}Mn_{0.5})_{1-x}O_2$ ($0 \leq x \leq 0.24$) (c) $Li_{1+x}(Ni_{0.2}Mn_{0.8})_{1-x}O_2$ ($0.20 \leq x \leq 0.32$) between 2.5 – 4.6V.

B- APPENDIX B

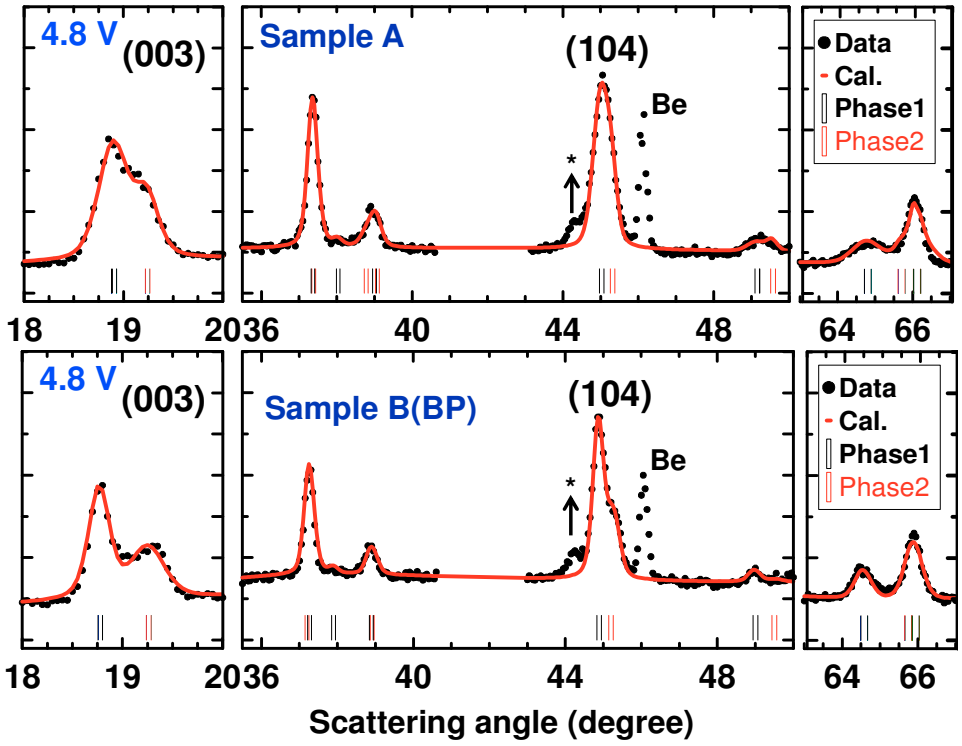

Figure B.1 Examples of the two-phase fitting for Sample A and Sample B(BP) at the top of charge (4.8 V). The stars indicate the peak from some impurities.

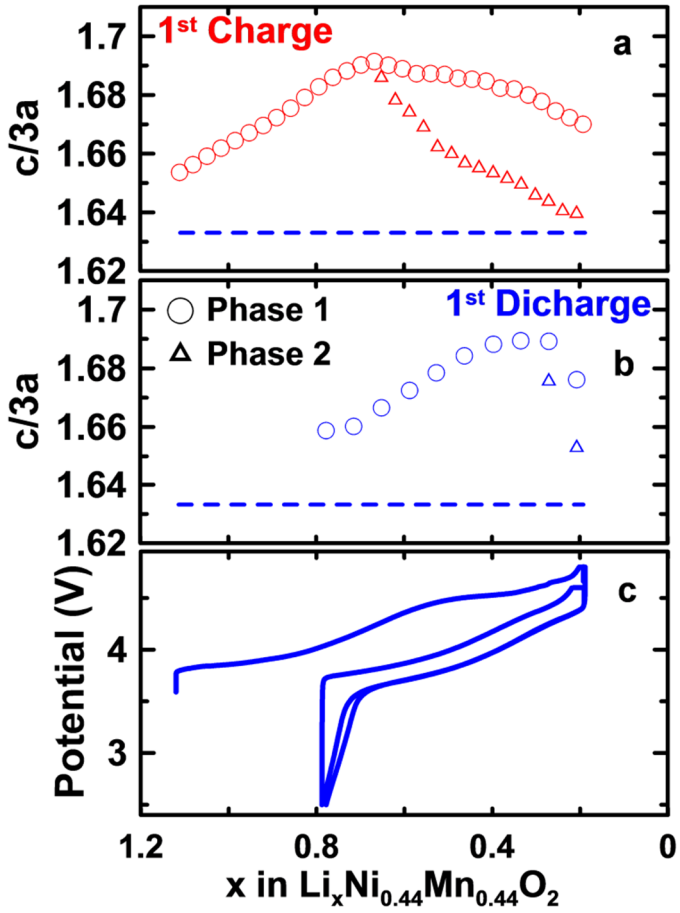

Figure B.2 The c/3a ratio of the two phases during the first charge (a) and discharge (b) as well as the cell voltage during the first cycle as a function of the lithium content (x in $Li_xNi_{0.44}Mn_{0.44}O_2$) for sample A. The blue dashed line shows the ideal cubic closed packed (ccp) value of 1.633 that is expected for a long-range spinel ordering.

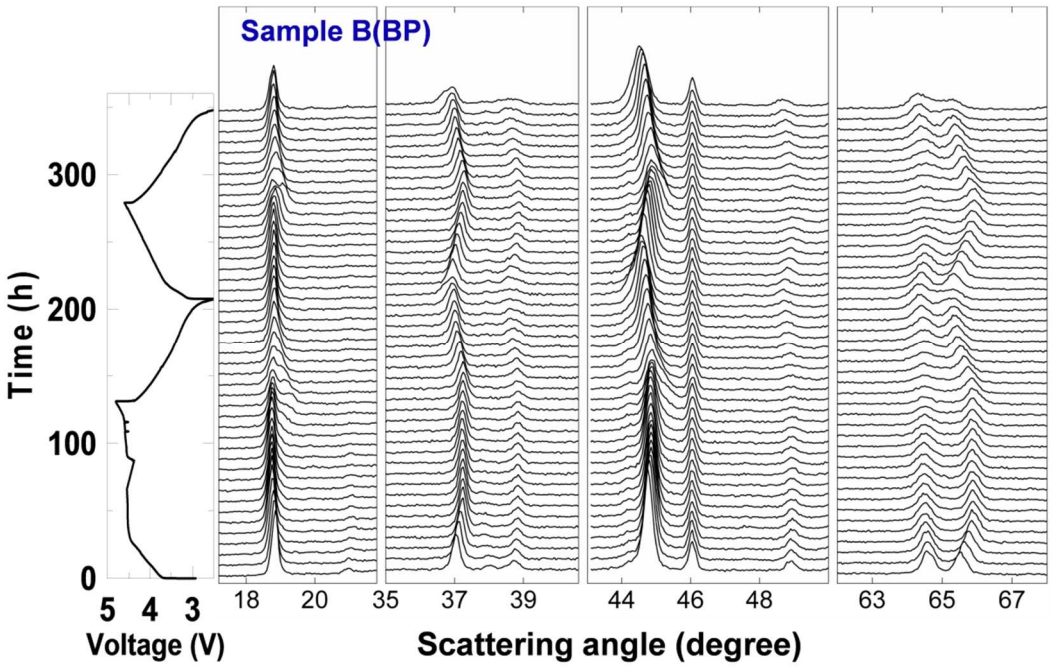

Figure B.3 The *in-situ* cell voltage and XRD patterns of sample B(BP) as a function of time (Two cycles). Only every third pattern is shown for clarity.

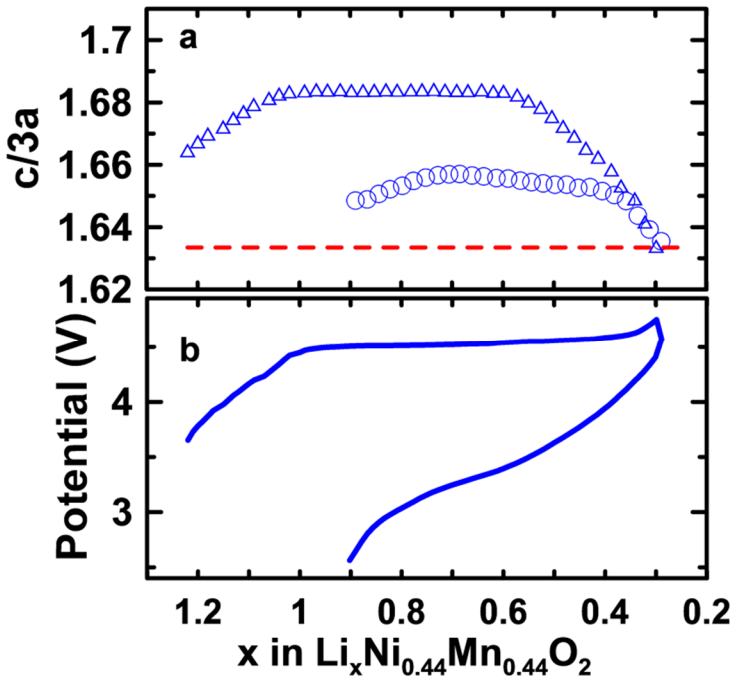

Figure B.4 The c/3a ratio (a) and the cell voltage (b) for sample B(SP) during the first cycle as a function of the lithium content (x in $Li_xNi_{0.44}Mn_{0.44}O_2$). The blue dashed line shows the ideal cubic closed packed (ccp) value of 1.633 that is expected for a long-range spinel structure. The blue triangles show the bulk phase and the blue circles show the surface phase.

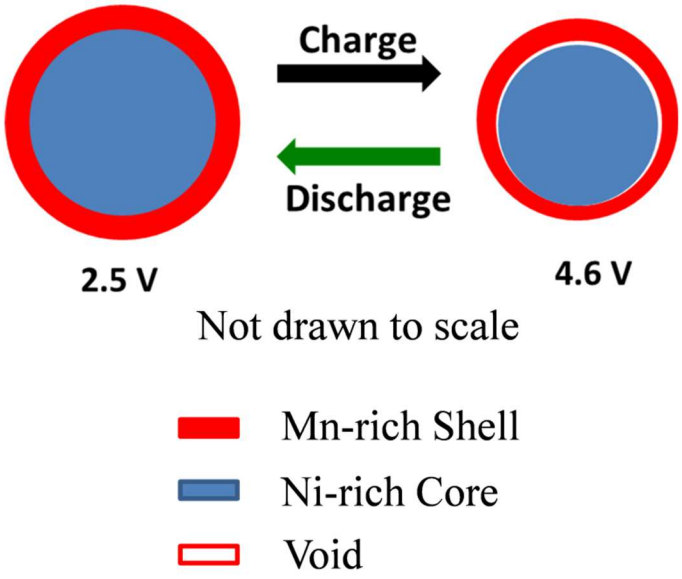

Figure B.5 The unit cell volume of the Ni-rich core changes faster than the Mn-rich shell with voltage during charge and discharge. This suggests that there should not be a pressure build up between the core and shell materials (same potential) during cycling in core-shell structures, that contain nickel rich materials as the core (e.g. NMC811) and Mn-rich materials as the shell (e.g. sample B).

C- APPENDIX C

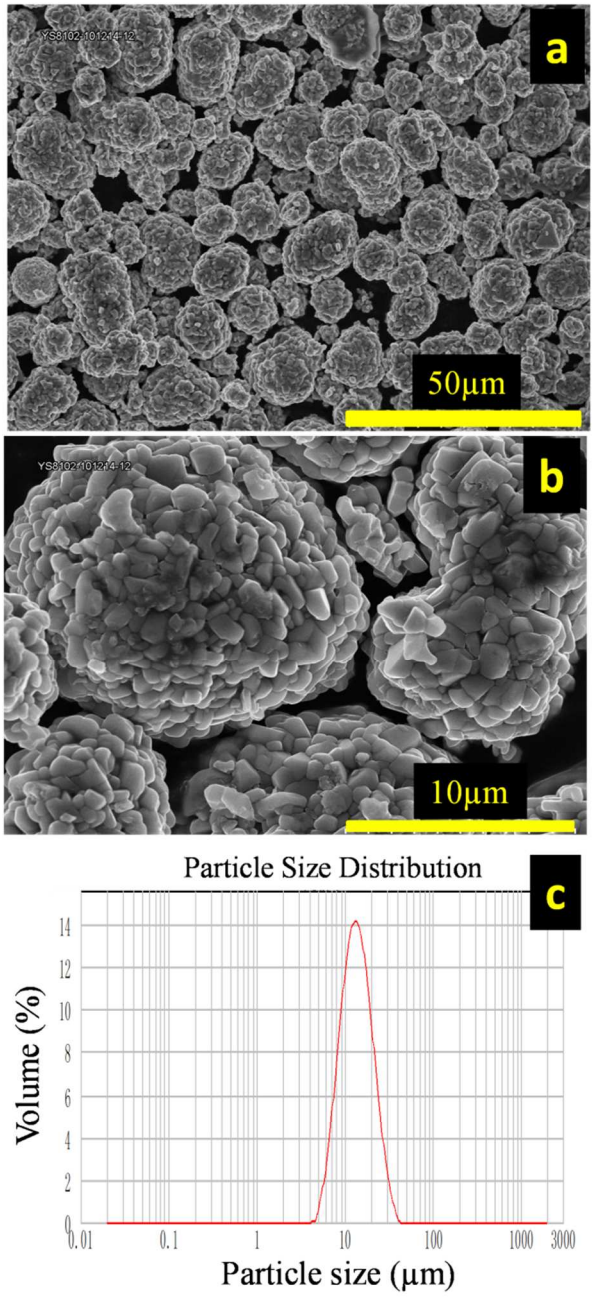

Figure C.1 Scanning electron microscopy images of NMC811 particles (a,b) and the particle size distribution (c). The data were provided by Li-Fun

Table C.1 Elemental composition of NMC811 provided by Li-Fun.

Item	Unit	Requirement	Typical
Co+Ni+Mn	wt%	57.00-59.50	58.73
Ni	wt%	45.00-47.00	45.8
Co	wt%	7.00-8.00	7.42
Mn	wt%	4.50-5.50	5
Li	wt%	7.30-7.65	7.4
Fe	wt%	≤0.0050	0.0015
Cu	wt%	≤0.0050	0.0024
Ca	wt%	≤0.0050	0.0022
Na	wt%	≤0.0150	0.0108
Zn	wt%	≤0.0050	0.0004
PH	-	11.5-12.00	11.77
H_2O	wt%	≤0.050	0.0250

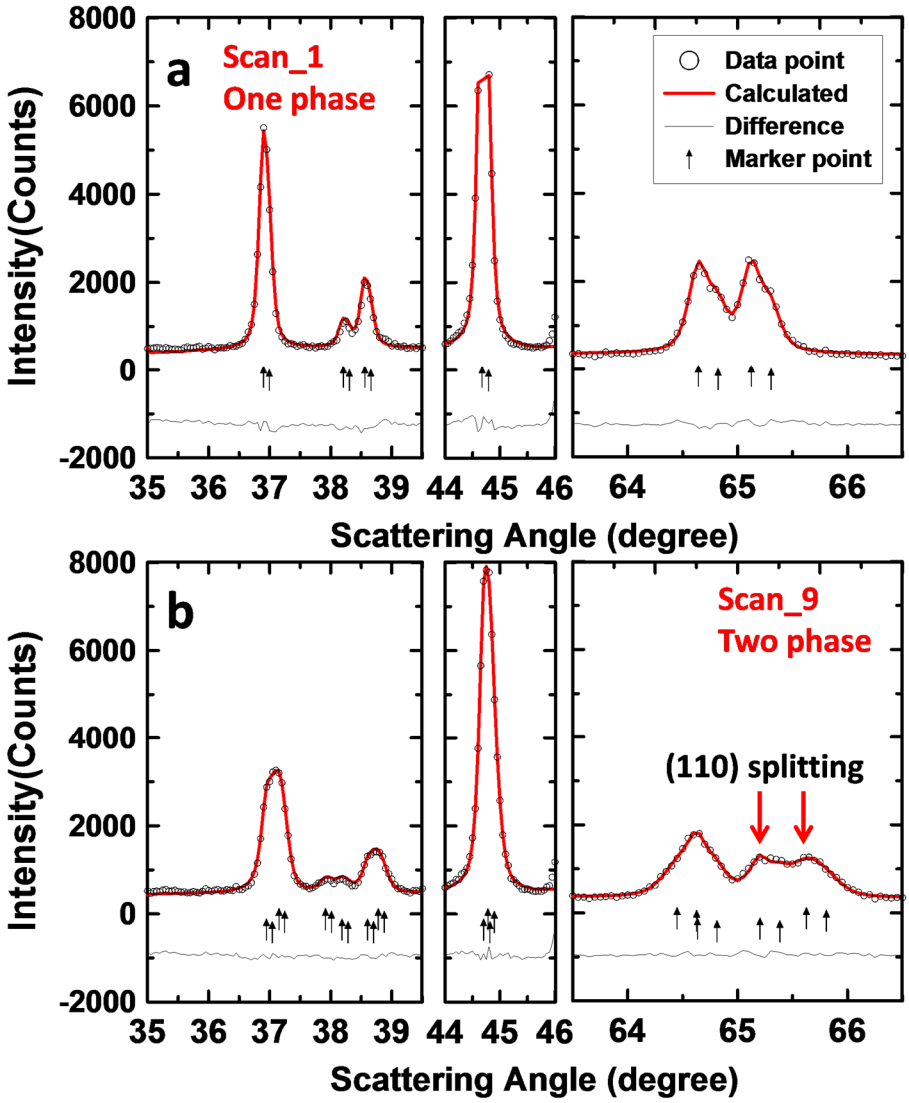

Figure C.2 X-ray diffraction patterns with Rietveld refinement of the first scan showing single phase material (a), the ninth scan showing two-phases in the sample (b).

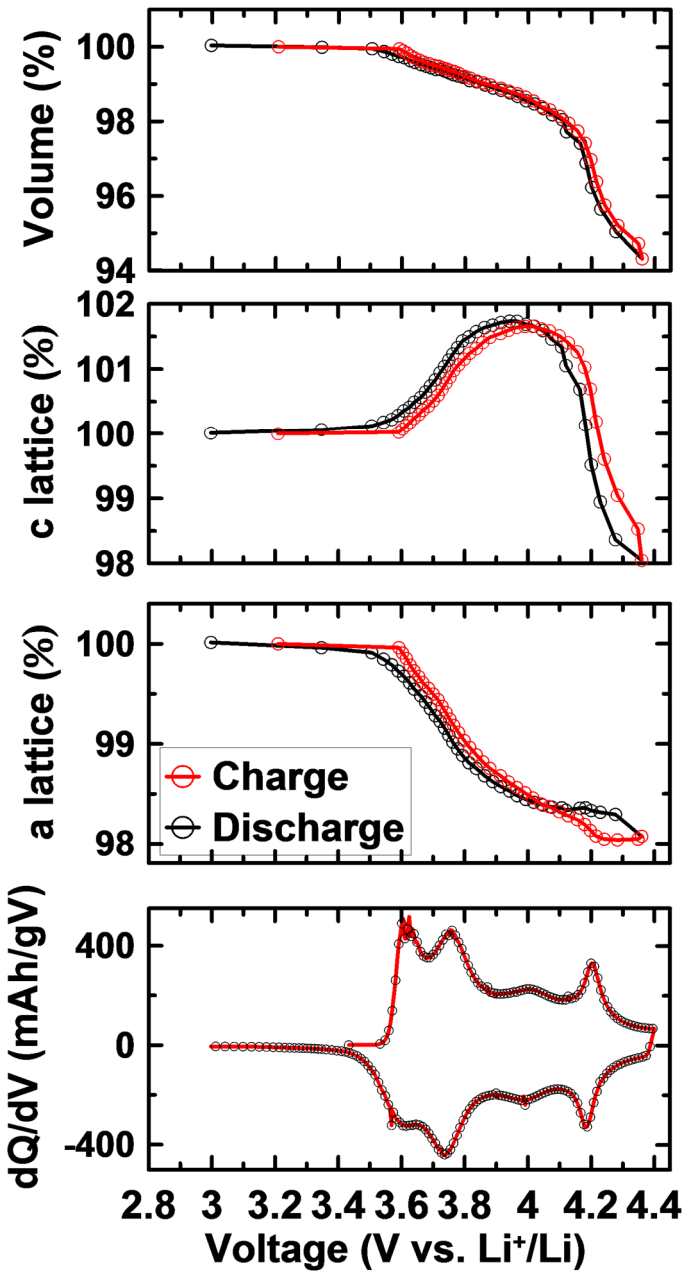

Figure C.3 Percent changes in the unit cell parameters including unit cell volume, c-axis and a-axis as well as dQ/dV as a function of cell voltage during the second cycle.

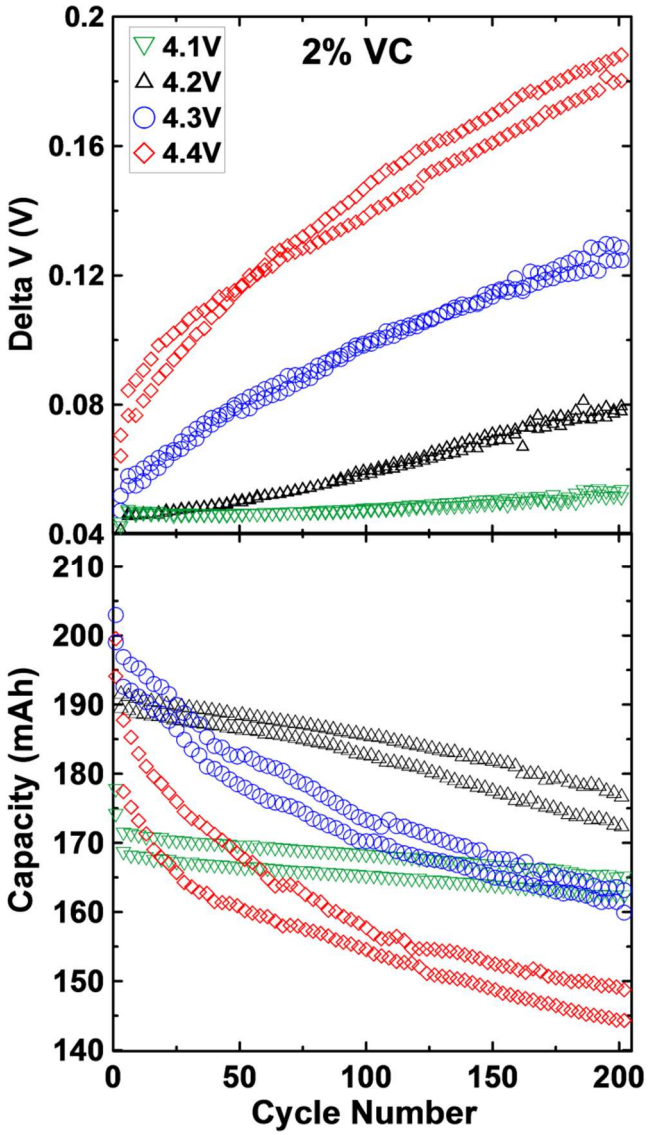

Figure C.4 Capacity (a) and ΔV (b) of NMC811/graphite cells with 2% VC as a function of cycle number for 200 cycles at a rate of C/5 in a temperature box at 30°C.

D- APPENDIX D

Table D.1 Elemental Analysis results. The average compositions for the CS samples are shown.

$Li_{1+x}(Ni_{0.67}Mn_{0.33})_{1-x}O_2$			
ID	Sample	x	Elemental Analysis
1	$LiNi_{0.67}Mn_{0.33}O_2$	0.00	$Li_{0.954}Ni_{0.679}Mn_{0.367}O_2$
2	$Li_{1.02}Ni_{0.653}Mn_{0.326}O_2$	0.02	$Li_{0.978}Ni_{0.667}Mn_{0.355}O_2$
3	$Li_{1.04}Ni_{0.64}Mn_{0.32}O_2$	0.04	$Li_{0.993}Ni_{0.658}Mn_{0.348}O_2$
4	$Li_{1.06}Ni_{0.627}Mn_{0.313}O_2$	0.06	$Li_{0.998}Ni_{0.653}Mn_{0.348}O_2$
5	$Li_{1.08}Ni_{0.613}Mn_{0.307}O_2$	0.08	$Li_{1.021}Ni_{0.636}Mn_{0.343}O_2$

$Li_{1+x}(Ni_{0.2}Mn_{0.6}Co_{0.2})_{1-x}O_2$			
ID	Sample	x	Elemental Analysis
1	$Li_{1.12}Ni_{0.176}Mn_{0.528}Co_{0.176}O_2$	0.12	$Li_{1.083}Ni_{0.174}Mn_{0.559}Co_{0.187}O_2$
2	$Li_{1.16}Ni_{0.168}Mn_{0.504}Co_{0.168}O_2$	0.16	$Li_{1.127}Ni_{0.164}Mn_{0.533}Co_{0.175}O_2$
3	$Li_{1.2}Ni_{0.16}Mn_{0.48}Co_{0.16}O_2$	0.20	$Li_{1.163}Ni_{0.159}Mn_{0510}Co_{0.168}O_2$
4	$Li_{1.24}Ni_{0.152}Mn_{0.456}Co_{0.152}O_2$	0.24	$Li_{1.176}Ni_{0.155}Mn_{0.504}Co_{0.165}O_2$
5	$Li_{1.28}Ni_{0.144}Mn_{0.432}Co_{0.144}O_2$	0.28	$Li_{1.193}Ni_{0.155}Mn_{0.491}Co_{0.161}O_2$

$Li_{1+x}(Ni_{0.4}Mn_{0.5}Co_{0.1})_{1-x}O_2$			
ID	Sample	x	Elemental Analysis
1	$LiNi_{0.4}Mn_{0.5}Co_{0.1}O_2$	0	$Li_{0.958}Ni_{0.389}Mn_{0.544}Co_{0.108}O_2$
2	$Li_{1.04}Ni_{0.384}Mn_{0.48}Co_{0.096}O_2$	0.04	$Li_{0.996}Ni_{0.375}Mn_{0.524}Co_{0.104}O_2$
3	$Li_{1.08}Ni_{0.368}Mn_{0.46}Co_{0.092}O_2$	0.08	$Li_{1.072}Ni_{0.353}Mn_{0.478}Co_{0.096}O_2$
4	$Li_{1.12}Ni_{0.352}Mn_{0.44}Co_{0.088}O_2$	0.12	$Li_{1.091}Ni_{0.336}Mn_{0.478}Co_{0.094}O_2$
5	$Li_{1.16}Ni_{0.336}Mn_{0.42}Co_{0.084}O_2$	0.16	$Li_{1.104}Ni_{0.339}Mn_{0.463}Co_{0.092}O_2$

$0.67Li_{1+x}(Ni_{0.67}Mn_{0.33})_{1-x}O_2 \bullet 0.\ Li_{1+y}(Ni_{0.4}Mn_{0.5}Co_{0.1})_{1-y}O_2$

CS2 average composition

ID	Sample	(x,y)	Elemental Analysis
1	$Li\ Ni_{0.578}Mn_{0.389}Co_{0.033}O_2$	(0, 0)	$Li_{0.965}\ Ni_{0.581}\ Mn_{0.418}Co_{0.036}O_2$
2	$Li_{1.027}\ Ni_{0.564}\ Mn_{0.378}Co_{0.032}O_2$	(0.02, 0.04)	$Li_{0.987}\ Ni_{0.571}\ Mn_{0.405}Co_{0.036}O_2$
3	$Li_{1.053}\ Ni_{0.549}\ Mn_{0.367}Co_{0.031}O_2$	(0.04, 0.08)	$Li_{1.004}Ni_{0.556}\ Mn_{0.402}Co_{0.037}O_2$
4	$Li_{1.08}Ni_{0.535}\ Mn_{0.356}Co_{0.029}O_2$	(0.06, 0.12)	$Li_{1.033}Ni_{0.543}\ Mn_{0.388}Co_{0.034}O_2$

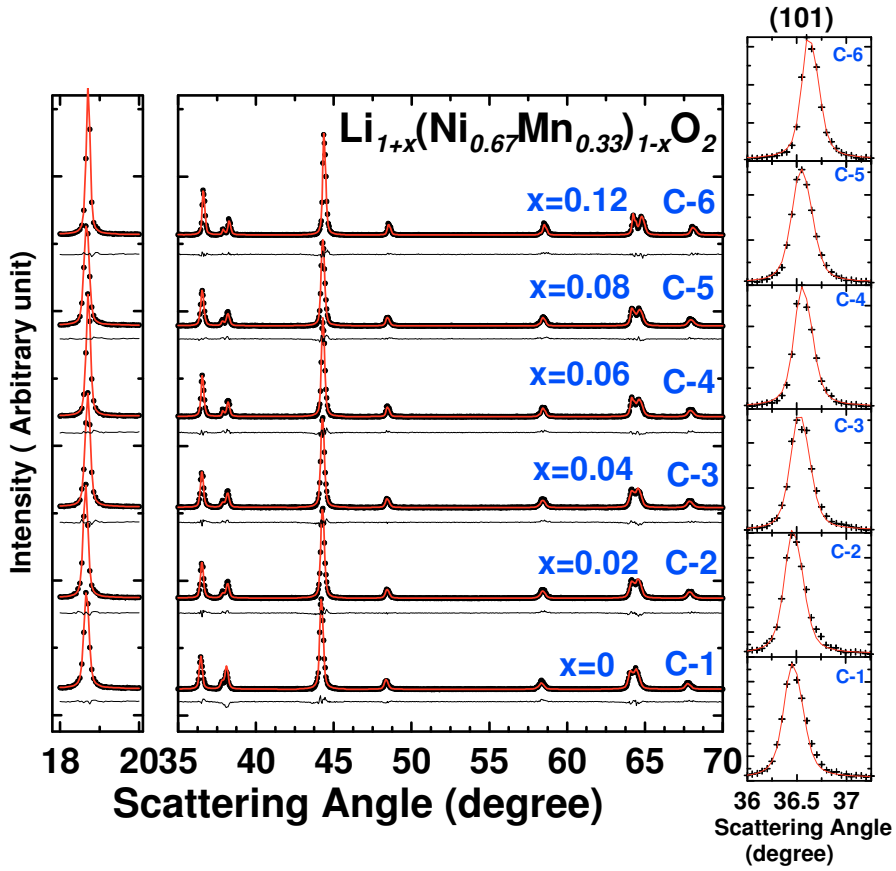

Figure D.1 XRD patterns for the core series $Li_{1+x}(Ni_{0.67}Mn_{0.33})_{1-x}O_2$.

Table D.2 Rietveld refinement results for the core series

$Li_{1+x}(Ni_{0.67}Mn_{0.33})_{1-x}O_2$							
ID	Sample	x	a(Å) (± 0.0004)	c (Å) (± 0.002)	Ni_{Li} (%)	Single phase	R-factor
C-1	$Li\ Ni_{0.67}Mn_{0.33}O_2$	0.00	2.8913	14.281	19.4	yes	5.67
C-2	$Li_{1.02}Ni_{0.656}Mn_{0.323}O_2$	0.02	2.8881	14.272	10.4	yes	3.77
C-3	$Li_{1.04}Ni_{0.643}Mn_{0.317}O_2$	0.04	2.8876	14.273	8.9	yes	3.45
C-4	$Li_{1.06}Ni_{0.629}Mn_{0.310}O_2$	0.06	2.8860	14.270	7.6	Yes	4.31
C-5	$Li_{1.08}Ni_{0.616}Mn_{0.303}O_2$	0.08	2.8829	14.264	6.8	Yes	3.43
C-6	$Li_{1.12}Ni_{0.589}Mn_{0.290}O_2$	0.12	2.8784	14.253	5.4	No*	3.61

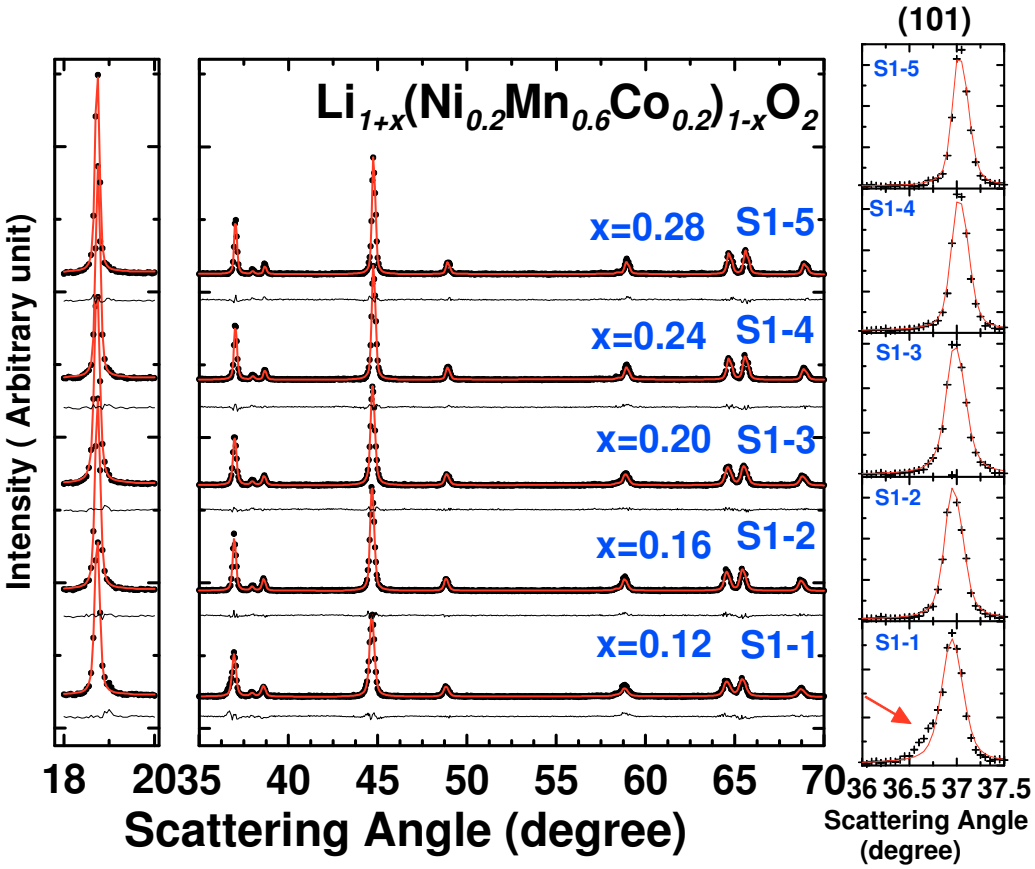

Figure D.2 XRD patterns for the S1 series $Li_{1+x}(Ni_{0.2}Mn_{0.6}Co_{0.2})_{1-x}O_2$.

Table D.3 Rietveld refinement results for the S1 series.

$Li_{1+x}(Ni_{0.2}Mn_{0.6}Co_{0.2})_{1-x}O_2$							
ID	Sample	x	a(Å) (± 0.0004 Å)	c (Å) (± 0.002 Å)	Ni_{Li} (%)	Single phase	R-factor
S1-1	$Li_{1.12}Ni_{0.176}Mn_{0.528}Co_{0.176}O_2$	0.12	2.854	14.237	2.3	No	3.52
S1-2	$Li_{1.16}Ni_{0.168}Mn_{0.504}Co_{0.168}O_2$	0.16	2.854	14.239	1.4	yes	3.16
S1-3	$Li_{1.20}Ni_{0.16}Mn_{0.48}Co_{0.16}O_2$	0.20	2.8497	14.222	0.3	yes	2.5
S1-4	$Li_{1.24}Ni_{0.152}Mn_{0.456}Co_{0.152}O_2$	0.24	2.8470	14.213	0.3	Yes	3.25
S1-5	$Li_{1.28}Ni_{0.144}Mn_{0.432}Co_{0.144}O_2$	0.28	2.8450	14.209	0.03	Yes	3.38
S1-6	$Li_{1.28}Ni_{0.136}Mn_{0.408}Co_{0.136}O_2$	0.32	2.8434	14.201	0.02	NO*	3.12

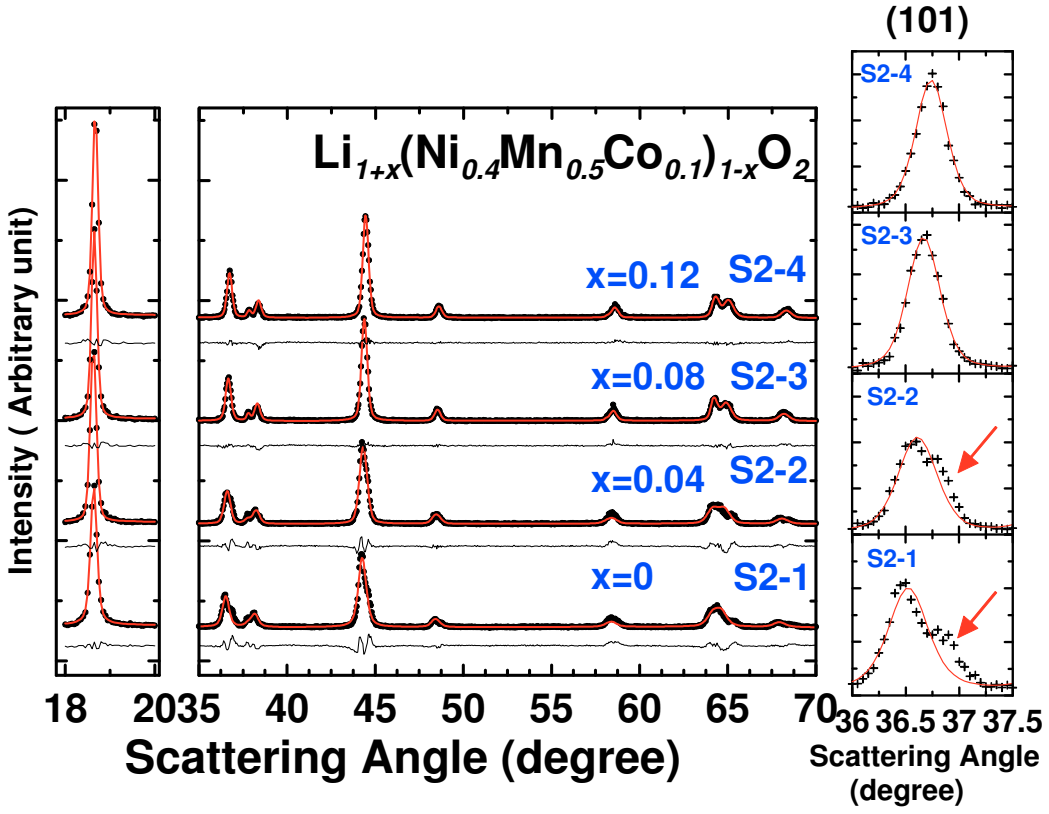

Figure D.3 XRD patterns for the S2 series $Li_{1+x}(Ni_{0.4}Mn_{0.5}Co_{0.1})_{1-x}O_2$.

Table D.4 Rietveld refinement results for the S2 series

$Li_{1+x}(Ni_{0.4}Mn_{0.5}Co_{0.1})_{1-x}O_2$							
ID	Sample	x	a(Å) (± 0.0004)	c (Å) (± 0.002)	Ni_{Li} (%)	Single phase	R-factor
S2-1	$LiNi_{0.4}Mn_{0.5}Co_{0.1}O_2$	0	2.8836	14.272	9.3	No	5.09
S2-2	$Li_{1.04}Ni_{0.384}Mn_{0.48}Co_{0.096}O_2$	0.04	2.8779	14.293	9.3	No	4.8
S2-3	$Li_{1.08}Ni_{0.368}Mn_{0.46}Co_{0.092}O_2$	0.08	2.8738	14.280	8.4	yes	3.28
S2-4	$Li_{1.12}Ni_{0.352}Mn_{0.44}Co_{0.088}O_2$	0.12	2.8688	14.267	7.3	Yes	3.1

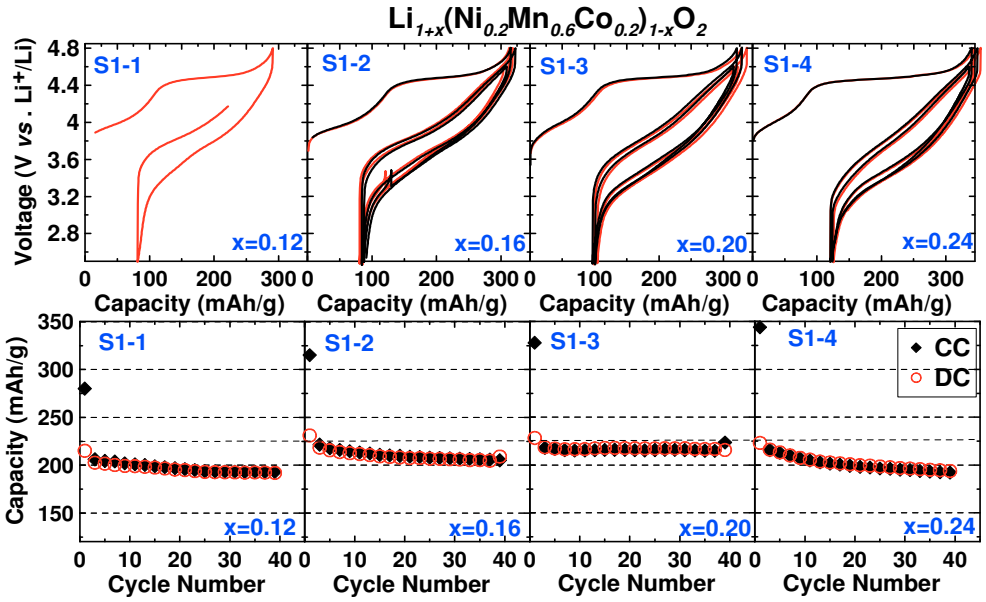

Figure D.4 Voltage versus capacity curves and capacity as a function of cycle number for the S1 series with the composition of $Li_{1+x}(Ni_{0.2}Mn_{0.6}Co_{0.2})_{1-x}O_2$.

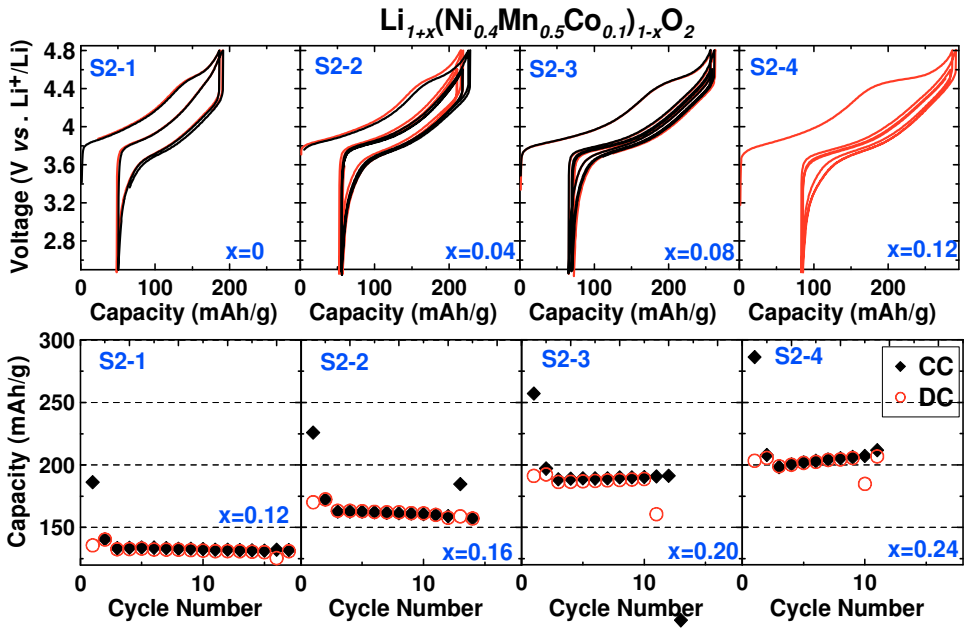

Figure D.5 Voltage versus capacity curves and capacity as a function of cycle number for the S2 series with the composition of $Li_{1+x}(Ni_{0.4}Mn_{0.5}Co_{0.1})_{1-x}O_2$.

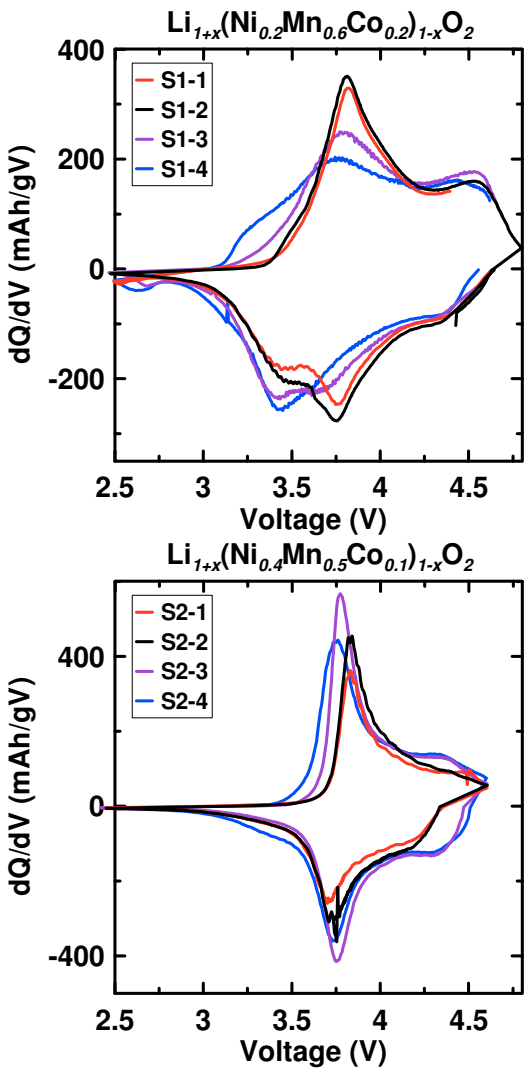

Figure D.6 The differential capacity as a function of the cell voltage (vs Li^+/Li) (dQ/dV) between 2.5 – 4.6 V for S1 and S2 series after the charge to 4.8 V (the third cycle).

E- APPENDIX E

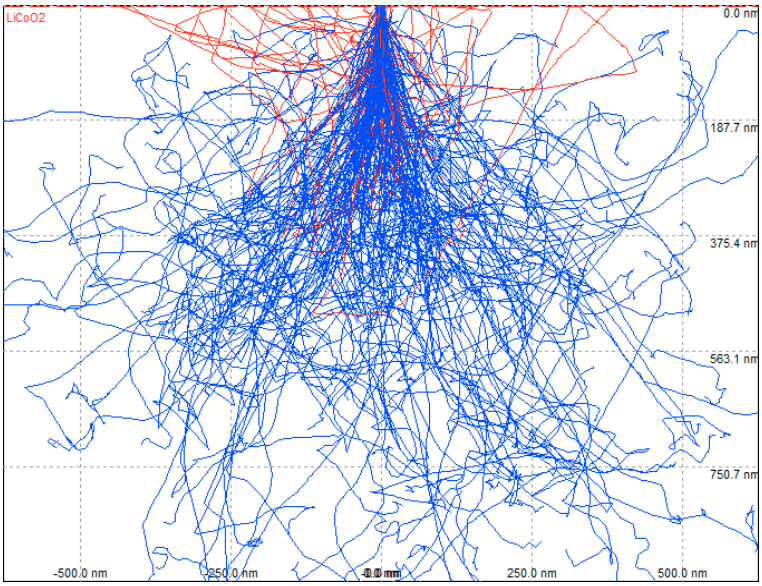

Figure E.1 Electron trajectory in a thin film of $LiCoO_2$ (1000 nm) with a density of 5.09 g/cc simulated with a 15 kV accelerating voltage and 15 mA current using CASINO.

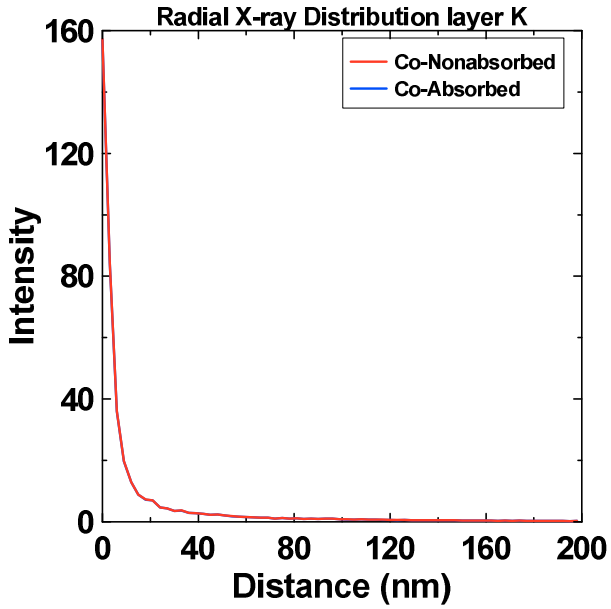

Figure E.2 Radial Co K-edge X-ray distribution for the thin film of $LiCoO_2$ simulated with a 15 kV ccelerating voltage and 15 mA current using CASINO.

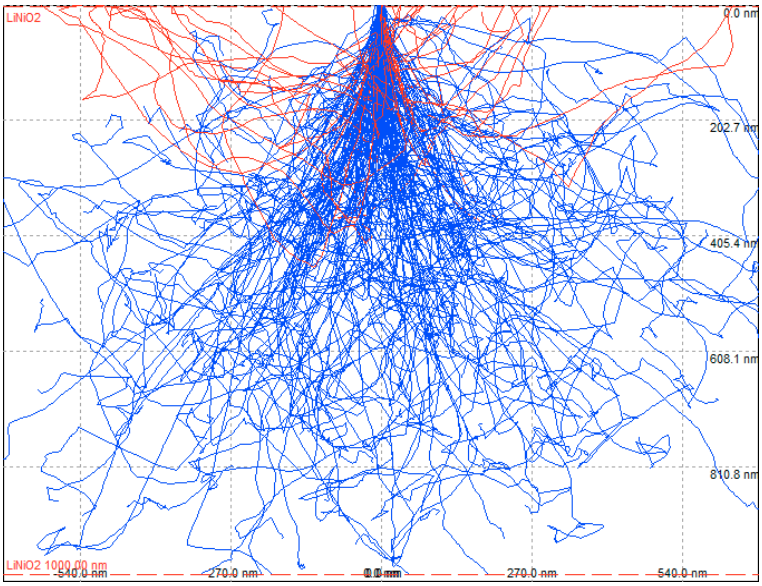

Figure E.3 Electron trajectory in a thin film of $LiNiO_2$ (1000nm), simulated with a 15 kV accelerating voltage and 15 mA current using CASINO.

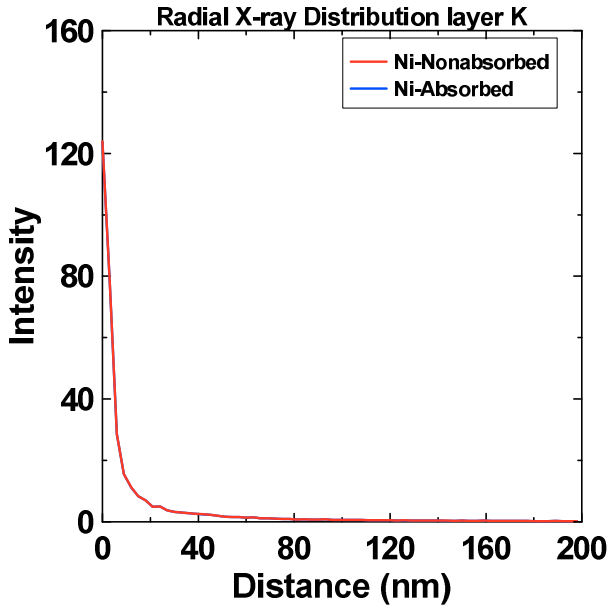

Figure E.4 Radial Ni K-edge X-ray distribution for the thin film of $LiNiO_2$ simulated with a 15 kV ccelerating voltage and 15 mA current using CASINO.

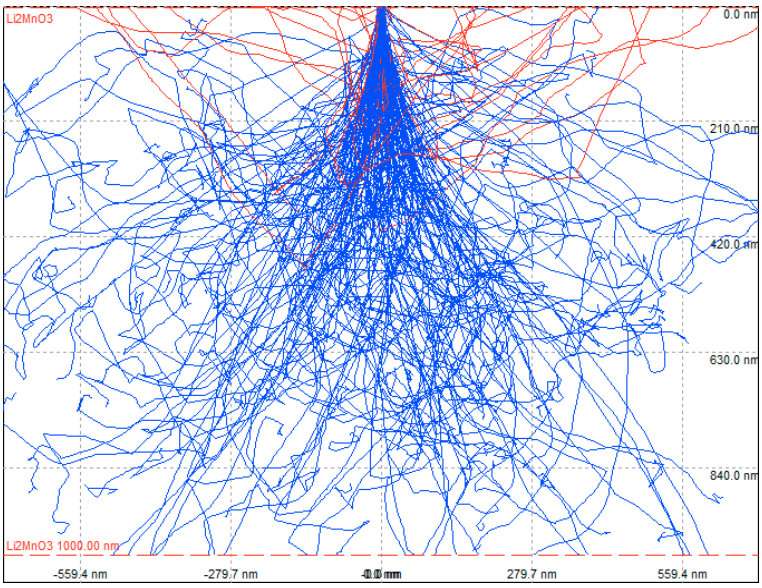

Figure E.5 Electron trajectory in a thin film of Li_2MnO_3 (1000 nm), simulated with a 15 kV accelerating voltage and 15 mA current using CASINO.

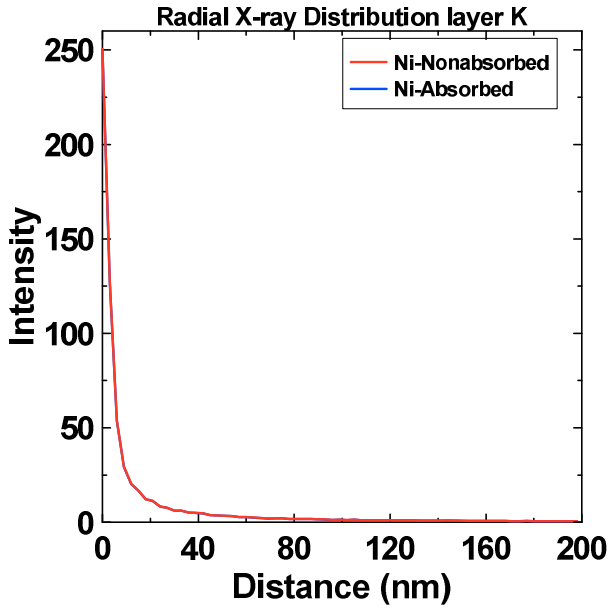

Figure E.6 Radial Mn K-edge X-ray distribution for the thin film of Li_2MnO_3 simulated with a 15 kV accelerating voltage and 15 mA current using CASINO.

F- APPENDIX F

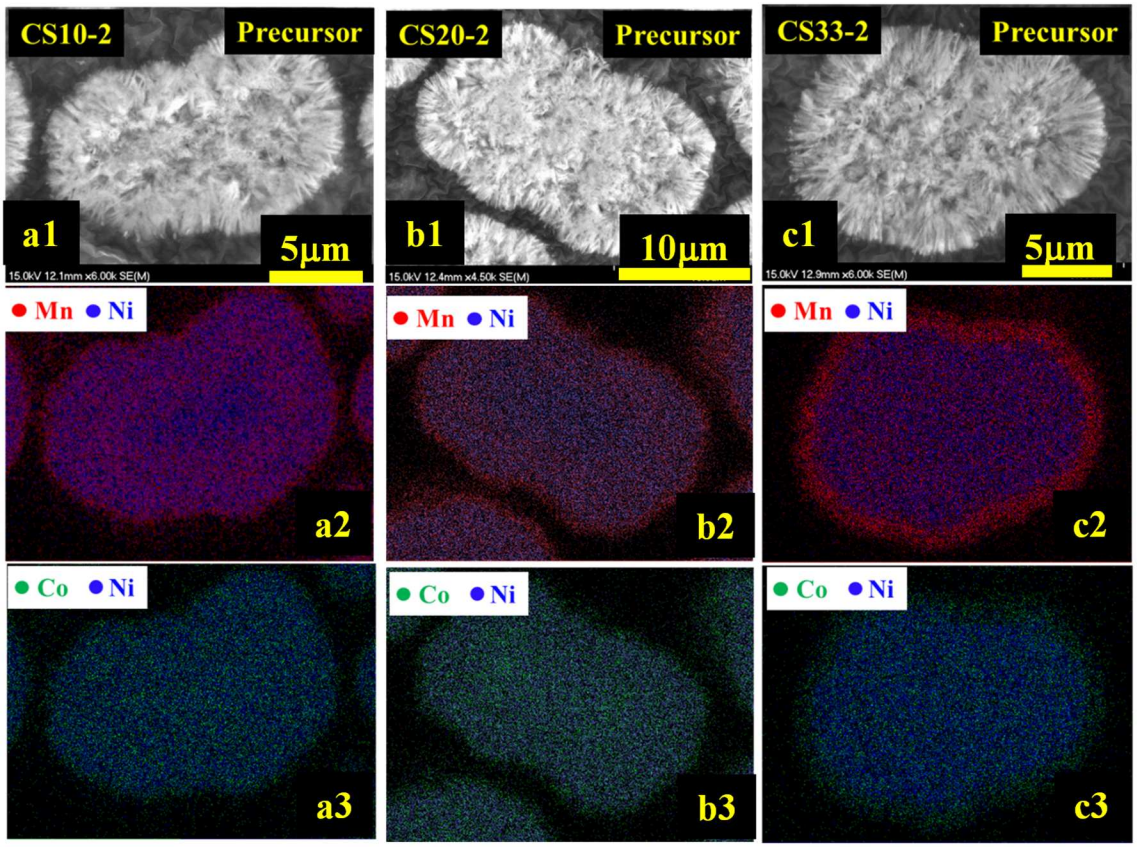

Figure F.1 SEM images and EDS mapping results of CS10 (a1 – a3), CS20 (b1 – b3) and CS33 (c1 – c3) precursors.

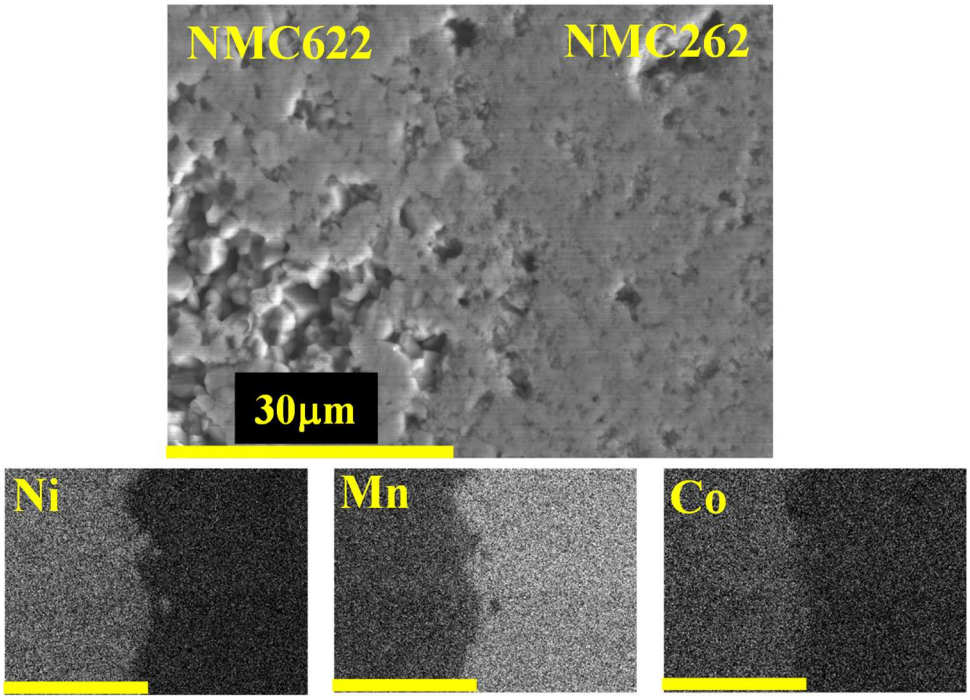

Figure F.2 The SEM image and EDS mapping of the NMC622/NMC262 pellet.

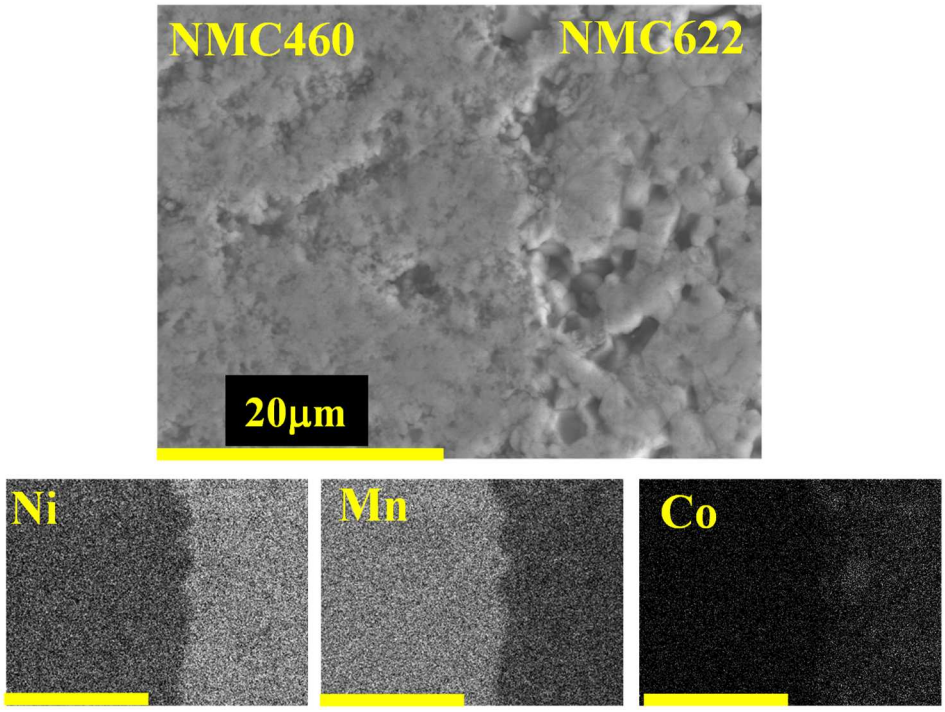

Figure F.3 The SEM image and EDS mapping of the NMC622/NMC460 pellet.

Table F.1 Lattice constants extracted from the XRD data for all the samples. The data were fit in $R\bar{3}m$ space group with an average phase for the CS samples.

Sample	850 °C		900 °C	
	a (± 0.0004 Å)	c (± 0.001 Å)	a (± 0.0004 Å)	c (± 0.002 Å)
C-1	2.8697	14.217	2.8739	14.232
C-2	2.8681	14.211	2.8721	14.227
C-3	2.8659	14.204	2.8706	14.223
CS10-1	2.8695	14.225	2.8723	14.235
CS10-2	2.8670	14.218	2.8705	14.231
CS10-3	2.8649	14.208	2.8694	14.228
CS20-1	2.8712	14.233	2.8705	14.238
CS20-2	2.8690	14.227	2.8692	14.229
CS20-3	2.8653	14.218	2.8674	14.230
CS33-1	2.8718	14.240	2.8729	14.249
CS33-2	2.8690	14.228	2.8699	14.233
CS33-3	2.8671	14.225	2.8684	14.234

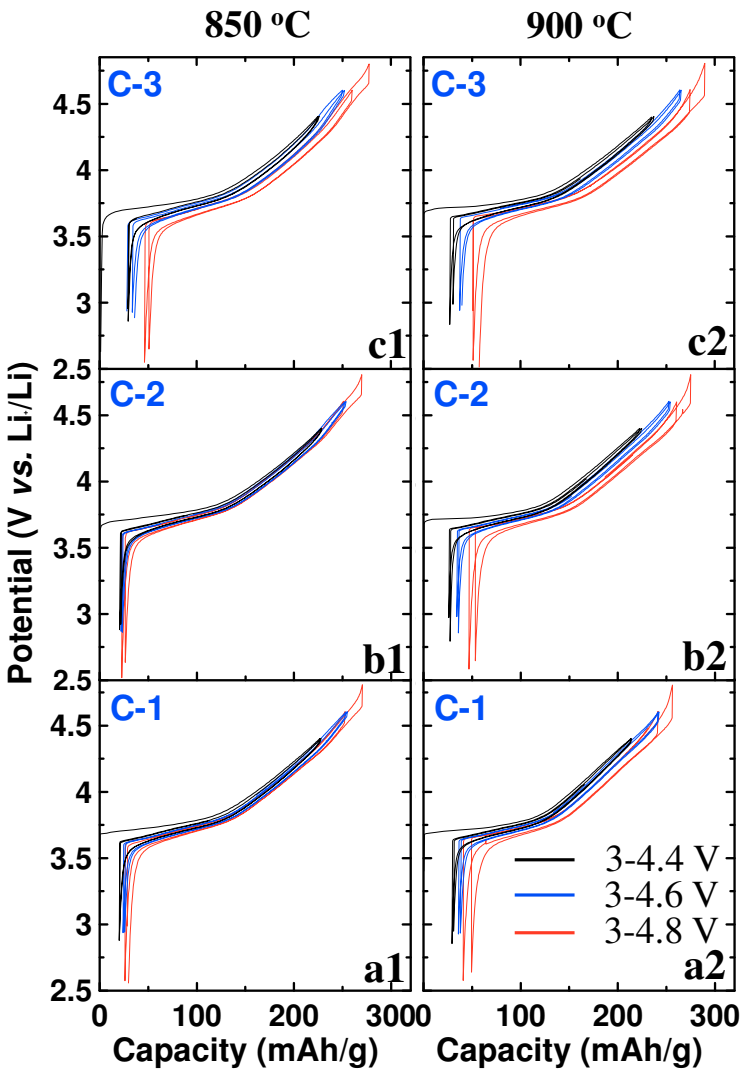

Figure F.4 Cell voltage as a function of specific capacity for C-1 (a1), C-2 (b1) and C-3 (c1) prepared at 850ºC and C-1 (a2), C-2 (b2) and C-3 (c2) prepared at 900ºC. The cells were tested between 2.5-4.4 V for 4 cycles, 2.5-4.6 V for 10 cycles, 2.5-4.8V for 1 cycle, and 2.5-4.6 V for another 10 cycles with a current of 10 mA/g at 30ºC.

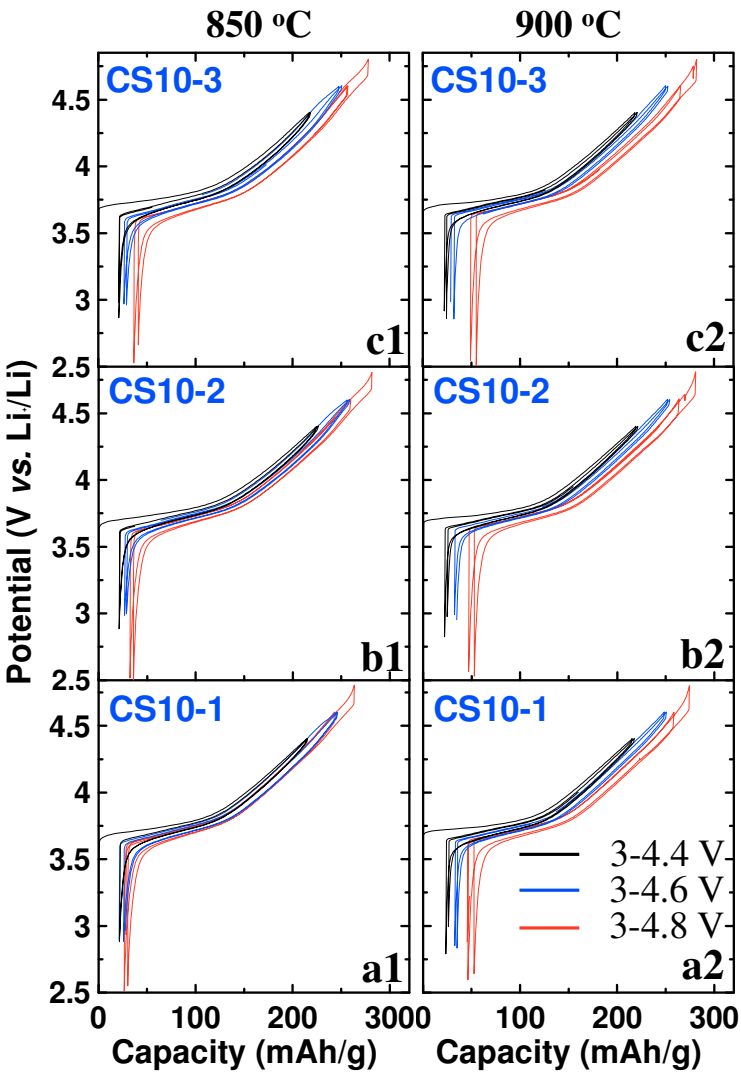

Figure F.5 Cell voltage as a function of specific capacity for CS10-1 (a1), CS10-2 (b1) and CS10-3 (c1) prepared at 850°C and CS10-1 (a2), CS10-2 (b2) and CS10-3 (c2) prepared at 900°C. The cells were tested between 2.5-4.4 V for 4 cycles, 2.5-4.6 V for 10 cycles, 2.5-4.8V for 1 cycle, and 2.5-4.6 V for another 10 cycles with a current of 10 mA/g at 30°C.

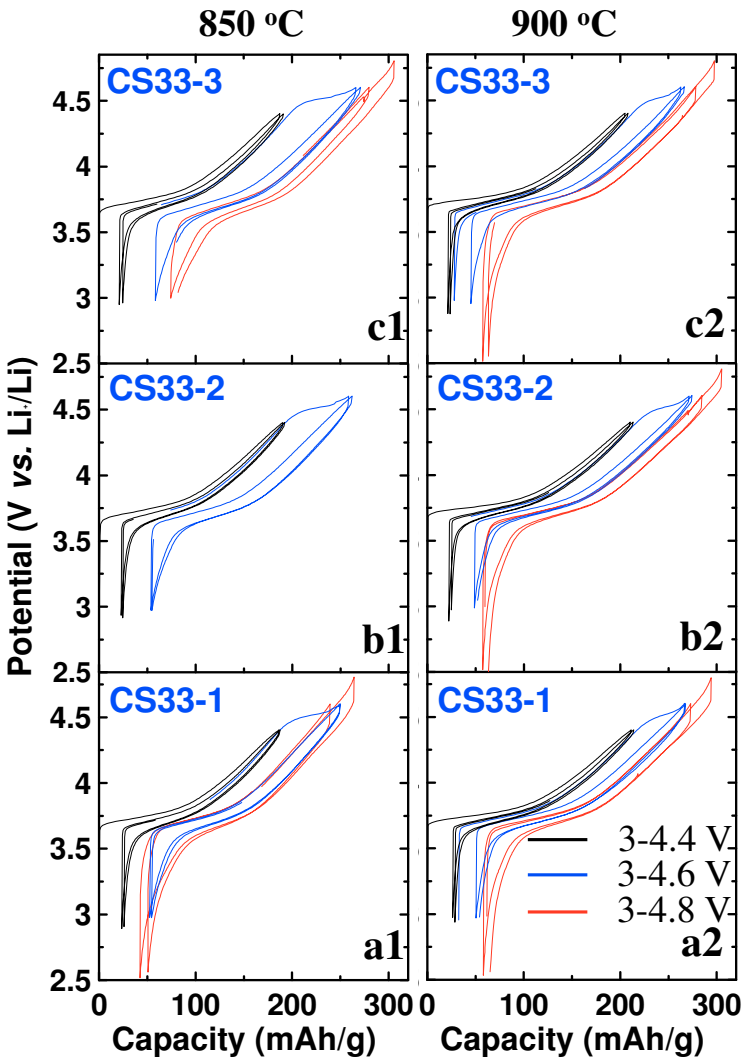

Figure F.6 Cell voltage as a function of specific capacity for CS33-1 (a1), CS33-2 (b1) and CS33-3 (c1) prepared at 850°C and CS33-1 (a2), CS33-2 (b2) and CS33-3 (c2) prepared at 900°C. The cells were tested between 2.5-4.4 V for 4 cycles, 2.5-4.6 V for 10 cycles, 2.5-4.8 V for 1 cycle, and 2.5-4.6 V for another 10 cycles with a current of 10 mA/g at 30°C.

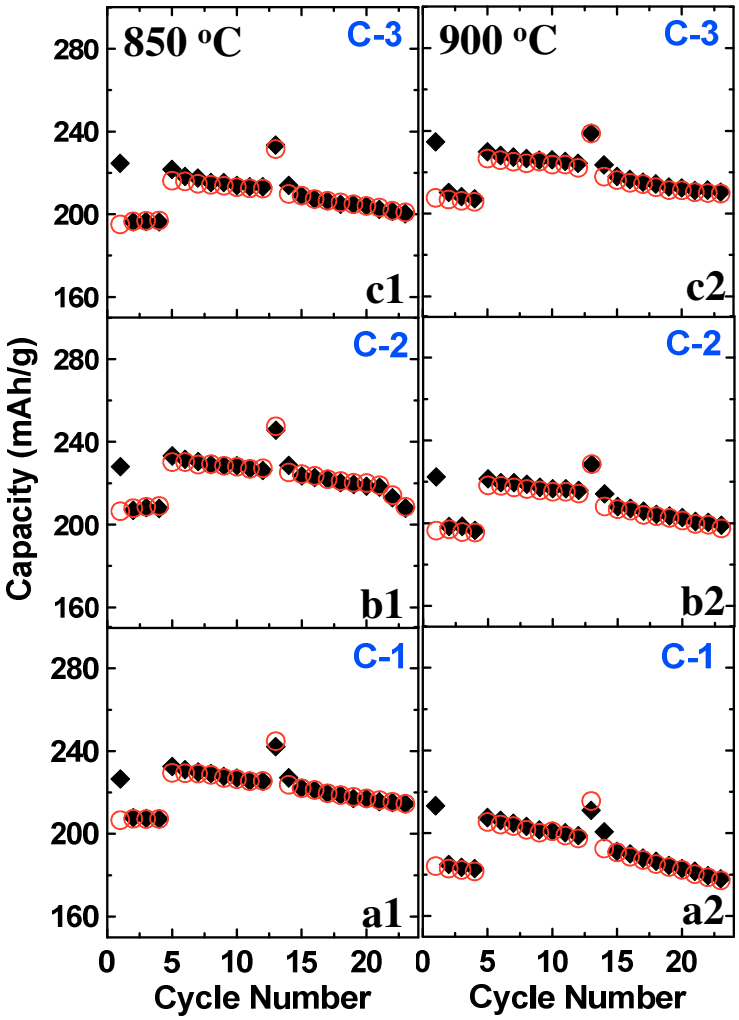

Figure F.7 Specific capacity as a function of cycle number for C-1 (a1), C-2 (b1) and C-3 (c1) prepared at 850°C and C-1 (a2), C-2 (b2) and C-3 (c2) prepared at 900°C. The cells were tested between 2.5-4.4 V for 4 cycles, 2.5-4.6 V for 10 cycles, 2.5-4.8 V for 1 cycle, and 2.5-4.6 V for another 10 cycles with a current of 10 mA/g at 30°C.

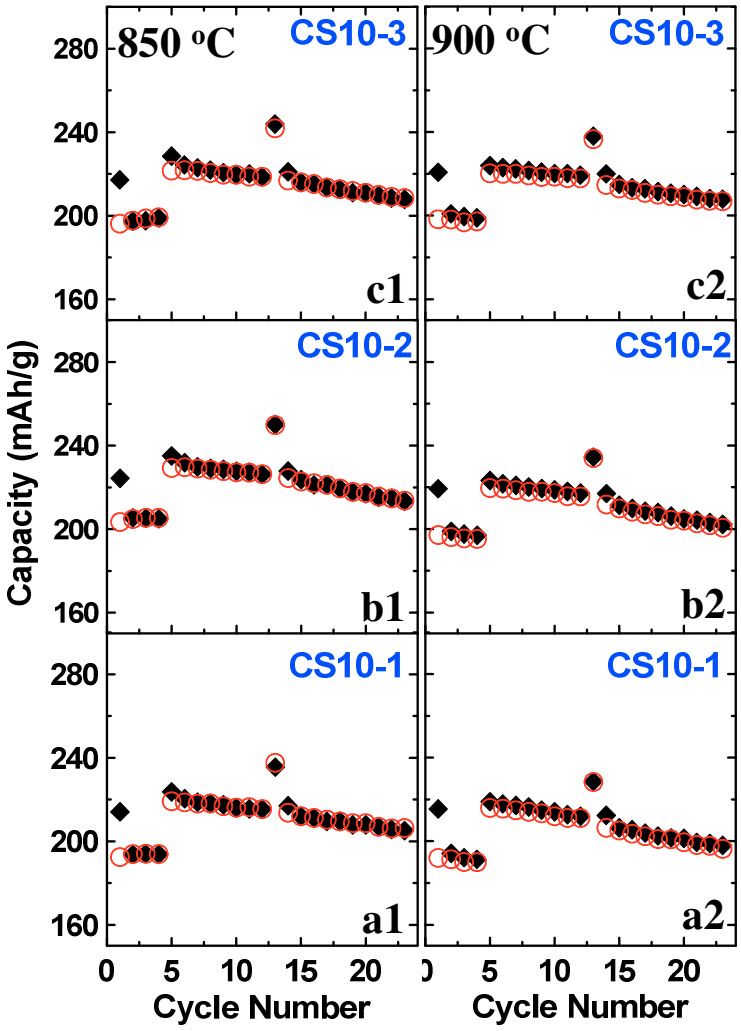

Figure F.8 Specific capacity as a function of cycle number for CS10-1 (a1), CS10-2 (b1) and CS10-3 (c1) prepared at 850 °C and CS10-1 (a2), CS10-2 (b2) and CS10-3 (c2) prepared at 900 °C. The cells were tested between 2.5-4.4 V for 4 cycles, 2.5-4.6 V for 10 cycles, 2.5-4.8 V for 1 cycle, and 2.5-4.6 V for another 10 cycles with a current of 10 mA/g at 30 °C.

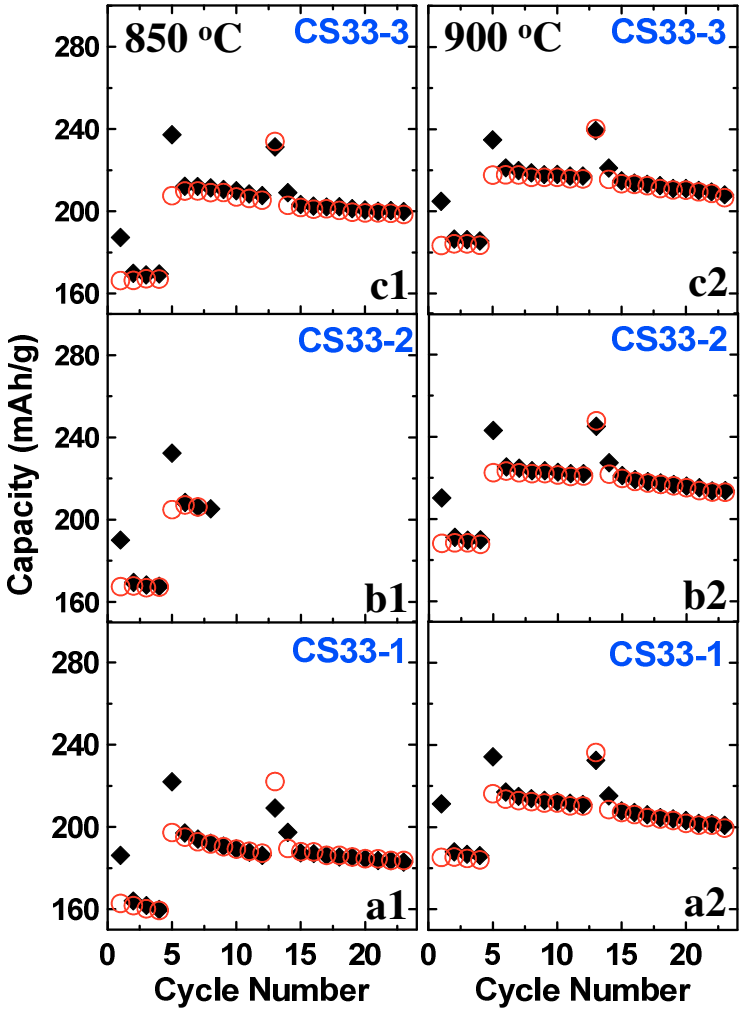

Figure F.9 Specific capacity as a function of cycle number for CS33-1 (a1), CS33-2 (b1) and CS33-3 (c1) prepared at 850 °C and CS33-1 (a2), CS33-2 (b2) and CS33-3 (c2) prepared at 900 °C. The cells were tested between 2.5-4.4 V for 4 cycles, 2.5-4.6 V for 10 cycles, 2.5-4.8 V for 1 cycle, and 2.5-4.6 V for another 10 cycles with a current of 10 mA/g at 30 °C.

G- APPENDIX G: COPYRIGHT PERMISSIONS

Title:	Effect of turbostratic disorder in graphitic carbon hosts on the intercalation of lithium
Author:	Tao Zheng, J. N. Reimers, and J. R. Dahn
Publication:	Physical Review B
Publisher:	American Physical Society
Date:	Jan 1, 1995

Logged in as:
Jing li
Account #:
3001019058

LOGOUT

Order Completed

Thank you for your order.

This Agreement between Jing li ("You") and American Physical Society ("American Physical Society") consists of your license details and the terms and conditions provided by American Physical Society and Copyright Clearance Center.

Your confirmation email will contain your order number for future reference.

Get the printable license.

License Number	3860330170052
License date	May 01, 2016
Licensed Content Publisher	American Physical Society
Licensed Content Publication	Physical Review B
Licensed Content Title	Effect of turbostratic disorder in graphitic carbon hosts on the intercalation of lithium
Licensed Content Author	Tao Zheng, J. N. Reimers, and J. R. Dahn
Licensed Content Date	Jan 1, 1995
Licensed Content Volume	51
Type of use	Thesis/Dissertation
Requestor type	Student
Format	Print, Electronic
Portion	image/photo
Number of images/photos requested	2
Portion description	Figure 1 and Figure 2
Rights for	Main product
Duration of use	Life of Current Edition
Creation of copies for the disabled	no
With minor editing privileges	no
For distribution to	Worldwide
In the following language(s)	Original language of publication
With incidental promotional use	no
Lifetime unit quantity of new product	100000 or more
The requesting person/organization	Jing Li
Order reference number	None
Title of your thesis / dissertation	STUDY AND DEVELOPMENT OF LAYERED LI-NI-MN-CO OXIDE POSITIVE ELECTRODE MATERIALS FOR LITHIUM ION BATTERIES
Expected completion date	Jun 2016

Title: Comparison of the structural and electrochemical properties of layered Li[NixCoyMnz]O2 (x = 1/3, 0.5, 0.6, 0.7, 0.8 and 0.85) cathode material for lithium-ion batteries

Author: Hyung-Joo Noh,Sungjune Youn,Chong Seung Yoon,Yang-Kook Sun

Publication: Journal of Power Sources

Publisher: Elsevier

Date: 1 July 2013

Order Completed

Thank you very much for your order.

This is a License Agreement between Jing li ("You") and Elsevier ("Elsevier"). The license consists of your order details, the terms and conditions provided by Elsevier, and the payment terms and conditions.

Get the printable license.

License Number	3860380282203
License date	May 01, 2016
Licensed content publisher	Elsevier
Licensed content publication	Journal of Power Sources
Licensed content title	Comparison of the structural and electrochemical properties of layered Li[NixCoyMnz]O2 (x = 1/3, 0.5, 0.6, 0.7, 0.8 and 0.85) cathode material for lithium-ion batteries
Licensed content author	Hyung-Joo Noh,Sungjune Youn,Chong Seung Yoon,Yang-Kook Sun
Licensed content date	1 July 2013
Licensed content volume number	233
Licensed content issue number	n/a
Number of pages	10
Type of Use	reuse in a thesis/dissertation
Portion	figures/tables/illustrations
Number of figures/tables /illustrations	1
Format	both print and electronic
Are you the author of this Elsevier article?	No
Will you be translating?	No
Original figure numbers	Figure 11
Title of your thesis/dissertation	STUDY AND DEVELOPMENT OF LAYERED LI-NI-MN-CO OXIDE POSITIVE ELECTRODE MATERIALS FOR LITHIUM ION BATTERIES
Expected completion date	Jun 2016
Estimated size (number of pages)	400
Elsevier VAT number	GB 494 6272 12

Title: Different oxygen redox participation for bulk and surface: A possible global explanation for the cycling mechanism of Li1.20Mn0.54Co0.13Ni0.13O2

Author: Hideyuki Koga,Laurence Croguennec,Michel Ménétrier,Philippe Mannessiez,François Weill,Claude Delmas

Publication: Journal of Power Sources

Publisher: Elsevier

Date: 15 August 2013

Order Completed

Thank you very much for your order.

This is a License Agreement between Jing li ("You") and Elsevier ("Elsevier"). The license consists of your order details, the terms and conditions provided by Elsevier, and the payment terms and conditions.

Get the printable license.

License Number	3876681464894
License date	May 26, 2016
Licensed content publisher	Elsevier
Licensed content publication	Journal of Power Sources
Licensed content title	Different oxygen redox participation for bulk and surface: A possible global explanation for the cycling mechanism of Li1.20Mn0.54Co0.13Ni0.13O2
Licensed content author	Hideyuki Koga,Laurence Croguennec,Michel Ménétrier,Philippe Mannessiez,François Weill,Claude Delmas
Licensed content date	15 August 2013
Licensed content volume number	236
Licensed content issue number	n/a
Number of pages	9
Type of Use	reuse in a thesis/dissertation
Portion	figures/tables/illustrations
Number of figures/tables /illustrations	1
Format	both print and electronic
Are you the author of this Elsevier article?	No
Will you be translating?	No
Title of your thesis/dissertation	STUDY AND DEVELOPMENT OF LAYERED LI-NI-MN-CO OXIDE POSITIVE ELECTRODE MATERIALS FOR LITHIUM ION BATTERIES
Expected completion date	Jun 2016
Estimated size (number of pages)	400
Elsevier VAT number	GB 494 6272 12
Permissions price	0.00 USD

Title: Structural transformation of a lithium-rich Li1.2Co0.1Mn0.55Ni0.15O2 cathode during high voltage cycling resolved by in situ X-ray diffraction

Author: Debasish Mohanty,Sergiy Kalnaus,Roberta A. Meisner,Kevin J. Rhodes,Jianlin Li,E. Andrew Payzant,David L. Wood,Claus Daniel

Publication: Journal of Power Sources

Publisher: Elsevier

Date: 1 May 2013

Published by Elsevier B.V.

Order Completed

Thank you very much for your order.

This is a License Agreement between Jing Il ("You") and Elsevier ("Elsevier"). The license consists of your order details, the terms and conditions provided by Elsevier, and the payment terms and conditions.

Get the printable license.

License Number	3876690091555
License date	May 26, 2016
Licensed content publisher	Elsevier
Licensed content publication	Journal of Power Sources
Licensed content title	Structural transformation of a lithium-rich Li1.2Co0.1Mn0.55Ni0.15O2 cathode during high voltage cycling resolved by in situ X-ray diffraction
Licensed content author	Debasish Mohanty,Sergiy Kalnaus,Roberta A. Meisner,Kevin J. Rhodes,Jianlin Li,E. Andrew Payzant,David L. Wood,Claus Daniel
Licensed content date	1 May 2013
Licensed content volume number	229
Licensed content issue number	n/a
Number of pages	10
Type of Use	reuse in a thesis/dissertation
Portion	figures/tables/illustrations
Number of figures/tables /illustrations	1
Format	both print and electronic
Are you the author of this Elsevier article?	No
Will you be translating?	No
Title of your thesis/dissertation	STUDY AND DEVELOPMENT OF LAYERED LI-NI-MN-CO OXIDE POSITIVE ELECTRODE MATERIALS FOR LITHIUM ION BATTERIES
Expected completion date	Jun 2016
Estimated size (number of pages)	400
Elsevier VAT number	GB 494 6272 12
Permissions price	0.00 USD